Institute of Electrical Power Systems

Conceptual Power System Design for the Future Circular Collider

A Dissertation by
Thomas Michael Höhn

Supervisor
Herwig Renner

Reviewer
Drazen Dujic

October 2022

Intern

Statutory Declaration

I declare that I have authored this thesis independently, that I have not used other than the declared sources / resources, and that I have explicitly marked all material which has been quoted either literally or by content from the used sources.

Graz, October 2022

Thomas Höhn

Eidesstattliche Erklärung

Ich erkläre an Eides statt, dass ich die vorliegende Arbeit selbstständig verfasst, andere als die angegebenen Quellen/Hilfsmittel nicht benutzt, und die den benutzten Quellen wörtlich und inhaltlich entnommenen Stellen als solche kenntlich gemacht habe.

Graz, Oktober 2022

Thomas Höhn

Acknowledgements

All my gratitude and my deepest thanks go to Professor Herwig Renner. Sovereign as a guide, highly skilled in scientific working and being particularly an expert in the field of electrical engineering, he has been a dedicated supervisor with integrity and the honest will to help.

I thank Francisco Blanquez, for being a passionate and helpful CERN supervisor. Francisco had always time for discussions, even late after work or in his free time. He taught me much about power grids and power converters. I thank Karsten Kahle for teaching me in technical communication and presentations. I also thank Gilles Le Godec for helping me with complex power converter topologies and Davide Aguglia for precious hints about sensibility analyses and explanations about middle-frequency transformers. I appreciated the interdisciplinary work within the FCC working group of Volker Mertens and the help of the many colleagues within the Electric Power Converters Group of Jean-Paul Burnet.

Grateful for my friends, I thank Anton, Christoph and Florian, for the comforting and helpful time they spend for me whenever and wherever I needed it.

The warmest thanks go to my family. I am infinite thankfully for all they have done for me, so I use this occasion to thank my grandparents Kunigunde and Ägidius, my parents Anita and Otto, and my two sisters, Julia and Sophie.

Milady Marion proved to be a true companion and counsellor, having always wise, calming and motivating words for me.

Grazie cara.

Abstract

The Future Circular Collider (FCC) needs a very large electrical infrastructure and complex power systems to supply many types of loads, with ratings from some MW up to hundreds of MW. The goal is to find a powering topology, which guarantees the required reliability, is immune against transient voltage dips, and is optimised in terms of space demand, losses and investment costs.

Three in principle different powering topologies have been identified as potentially applicable. A comparative study was the key to highlight their advantages how their performance relates to one another. A DC-based power supply appeared to be the optimised solution.

The dip immunity strategy is based on the analysis of dips, dip-sensitive load and countermeasures. Full dip immunity is guaranteed for the complete FCC by practical measures and no large and expensive active dip mitigation device (DVR or HVDC back-to back link) is needed. Because all dip sensitive load is powered already by a converter and small design upgrades lead automatically to dip immunity. Dedicated studies for the main bending magnets and the cryogenic system are proofing this concept and act also as a principal design guide for dip immune power converters.

The converter control concept for the main bending dipole power converter has been successfully proven by a simulation model. The dipole magnets can be ramped up, by using partly the power and energy from the integrated battery energy storage. This battery is directly connected to the low voltage DC bus of the converter, thus representing a highly efficient integration.

The high-power cryogenic compressor system is fully represented in a simulation model, reflecting the electrodynamic and mechanical behaviour. The direct torque and space vector control concept for this application has been successfully verified during normal operation and transient voltage dips.

Synergies can be realised if the individual power systems are combined to a universal and dip immune DC grid. In this case, the battery energy storage can be used for peak shaving and dip mitigation. A simulation study proofs the concept, emphasising a modular switch-mode-based converter with a digital polynomial controller for a precise release of power from the energy storage.

Kurzfassung

Zukünftige Kreisbeschleuniger wie der Future Circular Collider (FCC) benötigen eine sehr große elektrische Infrastruktur zur Versorgung vieler Lasten, mit Nennleistungen von einigen MW bis Hunderten von MW. Ziel ist es, eine Versorgungsstruktur zu finden, die ausreichend Zuverlässigkeit ist, Immunität gegen Spannungseinbrüche aufweist und hinsichtlich des Platzbedarfes, Verlusten und Investitionskosten optimiert ist.

Drei unterschiedliche Topologien sind als potenziell anwendbar identifiziert worden. Deren systematischer Vergleich zeigt die relativen Vor- und Nachteile. Eine DC-basierte Versorgung für Lasten im Untergrund ist dabei die optimierte Lösung.

Die Dip Immunität Strategie basiert auf der Analyse der Dips, der Dip-Sensiblen Lasten und einer Evaluierung von Abhilfen. Durch einfache Maßnahmen wird volle Dip-Immunität für FCC gewährleistet. Da alle Dip-empfindlichen Lasten von einem Umrichter gespeist werden, sind direkte Maßnahmen an selbigen Umrichter die effizienteste Methode. Dedizierte Studien für die Dipole und das kryogene Kühlsystem zeigen die Wirksamkeit und dienen gleichsam als Leitfaden für das empfohlene Umrichter Design.

Das Regelungskonzept für den Dipol-Stromrichter wurde durch ein Simulationsmodell erfolgreich nachgewiesen. Die Dipolmagnete können hochgefahren werden, indem teilweise die Leistung und Energie aus dem integrierten Batteriespeicher verwendet wird. Diese Batterie ist direkt mit dem Niederspannungs-DC-Bus des Umrichters verbunden und stellt somit eine hocheffiziente Integration dar.

Der hochleistungsfähige Kompressor für das kryogene Kühlsystem wird vollständig in einem Simulationsmodell abgebildet und das elektrodynamische sowie mechanische Verhalten sind analysiert worden. Das Konzept der direkten Drehmoment- und Raumvektorregelung für diese Anwendung wurde im Normalbetrieb und bei transienten Spannungseinbrüchen erfolgreich verifiziert.

Eine Synergie für den Energiespeicher wird realisiert, wenn er nicht nur zum Decken von Leistungsspitzen, sondern auch für Dip-Immunität genutzt wird. Bedingung ist, dass der Energiespeicher und alle Lasten an ein eigens designtes Gleichstromnetz angeschlossen sind. So entsteht ein optimiertes, universelles und dip-immunes DC-basiertes Stromversorgungssystem für den FCC. Dieses Konzept ist in einem Simulationsmodell verifiziert und dabei speziell gezeigt ist die effiziente Funktionsweise eines modularen Umrichters, der mit einem digitalen Polynom Controller den Leistungsfluss aus dem Energiespeicher steuert.

List of Symbols

ASD	Adjustable speed drive
cv	Constant voltage ramping
cp	Constant power ramping
C_i	Costs of the supplying infrastructure
c_{es}	Specific costs of energy storage capacity (in €/kWh)
C_{es}	Costs of the energy storage
DAB	Dual active bridge topology, two full H-bridges with middle-frequency transformers
f_c	The cost function for the optimisation
$f_{sw\ stage\ 3}$	Switching frequency of the DC-DC H-bridge converter in stage 3
$f_{sw\ DAB}$	Switching frequency of the DAB in stage 2
i_{batt}	Current flowing in or out of the battery energy storage on converter module level
i_m	Current in the magnet circuit
i_{out}	Current flowing in or out of one converter module
$I_{m\ nom}$	Nominal current in the magnet circuit, the desired current level for stable beams operation
I_{stator}	Stator current of the three-phase induction machine in the compressor study
LHC	Large Hadron Collider
L_m	Apparent inductance of one main bending magnet circuit
L_{DAB}	Total inductance for power transfer of the mf transformer (transformer leakage and additional inductance)
mf	Middle frequency
MTBF	Meantime between failure
R_m	Resistance of one main bending magnet circuit

R_{batt}	The internal resistance of the battery used as energy storage in the converter modules
p_i	Actual power delivered by the supplying infrastructure
P_i	Power rating of the supplying infrastructure
$p_{loss\ infr.\ >36kV}$	Losses occurring in the infrastructure above 36kV
$p_{loss\ m}$	Losses occurring in the magnet circuit
$p_{loss\ stage\ 1}$	Losses occurring in stage 1
$p_{loss\ stage\ 2}$	Losses occurring in stage 2
$p_{loss\ stage\ 3}$	Losses occurring in stage 3
$p_{stage\ 3}$	Actual power demand of the converter output of MPS stage 3
sf	Scaling factor for a specific energy storage capacity (overrating)
t_i	Time until p_i reaches P_i during the ramping
u_{DC}	DC link voltage
u_{Lm}	Voltage directly at L_m, to create the desired di/dt
u_{in}	Input voltage of the stage 2 converter module
u_{out}	Output voltage of the stage 2 converter module
u_m	Voltage at the input terminals of the magnet circuit
$u_{m\ max}$	Maximum voltage at the input terminals of the magnet circuit
W_{es}	Capacity of the energy storage (in kWh)
$W_{es\ batt}$	Capacity of battery energy storage (in kWh)
$W_{es\ max}$	Maximum capacity of the energy storage (in kWh)
W_i	Energy supplied by the infrastructure
W_m	Energy stored in the magnet circuit
$W_{loss\ m}$	Lost energy in the magnet circuit
$W_{loss\ stage\ 3}$	Lost energy in the MPS stage 3
x	The optimisation variable

Table of Contents

1 Motivation of the thesis

1.1 Purpose and technical challenges of the Future Circular Collider

Humanity craves for discovering the mysteries of our universe. To find explanations for phenomena as dark matter or the matter/antimatter asymmetry, new large-scale research laboratories are essential. Among these new laboratories currently under study is the Future Circular Collider (FCC) at the European Organization for Nuclear Research CERN. A collision energy seven times higher than the most powerful particle accelerator nowadays can lead to discoveries beyond the standard model. In this dissertation, the main focus is on FCC as a hadron-hadron collider version (FCC-hh). The foreseen collision energy is 100 TeV. In comparison, at the Large Hadron Collider (LHC) 14 TeV as collision energy is reached.

Figure 1: The Future Circular Collider, source: [1] [2].

To build a particle accelerator as large and powerful as FCC, many technical challenges must be managed. From an electrical power supply point of view, the following has to be highlighted. The peak power demand of FCC exceeds the actual power limit of the 400 kV grid and cannot be operated at all unless remedies are found. This was presented at the international FCC week workshops 2017 [3] and 2018 [4]. The large extent of FCC means also a widely distributed electrical infrastructure and equipment around its 100 km ring. A large part is in addition installed in underground structures, on average 200 m below the surface. This makes it hard to achieve high reliability. A large part of the load needs specially designed power converter systems. Super conducting magnets need very high direct current – tens of kA – with high precision during all phases of their cycling operation, whereas their voltage demand of tens to some hundreds of volts is rather low. The cryogenic high speed compressors need adjustable speed drives which are rated to tens of MW and can operate up to 200 Hz. Particle accelerators are sensitive to disturbances happening in the supplying transmission grid. In particular, transient voltage dips, which can arise during thunderstorms, are penetrating the whole FCC power grid and potentially leading to a full stop of the particle accelerator operation. Thus causing restart and maintenance operations and most of all, delaying physical research. Certainly, the goal of a multi-billion [5] research laboratory is to be immune against such disturbances.

All requirements and constraints are closely interwoven. They need to be dissolved, analysed, and brought harmoniously together, as this work has the goal to find an overall solution for the FCC power supply.

1.2 Principle power supply of the main FCC loads

The Future Circular Collider is with a large spatial extent and a high power demand, an outstanding proposal for a future large-scale research laboratory.

Particle accelerators consist of many different types of load. From general AC-loads like lighting and other auxiliary demands to very particular loads like a radio frequency power source or super conducting magnets. Concerning this dissertation, the main load categories are characterised as shown in the table below. The given power demand estimations are from the international FCC week workshops 2017 [3] and 2018 [4].

Table 1: Main FCC load types and their estimated power demand

Load type	Power demand	Remark
Main bending dipole magnets	**± up to 287MW peak**	**Power peaks occur during the ramp-up and ramp down of FCC**
All other magnets	80MW	Magnets for beam guiding and in experimental zones
Cryogenic system	250MW	Cryogenic cooling for superconducting magnets and all cryogenic connection lines
Radio frequency (RF)	26MW	Klystrons are used to generate RF power
Injectors	68MW	Pre-accelerating stages
Cooling, ventilation, data centres and general supply for infrastructure and services	130MW	Standard load
Sum	$554MW_{avg.}$ ±287MW	

The main focus in this dissertation is on the power supply for the main bending dipole magnets, the cryogenic compressors and to seamlessly integrate both of them into a larger part of the FCC power supply. Further, also all load other parts are analysed and brought in relation with each other, culminating in a universal power system design guideline for FCC.

In terms of powering, the planned FCC layout has three powering points of the 400 kV grid. These are the substations “Bois-Tollot”, “Genissiat” and “Cornier”, all connected to the French 400 kV system, which is operated by Réseau de Transport d’Electricité (RTE). Although substation “Genissiat” is strongly connected to the grid and rather close to nuclear power plants (NPP Bugey, NPP Saint-Alban), the overall supply capacity is limited. In each 400 kV substation, two 220 MVA transformers will supply the underlying distribution system.

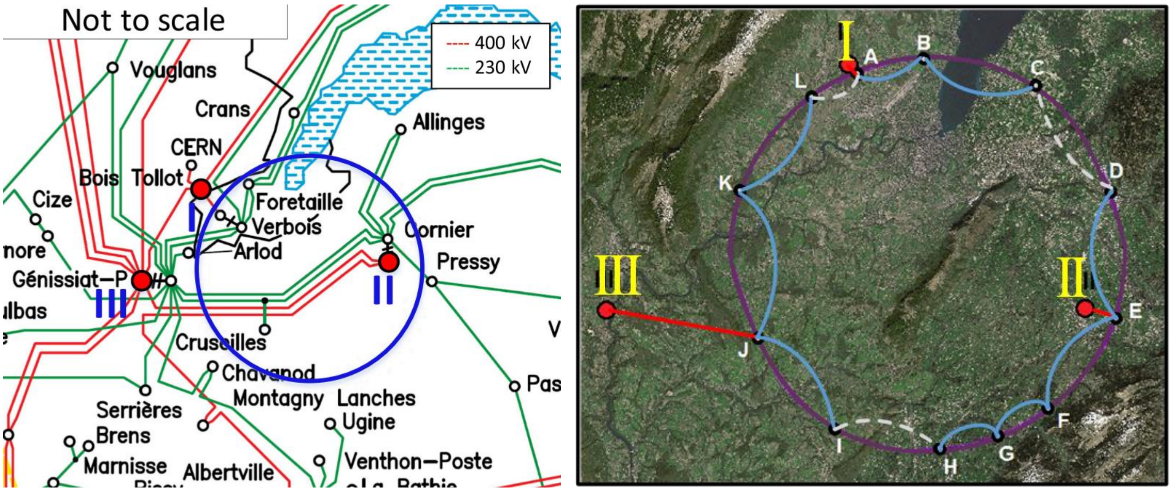

Figure 2: Preliminarily powering layout for FCC on the transmission grid level. Highlighted are the three 400kV substations (I, II and III) and their connection to the twelve FCC powering points (A-L), source: [4] [5].

For the distribution below 400 kV, FCC has its own 135 kV cable distribution grid to supply twelve FCC surface powering points A to L. The cable distribution is radially connecting these powering points and has the option of forming a complete ring supply to increase reliability. The planned distribution scheme is shown in Figure 3.

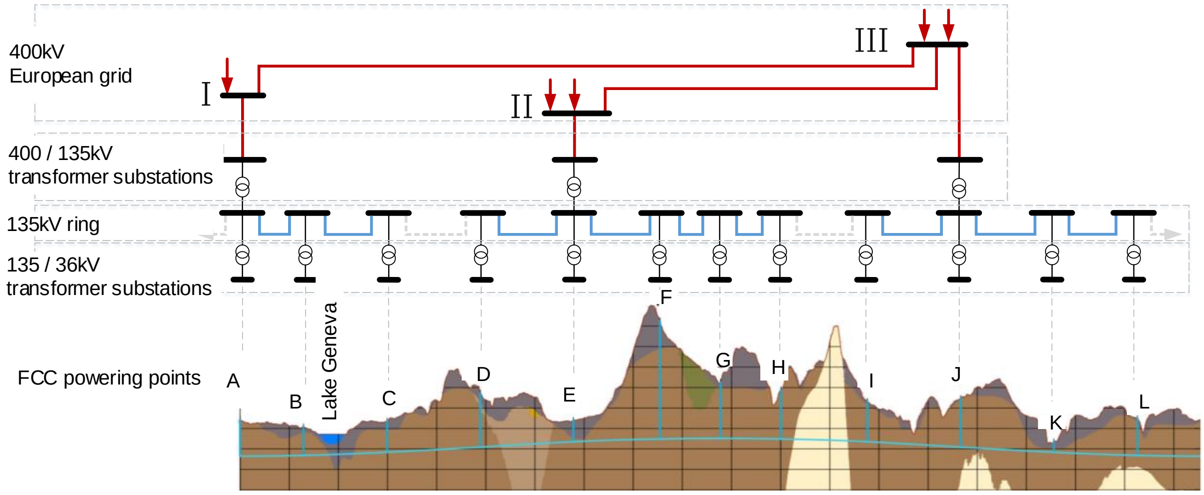

Figure 3: Main powering layout for FCC, source: [4].

At each of the twelve surface powering points, a local 36 kV distribution grid[1] is connected with two transformers, each with a rated power of 60 MVA (or 25 MVA for points with lower power demand). The 36 kV level is the starting point for the analysis in this dissertation as all complex load and their supplying power converters are found there. Only by a look close to the load (concerning the voltage level), their particular challenges can be revealed and power system design recommendations can be deducted.

1 The 36kV of the referred local distribution grid is the highest allowed voltage level within the grid and it used throw-out the whole work, thus it is conform with the presentations from CERN [4]. The nominal voltage of the local distribution grid is in the range of 30-33kV.

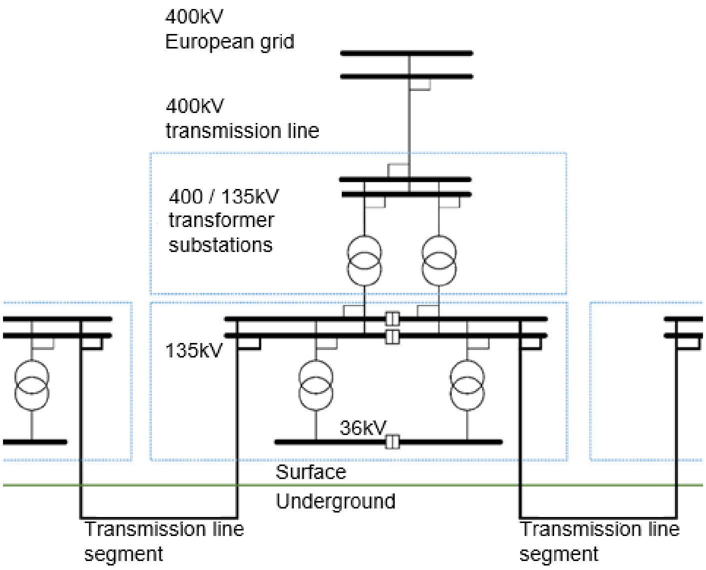

Figure 4: Radial supply scheme, exemplarily shown from the 400 kV connection point I. The 135 kV cable is connecting neighbouring FCC surface powering points. At each of these points, a local 36 kV distribution grid is supplying the actual load on the surface and underground. Source: [4].

From the principle supply challenges, the motivation of this work and the state of the art in powering large-scale research infrastructures can be deducted.

1.3 Motivation for this work

The performance of a multibillion research laboratory is the most important design aspect. If hundreds of millions are to be invested into the electrical supply, the chosen design need to guarantee the foreseen operation in the best way.

Starting from principle FCC power supply challenges with respect to the large extent, high average power and high peak power demand, this work looks below the 36kV level and shows the actual design of power converter systems for the challenging FCC loads.

These loads are very heterogeneous, have demanding requirements and are interdependent. All potentially identified power system designs need to be evaluated against performance criteria and can thus be evaluated also against each other.

1.4 Outline of the thesis

FCC is the continuation of building large research infrastructures for new discoveries in physics. Chapter 2 shows the state of art in powering research facilities previous to FCC. It also starts basic considerations if AC or DC based power supply systems are the preferred choice.

As FCC outperforms its predecessors in size, power and energy demand, research questions are derived and presented in chapter 3.

Chapter 4 describes actually the load of FCC. Their classification is done in terms of power and energy demand, constant or pulsing behaviour, and if they are considered sensitive to transient voltage dips. The subchapter peak power discussion shows the consequences of a high peak power demand from a grid and load side perspective, whereby for the load side a dedicated simulation model is used to show an instability effect. Finally, remedies against the high peak power demand are presented.

Chapter 5 discusses the power grid design option – AC or DC based – with respect to a power supply for particle accelerators. Three case studies are highlighting possible advantages of one over the other, whereby the first case study focus on an existing particle accelerator and the other two on a potential supply for FCC.

Chapter 6 presents the required functions of a potential powering topology for the main bending dipoles. Then three powering topology variants are identified and compared against each other. The performance indicators are reliability, losses, space demand and investment costs. As in each powering topology energy storage can be integrated, a cost function is used to find the optimised capacity of the energy storage and power rating for each of the powering variants A sensibility analysis gives further insight. The best powering variant is chosen to be further developed and analysed in the following chapters.

Chapter 7 starts with presenting the transient voltage dip problem in general and then in context of FCC whereby a simulation model is used to predict the dip situation for the FCC power supply. A simulation study for the biggest constant power load of FCC – the cryogenic compressor system – with respect to its behaviour during transient is done. Further, another simulation study shows how the best powering variant of chapter 6 can be extended to form a voltage dip immune power supply grid for the most important loads of FCC.

All conclusions are presented in chapter 8. They are in connection with the research questions and given their interdependency, they are also related to each other.

2 State of art in powering large-scale research infrastructures

2.1 Peak power and energy storage aspects

Peak power reduction to save energy is among the most important aspects when designing power systems for large-scale research infrastructures. Ways towards higher energy efficiency are funded by the European Union [6]. CERN initiated also a dedicated workshop e.g. [7] to discuss ideas about better use of energy in research laboratories, and one of the key concepts presented there is combining power converter systems and energy storage [8].

Existing power systems at CERN or in other research infrastructures e.g. the European Spallation Source ESS [9], use this concept mainly with capacitors as energy storage to cover power peaks with high power density. If the power peaks are lasting for a long time e.g. in the range of minutes, additional requirements towards the type of energy storage arise, as it needs not only to be power-dense but also energy-dense. A potential peak power limitation from the supplying AC transmission grid is another reason to consider energy storage. In the design study for the Compact Linear Collider (CLIC) [10], high voltages and capacitor banks are used to provide power peaks that are in the range of tens of GW.

For comparison, the fusion reactor research laboratory ITER [11] and FCC have about the same active peak power demand during their main magnet operation. But ITER has a much lower average power demand than FCC, and the active peak power can be provided by the transmission grid. For FCC, the total active power demand cannot be supplied by the transmission grid, as its limits are exceeded [3], [4].

The cycling operation of the main bending magnets of FCC leads to power peaks that are high in amplitude and duration. The total stored energy in the main magnets is 46MWh, thus capacitors as used in power system designs of other research laboratories, cannot be used anymore. Namely, batteries are to be considered in the design of FCC. To pave the way for this development, the high-luminosity upgrade of the LHC (HL-LHC) emphasizes batteries integrated into power converters for superconducting magnets [12].

The actual electrically connection of energy storage systems to power systems is done in general by power converters. Here lies the big advantage of a low voltage DC bus system. Under certain conditions, the energy storage system can be connected directly (without converters), as it is the case with electric cars. Other analysed examples are found in the high-quality supply system for sensitive loads [13], [14], or in the power supply of a commercial building [15]. The DC grid at the right voltage level is superior in technical and economic terms to the AC variant.

2.2 Reliability aspect

In general reliability is understood as the ability of a system to work under desired conditions within a specific period of time [16, 17]. In the design of power grids for future large-scale research laboratories, power converters are constituting a large and essential part of equipment and thus contributing to the total power system reliability [18]. In particular they are prone to aging and wear out failures, causing downtime and maintenance costs [19, 20].

The LHC has a total circumference of 27 km and has eight high inductive magnet circuits which require eight converters in the MW class. All eight converters have to work simultaneously and perfectly synchronised. These converters have no redundancies, though the reliability of the system is high enough to guarantee an acceptable operational performance of the LHC.

FCC has a circumference of 98 km and has 100 high inductive superconducting magnet circuits which require 100 converters in the MW class. The even larger spatial extent and the high number of high-power converters makes the reliability requirement much more evident than in previous large-scale research laboratories. Similarities can be found in large off-shore wind farms, where widely distributed generators in the MW class are connected in a collector grid. Also here the aim is to have high reliability, which is evaluated with dedicated studies [21]. With the difference that FCC stops completely if just one (out of hundred) converter fails.

Also in the design of the next generation of linear particle colliders, redundancies are respected. In the study for the Compact Linear Collider (CLIC) modular multilevel converter (MMC) topologies have been considered to power a medium-voltage DC grid [22]. The MMC topologies allow redundancies by the installation of additional spare converter modules. However, the high inductive superconducting magnet circuits of FCC, require a very high current and a low voltage supply, thus a common modular topology (MMC) cannot be used. Only input-series-output-parallel (ISOP) topologies fulfil the magnet-specific requirements due to the ISOP configuration and reliability requirements due to additional spare modules.

2.3 Equipment utilisation improvements by DC

When designing a power supply system, a principle choice between AC and DC based elements can be made. The comparison between medium voltage direct current (MVDC) grids and medium voltage alternating current (MVAC) grids within the scientific literature indicates the following points. For urban area distribution grids, reduced investment costs of an MVDC grid are shown [23]. The comparison in [24] shows that both, the MVDC and MVAC grid, have marginal differences in terms of electrical losses, and the efficiency of the MVDC depends on the DC/DC converter and the relative amount of DC to AC load. The distribution grid comparison in [25] shows higher losses for the MVDC grid. But on the other hand, better use of the installed transformer rating, and the reduction of compensation equipment are counted as benefits of the MVDC grid. For an offshore 50 km subsea transmission line, a study shows a loss reduction of up to 50% and a higher stability for the MVDC grid, having the converter costs for the high DC voltage as the main drawbacks [26].

In the field of future traction power systems, a 9 kV DC supply grid is compared with a 25 kV AC grid, showing a high potential in equipment reduction for MVDC grid while having the same performance [27]. A multi-terminal 24 kV DC power system compared with a 2x25 kV AC system resulted again in much reduced installed powering equipment and better interconnection to other DC sources and the main AC system [28]. A case study for the Swedish railway system highlights the advantages of equipment reduction by using a supplying DC power grid [29], and existing DC railway systems might be upgraded towards higher DC voltages [30], [31].

Future shipboard power systems have key design elements as simplicity, reliability, economics, and studies are showing that they can be best realised with an MVDC grid [32]. It reduces the weight of installed equipment on the ship and allows multiple loads (like propulsion, energy storage, and general constant load) to connect to the same power system. This leads to a highly efficient use of energy, shown in an example grid with a voltage in the range of 15-20 kV DC and a power rating of 40 MW [33]. The elimination of reactive power flow, power imbalances, harmonics, and bulky 50 Hz transformers, the easier integration of power sources and energy storage systems are stated as benefits for an MVDC shipboard grid study in [34].

2.4 Solid-state transformer and DC grids

The solid-state transformer (SST) is an important and actual research topic in the field of future power systems. The SSTs allow the interconnection of AC-based systems (grids or loads) with medium voltage DC grids or the interconnection of DC grids with different voltage levels. Even though they are identified as one of the key elements to improve future power systems, the costs of medium voltage power electronic switches are the main obstacle for the widespread use of the SST [35]. However, in applications with tight space or weight restrictions, the SST remains interesting despite a cost disadvantage [36]. A highly advantageous application of the

SST is in AC/DC conversion systems, as losses can be reduced to half, volume and weight reduced to a third, in comparison to line frequency transformer with a rectifier system [37].

The SST development in the last 60 years has brought in principle five topologies [38], where all of them are based on a single AC supply line. However, if an AC power line supplies the SST, the input stage must include AC line filters, and several SSTs connected to the same line leads to mutual influences of harmonics [39]. Further, the three-phase AC supplying infrastructure suffers from negative sequence currents caused by power imbalances due to the single AC line connection of the SST. In railway power systems special transformers, static VAr compensators, railway static power conditioner (RPC), or active power compensators (APC) are among the realized solutions for improving power quality [40].

The combination of an SST and a supplying DC grid improves further the advantages of volume and weight reduction. For railway power systems, an AC supplied SST is an actual research topic and has been successfully tested on a real locomotive [41]. The introduction of a DC grid at the railway power station has many advantages. It avoids power imbalances and allows a seamless integration of renewable power sources and energy storage [42]. If further, a DC grid is used to supply the train itself, a lighter and smaller Power Electronic Traction Transformer (PETT) could be installed on the train as a complete conversion stage, from AC to DC, is already done at the central DC grid forming rectifier. This is graphically shown but not explicitly discussed in [27].

The SST as a dual active bridge DC/DC converter is studied for a two-stage DC collector system for a 300 MW offshore wind farm, where it is shown that DC improves efficiency by 2% and reduces the investment costs up to 32% compared to an AC collector grid. Due to the lower wind turbine drivetrain output voltages in DC, the cable losses are higher, thus the DC benefits are valid up to a certain distance [43].

2.5 Voltage dip immunity

Particle accelerators can be considered sensitive to transient voltage dips. Either due to a sensible load itself or due to the sensibility of the power converters supplying the load. In any case, dip immunity considerations are very important in the design phase, as retrofitting to achieve dip immunity becomes very expansive.

Depending on the power rating of the dip-sensitive load, several solutions exist today. Among them are the static transfer switch or an uninterruptable power supply (UPS). For higher ratings, other solutions than the UPS are becoming interesting.

Sometimes found in dip-sensitive industrial production processes is the retrofitted Dynamic Voltage Restorer (DVR) as an active dip mitigation device. The application cases are rare, and the DVR remains a niche product for active dip mitigation. An illustrative example of a realized DVR project can be found in [44], where a sensitive and expensive chip production process was suffering frequently from dips. After the installation of a DVR, a continuous production process was possible. For even higher load ratings, the scientific literature proposes High Voltage Direct Current (HVDC) systems to supply large passive networks.

Dip immunity plays an important role in the operational performance of particle accelerators. For the multipurpose research reactor MYRRA, a perfect continuous operation of a linear particle accelerator is required as it is in relation with a very sensible reactor process [45]. In the case of synchrotrons, a storage ring is filled with high-energy proton beams, and a voltage dip can lead to a beam dump to protect the synchrotron from its own generated particle beams. A dip immune supply leads in this case to a more time-efficient operation, as no dip-caused beam dumps are occurring. A good example is the Large Hadron Collider (LHC), which needs some hours to fill its ring with high-energy proton beams. In the case of a severe voltage dip, the protection system extracts the beam immediately and precious time for physical data gaining is lost. If the cryogenic system also stops, the restart of the LHC can be delayed by days. The solution was to analyse the very sensitive processes and upgrade their specific supplying power converters [46].

The most efficient way to guarantee a full dip immunity for FCC is to analyse the load of FCC in detail, and directly upgrade the supplying power converter. Because all dip-sensitive load is powered by a power converter anyway. The vast experience from the LHC operation provides the guideline for these measures, as dip immunity is achieved exactly in this way: power converter upgrade instead of installing large and expensive additional equipment. The combination of power converter systems with integrated energy storage leads to synergies, as the energy storage (primarily installed for reducing power peaks) can also be used to stabilise the FCC distribution grid during a voltage dip.

At the level of a distribution grid the following distinction can be made. For MVAC grids voltage dip immunity can be achieved by a dynamic voltage restorer. This is a rather economic solution as it works only during the time of a voltage dip, to protect dip-sensitive loads, found for example in the semiconductor, or pulp and paper production industry. Different design options for the DVR are possible, whereby the differences are found in the type of energy storage (usually capacitors) and their specific charging topologies. Its design is under continuous study and development as the references [47–49] are indicating. A more versatile high-performance solution is the HVDC back-to-back link, which can provide in addition also reactive power. In [50] a multi-terminal hybrid HVDC grid is presented, in [51, 52] completely VSC-based converters are shown, whereby their compensation effect comes either from redundancies or from drawing overcurrent during the dip. In modular multilevel converter (MMC) based HVDC links, the compensation effect comes also from the installed capacitors in the modules. Their sizing may follow a dedicated design guideline [53]. In principle, it can be expected that they provide the fastest response [54], meaning the load should not experience the slightest disturbance.

For MVDC grids, a pulse width modulated (PWM) rectifier can be used to counteract transient voltage dips [55]. The switches must be designed for higher currents to compensate the voltage drop. Another option is to use an MMC as a rectifier to form a dip immune DC grid, following the same design guidelines as presented in [53]. For a certain class of DC grids, a very efficient, but much simpler and cheaper method can be applied. This method is based on using a dedicated boost converter in combination with a robust diode rectifier [56]. In this method, the leakage inductance of the rectifier-transformer is used for the boost-converter effect. The overall compensation effect comes from increased line currents, drawn by the boost converter during the voltage dip. For low voltage DC grids, it is also possible to connect a battery energy storage to achieve dip immunity.

2.6 Summary

A design for the power supply of FCC, which is to be built in the future, has to consider in principle all upcoming technologies and use their potential advantages. Among the challenging driving factors are the efficient integration of energy storage, dip immunity, savings in equipment weight and reduction in space requirements.

To reduce the peak power consumption from the transmission grid, the integration of energy storage is essential. For FCC important is to use an energy and power dense storage to overcome the limitation of the 400kV transmission grid.

The LHC has eight main bending converters with a non-modular design but FCC has 100 main bending converters which have to run simultaneously. To achieve an acceptable level of reliability, modular configurations of converters with spare module units are the key.

A principle design option for power grids is to choose between AC or DC based systems. If DC is superior over AC depends on the application, specific requirements, and the load. For the radio frequency system DC is even an essential requirement. An MVDC grid can improve power quality and reduce electrical infrastructure. Depending on the respective distances covered by the grid, also the losses can be reduced.

Voltage dip immunity is easier for DC grids, as the DC grid forming rectifier can already counteract, either by integrated energy storage in case of MMC rectifier or by drawing high currents with overrated power electronic switches. Also, a simple boost converter adaption can achieve the desired compensation effect.

DC grids are prone for equipment reduction. In particular, DC grids in combination with solid-state transformers have great potential for size and weight reduction compared with AC based power systems.

From the principle electrical supply challenges of FCC and the state of the art in powering such research infrastructures, the actual research questions in chapter 3 can be deducted. The chapters 4-7 are dedicated to answer these research questions.

3 Research questions

In general, a good power system design considers standardized components to reduce supply risks and to benefit from market competition. Additional margins in component ratings allow flexibility towards load increases in the future. When designing a power system for a certain load, power quality measures should avoid any negative system feedback. On the other hand, any potential disturbance spreading downstream must be avoided to achieve a continuous operation of the installation. Also important for a continuous power supply are redundancy concepts, as each component might fail with a certain probability. A redundancy concept which is considered already in the design phase, leads to low maintenance costs and high availability.

A good power system design considers the risk of margin stacking and any kind of over-engineered installations. Instead, simple and practical solutions are to be preferred. This means in particular for FCC that all powering challenges are to be solved directly at the power converter system which is the closest to the load. As FCC is to build in the future, the design should consider also upcoming technologies which are now in a prototype and standardization phase. In particular, future power systems can be based on DC and middle-frequency technology, as they allow under certain conditions, improvements in all the stated power system design aspects.

RQ1: Which power converter topology is best to power the main FCC loads?

A set of potential topologies need to be evaluated and compared against each other, considering the given constraints and requirements. The topology needs to implement a high-reliability design for the very large extent of FCC, with hundreds of separate power converter systems in the MW range. Further, the power limitation from the 400 kV grid leads to the requirement of energy storage integration.

RQ2: What are the differences if the topology is based on AC or DC?

A principal choice is to go either for an AC or DC based powering topology for systems below the 36 kV level. If DC is superior to AC depends on the application. As FCC has many DC loads and special requirements, a comparison study between AC vs. DC can highlight differences in terms of space demand, costs, losses and flexibility towards energy storage integration.

RQ3: Is a central or modular topology preferred?

To fulfil the requirement of high reliability, the options of central and modular-based power converter topologies need to be evaluated.

RQ4: What is the optimal voltage level for this topology?

The goal is to transfer power from the substation on the surface to the load located in the tunnel or in a cavern. The voltage level is directly proportional to the required power flow. As the integration of energy storage reduces the peak power demand, also the voltage level depends on the integrated energy storage. In any case, the current-carrying capacity of the cables or bus bars, and the fault current clearing capacity of protective equipment need to be considered.

RQ5: How can energy storage be integrated best?

The peak power demand of FCC overloads the 400 kV transmission grid [3], [4]. To avoid this negative system feedback, energy storage used for covering power peaks is a solution. The topology design must consider an efficient integration of energy storage.

RQ6: What is the optimum energy storage capacity?

The installation of energy storage reduces the peak power demand and thus reduces also the rating of the complete supplying electrical infrastructure. An optimisation between costs for energy storage and costs for electrical infrastructure determines the optimum capacity. Additional constraints in the optimisation arise from the dip immunity strategy, as the same energy storage can be used also for dip mitigation.

RQ7: What is the best strategy for dip immunity?

Particle accelerators are voltage dip sensitive. The large extent and the high power demand of FCC require a sophisticated strategy for dip immunity, which is based on a detailed analysis of the actual dip sensitive load, the expecting amount and severity of dips, and all potential mitigation techniques, including also synergies with the integrated energy storage used primarily for peak power covering.

FCC's large spatial extent on the surface and in the underground, its high peak and average power demand, operational performance goals and the specific load types, lead to a challenging set of design requirements. A part of these challenges can be found at other large-scale research infrastructures, but in the case of FCC all of them need to be solved.

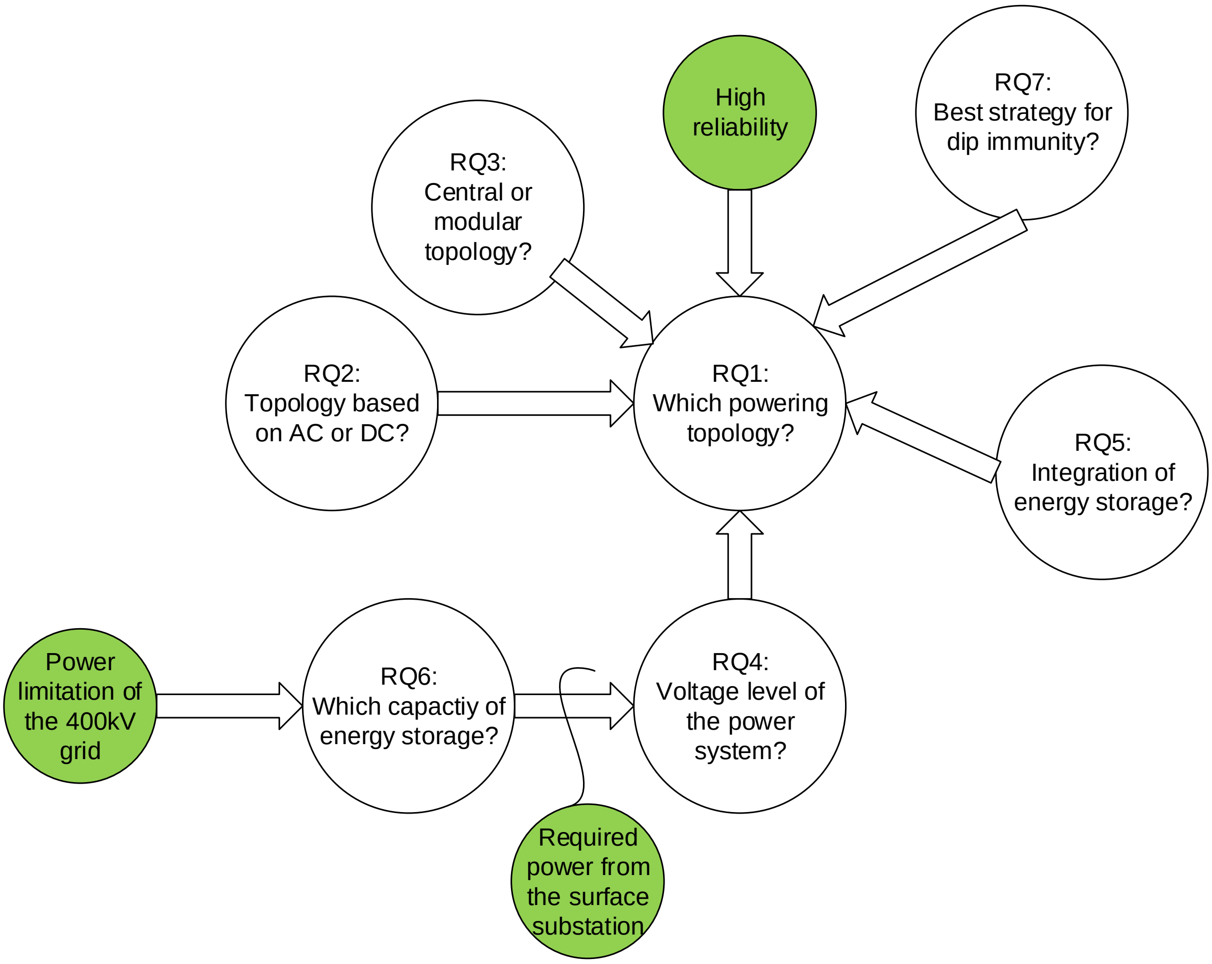

Figure 5: Research question in graphical representation.

4 FCC from a load perspective

FCC has many types of load. They can be categorized in terms of electrical parameters like voltage and current, and also on their sensitivity towards transient voltage dips, hence on called just “dips”.

4.1 Main bending magnet circuits

To bend high-energy particle beams around the arcs, dipoles are needed. In particular, they are 16 T twin aperture dipoles, based Nb_3Sn superconducting technology. These dipoles are connected to series circuits and are distributed around the total circumference of FCC. These circuits are powered at 10 (out of 12) FCC surface powering points.

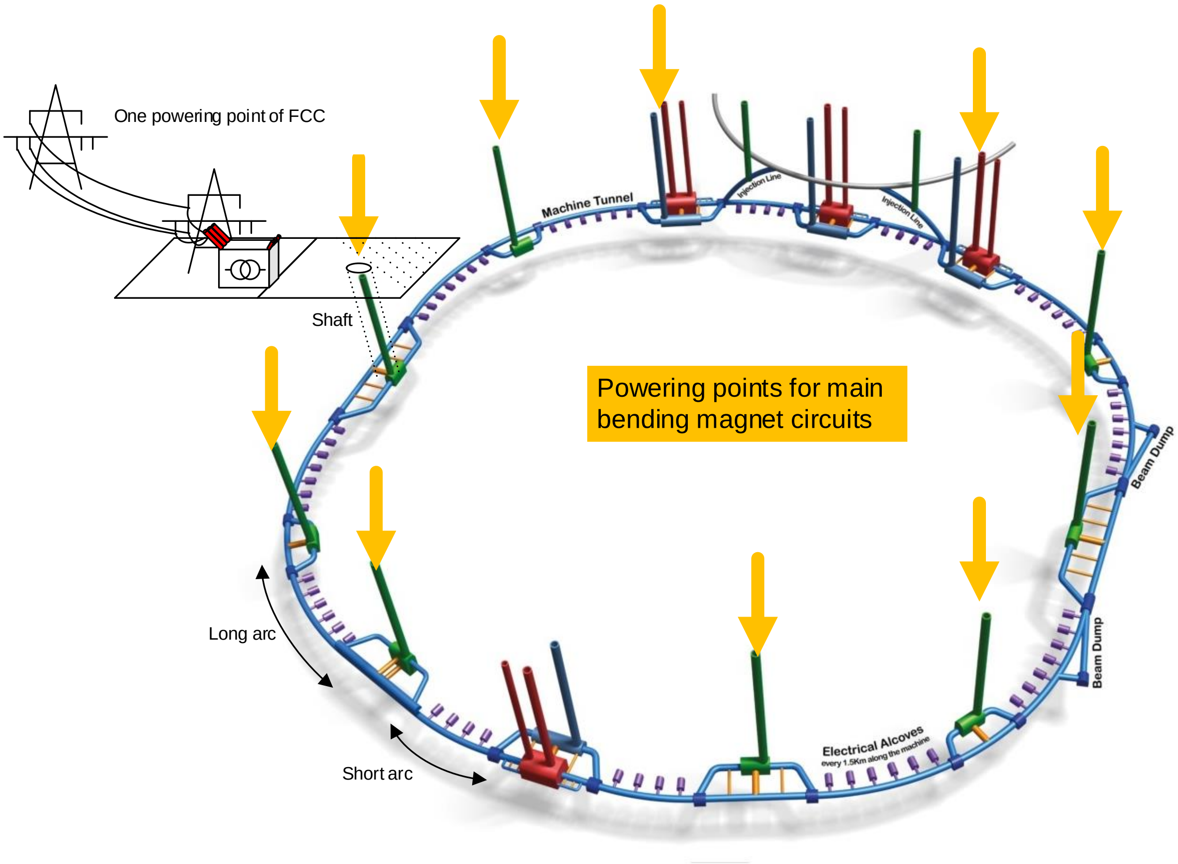

Figure 6: Powering points for the main bending dipole magnet circuits.

All powering points for the main bending magnets are highlighted by the yellow arrows. A closer look at one of these points is shown in the figure below.

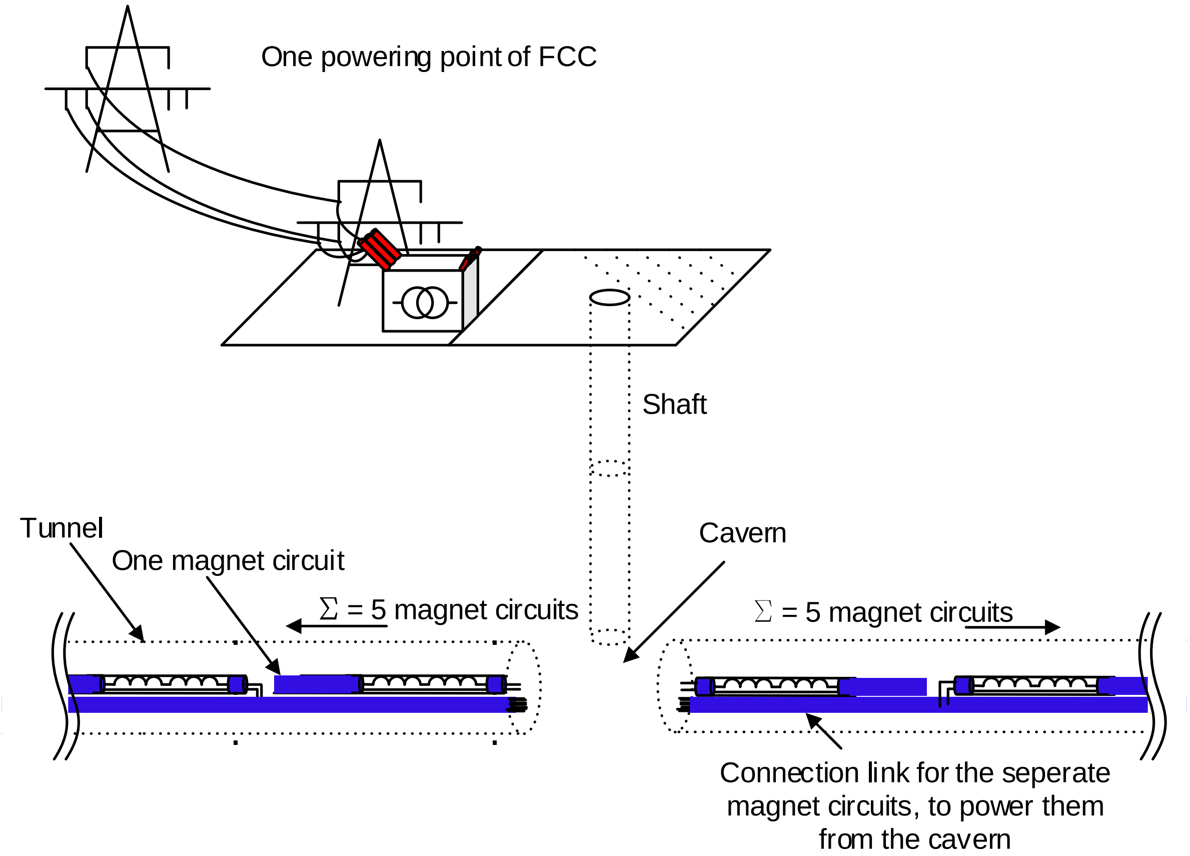

Figure 7: Location of the main bending dipole magnet circuits, shown at the level of one FCC powering point.

From the table below, all relevant parameters for the powering of the main bending dipoles can be observed.

Table 2: Main bending dipole magnet, and magnet circuit parameter

Item	Unit	Value
Operating current	A	11441
Self-inductance, single magnet	mH	570
Stored energy, single magnet	MJ	37.31
Magnetic flux density	T	16
44 single magnets are connected to one magnet circuit[2]		
Apparent inductance, magnet circuit	H	25.08
Stored energy, magnet circuit	GJ	1.641
Peak power demand, one circuit[3]	MW	2.87
Peak power demand, one powering point[4]	MW	28.7
Peak power demand, all circuits of FCC[5]	MW	287

The main parts of the operation cycle of the dipoles are:

- ramp the up: when the collider is filled enough with particles from the injector system, the particles are accelerated further, and to keep them on the right trajectory, the magnetic field of the dipoles has to be increased synchronously. Energy is transferred from the electrical power grid into the magnetic field of the dipoles until they are fully ramped up.
- flat top: this is the desired experimental phase, the particle beams are colliding at the detectors, and out of their collision energy, new elementary particles are created. As

[2] The decision to connect exactly 44 magnets together comes from magnet protection requirements [57]. It is an optimisation between number of circuits in total (reliability), and the energy within one circuit (fast energy extraction in the occurrence of a quench).

[3] The power demand depends on the ramping time and method. The values here refer to ramping with constant di/dt for a total ramping time of 20 minutes.

[4] Per powering point, 10 magnet circuits are to be powered.

[5] For the total number, 100 magnet circuits are used. A more detailed look could lead to a slightly different number, see here the appendix chapter FODO cell.

the main magnetic dipole field remains constant in this phase, only the losses of the magnet circuits must be covered by the electrical grid.

- ramp down: after some hours of flat-top phase, the remaining part of the particle beams (which are not used up due to collisions) are discarded by a beam dump system, leaving the collider empty. To fill it again with particles from the injector, the magnetic field of the dipoles has to be lowered at the initial level, this means that energy is taken out of the magnetic field and ideally recovered.

This cycling operation leads to power peaks up to ±287 MW[3]. See the figure below.

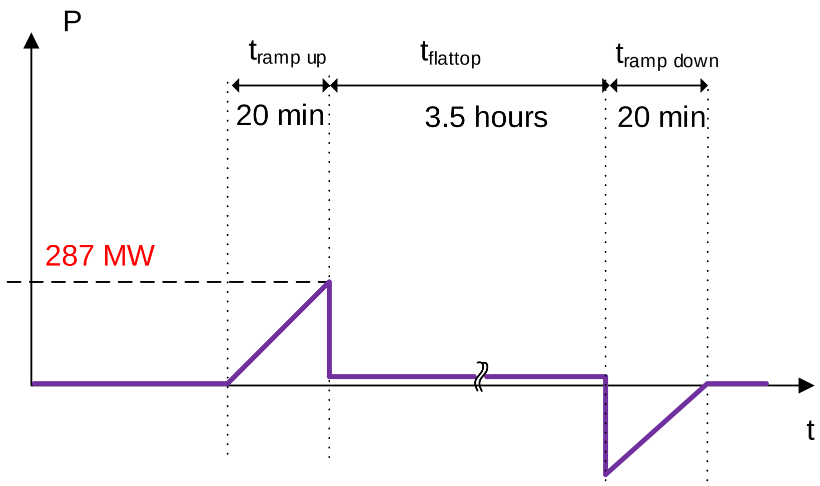

Figure 8: Peak power demand of the main bending dipoles.

Concerning dip sensitivity, the following has to be considered. In the case of a voltage dip occurring on the transmission grid level, the whole FCC will see this drop of voltage. Thus also all power converters for the main bending dipoles experience the drop of the supply voltage. If now as a consequence the u_{mag} at all magnet circuits is reduced, the complete bending field in all FCC arcs is changed. The bending field must remain within a certain margin otherwise the particle beam is to be extracted by the protection system.

From theoretical LHC analysis [58] the following is obtained. If a failure leads to a systematic and complete stop of all dipole converters, the time until a beam abort has to be initiated is about 1.3 seconds.

From practical LHC experience, dips causing a trip of the dipole converter due to a saturation of the active filter (see the appendix). Thus, the actual dip is not the problem. An internal converter or powering point failure is the main concern. If the converter design respects a fault ride-through capability, dip immunity is guaranteed.

Of high interest is to use a potentially installed energy storage as anti-dip protection.

4.1.1 Peak power discussion

This high peak power demand comes from:

- the main dipoles
- the main quadrupoles
- the cryogenics (refrigeration power rises until stable beams operation)

This high consumption of peak power could lead to negative system feedback and possible load instabilities. Remedies are found in the ramping strategy and the integration of energy storage.

4.1.1.1 Negative consequences of peak powers for FCC

Load side Instability

In addition to the cycling magnet power load, also other load has to be powered from at the point of common coupling (PCC), see the figure below.

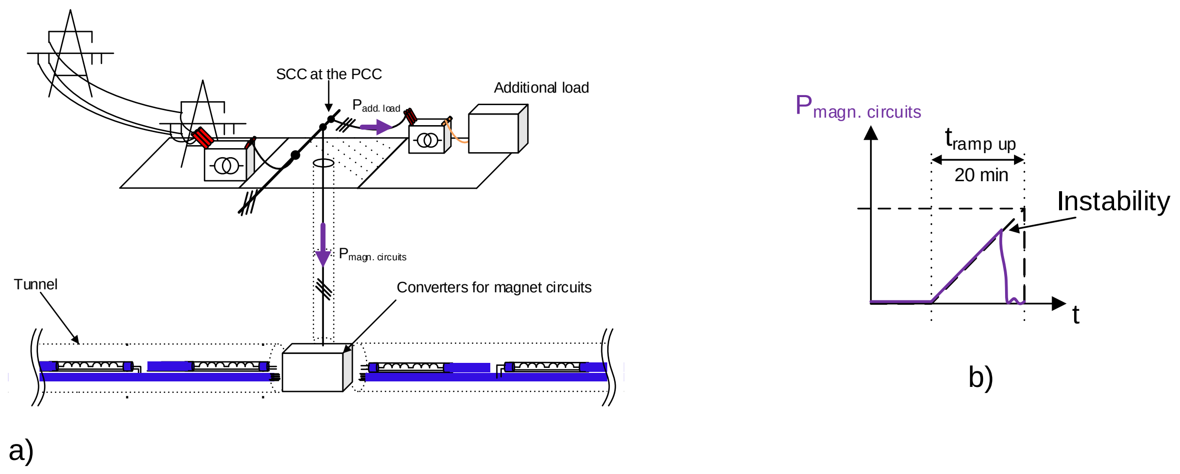

Figure 9: Load situation at a powering point of FCC on the left side, and instability occurrence during the magnet ramp up if the SCC is insufficient.

The total power demand at one powering point of FCC consists of power for the magnet circuits and all other additional loads. Under certain conditions, instability occurs during the magnet ramp up if the short circuit capacity (SCC) at the point of common coupling (PCC) is not sufficient. This phenomenon was analysed by using a simulation model which is based on the equivalent circuit in the figure below. Shown is the power demand from the additional load ($P_{add.}$) and from the magnet circuits (P_{AFE}). P_{AFE} is the power flowing into the input stage of an exemplary converter for the magnet circuits. The variable resistance is used to simulate the rising power demand during the ramping.

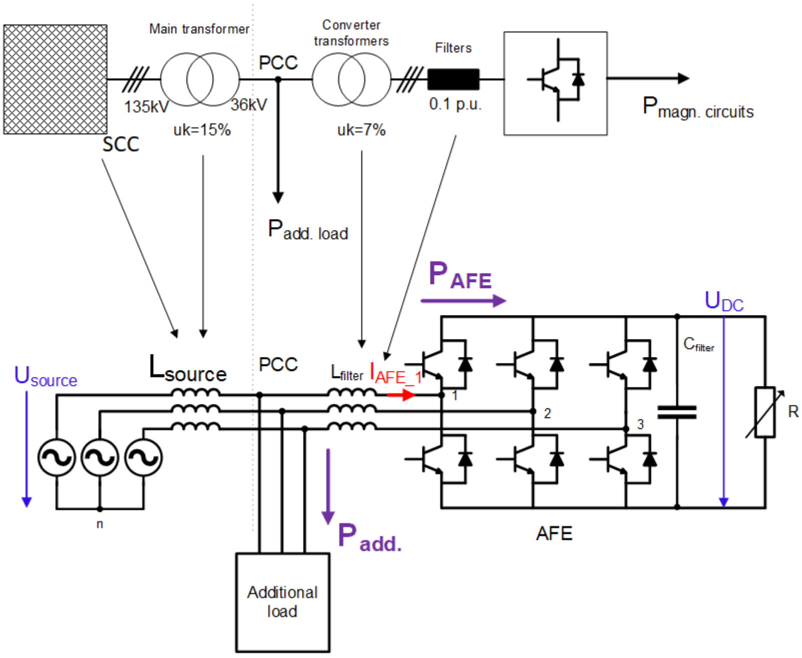

Figure 10: Equivalent circuit and the derived simulation model to show the instability phenomena. The simulation model represents an aggregate of input stages of exemplary converters for the main bending magnet circuits. The additional load represents all other loads connected to the PCC.

The short circuit capacity (SCC) at the 135 kV level and the leakage inductance of the main transformer are summarised to L_{source}. The leakage inductance of the converter transformer and the AFE filter is summarised to L_{filter}. The additional load will be a constant power load. The power for the magnet circuit ramp-up is simulated with a current source and the resistance R.

The critical parameters in the simulation are the value for SCC and the rating of the additional load. For the detailed simulation parameter values see the appendix.

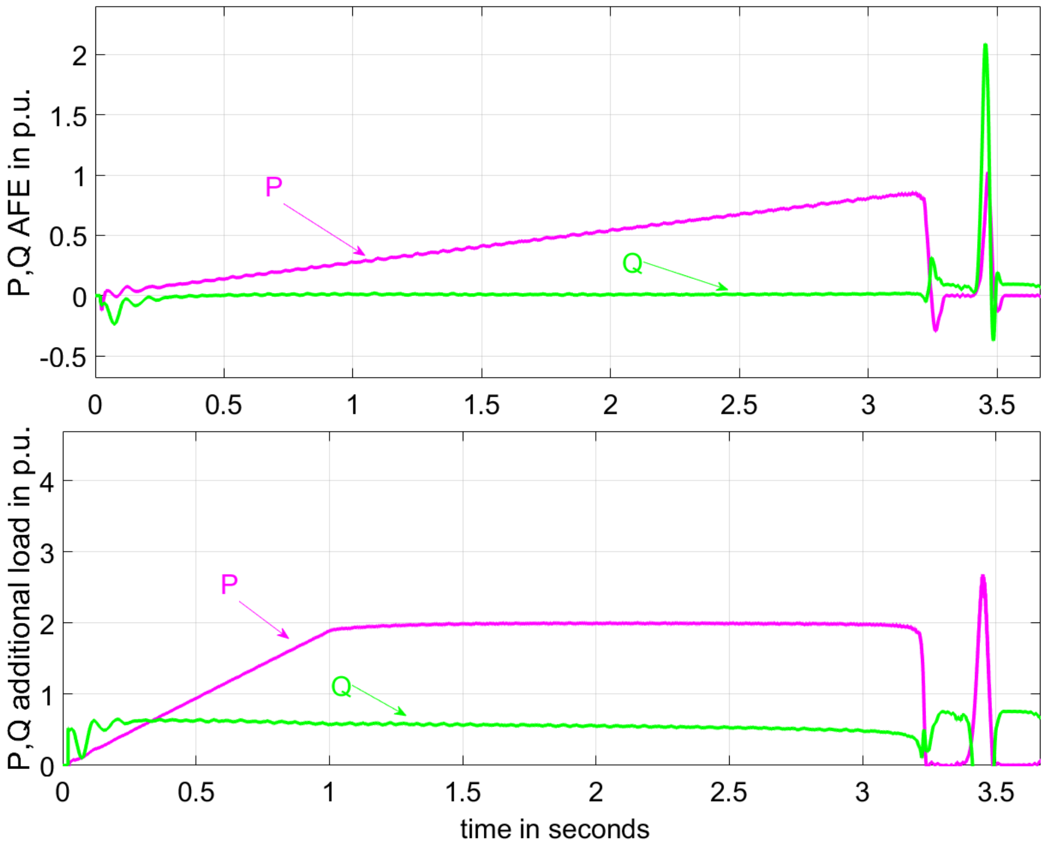

Figure 11: Simulation results for the power flow at the PCC. Shown is the power demand from the AFE and from the additional load. As the demand AFE power demand keeps rising, the instability occurs at the PCC (at t=3,25 s).

The cause for the breakdown is a mismatch of active power needed from the magnet circuits and the active power which can be transferred from AFE. When the DC link voltage U_{DC} starts dropping, the d-component (d-q control is used of the active rectifier) will increase more and more until the line current I_{AFE} limitation is reached. Then, the converter goes into non-linear operation of over modulation, which means in this case that the PWM signal will drop pulses. The converter is then consuming mainly reactive power from the grid, and the converter cannot come back to normal operation by just reducing the load parameters. This instability phenomenon was also analysed in [59] for a boost rectifier, connected to a non-ideal power grid.

High costs of electrical infrastructure

In general, electrical infrastructure becomes very costly if rated to peak powers. For FCC a high amount of electrical infrastructure is needed e.g. three 400/135 kV substations, a 135 kV cable distribution grid to supply twelve surface powering points, a local 36 kV distribution grid for each powering point, and finally all power converter systems for the load itself. In the case of FCC, the costs for the power peak consumption are expected to be much higher, as the total power demand (peak and average) of 800 MW requires reinforcements of the transmission grid itself. Additional costs for consuming peak powers from the transmission grid can arise. This is a complex point, as the costs to be paid to the operator depend mainly on the energy consumption and there is no general calculation method for taking power peaks from the transmission grid. However, there are efforts from the transmission grid operator to discourage power peak consumption during peak hours (for some limited days during the year) in the grid.

4.1.1.2 Remedies to the peak power problem

Ramping strategy

To bring the peak power situation at ease, different ramping strategies are considered [60]. The options are constant voltage ramping and constant power ramping[6].

In constant voltage ramping (cv), a constant di/dt at the magnet is applied. The voltage rises only to compensate for the voltage drop on the resistance of the magnet. This ramping method is established in the LHC.

As an alternative, constant power ramping (cp) ramps with a higher di/dt in the beginning and reduces at a certain point the voltage on the magnet in order not to exceed the set power limit.

The ramping strategy influences the power rating of all equipment used for powering the main bending dipole magnet circuit. With cp ramping the rating of the supplying infrastructure can be reduced. On the other hand, the last stage i.e. the actual magnet supply stage, needs to be rated to the peak current and to the peak voltage, see the figure below.

[6] Another parameter in the ramping is the ramping time. As for this dissertation the ramping time is kept at 20 minutes, as it is the operational target coming from the particle accelerator design. In general, the magnetic ramping is also of interest for other systems, as cryogenics or radiofrequency. Thus, the power converter design should not introduce another constraint.

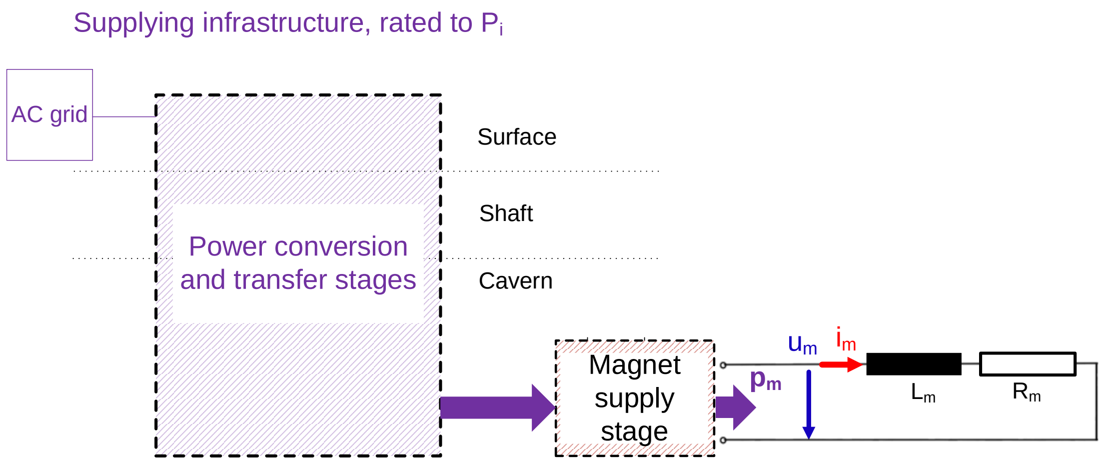

Figure 12: Principal powering layout for the magnet powering system for one main bending magnet circuit. The layout comprises two parts, the supplying infrastructure and the magnet supply stage.

Table 3: Equipment power rating in dependency of the ramping strategy (losses in the magnet supply stage are not accounted), source:[60].

	P_i	$P_{magnet\ supply\ stage}$	$u_{m\ max}$	Max. di_m/dt[7]
	MW	MW	V	A/s
Constant voltage	2.87	2.87	250	9.53
Constant power	1.79[8]	3.43[9]	300	12

The figure below shows for both ramping variants the magnet parameters i_m, u_m and p_m, and the infrastructure parameters P_i, and W_i.

[7] Calculated by $u_{mag\ max}/L_{mag}$

[8] This value is calculated by using the energy balance equation(54). See also right-bottom part of Figure 3.

[9] In constant power ramping the magnet supply stage needs to be rated to peak current and peak voltage.

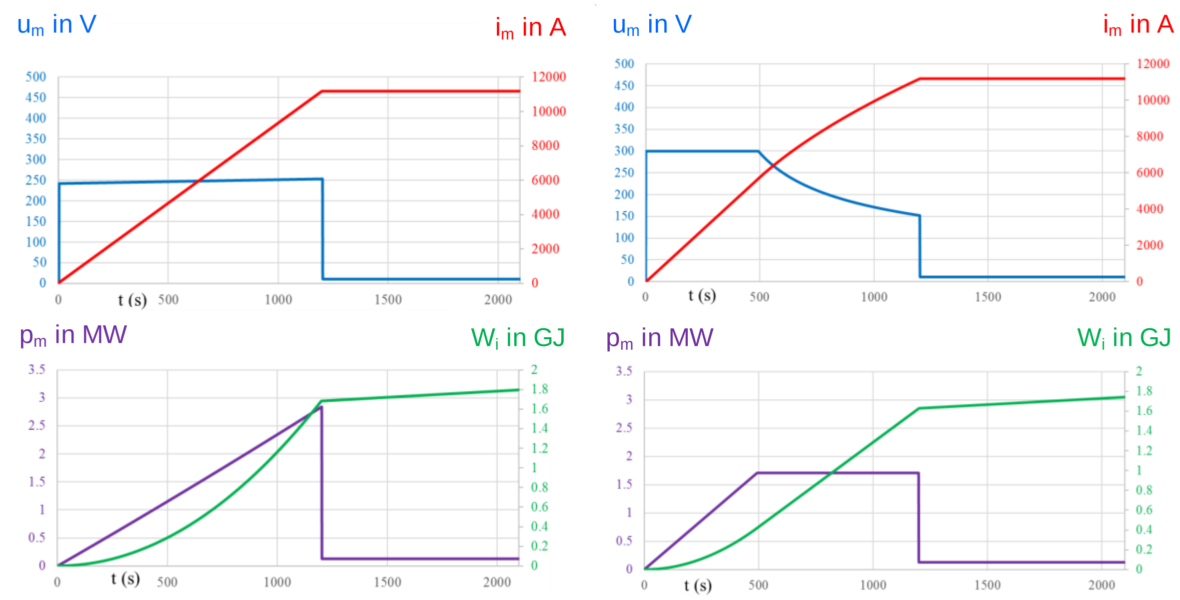

Figure 13: Ramping strategies for the main bending dipoles, with constant voltage ramping on the left and constant power on the right, both with a ramping time of 20 minutes, source:[60].

Energy storage integration

As the ease of the peak power consumption by changing the ramping strategy may not be sufficient and additional measures need to be considered. The integration of large-scale energy storage within the powering topology (right before the magnet supply stage) immediately reduces the peak power consumption from the AC supplying grid.

Generally seen, the integration of energy storage has the advantages of supplying infrastructure reduction, which in turn reduces costs and losses. As the integration itself is also connected to costs (energy storage capacity, integration into the topology, installation and safety requirements), an optimisation problem is triggered.

Further, it yields the potential to create are universal power supply system which is completed immune to transient voltage dips.

4.2 Cryogenic system

At FCC superconducting magnet technology is used and the cryogenic system has the main purpose to keep the electromagnets in their superconducting state. See for this introduction chapter the references [61, 62]. The general structure of a cryogenic system for a circular collider is shown in the figure below.

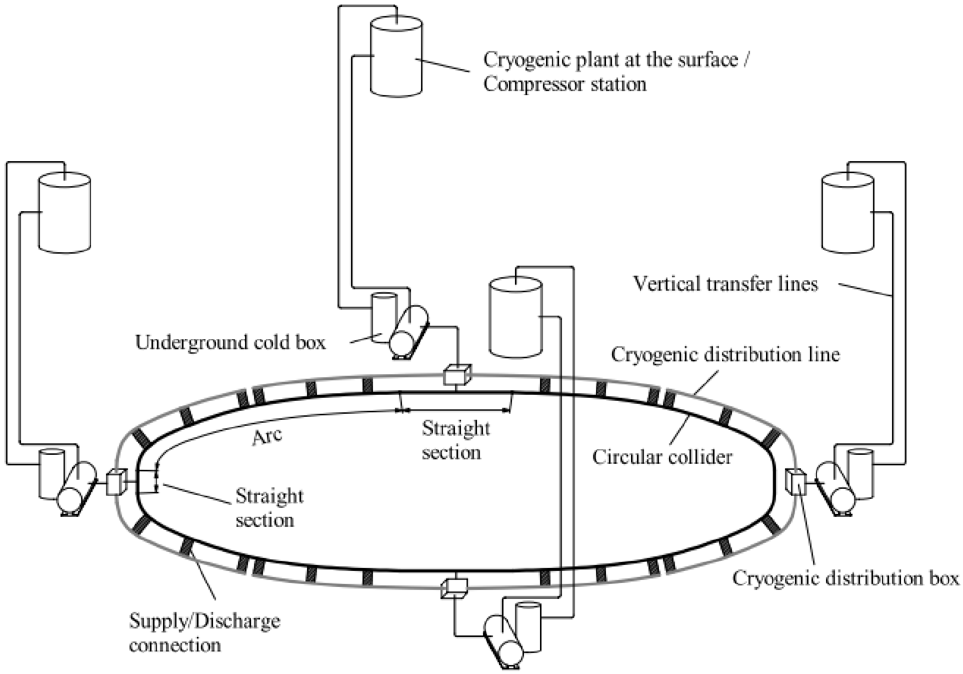

Figure 14: General layout of the cryogenic system for circular colliders as LHC or FCC, source:[61].

The cryogenic system consists of large compressor stations on the surface and a wide distribution system for the cryogen. The FCC cryogenic system is constituted by ten cryogenic plants, distributed over six powering points. Their specific refrigeration purposes are the provision of pressurized superfluid helium at 1.9 K[10] to cool the coils, collars, and the iron yoke of the superconducting magnets (cold mass cooling), and the removal of synchrotron radiation produced heat with dedicated beam screen cooling at 40-60 K[11] (beam screen cooling). Also, the thermal shielding of the cold mass is done at this temperature. The total thermic heat load consists of a static part and a dynamic part. The dynamic part is closely related to the synchrotron radiation – the dynamic heat load for the 40-60 K temperature level is six times higher than the static. This transition is particularly challenging for cryogenic plants.

For nominal operation FCC, an electrical power demand of 220 MW for the beam bending parts are calculated. Considering also the superconducting link, the total cryogenic electrical power demand is assumed to be 250 MW. The specific need for electrical powering equipment comes from the compressor stations on the surface. Their compressors need electrical motors

[10] This temperature comes from a techno-economic optimisation, cryogenic costs against super conducting material costs; further this temperature allows to use the advantages of superfluid helium

[11] Optimisation between vacuum quality and beam tube wall-impedance considerations

with a power rating in the range of 10 MW. In particular, the Turbo-Brayton cycle, demands high-power and 200 Hz high-speed centrifugal compressor systems. Due to their high power rating and the high rotational speeds, the application of adjustable speed drives (ASD) is necessary.

4.3 Other superconducting magnets

In general, all magnets could be distinguished between lattice magnets (the elementary arrangement is called FODO cell, see also the appendix.) and insertion magnets. The lattice magnets are for beam guiding around the arcs and the insertion magnets are taking over when it comes to the experimental areas [63].

The dipoles in the lattice fill up most of the beam guiding circle. Their large apparent inductance and the large energy stored in the dipoles require immense considerations for their power system (chapter 4.1).

All other superconducting magnet circuits in the lattice (or in the experimental area) have a much lower apparent inductance and require partly an even higher operating current. Thus their powering requirements are different. The main lattice quadrupoles have the function of keeping the particle beam tight together. they are also connected electrically together into a series circuit, see the table below the main parameters.

Table 4: Main quadrupole magnet, and magnet circuit parameters

Item	Unit	Value
Operating current	kA	20.5
Self-inductance, single magnet	mH	14.4
Apparent-inductance, magnet circuit[12]	mH	532.8
Peak magnetic flux density	T	10.51
Peak power demand, one circuit[13]	kW	731
Peak power demand, all circuits of FCC[14]	MW	14.62

[12] If two main quadrupole circuits are assumed per long arc, up 37 quadrupoles are connected in series for one circuit. For the complete FCC, 20 quadrupole circuits are needed. See also the appendix.

[13] Assuming an ohmic resistance of the circuit of 1 mΩ and a ramp from I=0 to 22.5 kA in 20 minutes gives $p_{peak} = u_{peak} \cdot i_{nom}$ = (0.5328 H*22.5 kA/1200 s+22.5 kA*1 mΩ)*22.5 kA.

[14] This value is derived if for all 20 quadrupole circuits of FCC the same number of magnets are taken. In fact, for a short arc only 30 magnets are connected. See also the appendix chapter FODO cell.

Other lattice magnets as sextupoles, octupoles or decapoles compensate for other effects, like imperfections of the dipoles or gravity. Their power demand will be lower than for the main quadruples. Among the insertion magnets are for example the inner triples, to prepare the beams shortly for their collision point. The challenge here is their complex control, as their powering topology consists of two galvanically coupled magnet circuits with nested converters [64].

The spectrometer magnets at the detectors are superconducting magnets with a field of 4 T. Their powering will require a converter that delivers about 20.5 kA current and a maximum voltage of 18 V. Per detector, a central solenoid and two forward magnets are needed. Two detectors are foreseen for FCC. Concerning dip sensitivity, the following has to be considered. Similar to the case for the main bending dipoles, a voltage dip leads to a reduced voltage u_m on the magnet, thus influencing the particle beam on its trajectory.

Depending on the type of magnet and its optical function, only a certain variation of its magnetic field is allowed. Otherwise, the particle beam is to be extracted by the protection system. For the main quadrupoles it is obtained from theoretical LHC analysis [58], that by a complete stop of all main quadrupole converters the time until a beam abort has to be initiated, is about 0.048 seconds.

From practical LHC experience, it is obtained that dips have the potential to trip the converter. For example, the converters for the ATLAS solenoid and toroid magnets trip due to voltage control loop feedback. An internal converter or powering point failure is the main concern. If the converter design respects a fault ride-through capability, dip immunity is guaranteed.

Also, to be considered is the powering with a dip immune power system. See here chapter 7, presenting a DC-based grid with integrated energy storage.

4.4 Warm magnets

Superconducting magnets cannot always be used, as at some positions of the collider a high radiation level would induce too much thermal stress, and the magnet would lose its superconducting state. The solution is then to use warm magnets.

Warm magnets are those magnets that are kept at room temperature. Their ohmic resistance is in the order of 1 Ω. In comparison with some $\mu\Omega$ for a superconducting magnet. This fact leads also to very short time constants for the magnet current.

They interact with the particle beam at very specific positions and fulfil special optical functions as beam cleaning at the collimators, or beam separation and recombination after the interaction points.

To protect a particle accelerator from its high-energy particle beams, so-called beam loss monitors need to be installed. In the case of the warm magnet circuits, additional protective requirements are necessary, as these beam loss monitors are not fast enough. The Fast Magnet Current change Monitor (FMCM) allows measuring a Δi_m of 100ppm in less than 1 ms. This is achieved by measuring the converter voltage (a voltage can be faster measured than a current) and the current in the magnet circuits is then estimated. If the current in the magnets exceeds its relative allowed limit, the FMCM system extracts the particle beam.

At the LHC in total 12 circuits with warm magnets are monitored by the FMCM system. The total installed converter rating for these circuits is about 6 MW. For FCC warm magnet circuits are foreseen for beam separation and recombination at the interaction points. Thus, they remain a limited number of circuits, with a high sensitivity to dips. Concerning dip sensitivity and strategy for dip immunity, the following has to be considered. Warm magnets constitute the highest dip-sensitive load, as they have very small time constants and fulfilling special optical functions (positions with a high β-function). From theoretical LHC analysis [58] it is obtained for the most sensitive warm dipole circuit, the time until a beam abort has to be initiated is about 0.0005 seconds.

From practical LHC experience comes the observation that in the case of a voltage dip, the FMCM was always initiation a beam dump. The solution was a dedicated power converter design to supply these warm magnets. The original thyristor based topology used active filters on the output. During dips they saturated and the converter tripped. The new design is based on capacitive energy storage and switch-mode converters.

All the FMCM monitored circuits that have been equipped with the new power converter have never caused a beam dump ever since [46]. All those FMCM circuits, which have not yet been updated, still initiate beam dumps during voltage dips. Due to this very sensitive process, active dip mitigation concepts need to be applied. Either by a converter topology upgrade with capacitive energy storage or by connecting the converters to a universal dip immune power system. See here chapter 7.

4.5 Radiofrequency

The radiofrequency (RF) system generates a high voltage for accelerating the particle beams. Each of the two particle beams has an independent RF system.

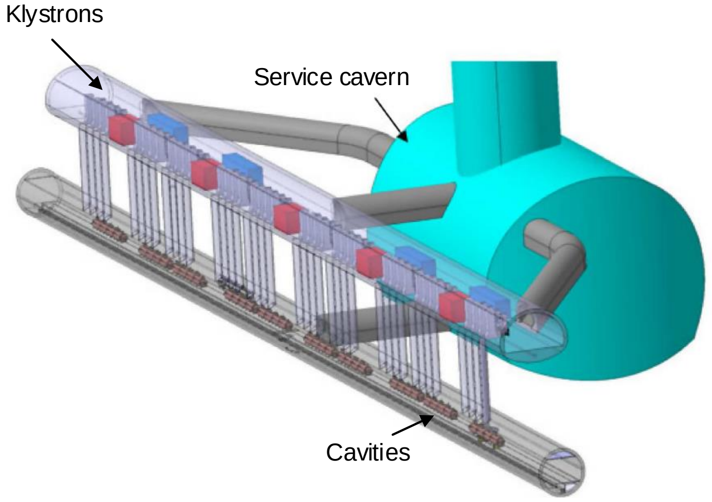

Figure 15: Location of the RF system for FCC, with the klystron gallery shortly above the main accelerator tunnel, source: [5].

One RF system consists of 24 cavities, whereby each cavity generates 2 MV. The cavity features a 400 MHz continuous wave, and several feedback loops allow the precise control of the field in the cavity. The actual RF power comes from klystrons and is brought via power couplers into the cavities. The klystron plant needs a high DC voltage of about 40-60 kV as input. Further for each cavity, a power demand of 500kW is assumed [5]. For two times 24 cavities this gives 24 MW of total power demand, which has to be delivered from the klystron plant to the cavities. Assuming an efficiency of 70%, the electrical power demand of the klystron plant is 34.3 MW.

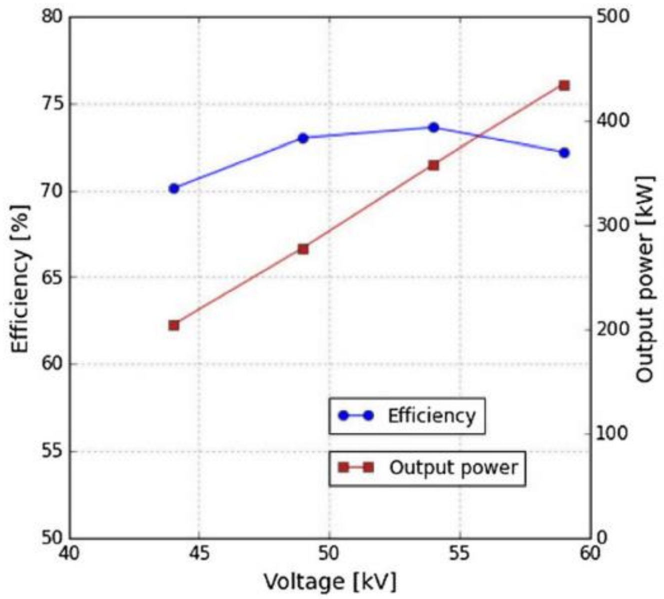

Figure 16: Efficiency curve of the klystron, depending on the output power and voltage level, source: [5].

These parameters make modular multi-level converters (MMC) very applicable. Also in the design study for the compact linear collider (CLIC) [10], MMCs are used to power the klystrons. In general, MMCs are very suitable for voltages above 10 kV DC and a power of 2 MW [65]. MMCs have further the great advantage of having a high fault run through capability.

From practical LHC experience, it is obtained that the converter for the RF system is likely to trip during the occurrence of voltage dips. This converter is the re-used converter from the times before LHC. It has a thyristor-based AC/AC stage and a diode-based AC/DC stage. The AC/AC stage is controlled to deliver a constant output voltage. In the case of a reduced voltage on the input side (due to the voltage dip), a higher line current is drawn. The consequence is the tripping of the line current protection. The sudden change of input voltage causes also an oscillation of the DC filter current, tripping the filter over current protection.

As for the RF system, a new converter is needed anyway, the solution for dip immunity is to consider it in the converter specification. Given the level of DC voltage and power, MMC-based topologies are becoming highly interesting. It contains capacitive energy storage and one gets by adequate dimensioning [53] dip immunity for free.

4.6 Summary

The most challenging load to power are the main bending dipoles, as they have a cycling power demand of ±287 MW. Further, the about 100 dipole circuits are located around the 98km circumference of FCC. The high peak power demand can result in negative system feedback and load instabilities. The ramping strategy and integrated energy storage could ease the situation.

For FCC many types of loads need to be supplied. In terms of dip sensitivity, all power converters are to be seen as dip sensitive due to their equipment protection elements. The most efficient and most economical way is to act directly on the converter level and implement fault ride-through specifications in the design requirements. Another option can be a universal dip immune DC grid, which uses the energy storage from the dipole powering.

All cryogenic compressors need adjustable speed drives with a total rating of 250 MW. At least 100 MW needs to be high-speed ASDs, the rest normal ASDs. The converters of the drives are regarded as dip sensitive and dedicated studies show requirements for the supplier for such ASDs. Warm magnet circuits are in connection with the most dip-sensitive processes, beam separation, and beam cleaning. For those two processes either a converter with integrated energy storage or the powering by a universal dip immune power system is the solution.

5 Analysis of AC versus DC based power supply for FCC

For a hundred years two power system domains are distinguished, AC and DC based systems. Upcoming technologies as DC grids are in principle interesting for the design of a future particle accelerator as FCC. All research questions are answered best in the medium and low voltage range, i.e. the highest considered AC voltage is the 36kV AC level, and the 40-60kV DC level for the radio frequency system. The AC vs. DC comparison in the state of the art chapter indicated that if DC is superior over AC depends on the application. Thus, three case studies are shown to evaluate potential advantages of DC grids for particle accelerators. Case study 1 is focusing on the LHC, as having the advantage with a high data availability. The results of case study 1 are then used as focus points for the following two case studies (case study 2 and 3), which are looking already on possible power supply systems for the FCC.

5.1 Case study 1: existing particle accelerator

This case study is focusing at the LHC. Particularly one powering point of the LHC is chosen for the analysis. See the figure below for the overview.

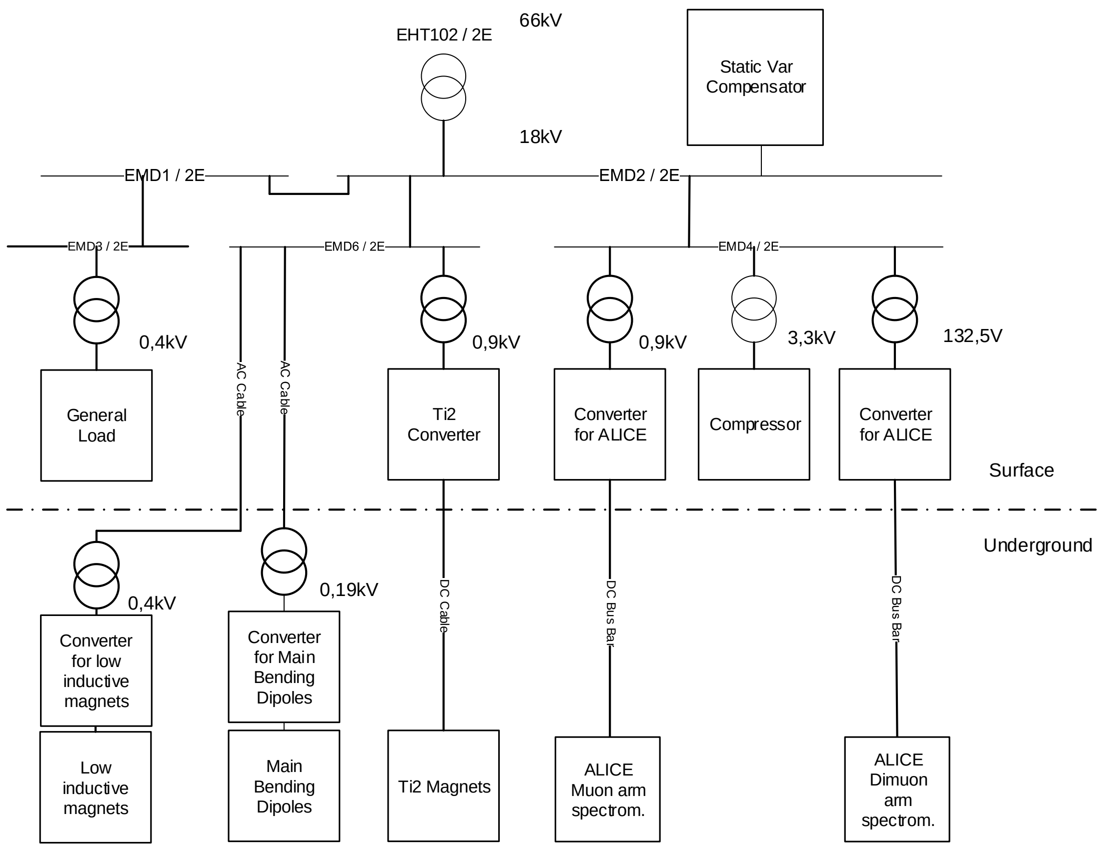

Figure 17: LHC point 2, simplified layout and overview of categorised load installed at this point.

If now a DC grid is introduced, the load must also be connected to it. If the original converters of the LHC point 2 load remain unchanged, additional DC/AC conversion stages need to be considered.

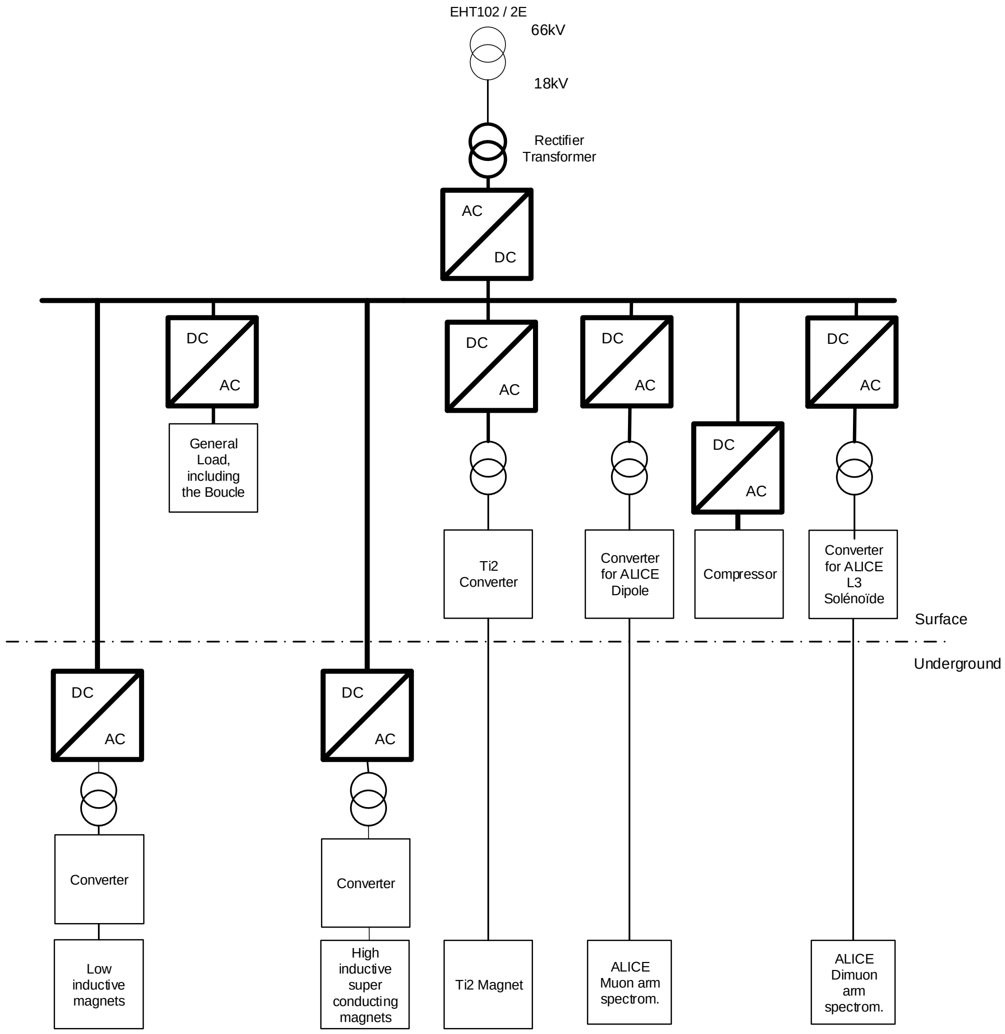

Figure 18: LHC point 2, simplified layout with a new introduced DC grid, and with the original converters for the load. No SVC is necessary anymore.

A priori it is observed that the introduction of a DC grid without changing the converter topologies for the load supply has the only advantage that reactive power can be supplied by all the inverters which are right before the existing thyristor based power converters. If further advantages of a DC grid for particle accelerators are to be realised, new power converter topologies must be introduced.

The requirements for these converter topologies are:

- Connect to a high DC voltage: assumed are at least 10 kV to transfer the required power,
- Deliver a high current to the magnets,
- Provide galvanic isolation due to the magnet grounding and safety requirements.

The best topologies for the given constraints are based on solid-state transformers (see also the chapter Solid-state transformer and DC grids). The figure below shows two variants, one with energy storage and the other without.

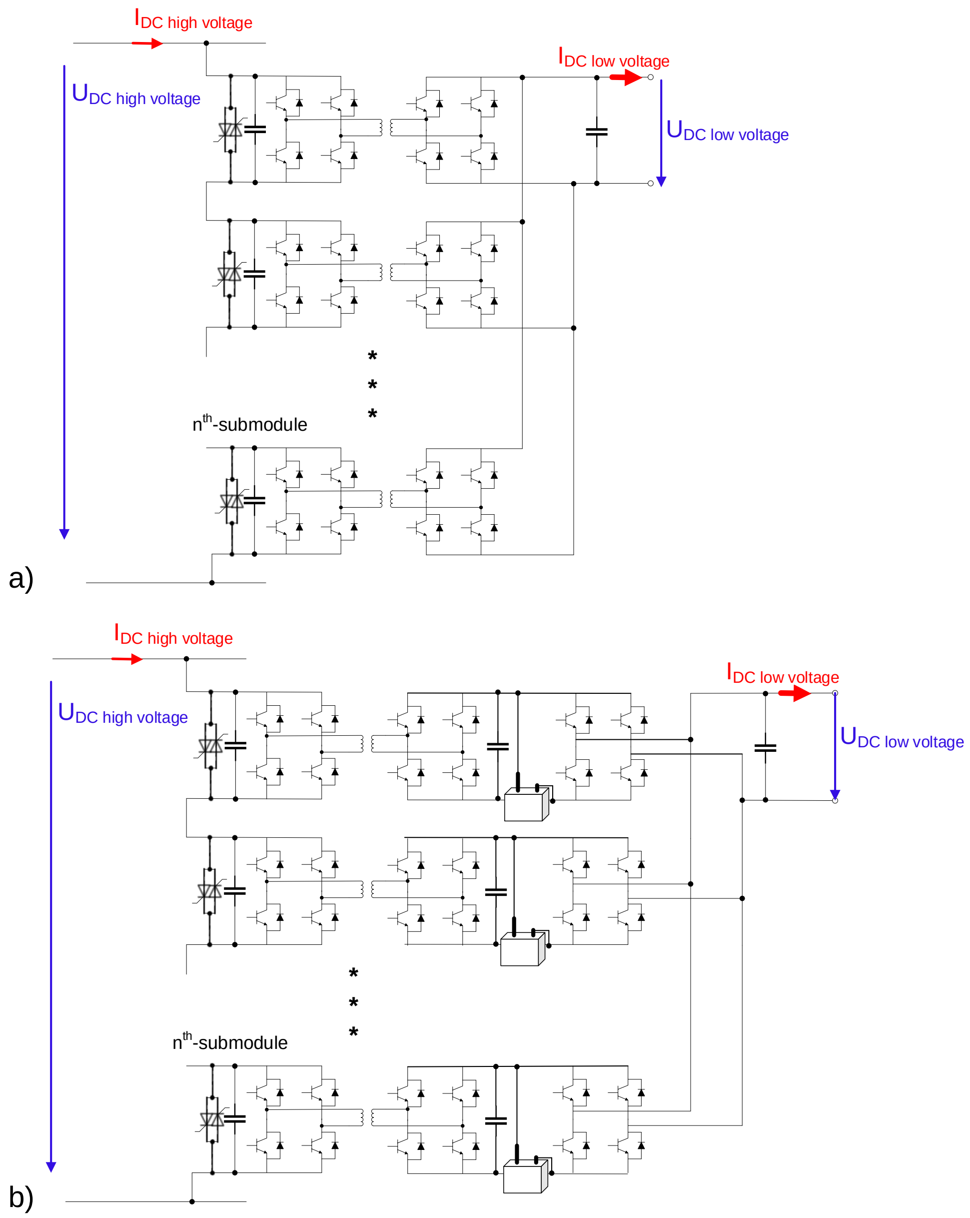

Figure 19: Solid-state transformer based topologies used for the DC grid case study; upper part: without energy storage, bottom part: with integrated energy storage.

The introduction of solid-state transformer (SST) based converter topologies fulfils the requirements and allows more design options, emphasising a medium voltage DC distribution grid for LHC point 2.

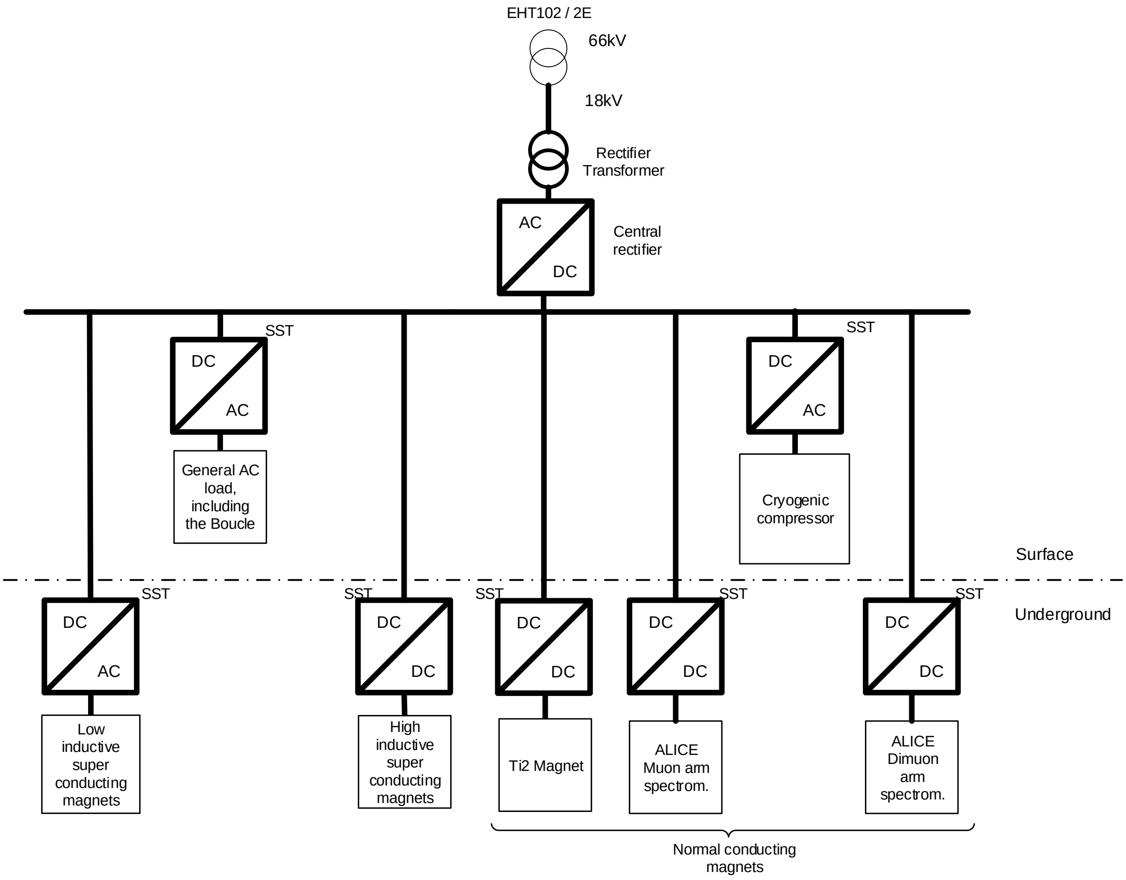

Figure 20: LHC point 2, simplified layout with a new introduced DC grid, and with new converters (SST topologies) for the load.

The categorized load with its power rating is shown in the table below.

Table 5: Categorized load for LHC point 2 case study

Item	Defined powering topology for power density comparison		Power rating
	AC	DC	in MW
Normal conducting magnets: Ti2 injection, ALICE muon arm and di-muon arm spectrometer, compensator	Transformer-rectifier combination	DC-DC unidirectional SST	20
Low inductive superconducting magnets: e.g. main focusing/defocusing quadrupoles, trim quadrupoles, insertion quadrupoles	Transformer, transformer-rectifier combination, DC-DC unidirectional SST	DC-DC unidirectional SST	1
High inductive superconducting magnets: the only magnets in this category are the main bending dipoles	Transformer-rectifier combination	DC-DC-DC bidirectional SST	5
Cryogenic compressors: in total 13 screw-type compressors are summarized	Transformer	DC-DC-AC unidirectional SST	7.6
General 50Hz load: cooling and ventilation, auxiliaries	Transformer	DC-DC-AC unidirectional SST	4.4

To highlight potential advantages, the original LHC point 2 is compared with the DC grid-based layout in terms of weight and volume of the respective installed equipment. For the assumed power density values (kg/kW and dm³/kW) and exemplarily calculations see the appendix.

Table 6: Results of the AC-DC-comparison for LHC point 2

	AC	DC
	Volume of installed equipment on the surface, in m³	
Central diode rectifier with rectifier transformer	-	171
Cryogenic compressor	24.3	15.2
Normal conducting magnets	90	-
General 50Hz load	14.1	8.8
	Weight of installed equipment on the surface, in tons	
Central diode rectifier with rectifier transformer	-	148
Cryogenic compressor	20.1	15.2
Normal conducting magnets	78	-
General 50Hz load	11.7	8.8
	Volume of installed equipment underground, in m³	
Low inductive super conducting magnets	9.2	2
High inductive super conducting magnets	22.5	10
Normal conducting magnets	-	30
	Weight of installed equipment underground, in tons	
Low inductive super conducting magnets	8.05	2
High inductive super conducting magnets	19.5	10
Normal conducting magnets	-	30
Total		
Volume, in m³	160	237
Weight, in tons	137	214

5.1.1 Results discussion

From the above table the following can be deducted for LHC point 2:

- As the DC grid requires a central rectifier station, the overall volume and weight demands are higher compared with the AC grid case.[15]
- However, if looked only at the superconducting magnets installed in the underground, the weight/volume reduction of DC-powered converters yields a high potential of advantages e.g. easier installation and easier maintenance (see the table above).
- For the load not powered by a converter, the DC introduction leads to increased complexity. The cryogenic compressors could in the AC case be connected directly to the 3.3kV AC grid, and due to the introduction of a DC grid, a converter is required. The same is true for the general 50Hz load.

The load at the FCC is constituted by a high number of superconducting magnets:

- The number of high inductive magnet circuits is at least 10-times more
- The magnets for the transfer line from the injector will be superconducting (at LHC point 2, normal conducting magnets which are powered on the surface are used).
- The spectrometer magnets found at the FCC experiments will also be superconducting (at LHC point 2, normal conducting magnets which are powered on the surface are used).
- Adjustable speed drives are needed for FCC's cryogenic system

Thus a great potential for DC based powering grids for FCC is obtained.

5.2 Case study 2: unified power supply of surface and underground load at FCC

The typical load found at an FCC powering point is shown in Figure 21, whereby two powering variants are shown. The upper part is based on AC distribution and the lower part on DC distribution. The DC grid-based variant emphasizes solid-state transformer (SST) topologies to connect the load to the DC bus. The categorized load with its power rating is shown in the table below.

15 To make comparison more adapt to FCC, the space/weight contribution of the SVC is neglected at all.

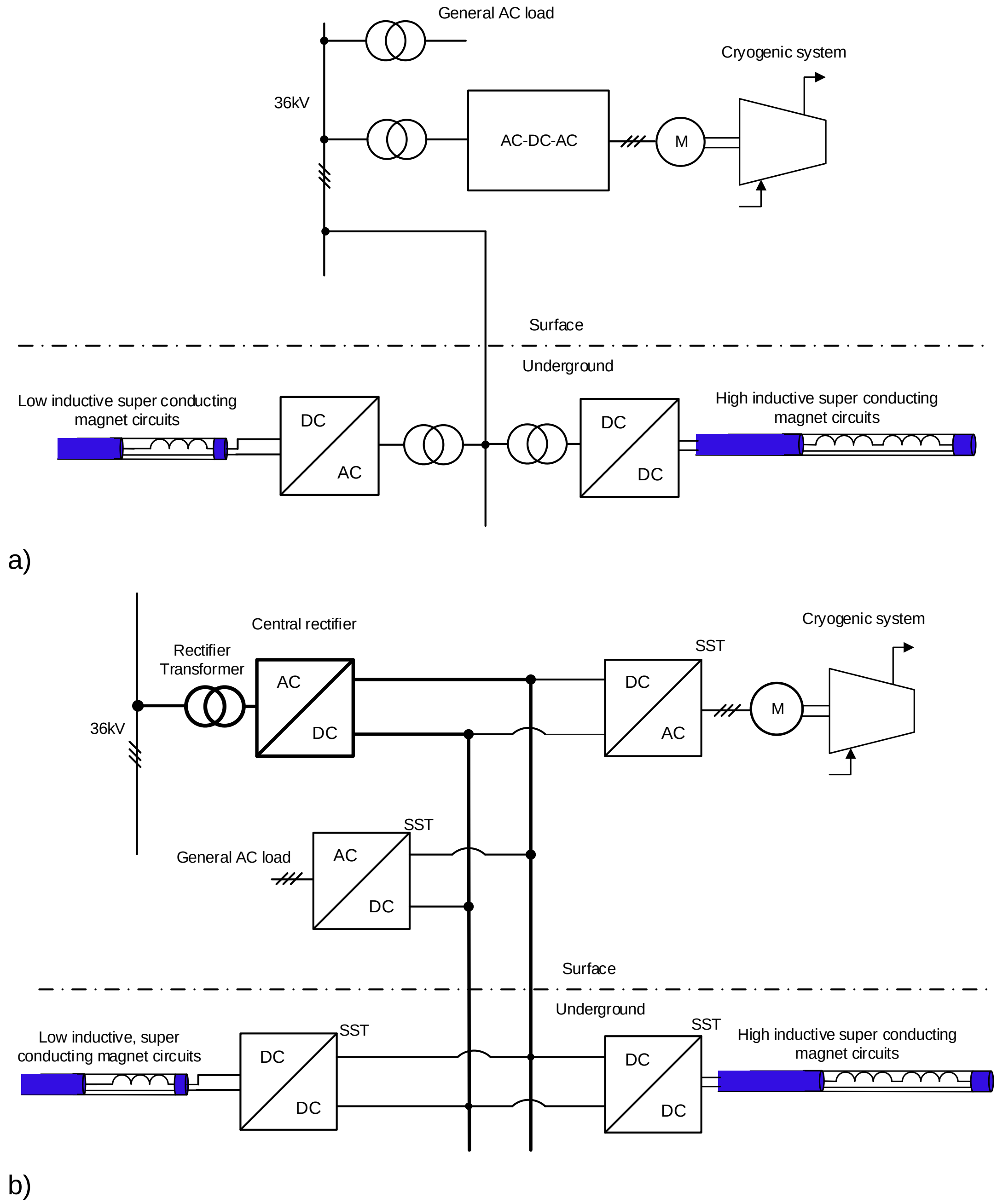

Figure 21: Case study overview, for a typical load, found at an FCC powering point. On the upper part the AC-powered variant and on the bottom part the DC variant is shown.

Table 7: Categorized load for an FCC powering point, used in the AC/DC comparison study

Item	Defined powering topology for power density comparison		Power rating
	AC	DC	in MW
Low inductive superconducting magnets: e.g. main focusing/defocusing quadrupoles, trim quadrupoles, insertion quadrupoles	Transformer, transformer-rectifier combination, DC-DC unidirectional SST	DC-DC unidirectional SST	1
High inductive superconducting magnets: main bending dipoles	Transformer-rectifier combination	DC-DC-DC bidirectional SST	30
Cryogenic compressors: e.g. centrifugal compressor for one Turbo-Brayton cycle	Transformer-rectifier combination, DC-DC-AC unidirectional SST	DC-DC-AC unidirectional SST	10
General 50Hz load: cooling and ventilation, auxiliaries	Transformer	DC-DC-AC unidirectional SST	5

The comparison results are shown in the table below.

Table 8: Results of the AC-DC-comparison for an FCC powering point

	AC	DC
	Volume of installed equipment on the surface, in m³	
Central diode rectifier with rectifier transformer	-	207
Cryogenic compressor	65	20
General 50Hz load	16	10
	Weight of installed equipment on the surface, in tons	
Central diode rectifier with rectifier transformer	-	179
Cryogenic compressor	59	20
General 50Hz load	13.3	10
	Volume of installed equipment underground, in m³	
Low inductive super conducting magnets	9.2	2
High inductive super conducting magnets	135	60
	Weight of installed equipment underground, in tons	
Low inductive super conducting magnets	8.05	2
High inductive super conducting magnets	117	60
Total		
Volume, in m³	225	299
Weight, in tons	197	271

5.2.1 Results discussion

The high potential for underground equipment reduction has to be pointed out as the main advantage of DC grids applied for FCC powering. For high inductive superconducting magnet circuits, the relative reduction of volume/weight is about -50%. Even more evidently for low inductive superconducting magnet circuits, with a volume/weight reduction of -80%. The advantage comes at the cost of the large central rectifier station. However, this station is located at the surface and thus easily accessible.

5.3 Case study 3: uninterruptable power supply of underground structures at FCC

To continue the AC-DC comparison, an uninterruptable power supply (UPS) for load points located in the FCC tunnel is formed. The UPS is designed with a nominal power of 1MW, to supply several radially distributed load points, up to a maximum distance of 10km. See the figure below for the case study overview.

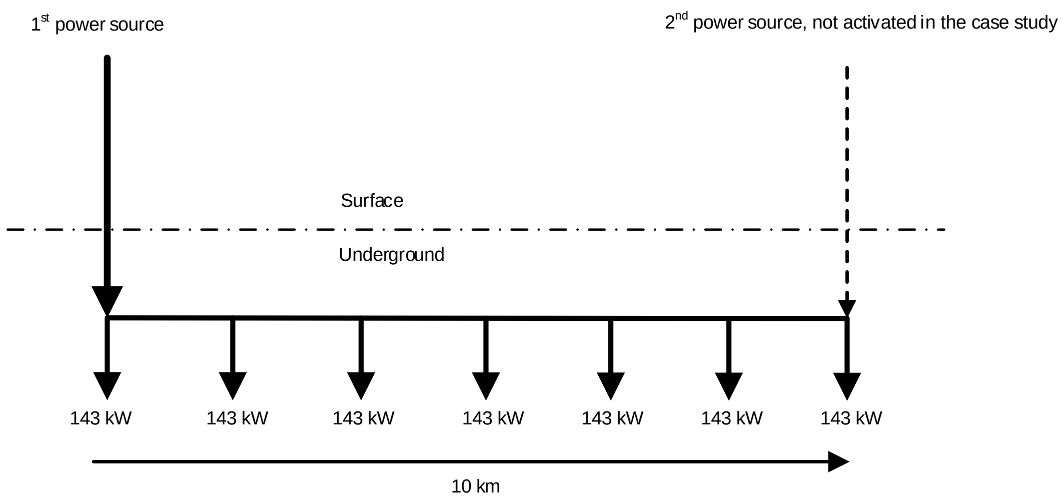

Figure 22: Simplified layout of the uninterruptable power supply for a tunnel, analysed in this case study.

The aspects to be analysed in this case study are:

- How energy storage is to be integrated (UPS requirement)
- Equipment utilisation
- The voltage-drop along the supply line
- The losses on the supply line

The two topologies – one based on AC, the other in DC – feature double redundancy. See the figure below for the full layout.

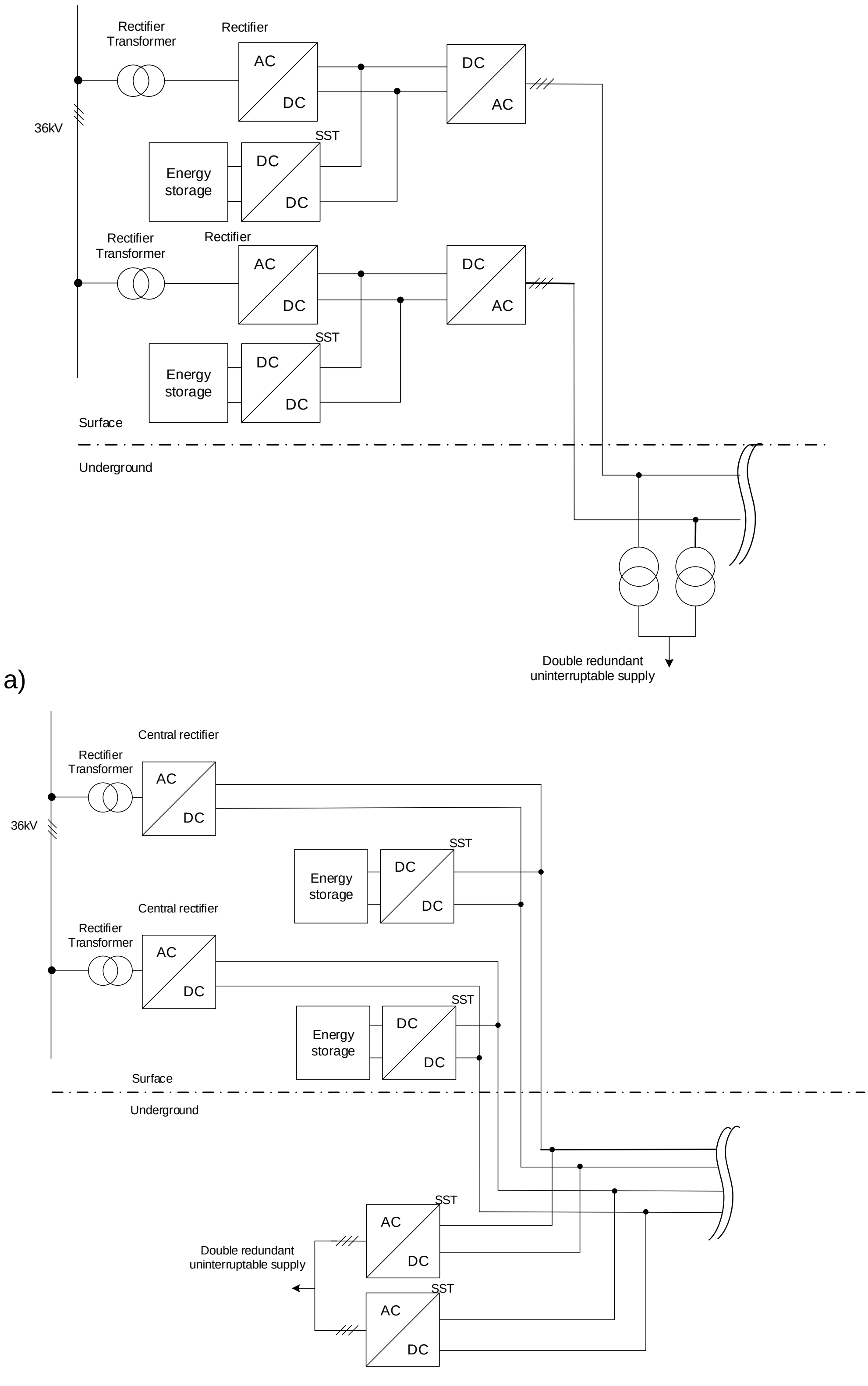

Figure 23: Simplified layout of the UPS topologies used in the case study. On the upper part: AC-based, on the bottom part: DC-based.

The parameters for the comparison study are shown in the table below.

For the study, a cable system consisting of three single-phase cables is used. In the case of the DC system, a two-pole system is formed, leaving one single-phase cable as redundancy. The categorized load with its power rating is shown in the table below.

Table 9: Parameters used in the AC-DC comparison study for the UPS

Distribution in:	**AC**	**DC**
Power per load point	143 kW, with a power factor of $\cos(\varphi)=0.9$	
Voltage level of U_{cable}	5 kV RMS, line-to-neutral	11.7 kV, line-neutral[16]
Cable type[66]	Nexans: single-core XLPE insulated cables with PE sheath, longitudinally watertight, cross section=35 mm², U_{nom}=6/10kV, $U_{max\ operating\ voltage}$=12 kV	
Cabling	two systems with 3x1, trefoil touching arrangement	two systems with 2x1
Cable resistance at 20°, in Ω/km	0.524	0.524
Cable reactance at 20°, in Ω/km	0.133	-

The calculation model for the voltage drop and the transmission losses assumes a constant power load at each of the seven powering points. The total cable length is discretized in sections and each section has its impedance. The voltage drop within one section depends then on the current flowing in the respective section. See below the single-phase equivalent circuit, used as a calculation model.

[16] The DC voltage is the rectified value of the AC voltage, if a 6-puls diode rectifier were used.

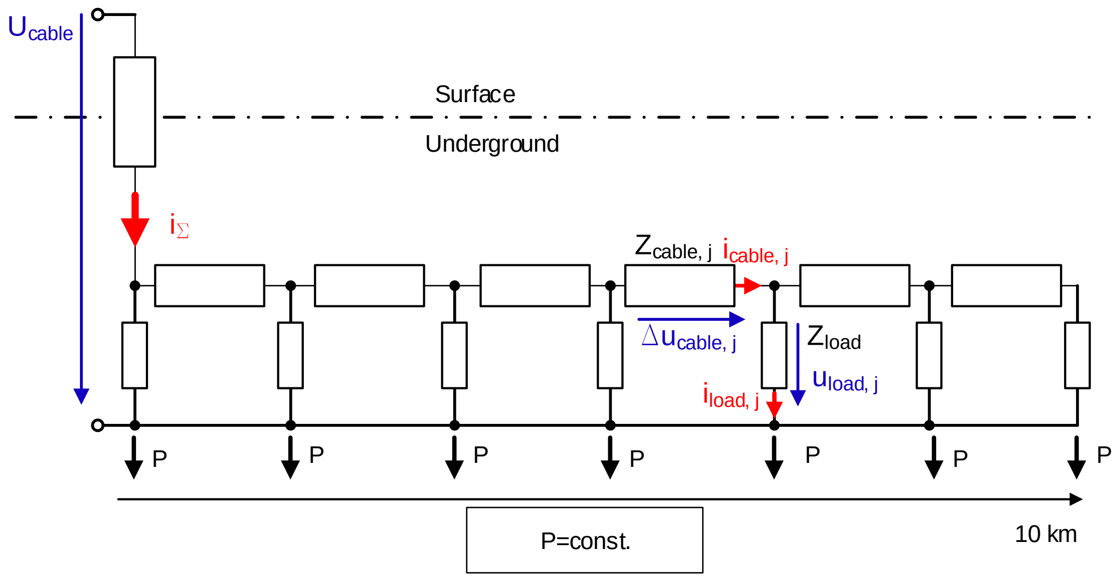

Figure 24: Calculation model for the voltage drop and losses, single-phase representation.

The voltage drop for each section along the transmission line is calculated with:

$$\Delta U_{AC} = I_{AC} \cdot R \cdot \cos\varphi + I_{AC} \cdot X \cdot \sin\varphi$$
$$P_{loss\ AC} = 3 \cdot I_{AC}^2 \cdot R \tag{1}$$

$$\Delta U_{DC} = I_{DC} \cdot R$$
$$P_{loss\ DC} = 2 \cdot I_{DC}^2 \cdot R \tag{2}$$

In the AC case, the result for the losses has to be multiplied by three. Due to load symmetry, no return path is needed. In the DC case, the voltage drop in each section has to be doubled to respect the return path cable. The result for the losses has to be multiplied by three two single-core cables forming one power transfer system. For the calculation of the voltage drop and the losses, see the appendix. The categorized load with its power rating is shown in the table below.

Table 10: Results for the UPS AC-DC comparison study

Distribution in:	AC	DC
Energy storage integration	Transformer-rectifier combination, DC-DC bidirectional SST, DC-AC inverter	DC-DC bidirectional SST
Equipment in the tunnel to connect the load, per load point	2 x transformer	2 x DC-DC-AC unidirectional SST
Total installed volume/weight of the equipment in the tunnel	6.4 m³ / 5.3 tons	4 m³ / 4 tons
Maximal voltage drop relative to U_{cable}	3.78%	4.12%
Transmission losses at P_{load}=P_{nom}=1 MW, transferred by the first power source and one cable system[17]	2.51% of P_{nom}	2.76% of P_{nom}

5.3.1 Results discussion

Once a DC grid is formed, the energy storage integration is easier than in the case of AC. The DC grid leads to reduced weight and volume of the load connecting equipment. Further, only 4 cables are needed (instead of 6 in AC case) to form a double redundant system. The voltage drop on the cable and the transmission losses are similar in both cases if particular AC losses (proximity and skin effect, eddy currents in the shielding) are not accounted. For a 10km long double redundant UPS, 1/3 of the total cabling is reduced by using DC.

5.4 Summary

The introduction of a medium voltage DC distribution grid to power particle accelerators has the great potential for equipment reduction i.e. reducing the weight and volume of power converters. This is especially important for underground installations as it eases the process of installation and maintenance. For superconducting loads, the weight/volume reduction with DC is -50%. Also, a reduction of the cabling can be achieved with DC.

The identified powering topologies in the next chapter are considering both AC and DC based variants. Thus the comparison of AC vs. DC is brought onto an even more detailed level, as weight and volume of the converter modules, their reliability and their losses are compared.

[17] Eddy current losses, proximity and skin effect losses which occur in the AC case are not included.

6 Comparison of principle power supply topologies for the main bending dipoles

The comparison is done for a set of performance indicators: reliability, losses, space demand and investment costs. The costs are drawn from CERN experience and may not reflect the costs if the electrical equipment were to be produced for real. However, the method of how these costs are used for the optimisation and the sensitivity analysis remains valid in any case. To give the outer frame of the comparison, a staged power supply (see the figure below) is introduced and the powering variants under comparison are fitted into the structure as presented in the following. The magnet powering system (MPS) for the main bending dipole consists of three stages.

- Stage 1: Transformation from 36 kV (surface) to appropriate input voltage for the converter (AC or DC), to supply the actual converters in the cavern.
- Stage 2: The charging stage supplies mainly the battery energy storage system and partly also the magnet supply stage
- Stage 3: The magnet supply stage is a bidirectional, non-isolated DC-DC converter; to provide current to the magnet circuit; the battery energy storage and the charger are the sources of power. The magnet supply stage remains unchanged in all MPS variants, they differ only in the charging stage (stage 2) and the transformation stage (stage 1) from 36 kV level.

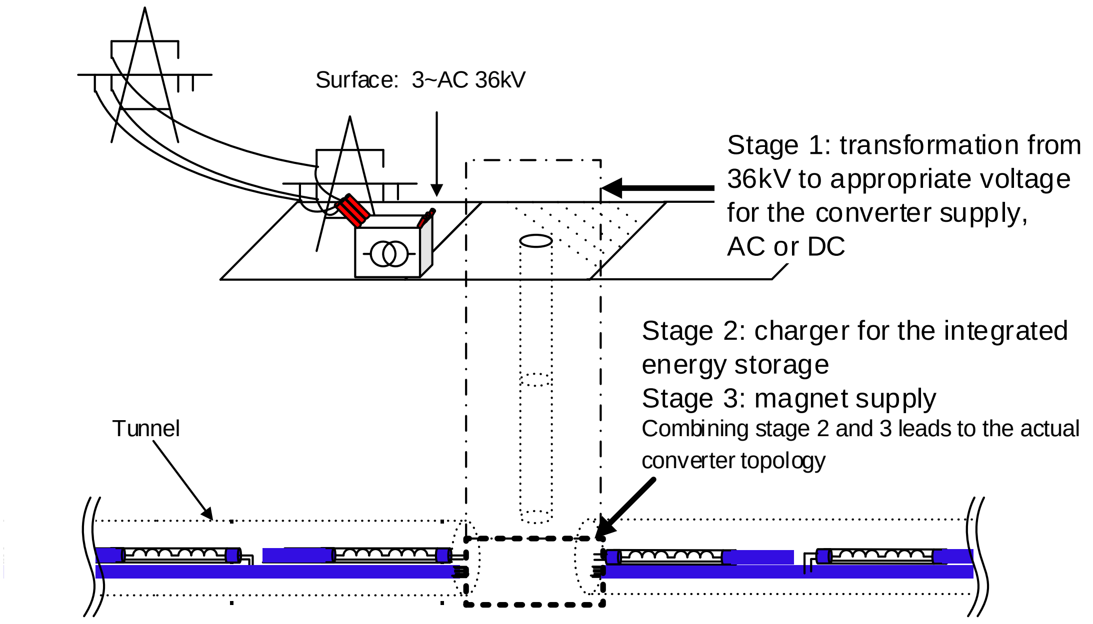

Figure 25: The staged magnet powering system (MPS) to power the main bending dipole magnet circuits.

Considering now all dipole circuits, one hundred power converters in the MW-class need to work perfectly synchronized and run permanently for a successful operation of FCC. These hundred power converters are located along the 98 km circumference and are installed caverns, on average 200 m below the surface. This brings up the very first design aspect for the MPS – reliability.

6.1 Reliability aspects

Reliability is the probability that after a certain time the equipment is running without a fault. For the analysis of the reliability, a series-connected reliability model of the complete magnet powering system is used. This model consists of two parts. The first part of the reliability model is always stage 1 (the transformation from the 36 kV level to a proper voltage level, AC or DC). The second part comprises stages 2 and 3 (the converter) of the MPS.

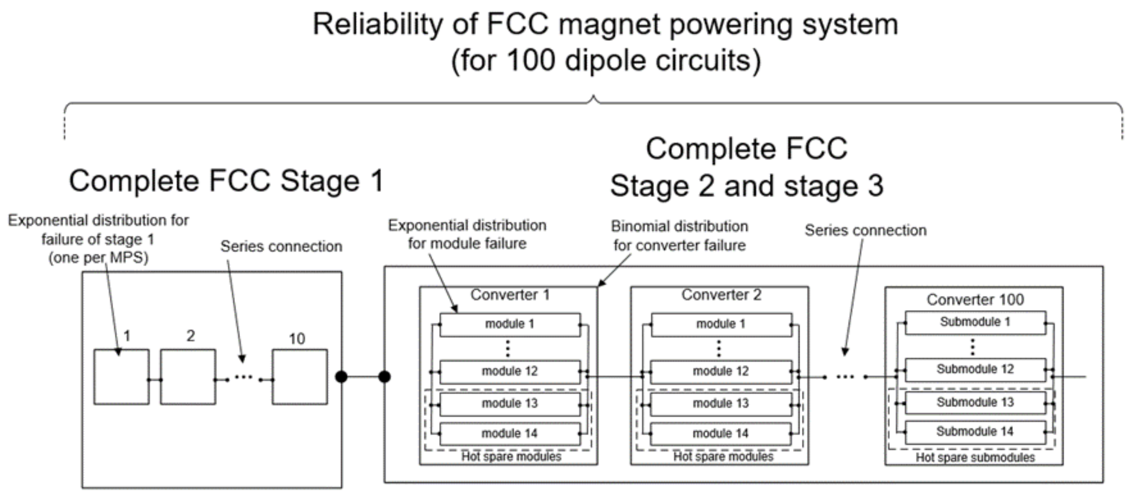

Figure 26: Reliability model of the FCC magnet powering system (MPS), for in total 100 dipole magnet circuits. The first block on the left represents 10 times stage 1 of the MPS, the second block represents 100 converters (10 converters per MPS). To calculate the reliability, several steps and different distribution functions are used. A series connection is formed within the block as well as for the total system reliability.

6.1.1 Stage 1 reliability analysis

In principle, this stage can be designed with 3-phase transformers (converters are supplied in AC), or with transformer-rectifier combinations (converters are supplied with DC).

In the case using only a 3-phase 50 Hz distribution transformer in stage 1, the reliability is calculated by using statistical numbers from the VDE (Association for Electrical, Electronic &

Information Technologies). For a time horizon of 1 year, the reliability of a single transformer is 0.997, and for ten transformers (series-connected as shown in Figure 26) the reliability is 0.97.

In the case where a 3-phase 50 Hz transformer and a rectifier are used in stage 1, a difference in terms of reliability comes with the type of rectifier i.e. if it is an active or passive rectifier.

A reliability model on a component level – using failure in time (FIT) values – is used to calculate the mean time between failure (MTBF) for two rectifier types. Both have the same and adequate rating of U_{DC}=10 kV and $P_{rectifier}$=6 MW. For the passive rectifier, a 12-puls diode rectifier is chosen. With the diode D1721NH90T with U_{block}=5000 V from Infineon, 12 diodes are necessary. For the active front-end rectifier, a 3-level neutral point clamped (NPC) rectifier is chosen. This topology has per phase 4 IGBTs (6.5 kV voltage class e.g. FZ750R65KE3 from Infineon) and 6 diodes.

Table 11: Reliability for each rectifier variant, based on FIT values of the respective components

Component	FIT value	12-puls diode rectifier	3-level NPC rectifier
		Amount of the respective component	
IGBT	100	-	12
Gate driver	150	-	12
Diode	10	12	6
Measuring unit	50	-	2
DC bus capacitor	50	2	2
Sum FIT of the rectifier		220	3200
MTBF in thousand hours		4545	313
Reliability of one rectifier		99.8%	97.1%
Reliability of ten rectifier (full FCC)		98.1%	75.7%
Reliability of ten rectifier-transformer combinations (full FCC)		95.2%	73.4%

In the case of the passive rectifier, the influence on the total system reliability is very small, as the reliability curve is just down-shifted slightly by 95.2%. The converter reliability is the dominant factor in the total MPS reliability.

In the case of the active rectifier, the downscaling is 73.4%. Stage 1 has a considerable influence and needs to be considered when determining the total MPS reliability.

6.1.2 Stage 2 and 3 reliability analysis

In principle, the converter can be designed non-modular or modular.

In the non-modular case, the converter can be seen as a complete block unit (see Figure 27). The installation of spare units has no sense, as they cannot overtake the magnet current (~12 kA) without having a complete system stop. As an example, the main dipole converters in the LHC are non-modular and the only way to improve the system reliability is to improve their MTBF.

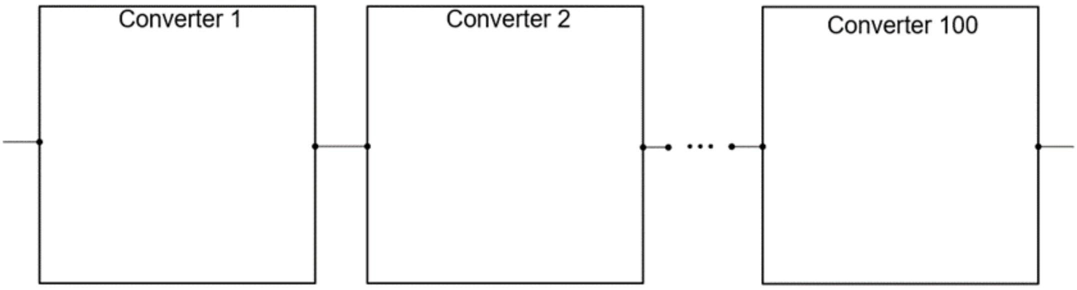

Figure 27: Reliability model, representing with each block one converter for one dipole circuit. A series system is formed because all blocks (converters) need to work simultaneously.

In the modular case, the converter can follow a B+x module concept to improve the reliability. B is the basic number of modules that need to work and x is the number of hot spare modules (see *Figure 28*). This gives an important design parameter as the reliability can be improved by simply increasing the number of spare modules.

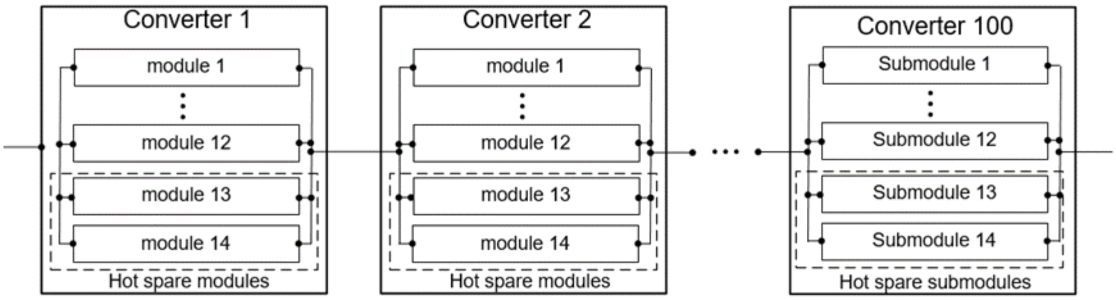

Figure 28: Reliability model representing each block as one converter, which is in turn build-up of modules.

For the calculation the following assumptions are made:

- The decision for B=12 comes from an output current consideration, as 12 modules can deliver a total current of 12 kA (11,4 kA are needed for the dipole magnet circuits). And an output current of 1 kA can easily be delivered by a converter module using standard components.
- The failure rate stays constant, with no infant nor wear-out failures. This allows using the exponential distribution
- Each of the submodules is independent of each other, if one submodule fails, it will not change the failure rate of the other ones. This allows using the binomial distribution to correctly represent the increased availability of one converter (block) due to the redundancy.
- The switching between the submodules is ideal

As a further step, the analysis could respect a more detailed analysis of the way the spare submodules are treated. For example, if they are used as hot spares or cold spares, see here for also [67].

If the mean time between failure (MTBF) for one submodule is defined, the probability for the next failure to happen at time t could be calculated as:

$$P(next\ failure\ is\ happening\ in\ t) = 1 - e^{-\frac{1}{MTBF} \cdot t} = q \tag{3}$$

Using now the binomial distribution to calculate the availability of the whole converter consisting of M submodules, where N submodules could fail and the converter still would work. If fewer or max N submodules are failing the converter is working.

$$\begin{aligned} P(converter\ is\ working\ until\ t) &= P(number\ of\ failed\ submodules\ until\ t\ is\ \leq N) = \\ &= \sum_{i=0}^{N} \binom{M}{i} \cdot q^i \cdot (1-q)^{M-i} \end{aligned} \tag{4}$$

This gives for all FCC converters a reliability of:

$$P(FCC\ is\ working\ until\ t) = P(converter\ is\ working\ until\ t)^{100} \tag{5}$$

The result of the theoretical analysis is shown below in Figure 39. The reliability is expressed as the probability to operate 1 year without a single failure. The LHC is taken as a reference for reliability performance.

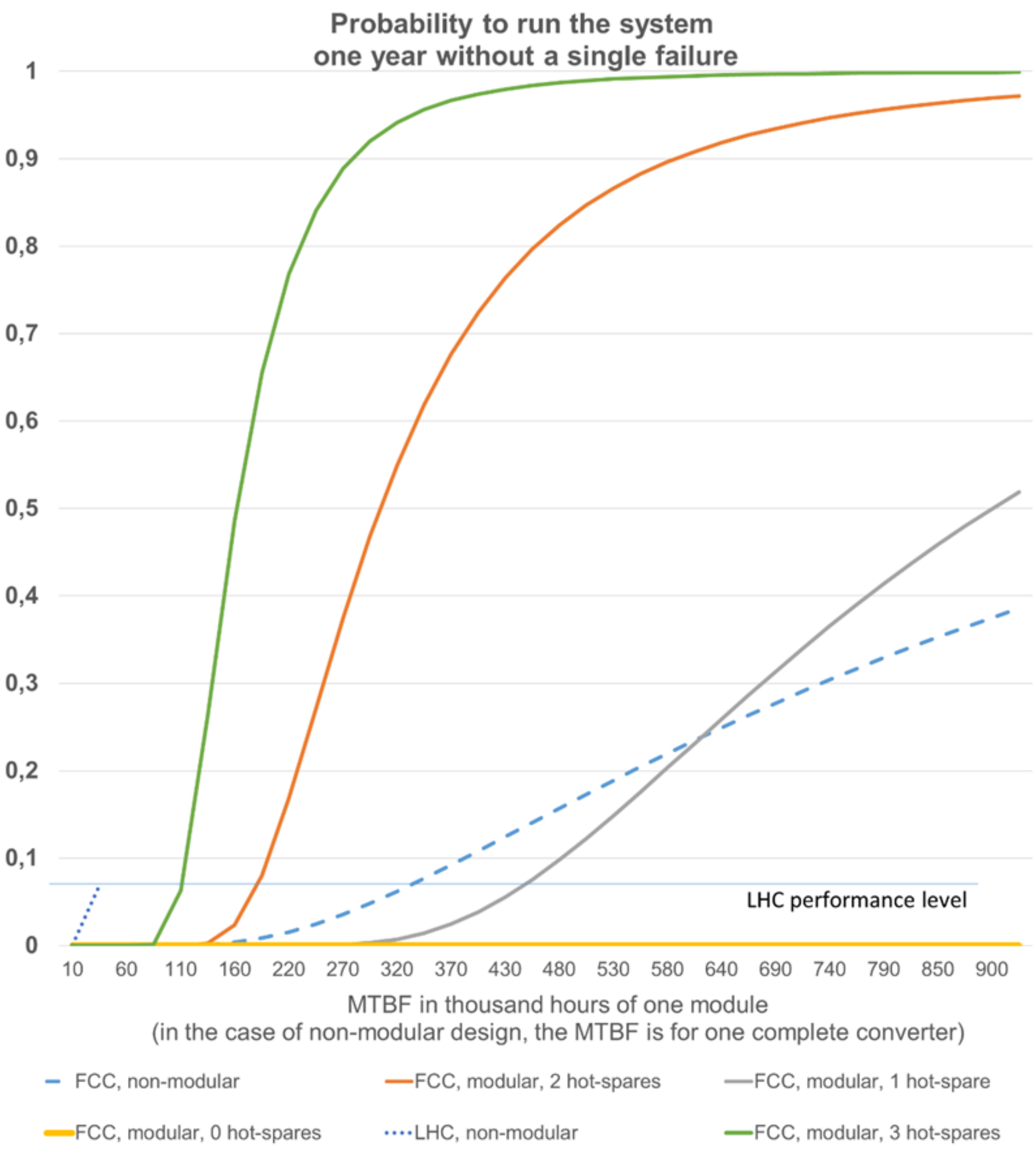

Figure 29: Reliability with a dependence of the MTBF of either a converter module (modular design) or the whole converter (non-modular design). For FCC 4 modular design variants are shown with 0 (yellow curve on the bottom), 1, 2, and 3 hot-spare modules, and one non-modular design variant. For comparison, the reliability performance of the LHC is indicated.

In the LHC, the non-modular converters for the main bending dipoles have an MTBF ranging within 6k-20k hours (see the Appendix). If for FCC a similar non-modular converter is used, then 10-times more failures and thus 10 times more stops are going to happen.

To reach the same LHC reliability of 0.07, the FCC non-modular converter needs a 10 times higher MTBF (see the LHC performance level line in Figure 39). Given the long experience with the LHC, a higher MTBF for a non-modular converter is hard to reach.

For FCC an even higher performance than with the LHC is desired. Thus the focus is laid on modular topologies.

A modular converter topology has the advantage that a prototype can be built more easily as only one module needs to be constructed and not the whole converter. This allows the performance of accelerated ageing tests, to indicate the achievable MTBF of a single module.

Based on this, the right level of redundancy (0, 1, 2, or 3 hot-spare modules) can be chosen.

For example, if a double redundant design (2 hot-spare modules) is chosen, and a converter module MTBF of about 400k is achieved, the reliability performance is 0.72 and this is already 10-times higher than in the LHC. Even though FCC has in total 100 converters, whereby LHC has 8.

The sensibility of the reliability towards the MTBF can also be observed in Figure 29. For the double redundant design, high sensitivity of the MTBF between 200k and 400k is observed. In this region, small changes of the module MTBF lead to large changes in reliability. MTBF improvements above this region have in turn only small reliability improvements.

The main conclusion is that only fully modular converter topologies, including hot spare modules, fulfil an acceptable performance.

6.2 Identified converter topologies for the comparison

There is a large variety of potential powering topologies, however the following functional core elements must be considered:

- Be fully modular to achieve an acceptable level of reliability
- Galvanic isolation of the magnet: to allow the grounding (direct or indirect with a ground current measurement) of the minus pole of the magnet circuit.
- Optional integration of energy storage: the transmission grid potentially cannot deliver the required power. Integrated energy storage reduces also the complete supplying infrastructure, triggering thus an optimisation problem (see here chapter 6.9).
- Bi-directionality: the energy stored in the superconducting main bending magnets needs to be recoverable into electrical power grid.
- Minimum power rating: A particular case is used to calculate the rating of stage 1 and stage 2. In the case of a quench of a superconducting magnet, the magnet protection extracts the stored magnetic energy into heat, thus leaving the energy storage empty as no regular recovery process can happen anymore. However, for the next ramp up the energy storage need to be fully charged. The total energy needed to ramp all ten magnet circuits up is 4.56 MWh. Respecting the foreseen preparation time [68] until in such a case the next ramp-up could be done, gives of 1h. This gives a minimum rating of 4.56 MW in total or 38 kW on converter module level.
- Deliver high currents and low voltages on the output side and receiving a high voltage on the input side. In numbers, the output current and voltage is up to 12kA respectively 300V. The input voltage is in the order of tens of kV to the deliver the required input power for the magnet ramping.
- Usage of standard power electronic components as good as possible i.e. by choosing the adequate voltage and current levels.

Common modular multilevel converter (MMC) topologies are not suitable as they deliver rather high DC voltages and low currents. Cascaded H-bridge (CHB) topologies savour a wide analysis in literature and wide usage in industry [69, 70]. By adequate paralleling of the CHB power cells all requirements are fulfilled and is with marginal difference represented in variant A – see the overview of the variants Table 12. Due to the paralleling on the output side, a very high apparent switching frequency is realised. Thus, a very good ripple performance is achieved on the magnet, even with a low switching frequency of the stage 3 converter module (DC-DC 4Q H-bridge) is realised. However, it leads to a heavy use of 50Hz components for the supplying of the power cells. In this regard a bad maintainability (weight of the equipment) and a large space demand is to be expected. Following the attempt to avoid 50Hz components brings up medium frequency transformers and their related topologies which are presented in variant B and C. The Input-Series-Output-Parallel (ISOP) converter configuration is the most promising topology. It is fully modular, allow to receive high power on the input side and deliver very high currents on the output side, and energy storage can be integrated. Due to the possible connection to a DC grid and the middle frequency components, it has the potential of weight and size reduction.

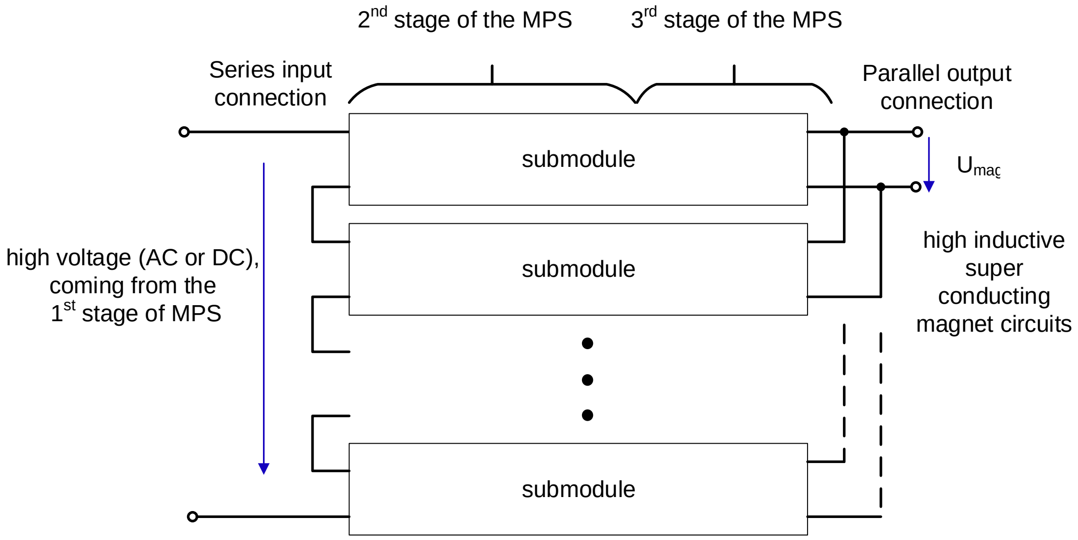

Figure 30: Input-Series-Output-Parallel (ISOP) converter configuration.

In order to use standard power electronic switches i.e. IGBTs which are widely used for industrial applications as e.g. motor drives, the following points are fixed:

- the number of modules per converter 12. Thus power electronic switches for the output module can easily be found. The current rating is about 1 kA, and 12 modules can easily deliver the required magnet current of 11,4 kA.
- The DC link voltage U_{DC} within the module is about 300-350 V. Thus a potential battery energy storage can optimally be connected and for this voltage rating, power electronic switches are easily available on the market.
- The input voltages of the modules using a dual active bridge (DAB) are in the range of 800-1000 V, as it is a comfortable input voltage level of the required middle frequency (mf) transformer and power electronic switches.

The following three identified topology variants are analysed and compared against each other. All variants fulfil the essential requirements they are chosen to highlight the importance of upcoming technologies as solid-state transformers and DC grids. They are compared in terms of reliability, losses, investment costs, weight and space demand. For each variant the power rating and the energy storage capacity is optimised. The variants are summarized below.

Table 12: Variants for the topology comparison study

Variant A: Line frequency components and energy storage integrated into the converter modules	Stage 1: 3-phase 50 Hz step-down transformer, from 36 kV to 150 V Stage 2: three-phase 50Hz converter transformer with 3-phase active front end rectifier to form a low voltage (LV) DC bus. Optional, the battery modules are connected to the LV DC bus Stage 3: DC-DC magnet supply stage A converter module comprises stage 2 and stage 3
Variant B: Single AC phase supplied solid-state transformer and energy storage integrated into the converter modules	Stage 1: 3-phase 50 Hz step-down transformer, from 36 kV to 12.5 kV Stage 2: AC-DC single-phase active front end rectifier, DC-DC full bridge with a middle-frequency isolation transformer to form an LV DC bus. Optional: the battery modules are connected to the LV DC bus Stage 3: DC-DC magnet supply stage A converter module comprises stage 2 and stage 3, and the converter modules are connected in an input-series-output-parallel configuration (input of charger and output of magnet supply)
Variant C: DC grid supplied solid-state transformer and energy storage integrated into the converter modules	Stage 1: 3-phase 50 Hz step-down transformer, from 36 kV to 8.7 kV and 3-phase (preferable passive) rectifier to form a ~12.3 kV DC bus Stage 2: DC-DC full bridge with a middle-frequency isolation transformer to form an LV DC bus. Optional: the battery modules are connected to the LV DC bus Stage 3: DC-DC magnet supply stage A converter module comprises stage 2 and stage 3, and the converter modules are connected in an input-series-output-parallel configuration (input of charger and output of magnet supply)

The following subchapters give a detailed representation of each of the topologies. Important in the comparison of the variants is how they relate to each other. The absolute performance is only shown then for the best variant.

For each topology, the power rating for each stage is presented, by showing the upper and the lower limit. The maximum power rating corresponds to 0% integrated energy storage and the minimum power rating to 100% integrated energy storage. Additional notes concerning ramping strategy and power ratings are made.

Values for specific volume and weight (dm^3/kW and kg/kW) are obtained from manufacture and research prototypes. Corridors and safety distances are needed in any case and are thus not regarded in this variant comparison. For calculation examples see also the Appendix.

6.2.1 Variant A: Line frequency components and energy storage integrated into the converter modules

Shown below is the topology of variant A, starting at the connection to the 36 kV distribution system on the surface, ending at the output stage which delivers the magnet current i_m. In the cavern, ten converters for ten magnet circuits are installed.

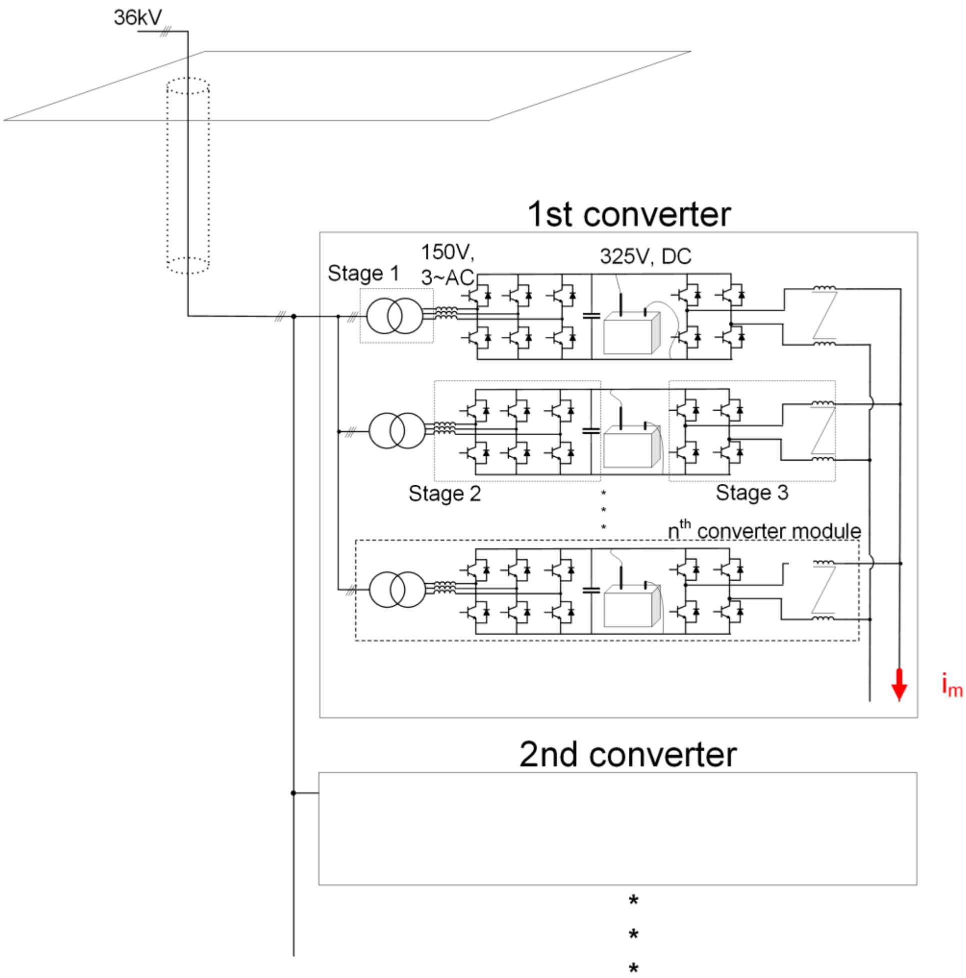

Figure 31: Topology of variant A.

Description

The combination of 50 Hz transformer, chokes, and active frond-end rectifier is proven and widely used topology, also at CERN.

A 50Hz transformers is needed and is located underground. Installation and maintenance with line frequency transformers is challenging due to their weight.

Also, the space demand with line frequency components becomes considerable, in particular in an underground installation.

Module design aspects

The converter transformer can be integrated into the module, but this also makes the module unhandy and any replacement becomes critical.

Power rating

Stage 1 is a 50 Hz converter transformer, and stage 2 is an active front-end rectifier. The power rating of stages 1 and 2 depends on the energy storage design. With full capacity internal installed energy storage, stage 1 has a rating of at least 4.5 MW, stage 2 in total also 4.5 MW or 0.45 MW for each converter. Assuming 12 modules per converter gives 38 kW per module.

The DC-DC H-bridge in stage 3 has only a max value for its rating, which depends on the ramping strategy. By considering 12 modules per converter, a rating of 250 kW per module for constant voltage ramping, and a rating of 283 kW per module for constant power ramping occurs.

In the table below the minimum and maximum ratings for power, weight and volume are shown. The power rating depends on the energy storage capacity, whereas weight and volume in turn depend on the power rating.

Note: the values in brackets refer to constant power ramping, otherwise to constant voltage ramping. The first part of the entries refers to one powering point of FCC i.e. 120 modules, and second part refers to a single module level

Table 13: Weight and volume of variant A

<table>
<tr><th>Item</th><th colspan="2">Power rating</th><th colspan="2">Weight</th><th colspan="2">Volume</th></tr>
<tr><td></td><td>Min</td><td>Max</td><td>Min</td><td>max</td><td>Min</td><td>max</td></tr>
<tr><td>120 converter transformers 6 kV to 150 V</td><td rowspan="2">* 4.56 MW in total, 38 kW per module *</td><td rowspan="2">* 30.2 MW (18 MW), 251 kW (150 kW) *</td><td rowspan="2">* 18 tons, 148 kg *</td><td rowspan="2">* 118 tons (70tons), 0.98 tons (0.59 tons) *</td><td rowspan="2">* 21 m^3, 171 dm^3 *</td><td rowspan="2">* 136 m^3 (81 m^3), 1.13 m^3 (0.68m^3) *</td></tr>
<tr><td>120 AC-DC active frond end rectifier modules</td></tr>
<tr><td>120 DC-DC H-bridge magnet supply modules</td><td colspan="2">30.2 MW (34 MW) total, 251 kW (283 kW) per module</td><td colspan="2">15 tons (17 tons), 125 kg (142 kg)</td><td colspan="2">15 m^3 (17 m^3), 125 dm^3 (142 dm^3)</td></tr>
<tr><td colspan="7">Notes: *values are for transformer-rectifier combinations, combining converter module transformers and AC-DC rectifier modules
Values in (…) refer to constant power ramping</td></tr>
</table>

6.2.2 Variant B: Single AC phase supplied solid-state transformer and energy storage integrated into the converter modules

Shown below is the topology of variant B, starting at the connection to the 36 kV distribution system on the surface, ending at the output stage delivering the magnet current i_m. In the cavern, ten converters for ten magnet circuits are installed.

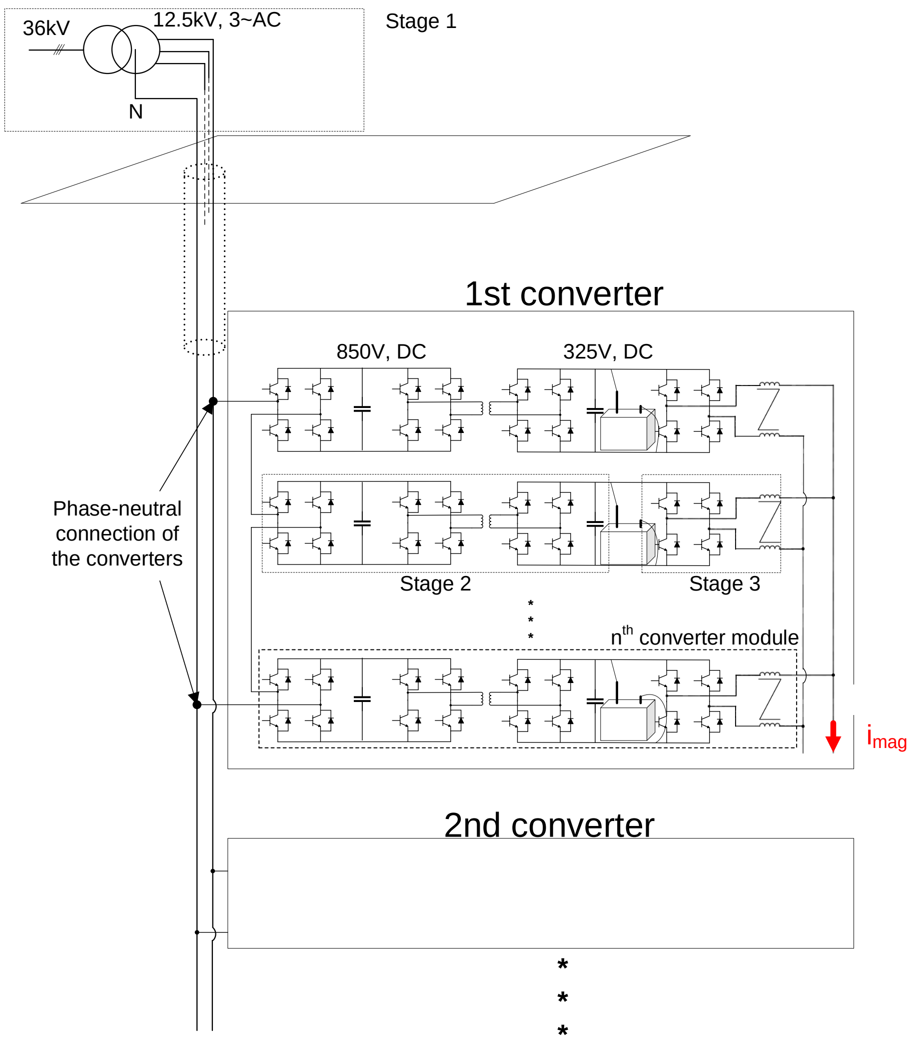

Figure 32: Topology of variant B.

Description

This variant is a single AC phase supplied solid-state transformer (SST). The SST development in the last 60 years has brought in principle five topologies [38], where all of them are based on a single AC supply line. A highly advantageous application of the SST is in

AC/DC conversion systems, as losses could be reduced to half, volume and weight reduced to a third, compared to line frequency transformer in combination with a rectifier system [37].

For the MPS topology it means that except for the transformer on the surface[18], all 50 Hz components are replaced by middle-frequency transformers. This allows a reduction in size and weight.

The disadvantages of using single-phase AC systems are harmonics and power imbalances. In single-phase AC systems the second harmonic is present. Thus if the SST is supplied by a single AC line, the modules need either a 2^{nd} harmonic filter which makes 10% of the total weight [71], or an oversized DC capacitor if not an adapted control is counteracting (but this compromises efficiency in turn) [41]. Also, the mutual influence of several converters connected to the same AC line needs to be considered, when designing the AC line-side filters [39].

The three-phase AC supplying infrastructure suffers from negative sequence currents caused by power imbalances due to the single AC line connection of the SST. For railway power systems special transformers, static VAr compensators, railway static power conditioner (RPC) or active power compensators (APC) in co-phase power systems are required [40], and considering the scale of FCC, it means very large additional infrastructure.

Module design aspects

The module comprises a single-phase AC-DC stage, DC-DC isolation stage, and the output DC-DC H-bridge. The battery is integrated on the LV DC bus within the module. The DC-DC isolation stage is realised with the dual active bridge, which fulfils the isolation requirement.

Power rating

Stage 1 comprises the 50 Hz transformer, stage 2 comprises a single-phase active front-end rectifier and a DC-DC converter realised as dual active bridge. The rating of stage 1 and stage 2 is at least 4.56 MW for the full MPS, and at least 38 kW on converter module level.

The DC-DC H-bridge has only a max value for its ratings, which depends on the ramping strategy. By considering 12 modules per converter, a rating of 251 kW per module for constant voltage ramping, and a rating of 283 kW per module for constant power ramping occurs.

[18] The step down transformer, may could be skipped but then the voltage rating of the IGBTs on the high voltage DC side of the dual active bridge (DAB) become rather high as the DC voltage level is then Udc hv side = (36 kV/sqrt(3)*sqrt(2)/12 = 2.45 kV. To keep the voltage rating of the IGBTs low, a converter module input voltage of 850 V is chosen. This leads to a secondary voltage of Uphase-phase RMS=12.5 kV of the step down transformer.

Note: the values in brackets refer to constant power ramping, otherwise to constant voltage ramping. The first part of the entries refers to one powering point of FCC i.e. 120 modules, and second part refers to a single module level

Table 14: Weight and volume of variant B

<table>
<tr><th>Item</th><th colspan="2">Power rating</th><th colspan="2">Weight</th><th colspan="2">Volume</th></tr>
<tr><td></td><td>Min</td><td>Max</td><td>Min</td><td>max</td><td>Min</td><td>max</td></tr>
<tr><td>Distribution grid transformer 36 kV to 12.5 kV</td><td>4.56 MW</td><td>30.2 MW (18 MW)</td><td>12 tons</td><td>80 tons (46tons)</td><td>15 m^3</td><td>96 m^3 (55 m^3)</td></tr>
<tr><td>120 AC-DC converter modules</td><td>4.56 MW in total, 38 kW per module</td><td>30.2 MW (18 MW), 251 kW (150 kW)</td><td rowspan="2">* 9 tons, 76 kg *</td><td rowspan="2">* 60 tons (34 tons), 0.5 ton (0.3 ton) *</td><td rowspan="2">* 9 m^3, 76 dm^3 *</td><td rowspan="2">* 60 m^3 (34 m^3), 0.5 m^3 (0.3 m^3) *</td></tr>
<tr><td>120 DC-DC isolation converter modules</td><td>4.56 MW in total, 38 kW per module</td><td>30 MW (18 MW), 251 kW (150 kW)</td></tr>
<tr><td>120 DC-DC H-bridge magnet supply modules</td><td colspan="2">30.2 MW (34 MW) total, 251 kW (283 kW) per module</td><td colspan="2">15 tons (17 tons), 125 kg (142 kg)</td><td colspan="2">15 m^3 (17 m^3), 125 dm^3 (142 dm^3)</td></tr>
<tr><td colspan="7">Notes: *values are for AC-DC-DC solid-state transformers, combining AC-DC and DC-DC modules
Values in (…) refer to constant power ramping</td></tr>
</table>

Compared to variant A, a reduction of volume and weight of this AC-fed SST topology is to be expected. To overcome the filtering efforts and power imbalances, a DC-fed SST is to be considered, see the following chapter.

6.2.3 Variant C: DC grid supplied solid-state transformer and energy storage integrated into the converter modules

Shown below is the topology of variant C, starting at the connection to the 36 kV distribution system on the surface, ending at the output stage delivering the magnet current i_m. In the cavern, ten converters for ten magnet circuits are installed. The rectifier station is kept on the surface for easier installation, maintenance and the DC grid can also be used to power loads on the surface.

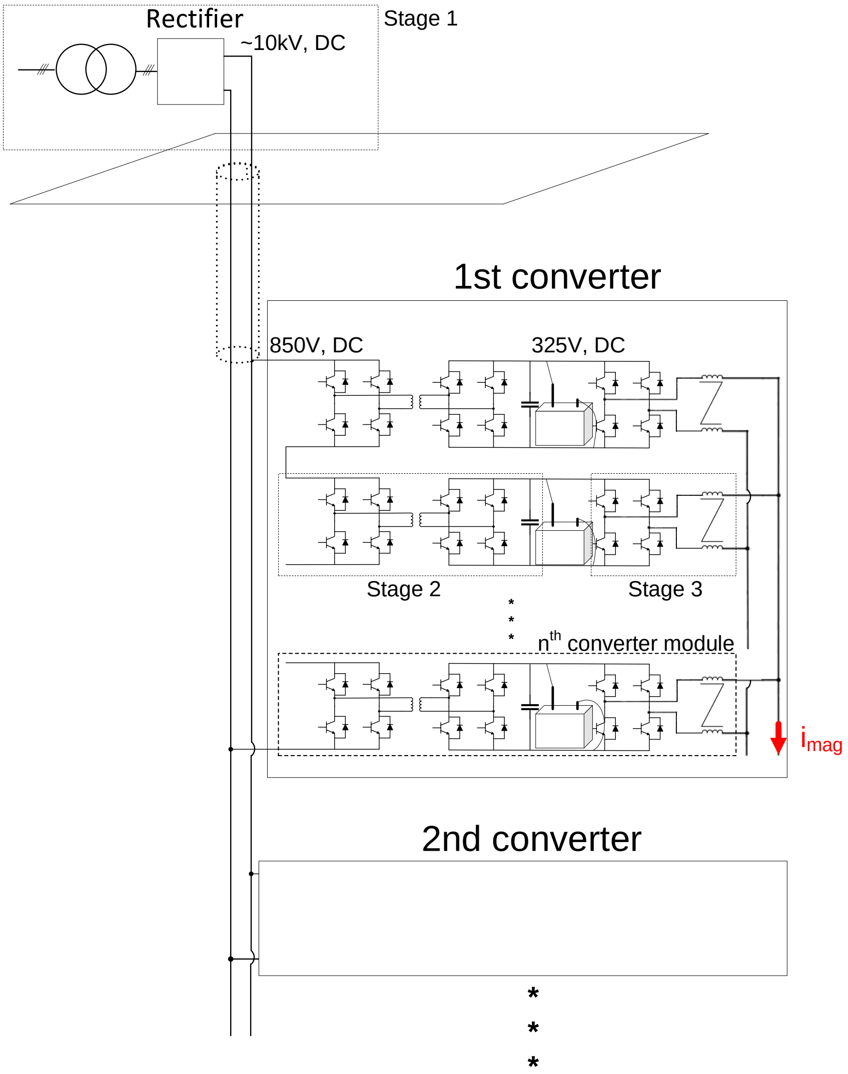

Figure 33: Topology of variant C.

Description

This variant is a DC supplied solid-state transformer. Except for the rectifier transformer on the surface, all 50 Hz components are replaced by middle-frequency transformers. This allows a reduction in size and weight. Compared to variant B, a rectifier is needed on the surface.

Due to the DC supply, all ten converters could be connected to the DC grid without fearing a power imbalance. Also, a mutual influence of several converters connected to the DC line is expected to be reduced, compared to variant B.

An active rectifier is needed if energy needs to be transferred to the network (and no other load can consume it). If enough energy capacity is installed (or other load connected to the DC bus), the rectifier could be reduced to a passive one.

The dc voltage is chosen such that the voltage rating of the IGBTs on the high voltage side of the converter module is between 800-1000 V. Considering 12 converter modules connected in series gives a required DC bus voltage of 9.6-12 kV.

Module design aspects

The module comprises a DC-DC isolation stage and the output DC-DC H-bridge. The battery is integrated on the LV DC bus within the module. The DC-DC isolation stage is realised with the dual active bridge, which fulfils the isolation requirement. The design is compared to variant B simpler.

Power rating

Stage 1 comprises the 50 Hz transformer and a central rectifier.

Stage 2 comprises now only a DC-DC converter realised as dual active bridge.

The rating of stages 1 and 2 is at least 4.56 MW for the full MPS and at least 38 kW on converter module level.

The DC-DC H-bridge has only a max value for its ratings, which depends on the ramping strategy. By considering 12 modules per converter, a rating of 251 kW per module for constant voltage ramping, and a rating of 283 kW per module for constant power ramping occurs.

Note: the values in brackets refer to constant power ramping, otherwise to constant voltage ramping. The first part of the entries refers to one powering point of FCC i.e. 120 modules, and second part refers to a single module level

Table 15: Weight and volume of variant C

Item	Power rating		Weight		Volume	
	Min	Max	Min	Max	Min	Max
Rectifier-transformer 36kV to 8.7kV combined with central AC-DC	* 4.56 MW *	* 30.2 MW (18 MW) *	* 18 tons *	* 118 tons (70 tons) *	* 21 m³ *	* 136 m³ (81 m³) *
120 DC-DC isolation converter modules	4.56 MW in total, 38 kW per module	30.2 MW (18 MW), 251 kW (150 kW)	6.8 tons, 57 kg	45 tons (27 tons), 377 kg (225 kg)	6.8 m³, 57 dm³	45 m³ (27 m³), 377 dm³ (225dm³)
120 DC-DC H-bridge magnet supply modules	30.2 MW (34 MW) total, 251 kW (283 kW) per module		15 tons (17 tons), 125 kg (142 kg)		15 m³ (17 m³), 125 dm³ (142 dm³)	
Notes: *values are for transformer-rectifier combinations Values in (…) refer to constant power ramping						

Variant A can be excluded due to the high demand in space and weight. Heavy and unhandy modules are expensive during installation and maintenance.

6.2.3.1 Variant C*

As a special sub design of variant C, the variant C* is explicitly designed with a passive rectifier in stage 1. This has advantages in reliability (see chapter 6.3.3) and in investment costs (see chapter 6.7.1).

The only requirement for such a design is that the recovered energy from the magnet circuits can be stored in the energy storage with a capacity large enough, or if it can be consumed by other loads connected to the high voltage DC bus in stage 1. Then a single directional power flow, from the 36kV AC grid to the stage 2 DC bus is sufficient and reasonable.

6.3 Realistic MPS reliability

The identified topology variants A, B and C are analysed in terms of reliability, which is probably the most important design criteria.

The basic evaluation criterion is the failure in time (FIT) parameter for each component installed in the respective submodule for each variant.

From the sum of the FIT value, the mean time between failures (MTBF) can be calculated and the reliability model from chapter 6.1 gives the MPS reliability.

6.3.1 Module component description

Variant A

Converter transformer, 6 IGBTs for the 3-phase active front end rectifier, low voltage DC capacitor, battery module unit, 4 IGBTs for the magnet supply stage

Variant B

4 IGBTs for the single-phase active front end rectifier, 8 IGBTs for the dual active bridge, 1 mf transformer, low voltage DC capacitor, battery module unit, 4 IGBTs for the magnet supply stage.

Variant C

8 IGBTs for the dual active bridge, 1 mf transformer, low voltage DC capacitor, battery module unit, 4 IGBTs for the magnet supply stage

All IGBTs need gate drivers, and each conversion stage needs to measure input and output currents, the voltage on the low voltage DC bus is measured in all variants, and in the two ISOP configured converters, the input voltages need also to be measured.

6.3.2 Realistic MTBF for each variant

The table below highlights the component utilization concerning its failure in time (FIT) number, leading to the MTBF for each of the variants.

Table 16: MTBF calculated for each variant, based on FIT values of the respective components

Component	FIT value	Variant A	Variant B	Variant C
		Amount of the respective component		
IGBT	100	10	16	12
Gate driver	150	10	16	12
Measuring unit	50	5	8	7
Low voltage DC bus capacitor	50	10	10	10
Input capacitor	50	-	1	1
50 Hz transformer	1	1	-	-
mf transformer	10	-	1	1
Battery module	500	1	1	1
Sum FIT module		3751	5460	4410
MTBF in thousand hours		**267**	**183**	**227**

Design variant A leads to an MTBF of 267k hours, which is the highest of the three. This comes mainly due to the relatively low amount of IGBTs.

Design variant B has the most complex designed converter module and thus with 183k hours also the lowest MTBF of all three variants.

Variant C is with an MTBF of 227k hours in between the other two.

6.3.3 Complete system reliability

The table below shows the total reliability for each of the variants.

Table 17: Complete system reliability based on the estimated MTBF values of stage 1 and stage 2+3

	Variant A	Variant B	Variant C (active rectifier)	Variant C* (passive rectifier)
Stage 1 reliability	---[19]	97%	73.4%	95.2%
2 hot spare modules				
Stage 2 and 3 reliability	37.4%	8%	23.7%	23.7%
Probability FCC MPS works 1 year without a single fault	**37.4%**	**7.7% (≈LHC performance)**	**17.4%**	**22.6%**
3 hot spare modules				
Stage 2 and 3 reliability	88.9%	65.5	82%	82%
Probability FCC MPS works 1 year without a single fault	**88.9%**	**63.5**	**60.02**	**78.1%**

The reliability of stages 2 and 3 is taken as a k.o. criterion because these stages are installed underground. Any maintenance or replacement is much more expensive than on the surface. Variant B is thus the worst and be excluded.

19 For variant A, stage 1 is included in the modules and its reliability is respected already in the point “stage 2 and 3 reliability”.

6.4 Converter module design considerations (stages 2 and 3)

In the module design, stage 2 is of high interest, as the complexity, weight, and volume of the converter module depend on it (note: stage 3 is the same in all variants).

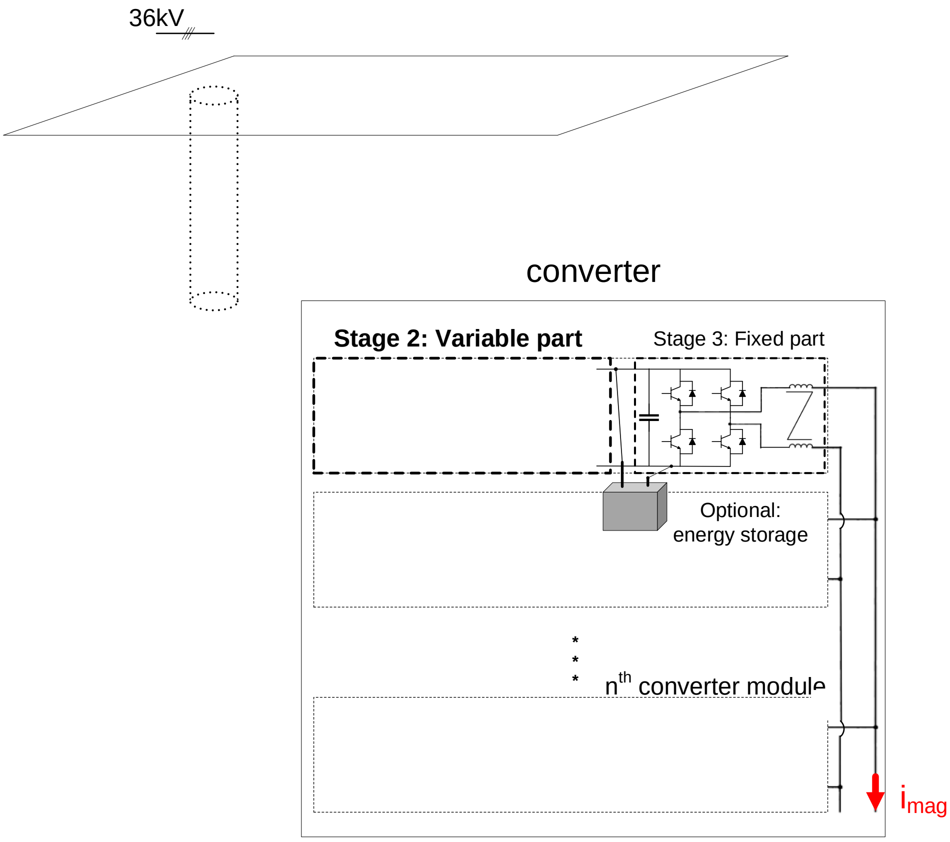

Figure 34: Comparison on converter module level. The complexity, weight, and volume of the converter module depend on the design for stage 2.

The topology of stage 2 is defined partly from stage 1, as it can deliver either AC or DC voltage. Stage 1 can deliver in principle a voltage classified into:

- three-phase AC (Variant A),
- single-phase AC (Variant B),
- DC (Variant C).

From this design parameter, also three in principle different topologies for stage 2 can be identified. These stage 2 topologies are shown in the figure below.

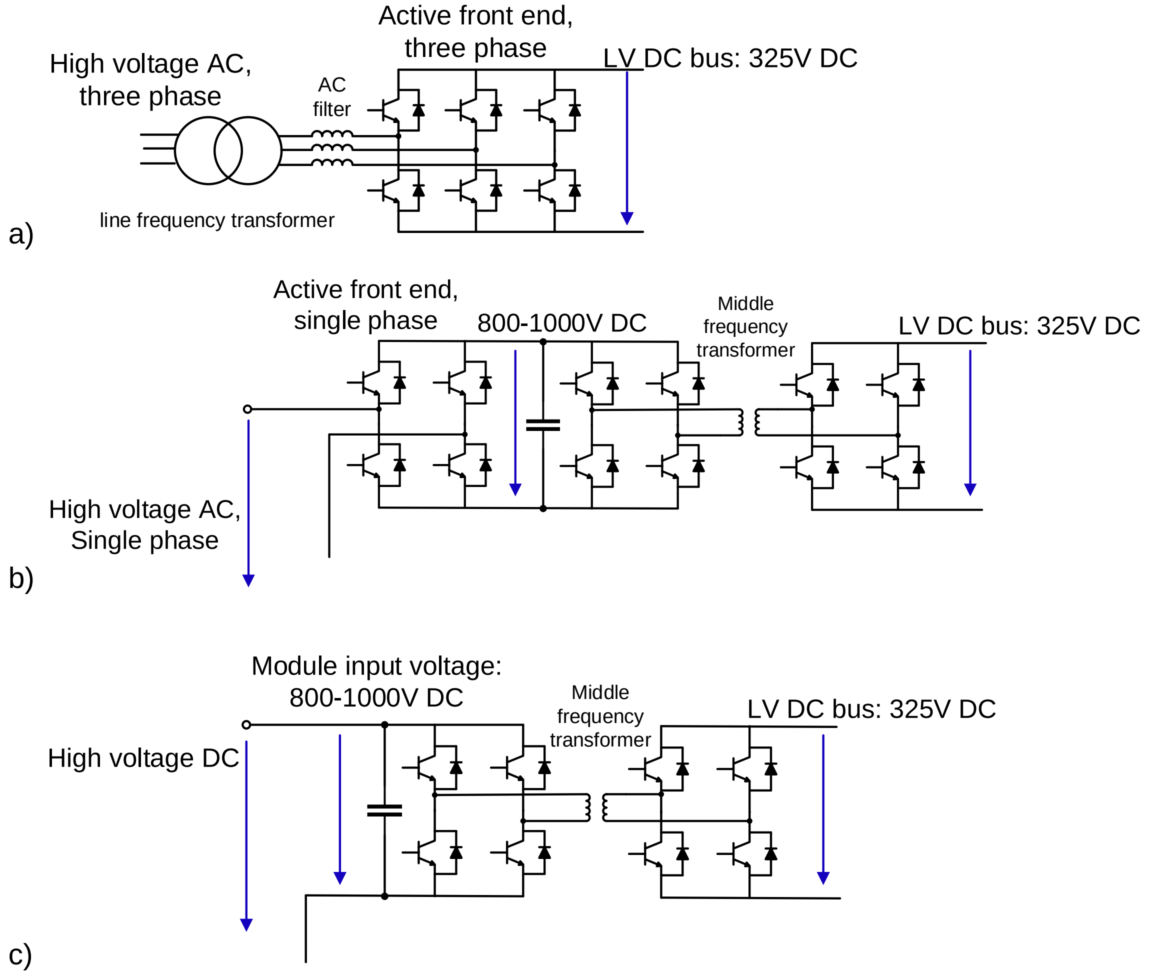

Figure 35: Topologies for stage 2, based on the type of input supply voltage from stage 1. In a) stage 1 supplies on three-phase AC, in b) stage 1 supplies single-phase AC, and in c) stage 1 supplies on DC.

The three topologies above have of course certain sub-variations. However, they are not changing the principle structure and are also not optimised for the given application.

For example, the shown module variants in b) and c) have an isolated back (IBE) end structure. If instead an isolated front end (IFE) is chosen (as shown in Figure 36), the topology is due to the bidirectional high power application not optimised anymore. An additional inductor (high cost part [72]) for the boost stage and more Si chip area is 2-3 times is needed to transfer the same power as in IBE. In summary, IFE is only for low power applications advantageous (low costs as the IFE has the measurement and control on the LV dc bus side)[73].

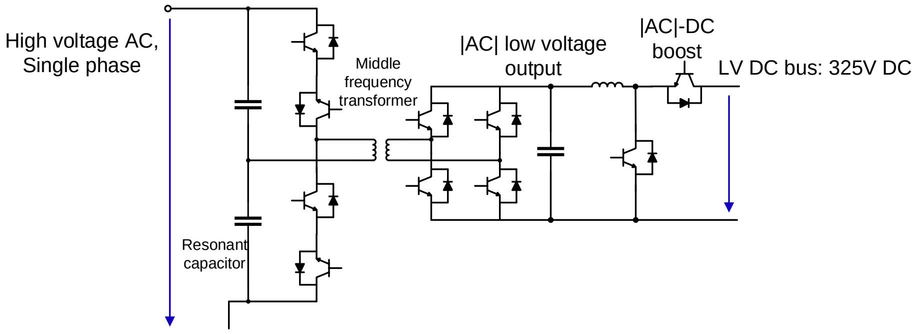

Figure 36: The isolated front end (IFE) topology as stage 2 sub-variation if supplied by a single-phase AC stage 1.

Other sub-variations (e.g. the series resonant DAB) have more potential for downsizing but also their complexity increases. This topology variant is thus left open for further studies. Focusing now on the three identified variants for stage 2 as shown in Figure 35, the table below highlights their influence on the module volume and weight. The values refer to peak power rating (no reduced rating due to energy storage integration is considered in this comparison).

Note: the values in brackets refer to constant power ramping.

Table 18: Comparison of stage 2 within the converter module

Stage 2 design for:	Power rating of the module in kW	Volume in dm³	Weight in kg
MPS variant A	251, (150)	1130, (675)	979, (585)
MPS variant B	251, (150)	502, (300)	502, (300)
MPS variant C	251, (150)	377, (225)	377, (225)

The stage 3 topology remains always the same. However, the power rating depends on the ramping strategy. See the table below which highlights the differences among the MPS variants A to C, in terms of the converter modules' volume and weight.

Table 19: Comparison of the converter module

Converter module design for:	Power rating of the stage 2 module in kW	Power rating of the stage 3 module in kW	Volume in dm³	Weight in kg
MPS variant A	251 (150)	251 (283)	1255, (817)	1104, (727)
MPS variant B	251 (150)	251 (283)	627, (442)	627, (442)
MPS variant C	251 (150)	251 (283)	502, (367)	502, (367)

Variant C has a clear advantage in terms of volume and weight for the converter modules.

6.5 Special design aspects for the DC grid-based stage 1 in variant C

The stage 1 distribution system in variant C is a DC grid. Elementary design options for this DC grid are the DC voltage level, the protection strategy and the grounding arrangement.

6.5.1 DC voltage level

Stage 1 forms the appropriate input voltage for stage 2, the charging stage of the magnet powering system. The voltage level is derived by considering:

1. The fault current level
2. The operational current level
3. Insulation requirements of the transfer medium and the components in stage 2 of the MPS.

Points 1 and 2 define the lower limit of the voltage level, whereas point 3 sets the upper limit.

The goal is to find the lower limit of the voltage level, as it eases the insulating requirements of all equipment used, particularly for the mf transformer in stage 2. The primary to secondary side insulation must withstand the full high DC to ground potential.

Operational current level

The power to be transferred depends on the installed energy storage capacity in the MPS. If no energy storage is installed, the full peak power needs to be transferred. The highest power demand which could occur is 30.2 MW.

For the given distances and the required power to be transferred, only medium voltage cables can be used[20]. As their construction is widely standardized, various voltage levels (e.g. from 6 kV-30 kV) are available and any AC cable can be used to transfer DC power. A comparison between AC and DC operation is shown in the table below, where the reduced losses respectively better equipment utilisation can be highlighted[21].

20 A busbar system with 1kV nominal voltage has to handle 30 kA of operational currents and has a weight of 250 kg/m [74].

21 When an AC cable is used for DC, the DC voltage can be Unom* √2 without exceeding the insulation limit. Further with DC current the following loss producing mechanism are avoided: eddy currents in the sheath, coat and reinforcement, proximity and skin effect in the conductor.

Table 20: DC power transfer with a medium voltage AC cable

Assuming the cable type: PROTOTHEN-X, single core with 500 mm², with a thermal limit corresponding to 74.5 kW/km		
Current domain	AC	DC
Power to be transferred	30.2 MW	30.2 MW
Effective resistance (at Temp.= 90°, laid in air)	0,068 Ω/km	0,0467 Ω/km
Current limit of the cable	1047 A_{RMS}	1263 A_{RMS}
Voltage level	8.7 kV $AC_{phase\text{-}phase\ RMS}$	12.3 kV DC (pole-pole)
Operational current	→ i_{AC} = 30.2 MW/8.7 kV/√3 = 2 kA_{RMS}	→ i_{DC} = 30.2 MW/12.3 kV = 2.46 kA
Number of cables needed in stage 1	6 (two per phase)	4 (two for +, two for -)

If a total power of 30.2 MW needs to be transferred, the line current of 2 kA_{RMS} corresponds then to a secondary line-line voltage of at least 8.7 kV_{RMS}.

The lowest possible DC voltage level for a simple 6-puls diode rectifier is then given by:

$$\mathrm{U}_{DC} = \frac{3 \cdot \sqrt{2}}{\pi}\, U_{sec.\ line-line\ RMS} = 12.3\ \mathrm{kV} \tag{6}$$

Fault currents

Assuming at the rectifier input side a nominal operational line current of 2 kA_{RMS} and a rectifier-transformer short-circuit voltage of uk=10%. A pole-pole short circuit on the DC side leads to a steady-state short circuit current of 20 kA_{RMS}, and the peak[22] can be assumed to be twice as high i.e. 40 kA_{peak}. This is the reference for the withstand capability of the equipment e.g. diodes (main rectifying diodes or freewheeling diodes), cables, or breaking equipment if used on the low voltage side of the rectifier transformer. The breaking capability of standard medium voltage breakers (placed on the high voltage side of the rectifier-transformer) is found well in the calculated range [75].

22 This is the worst case, covering fault locations on the AC side as well on the DC side. If additional circuit elements as the inductance of the upstream grid, transformer resistance, or inductive filters on the DC side are the respected as well, the peak fault current would be less.

For IGBT based voltage source active rectifiers, the DC voltage level needs to be higher to operate with the optimal modulation index e.g. m=0.8. For this type of rectifier, it is important during a short circuit to immediately block the IGBTs and let the freewheeling path conduct the fault current.

The MMC is superior in fault treatment compared with other voltage source converters (VSC) (e.g. two-level VSC) [8]. A full-bridge MMC topology could completely stop the fault current, and the half-bridge MMC based variant at least strongly reduces the peak fault current [65]. The maximal discharge current is much lower due to the distribution of the total energy among all the modules, and secondly, the discharge current is limited by at least the arm inductances (and additional inductances on the DC bus).

6.5.2 The protection strategy

To protect a DC-based power system two possibilities arise. A fault can be directly cleared with a DC breaker, or indirectly by acting on the AC side before the rectifier. For clearing a fault directly on the DC side (see [32, 76] for an overview of all methods) mechanical DC breakers can be used if the DC voltage is not higher than 3600 V DC [77]. Mechanical DC breakers are standard in DC railway powering. For higher DC voltages, only complex solid-state or hybrid (mechanical and solid-state combined) breakers can be used [78]. The advantage of using DC breakers is that each DC branch after the main rectifier can be disconnected selectively.

To clear a DC fault indirectly on the AC side, by using standard AC side breakers, is also common practice in existing [79–81], and in future DC railway powering [82, 83]. An AC breaker protected VSC multi-terminal DC grid is proposed in [84, 85] and protection with AC side fuses combined with active rectifier action in [86]. The advantage of this method is the usage of simple and standardised breaking technology.

Coming now to the DC grid of the MPS stage 1. The minimum DC voltage level is with U_{DC}=12.3 kV too high for mechanical DC breakers. As only one DC branch is to be protected, no selectivity is required. Thus a good option is to interrupt a DC fault on the AC side before the rectifier, by using standard AC breakers.

To guarantee the correct tripping of the breaker the experience from DC railway protection [87, 88] is used for guidance. A set of parameters from the DC system must be obtained and evaluated:

- Overcurrent: the main parameter obtained by measuring the DC bus current; a pole to pole fault leads to an immediate breaker tripping, in case of a pole-ground fault the DC system can still be operated due to a high resistive grounding of the DC minus pole, (this gives time for failure localisation and system shut down); the discharge current of the input capacitors of stage 2 is relatively low (modules are connected in series on the input side) and doesn't need to be considered specifically

- Under voltage: as an additional parameter obtained by measuring the DC bus voltage; important to identify any failure with a high resistive path

By using digital relays, more sophisticated parameters can be used as:

- Current level combined with current rate of rise ($\Delta i/\Delta t$) give a secure failure indication as operational currents and their slopes are well known,
- Apparent resistance combined with rate of rise ($\Delta i/\Delta t$) gives also a very good failure indication if fault currents are low. Current measurement is combined with voltage measurement.

6.5.3 Grounding

Equipment grounding

All metallic enclosures in stage 1 e.g. the rectifier enclosure is connected solidly to the ground. Thus eventually high touching voltages in the case of a pole to enclosure failure are avoided. Due to the high resistive grounded DC minus pole, no flashing arcs are occurring.

System grounding

For a monopole DC grid[23], a high resistive grounding for the minus pole is chosen. This has the advantages of system continuation for single pole-ground faults and localisation, as time for distance calculations is available [89]. The detection is done by measuring the current in the high resistance. The preferred DC grid protection layout is shown in the figure below.

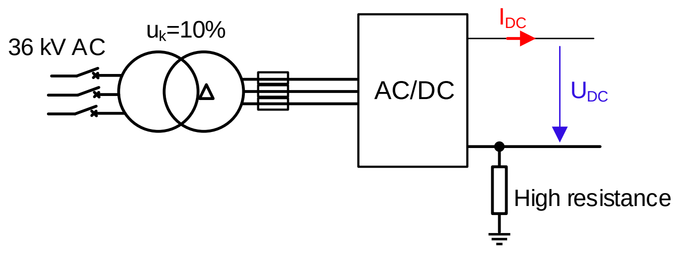

Figure 37: Principal layout of the protection strategy for the DC grid.

23 If a bipolar DC grid topology is chosen, the midpoint should be solidly grounded in order to avoid potential shifts stressing the insulation of the dipole converters. In this case will the first pole to ground fault trip the system already.

6.6 Consideration of energy storage systems

6.6.1 Energy Storage Options

The requirements for the right energy storage system per converter (per magnet circuit) are:

- Energy capacity up to 760 kWh
- Power rating up to 3 MW
- Cycle lifetime up to 20k cycles
- Highest possible lifetime (planned operational time for FCC-hh is 25 years)
- Highest safety requirements (underground installation)
- Highest energy and power density to save space and weight (installation is underground close to the magnet circuit)

Given these requirements, only batteries can be considered in order to design an efficient power system. Further, the upcoming electric vehicle industry guarantees supplier competition.

The electrical integration of the batteries is on the level of the converter module, connected directly to the low voltage DC bus. Thus, only conduction losses in the internal battery resistance are occurring and no converting losses by a battery converter occur.

The considered energy storage type is Li-ion batteries, whereby the LTO technology is the most promising one for the given application.

The main type of energy storage considered here is LTO batteries, as they fulfil energy density and lifetime requirements. For a save operation a certain overcapacity needs to be chosen, this allows the battery to remain within specific limits during the cycling operation [90].

At CERN this type of battery is also considered in the High Luminosity upgrade of the LHC.

6.6.2 Energy storage capacity, W_{es}

The required capacity of energy storage (W_{es}) depends on the power rating of the supplying infrastructure (P_i). If P_i is rated to the peak power, the required capacity is zero. Any power rating smaller than this, lead to the demand of a certain capacity.

The peak power demand for the ramp-up of magnet circuits depends on the ramping strategy. See here also chapter 4.1.1.2, where the two strategies are presented.

With the ramping mode in constant power (cp) the peak power demand is already significantly reduced. Thus, the aspect of energy storage integration is more important for the ramping mode in constant voltage (cv).

The principal relation between the required energy storage capacity $W_{es}(x)$, the power rating P_i and the two ramping strategies – cp and cv – is illustrated below.

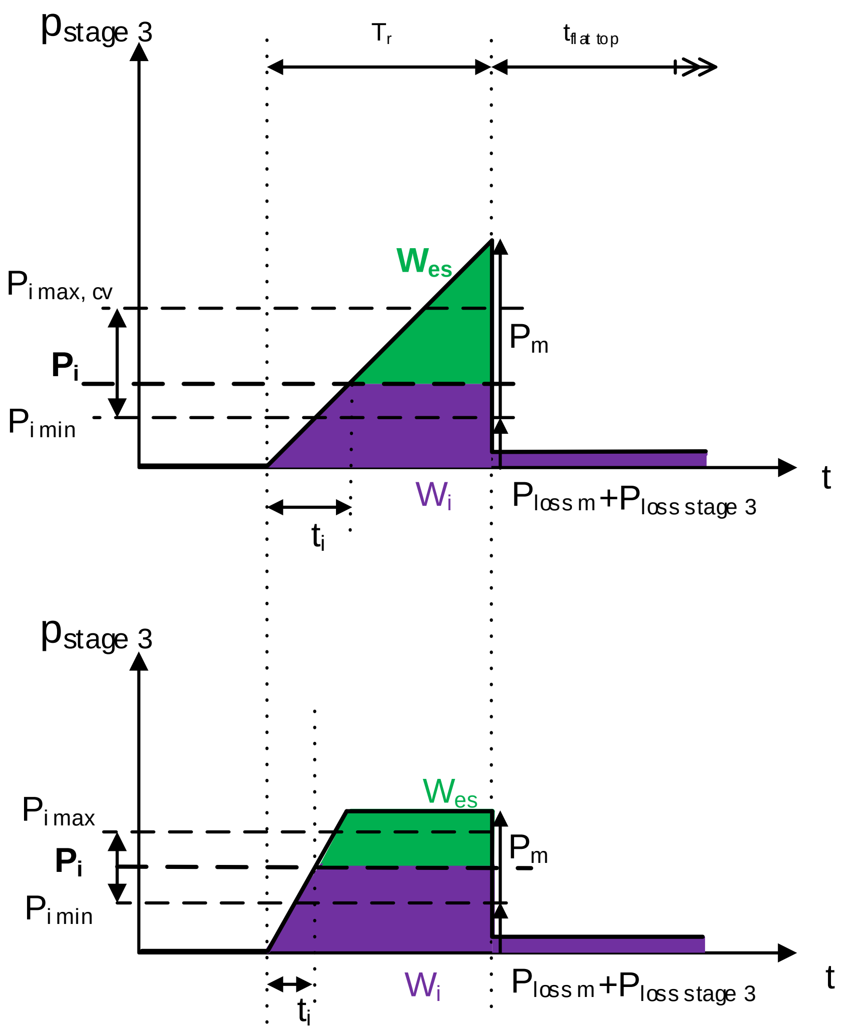

Figure 38: The two ramping strategies and their required energy storage capacity. Upper part: constant voltage ramping. Lower part: constant power ramping. Shown are also the borders for P_i. The minimum is to cover losses of the magnet circuit and stage 3, and the maximum comes from the transmission grid as it cannot deliver the full peak power.

After the completed ramp-up time (T_r), the magnet current (i_m) is on its nominal value $I_{m\ nom}$ and the stored energy in the magnet circuit is W_m. The total power demand of stage 3 ($p_{stage\ 3}$) is covered from the supplying infrastructure until the time t_i where its power rating limit P_i is reached. From this point on, also the energy storage delivers the required power and energy.

Further, the stage 3 losses ($p_{loss\ stage\ 3}$) and magnet circuit losses ($p_{loss\ m}$) have to be covered by the supplying infrastructure during the full ramp-up.

In the figure below, these quantities are shown also on the converter level. The power rating of the supplying infrastructure is such that at the output of stage 2, the power p_i is delivered. The investment costs for the supplying infrastructure of the optimisation refer to this p_i.

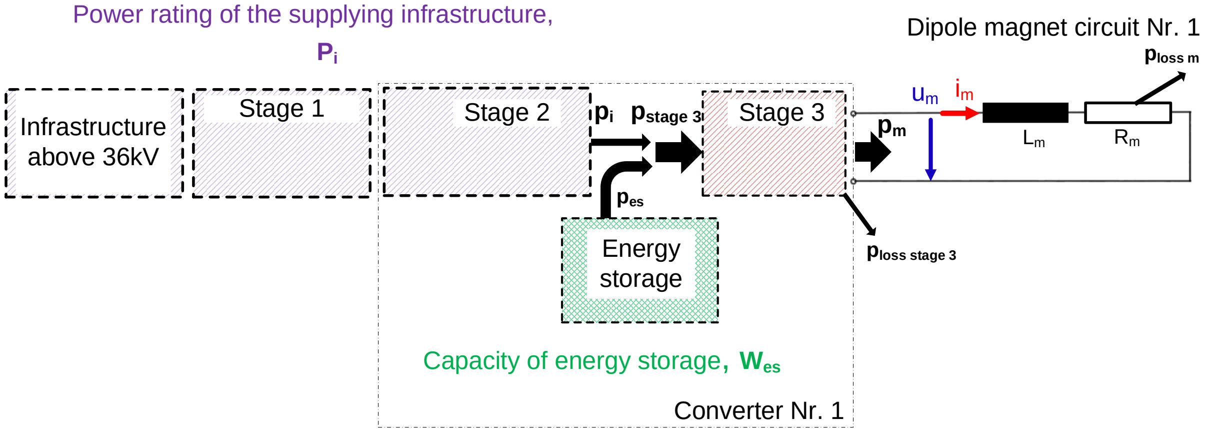

Figure 39: Representation of all relevant quantities for the P_i-W_{es} relation. All stages are on the level of a single converter, supplying one dipole magnet circuit.

The general calculation to derive the relation between P_i and W_{es} (for cv and cp ramping) is as follows. Starting with the energy stored in the magnet circuit (W_m) after the ramp-up i.e.:

$$i_m(T_r) = I_{m\,nom} = 11441\ A \tag{7}$$

$$\begin{gathered} W_m = \frac{1}{2} L_m \cdot I_{m\,nom}^2 \\ W_{loss} = W_{loss\ stage\ 3} + W_{loss\ m} \end{gathered} \tag{8}$$

If no energy storage is used, the total sum of the energy comes from the supplying infrastructure.

$$W_i = W_m + W_{loss} \tag{9}$$

With the integration of energy storage, the total energy is shared between the supplying infrastructure and the energy storage. The energy which comes not from the supplying infrastructure has to come from the energy storage:

$$W_{es} = W_m + W_{loss} - W_i \tag{10}$$

The energy which comes during the ramp-up from the supplying infrastructure depends on the power limit $\mathbf{P_i}$ in the following way:

$$W_i(x) = \int_{t=0}^{t_i(P_i)} p_{stage\,3}(t) \cdot dt + \int_{t_i(P_i)}^{T_r} P_i \cdot dt \tag{11}$$

The above equation describes the energy coming from the supplying infrastructure. It covers all losses occurring during the ramp-up, and partly the energy stored in the magnet circuit.

This energy equation needs to be solved to calculate the required energy storage capacity W_{es}, to a given P_i. The first integral considers the energy transferred during the ramp-up from t=0 until the time $t_i(P_i)$. When $p_{stage\,3}$ exceeds P_i, also the energy storage starts supplying power and energy.

The second integral considers the energy transferred from t_i until T_r.

The power demand $p_{stage\,3}$ delivered by the supplying infrastructure until t_i is given with:

$$p_{stage\,3}(t) = \{(u_{L_m}(t) + i_m(t) \cdot R_m)\} \cdot i_m(t) + p_{loss\,stage\,3}(t) \quad 0 \leq t \leq t_i\,(x) \tag{12}$$

In this formula, the losses of stage 3 and the magnet circuit are accounted for.

The power demand $p_{stage\,3}$ depends on the ramping strategy, and for both, the exact solution is complex (see here also the Appendix).

To show the principal relation between P_i and Wes, a simplified solution is used. By neglecting all losses (and assuming thus a completely linear rise of i_m), the following is obtained:

$$p_{stage\,3}(t) = u_{L_m}(t) \cdot i_m(t) \quad 0 \leq t \leq t_i\,(x) \tag{13}$$

The current rises now linearly, and the only difference between the two ramping strategies is the rate of rise ($\Delta i_m/\Delta t$), as for cp the maximal possible u_{Lm} is applied from t=0 until t=t_i.

$$i_m(t) = \frac{u_{L_m}}{L_m} \cdot t \tag{14}$$

With a given power limit P_i, the time t_i is calculated with:

$$t_i = \frac{P_i \cdot L_m}{{u_{L_m}}^2} \tag{15}$$

Using now also a simplified power demand $p_{stage\,3}$the following is obtained:

$$p_{stage\,3}(t) = \{u_{L_m}\} \cdot \frac{u_{L_m}}{L_m} \cdot t \tag{16}$$

The energy transferred by the supplying infrastructure with the power rating $\mathbf{P_i}$ during a full ramp-up is shown below.

$$W_i(x) = \int_{t=0}^{t_i} \{u_{L_m}\} \cdot \frac{u_{L_m}}{L_m} \cdot t \cdot dt + \int_{t_i}^{T_r} P_i \cdot dt = \frac{{u_{L_m}}^2}{L_m} \cdot \frac{(\frac{P_i \cdot L_m}{{u_{L_m}}^2})^2}{2} + P_i \cdot \{T_r - \frac{P_i \cdot L_m}{{u_{L_m}}^2}\} \tag{17}$$

Finally, the required energy storage capacity is given with:

$$W_{es}(P_i) = W_m - \frac{{u_{L_m}}^2}{L_m} \cdot \frac{(\frac{P_i \cdot L_m}{{u_{L_m}}^2})^2}{2} + P_i \cdot \{T_r - \frac{P_i \cdot L_m}{{u_{L_m}}^2}\} \tag{18}$$

Below shown is the graphical representation of the exact solution for cv and cp ramping.

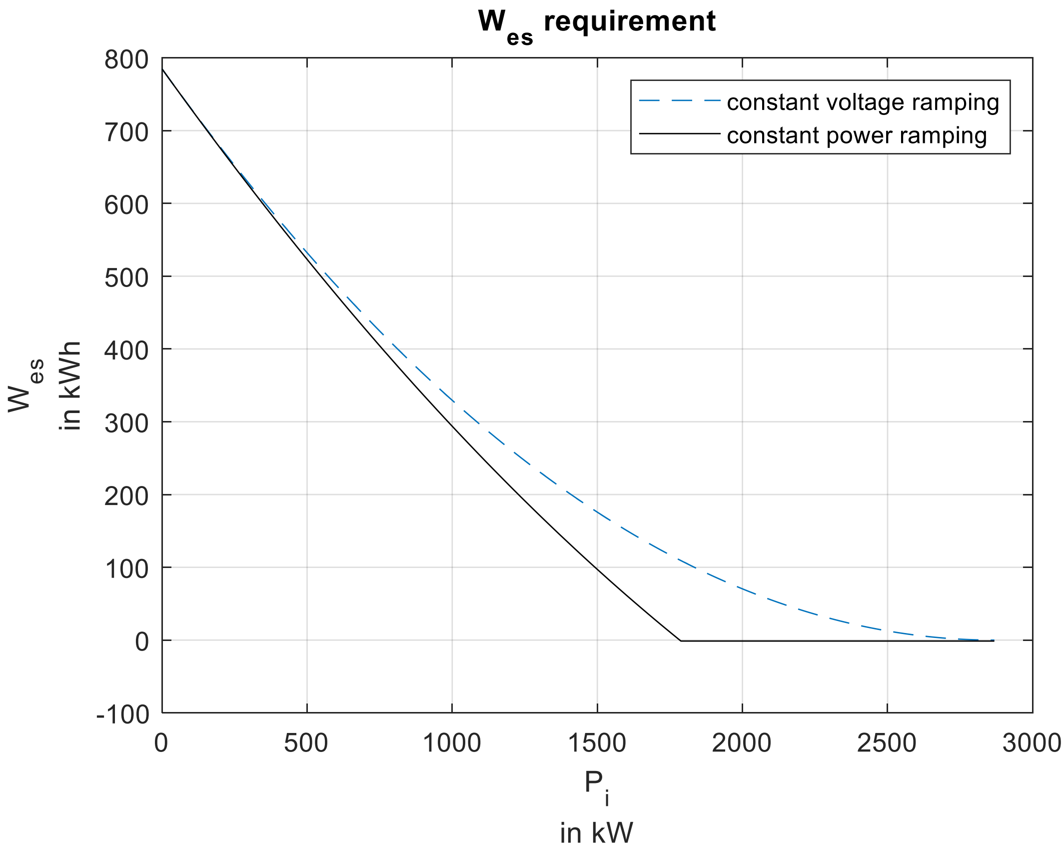

Figure 40: Relation between energy storage capacity W_{es}, power rating P_i and ramping strategy. The values are related to the level of a single converter, supplying one dipole magnet circuit.

The ramping strategy influences all shown parameters. Constant power ramping has a higher ramping voltage until Pi is reached, thus more energy is transferred and respectively less capacity of energy storage is required. For the same reason also the maximal P_i is lower for cp ramping. See below the relations between cv and cp ramping.

$$\begin{gathered} P_{i\,max,\ \ cp}(x) < P_{i\,max,\ \ cv}(x) \\ u_{Lm\,max,\ \ cp}(x) > u_{Lm\,max,\ \ cv}(x) \\ t_{i,\ \ cp}(x) < t_{i,\ \ cv}(x) \\ W_{i,\ \ cp}(x) > W_{i,\ \ cv}(x) \\ W_{es,\ \ cp}(x) < W_{es,\ \ cv}(x) \end{gathered} \tag{19}$$

For any given power rating P_i, the corresponding required energy storage capacity will be always lower for cp ramping. In addition, also the power density requirement of the energy storage system is lower.

If the energy storage capacity W_{es} is known, an additional scaling factor (sf) considers a capacity increase due to the specific type of energy storage and operational performance.

The optimal cycling operation for LTO batteries is between 20% and 80% of their state of charge (SOC). This means that only 60% of the installed capacity can be used for exchanging energy with the main bending dipole magnet circuits. Thus the capacity needs to be scaled up by a factor of 1/0.6, whereby here also an efficiency factor of the battery is already respected. The final required capacity of battery energy storage is:

$$W_{es\_batt} = W_{es} \cdot sf = \frac{W_{es}}{0.6} \tag{20}$$

6.7 Analysis of investment costs

The basic idea is to compare investment costs for the main electrical equipment needed for each of the MPS variants A to C. The two cost types are the costs for electrical power converters (including transformers) on one side and the costs for energy storage on the other side. The costs for the power converters are derived from similar converters at CERN or from price inquirers of supplier, thus the assumed costs may not represent the real costs if these converters were really produced in industry. The costs for energy storage are derived from realised energy storage projects found in literature, and are further parameterised to allow a sensibility analysis.

6.7.1 Investment costs for electrical power converters

The following parts are respected:

- Infrastructure above 36 kV: the main 135/36 kV distribution transformer
- All components used in the MPS, electrical power converters and transformers, electronics and converter module integration

The total costs are assigned on the level of a converter. This means the converter act as a cost bearer for all electrical equipment needed to power one main bending magnet circuit.

Each component has a cost model, representing a constant part, and a variable part depending linearly on the power rating $\mathbf{P_i}$. For two power rating points, the respective costs are obtained and then linearly interpolated, as shown below in Figure 41. For correct interpolating, the data points taken are after 1/3 and after 2/3 of the power range. The source of the costs is either CERN directly, websites or price inquires at manufactures. For detailed cost data see the Appendix.

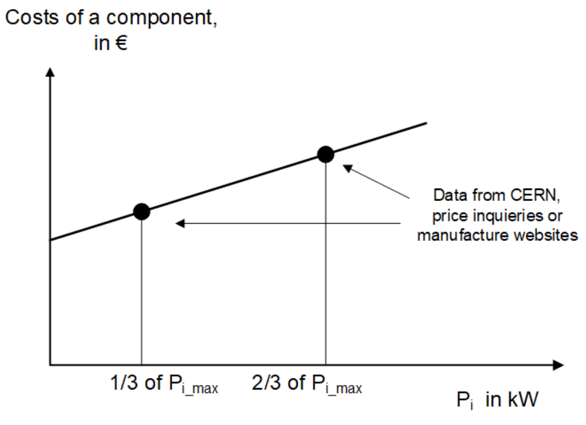

Figure 41: Model for the component costs.

Depending on the MPS variant A, B, C or C*[24], different costs arise as their topologies consist of different components, see the table below.

Table 21: Components used in the MPS variants.

<table>
<tr><th>Variant</th><th>Stage 1</th><th>Stage 2 converter[25]</th><th>Stage 3 converter[25]</th></tr>
<tr><td>A
50Hz transformer-based</td><td></td><td>Converter transformer; AC-DC three-phase</td><td rowspan="4">DC-DC single phase</td></tr>
<tr><td>B
AC grid with SST</td><td>Distribution transformer</td><td>DC-DC single-phase; DC-DC single-phase two conversion stages with mf transformer</td></tr>
<tr><td>C
AFE fed DC grid with SST</td><td>Distribution transformer, central rectifier (AFE)[26]</td><td>DC-DC single-phase, two conversion stages with mf transformer</td></tr>
<tr><td>C*
Diode fed DC grid with SST</td><td>Distribution transformer, central rectifier (diode)[26]</td><td>DC-DC single-phase, two conversion stages with isolation transformer</td></tr>
</table>

The converter costs are finally derived by summing up all components used in the respective MPS variant, and the results are shown in dependence on the power rating **P_i** of the converter. For the converter costs, also the module integration and costs for electronics are respected. For stage 3, always the same power rating is applied, which means this stage adds to the total costs with a constant part.

24 For variant C, a distinction is made in terms of the central rectifier, leading to a variant with AFE rectifier and a variant with diode rectifier. See the table below for their component structure.

25 All component costs on module level are based on CERN data. The converter module integration and electronics costs are based also on CERN data.

26 Cost data is based on price inquiries at ABB and Secheron.

The results are shown below on the level of a single converter (acting as a cost bearer), and the costs for the total installation are obtained by multiplying the respective result with the factor 10, to represent all magnet circuits located at one FCC powering point.

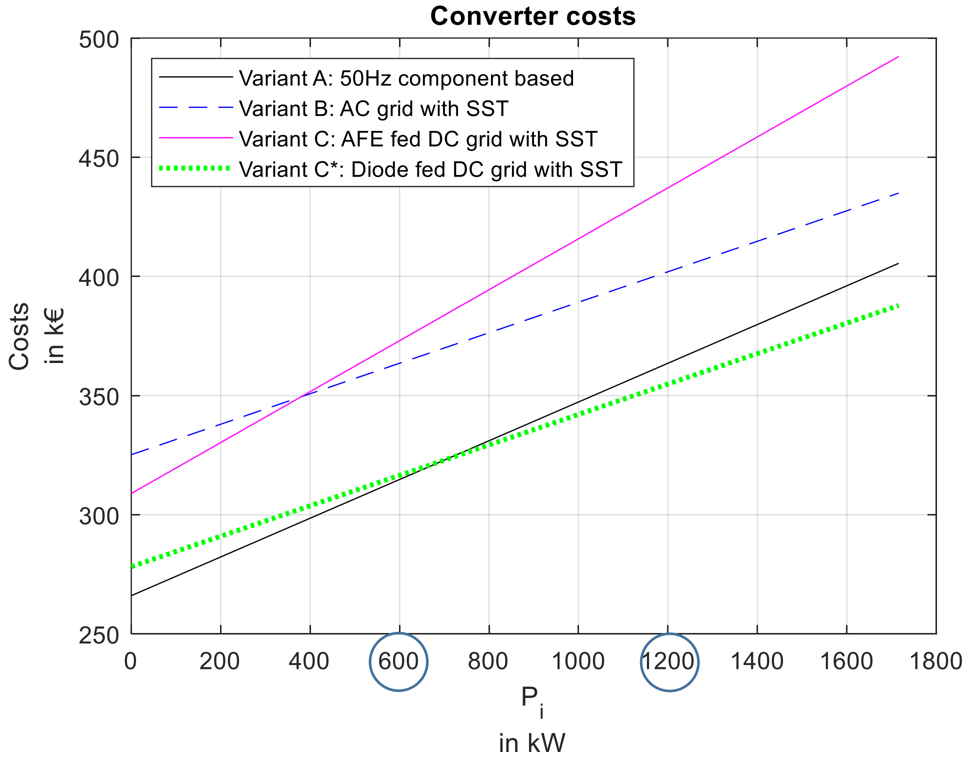

Figure 42: Investment costs comparison between the MPS variants, shown on the level of a converter. Considered are components costs, costs for electronics and cabinet integration costs. No energy storage is considered here. The circles indicate the power rating for which the cost data is taken from (up scaled from converter module level).

Above a certain Pi, variant C* becomes the cheapest of all (diode-based central rectifier is used in stage 1). Variant C is with an AFE central rectifier, and with raising Pi it becomes the most expansive variant. If a simple diode-based central rectifier can be used for variant C is depending on the energy balance of the MPS. If during the ramp down the energy stored in the magnet circuits can be recovered in the energy storage or consumed by any other load connected to DC grid found in stage 1. Due to the integration of energy storage the power rating of the AC grid above 36 kV, stage 1 and stage 2 can be reduced. The rating of stage 3 remains always the same.

As the integration of energy storage means additional costs (e.g. investment costs), an optimisation problem is triggered: infrastructure against energy storage capacity (see chapter 6.9).

6.7.2 Investment costs for specific battery storage capacity, c_{es}

The costs per capacity unit (in €/kWh) is rather hard to estimate. As a source of costs, realised small scale [91] and large-scale projects [92], and a bottom-up method are used.

Derived from small-scale projects: The data analysis of 28 different energy storage projects [91], in the range from 10-100 kWh, showed an average total cost of 1490 $/kWh. With a currency conversion of 0.9 €/$, this gives 1341 €/kWh. These costs are top down derived and contain everything: engineering, converter, mechanical integration.

Derived from large-scale projects: Analysing the costs for 60 MWh energy storage capacity [92] (lies well in the range of the FCC), costs of 601 $/kWh (=541 €/kWh) are obtained. Considering the MPS topology for FCC, cost reductions are possible.

Derived from the bottom up (specific for FCC): By taking only the battery costs (209 $/kWh = 188 €/kWh) found in [92], the rack-integration cost (based on SIRIUS[27] integration costs for a single rack:7000 € per 45 kWh = 155 €/kWh), and the additional fire safety investment from CERN safety group (90-450 k€ for one cavern with 7.5 MWh =12-60 €/kWh), the specific battery energy storage costs are about: 403 €/kWh.

Also important are the projections of price development into the future, as energy storage is under heavy research to improve its production methods, energy density and power density. The driving factors here are renewables and electric vehicles. The referred studies in [93] and [94], use a recently updated literature collection of cost projections for utility-scale storage systems. The median of the cost reduction (from now 2021) until 2030 is -60%.

For underground installations of energy storage, additional safety installations come into account [95]. It must be considered that the safety of energy storage systems is a topic under research, and could drive future costs to meet safety requirements [96]. The IEC standard highlights the enormous test conditions which a battery storage system (secondary batteries used in industry) have to undergo, even when they are placed on the surface [97].

To respect all the points above, the costs per unit capacity is parameterized. A realistic total cost-span ranges between [100 – 1350 €/kWh][28].

27 SIRIUS is a CERN designed converter with a modular topology.

28 Maintenance costs for energy storage are not considered specifically, as the realistic goal is to have an almost maintenance free converter design. Underground excavation costs for energy storage are not considered, as the additional space demand is low.

6.8 Analysis of losses

6.8.1 Calculation model for losses in the MPS

A dedicated loss model is used to analyse the losses occurring in each MPS variant. The results are shown on the level of a single converter, powering one main bending dipole circuit for a complete magnet operation cycle. The losses of stage 1 and the infrastructure above 36 kV (needed for ten magnet circuits) are divided by ten and added to the converter losses. See for the loss model Figure 43. The losses of stages 2 and 3 are calculated on module level and are thus multiplied by 12, to have them on converter level. To stress the loss comparison among the variants, constant voltage (cv) ramping is used as it has the highest peak power demand.

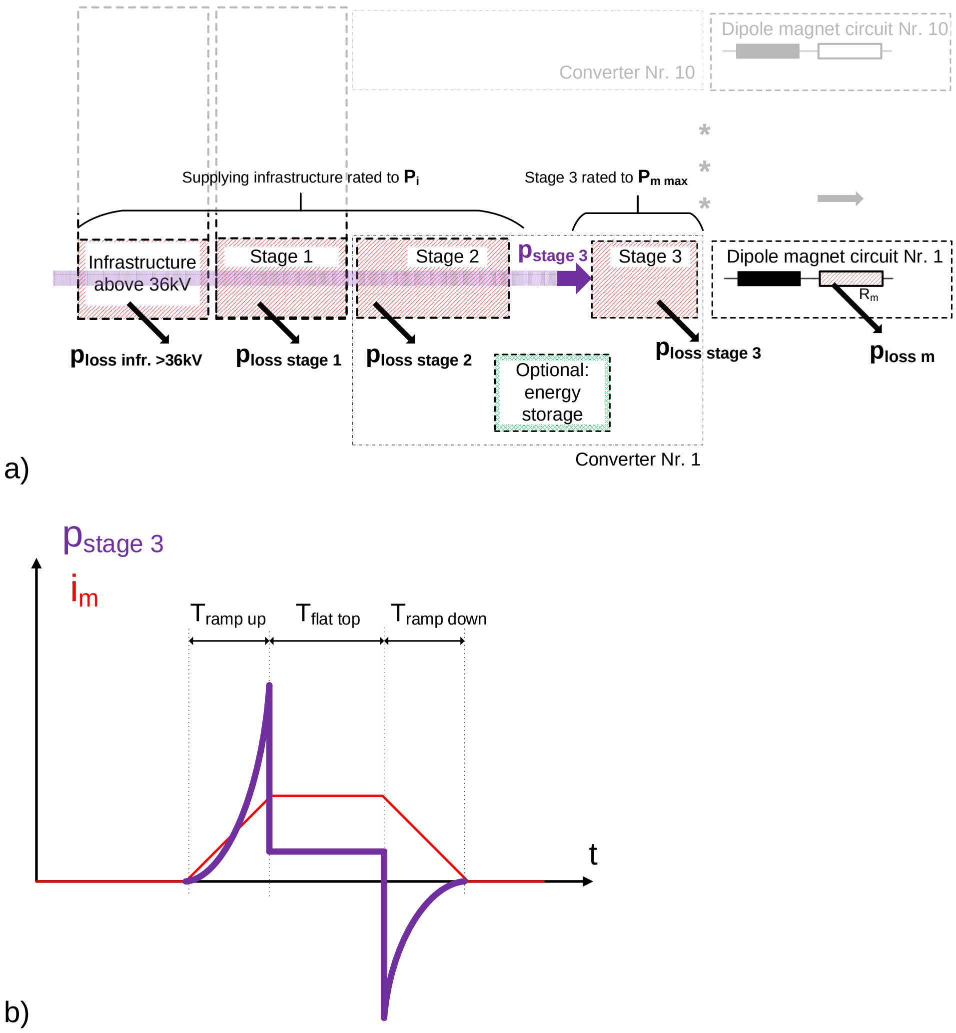

Figure 43: Model for the loss analysis. Shown in a) are the respected power losses occurring if the power demand of MPS stage 3 ($p_{stage\ 3}$) must be transferred. Shown in b) is the power demand p_{stage3} during a full magnet cycle. The ramping is in cv mode.

With the designed loss model, the variants themselves can be compared and the effect of the energy storage on the losses can be shown.

The loss model itself analyses the losses of each stage for each MPS variant. It considers load-dependent losses e.g. conduction or switching losses, and load-independent losses as e.g. auxiliaries or iron losses.

For each stage in the MPS, the power losses at zero load = P_0 and at full load = P_{load} are obtained by data sheets of the manufacturer or from results of loss studies in the literature. The power loss in between these two points is obtained by interpolation:

$$p_{loss}(t) = P_0 + \left(\frac{p_{stage\ 3}(t)}{P_{load}}\right)^2 \cdot (P_{load}) \tag{21}$$

For any MPS variant, the lost energy is then calculated by the time integral. This is performed for all MPS stages (shown with index i) of the variant and then summarized.

$$\begin{gathered} W_{loss} = \sum_i \int_0^T p_{loss\,,i} \cdot dt \\ with\ T = T_{ramp\ up} + T_{flat\ top} + T_{ramp\ down} \end{gathered} \tag{22}$$

If for example MPS variant A is considered, the following components with their power losses $p_{loss,\,i}$ as indicated in the formula above are occurring:

- AC grid above 36 kV, represented by its SCC and X/R (losses are divided by 10 to bring them on converter level)
- Distribution transformer 36/18 kV (losses are divided by 10 to bring them to converter level)
- Converter transformer 18/0.15 kV (losses are multiplied by 12 to bring them to converter level)
- Three-phase AC-DC stage (losses are multiplied by 12 to bring them on converter level)
- Single-phase DC-DC H-bridge (losses are multiplied by 12 to bring them on converter level)

For the loss model values and further description see the appendix.

6.8.2 Results of MPS losses comparison (without energy storage)

For the calculation of the losses a power profile as indicated in Figure 43 b) is used, whereby the magnet current i_m is fully ramped up from 0 to 11441 A, is remaining constant during the flat top and is ramped down again. The following time parameters are used:

Table 22: Ramping parameters for loss comparison between the variants.

Item	Unit	Value
$T_{ramp\ up}$	s	1200
$T_{ramp\ down}$	s	1200
$T_{flat\ top}$	s	12600
$p_{stage\ 3\ max}$	MW	3.02

The lost energy during a full magnet cycle, calculated on the level of a converter (but including all stages of the MPS), powering a single main bending dipole magnet circuit is presented in the table below. To obtain the losses for the total MPS at one FCC powering point, the results must be multiplied by ten.

Table 23: Lost energy during one magnet cycle, considering a single main bending dipole magnet circuit

		Variant A	Variant B	Variant C
Lost energy during ramping (up + down)	in MWh	0.15	0.17	0.18
Lost energy during flat top		0.39	0.50	0.53
Total		0.54	0.67	0.70

Remarkable are the much higher losses during the flat-top phase with a long time but low power demand, compared with the short-timed and high-power demanding ramping phase.

For 15600 cycles[29] and assumed energy costs of 40 €/MWh, the following costs for the lost energy are derived.

Table 24: Cost for the lost energy during 15600 magnet cycles, considering a single main bending dipole magnet circuit

		Variant A	Variant B	Variant C
Costs for losses on the level of a single converter (including all stages)	in M€	0.34	0.42	0.44
Costs for losses in a single main bending dipole magnet circuit		0.32		

29 The assumed FCC operation here is 3 cycles per day, for 260 days for 20 years in total.

The costs for the losses produced by the MPS is comparable with the costs for losses occurring in the superconducting magnet circuit. Further, the costs for losses among the variants vary not too much in the first place i.e. -23% between variant C and A.

From the given peak power limitation dictated by the 400 kV transmission grid, the installation of energy storage is an essential requirement. In terms of losses, this is also interesting as they are reduced.

6.8.3 Results of MPS losses comparison with integrated energy storage

The integration of energy storage as indicated in Figure 43 b) allows a reduction of the power rating for the supplying infrastructure (AC grid above 36 kV and the MPS stages 1 and 2). The losses are reduced by two factors:

- A lower power flow (until the integration point of the energy storage) means lower load-dependent losses; this is important during the ramp-up and the ramp-down
- The reduced power rating of the equipment reduces also the no-load losses; this comes into account during the flat-top phase.

To show the loss reduction effect a sensitivity analysis is performed. The rating of the supplying infrastructure varies from its minimum (means full energy storage capacity is installed) to its maximum (means zero energy storage capacity is installed). To show the loss reduction effect the best way, constant voltage ramping is chosen as the highest peak powers are occurring.

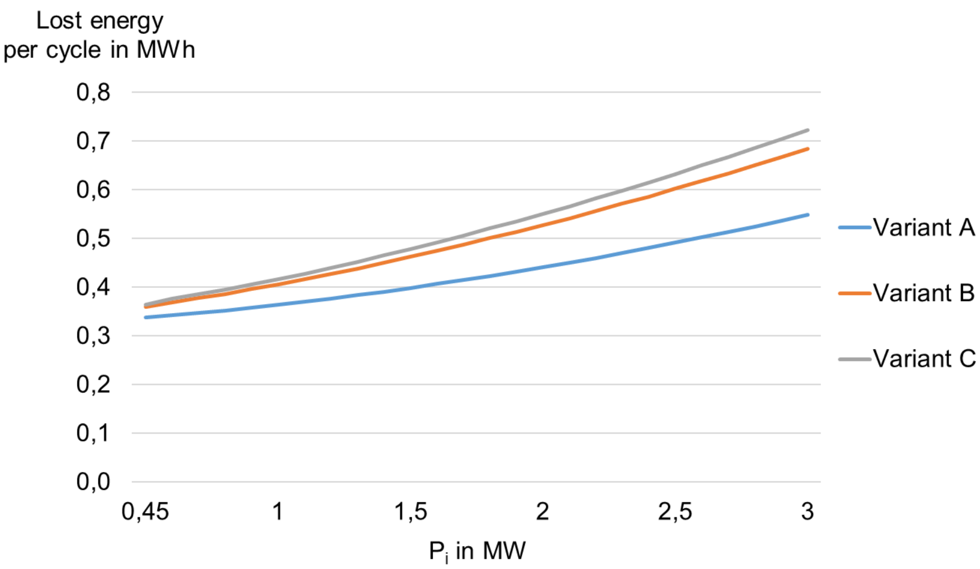

Figure 44: Shown are the MPS losses depending on the power rating P_i of the supplying infrastructure. Results are on the level of one converter.

In variants B and C, the losses have a higher sensitivity than in variant A. If their power rating is reduced by -85% (from 3 MW to 0.45 MW), the lost energy is reduced by about -50% for variants B and C, and by about -33% for variant A.

With the constructed loss model, the savings due to the reduced losses can be calculated. Against this savings, the costs for energy storage on the other hand must be considered.

Assuming again a total number of 15600 magnet cycles and electrical energy costs of 40 €/MWh, the maximal savings due to reduced losses are shown in the table below.

Table 25: Balance of savings due to reduced losses against investment costs of energy storage, for 20 years of operation

	Variant A	Variant B	Variant C
Energy savings[30]	0.10 M€	0.17 M€	0.19 M€
Investment costs for the required 0.55 MWh battery energy storage system[31]	0.55 M€		

The investment costs in the above example are more than double the potential savings due to reduced losses.

The installation of energy storage must be seen in a broader context. Firstly, the main requirement is to cover power peaks, and to overcome transmission grid limitations. Only this makes the operation of FCC possible.

Secondly, when thinking about investment costs, the costs for energy storage must be compared with the costs for the supplying infrastructure. Thus an optimisation problem is triggered, see therefor chapter 6.9.

[30] Savings when comparing losses at P_i = 4.56 MW with losses at P_i= 30.2 MW.

[31] Assumed is here the peak shaving concept applied in the case constant voltage ramping i.e. for P_i = 4.56 MW corresponds to a required battery capacity of 5.5 MWh and for the costs 1000 €/kWh are assumed (see here also chapter 6.7.2).

6.8.4 Estimation of losses during the ramp down

The goal is to estimate the amount of recoverable energy which can finally be captured by the energy storage, as it helps to optimise its capacity. An energy balance calculation is performed. The calculation is done on converter level, considering the theoretical recoverable energy in one magnet circuit of 456 kWh.

The losses in the magnet circuit during the ramp-down are calculated by the formula below. For the magnet current i_m a pure ramp-shape from 11.4 kA to 0 A is assumed.

$$\begin{gathered} W_{loss\ m} = \int_0^{T_{ramp\ down}} i_m^2 \cdot R_m \cdot dt = \\ = \int_0^{1200\ s} \left(11400 - t \cdot \frac{11.4}{1.2}\right)^2 \cdot 0.001 \cdot dt = 14.4\ kWh \end{gathered} \tag{23}$$

The losses in stage 3 of the MPS (the DC-DC magnet supply) are calculated according to the loss model, as shown in chapter 6.8.1 and the Appendix.

$$\begin{gathered} p_{loss\ stage\ 3}(t) = P_0 + \left(\frac{p_{stage\ 3}(t)}{P_{load}}\right)^2 \cdot (P_{load}) \\ W_{loss\ stage\ 3} = \int_0^{T_{ramp\ down}} p_{loss\ DC-DC}\ (t) \cdot dt \end{gathered} \tag{24}$$

$$\begin{gathered} p_{loss\ stage\ 3}(t) = 2{,}25\% \cdot 3{,}02\ MW + \left(\frac{p_{stage\ 3}(t)}{3{,}02\ MW}\right)^2 \cdot (3{,}02\ MW) \\ W_{loss\ stage\ 3} = 19\ kWh \end{gathered}$$

The losses in the battery will occur due to the internal battery resistance and are proportional to the square of the RMS battery current (I_b). The battery is integrated on converter module level, connected directly to the low voltage DC bus between stage 2 and stage 3. The losses are calculated in two steps.

Firstly, the RMS current ($I_{LV\ DC}$) flowing on the low voltage DC bus during the ramp down is calculated by using the RMS value of the magnet current (I_m), divided by 12 (number of converter modules) and multiplied by the voltage ratio of stages 2 and 3.

$$I_{LV\ DC} = \frac{I_m}{12} \cdot \frac{u_m}{u_{LV\ DC}} \tag{25}$$

Secondly, due to the peak shaving strategy, only a part comes from the battery, whereas the other part comes from stage 2 of the MPS. With M representing this sharing, the RMS value of the current flowing into the battery is:

$$I_b = I_{LV\,DC} \cdot M \tag{26}$$

Based on the two formulas above, the losses are finally calculated with:

$$I_{LV\,DC} = \frac{I_m}{12} \cdot \frac{u_m}{u_{LV\,DC}} = \frac{\frac{11.4\,kA}{\sqrt{3}}}{12} \cdot \frac{260\,V}{325\,V} = 438.78\,A \tag{27}$$

The maximal current coming from the battery is when the supplying infrastructure is rated to its minimum, which is 38 kW on module level. This makes 15% of the peak power rating (251 kW). Thus, M corresponds to 0.85 and the RMS battery current during the ramp-down is given by:

$$I_b = I_{LV\,DC} \cdot 0.85 = 372.97\,A \tag{28}$$

For the battery internal resistance $R_{in\,b}$ 0.033 Ω are obtained from the simulation model (see chapter 7.3). To get the value for the whole converter, the result is multiplied with 12.

$$\begin{aligned} W_{loss\,b} &= I_b^2 \cdot R_b \cdot T_{ramp\,down} \cdot 12 = \\ &= 373\,A^2 \cdot 0.033\,\Omega \cdot 1200\,s \cdot 12 = 18.36\,kWh \end{aligned} \tag{29}$$

In total, the lost energy during the ramp down process is 52 kWh on the level of the converter module. From the theoretical 456 kWh recoverable energy per converter module, only 404 kWh remain after accounting the losses.

6.8.5 Conclusions of the loss analysis

The MPS variant A has the least losses which are -23% less than variant C.

The main part of the losses during a magnet cycle occurs during the flat-top phase. They are at least 2-times higher than the losses during the ramp up and ramp down.

The loss reduction effect due to the integration of energy storage is higher in variants B and C. If the power rating of the supplying infrastructure is reduced by -85% (from 3.02 MW to 0.46 MW), the losses are reduced by about -½ for variants B and C, and by -⅓ for variant A.

During the ramp down, the energy stored in the magnet circuits is reduced by the losses in the magnet circuits themselves, the DC-DC magnet supply stage (MPS stage 3), and the battery internal resistance. From the theoretical 100% recoverable energy, -11.3% is lost and needs to be deducted to calculate the recoverable energy.

Potential cost savings due to energy storage caused reduced losses are overshadowed by the costs for the energy storage itself. Even for 20 years of operation, the battery investment costs are at least 2-times higher than the savings in energy.

The decision for the optimum capacity of energy storage must be derived within a wider optimisation process, considering the costs for the supplying infrastructure (AC grid above 36 kV, stages 1 and 2 of the MPS) and the energy storage capacity. This is done in chapter 6.9.

6.9 Optimisation of installed power and energy storage

The results of the optimisation are depending on two cost components, the power converter and the energy storage costs. As the energy storage costs are parameterised in the results, the uncertainty factor is coming from the costs for power converters. As they have been merely drawn at a certain moment from comparable converters at CERN, their real costs might be different. However, the method of how power converter rating is optimised against energy storage capacity remains valid in any case.

The integration of energy storage into the converter modules allows the downsizing of the complete supplying infrastructure. The purpose of the MPS is to ramp the magnet circuits. For this, a certain amount of power and energy is needed. This power and energy come partly from the supplying infrastructure, with the power rating P_i, and partly from the energy storage, with the capacity W_{es}. The higher W_{es}, the lower is the required P_i of the supplying infrastructure. This optimisation principle is shown in the figure below. The focus is on a single converter respectively on a single powering point of FCC (see chapter 4.1).

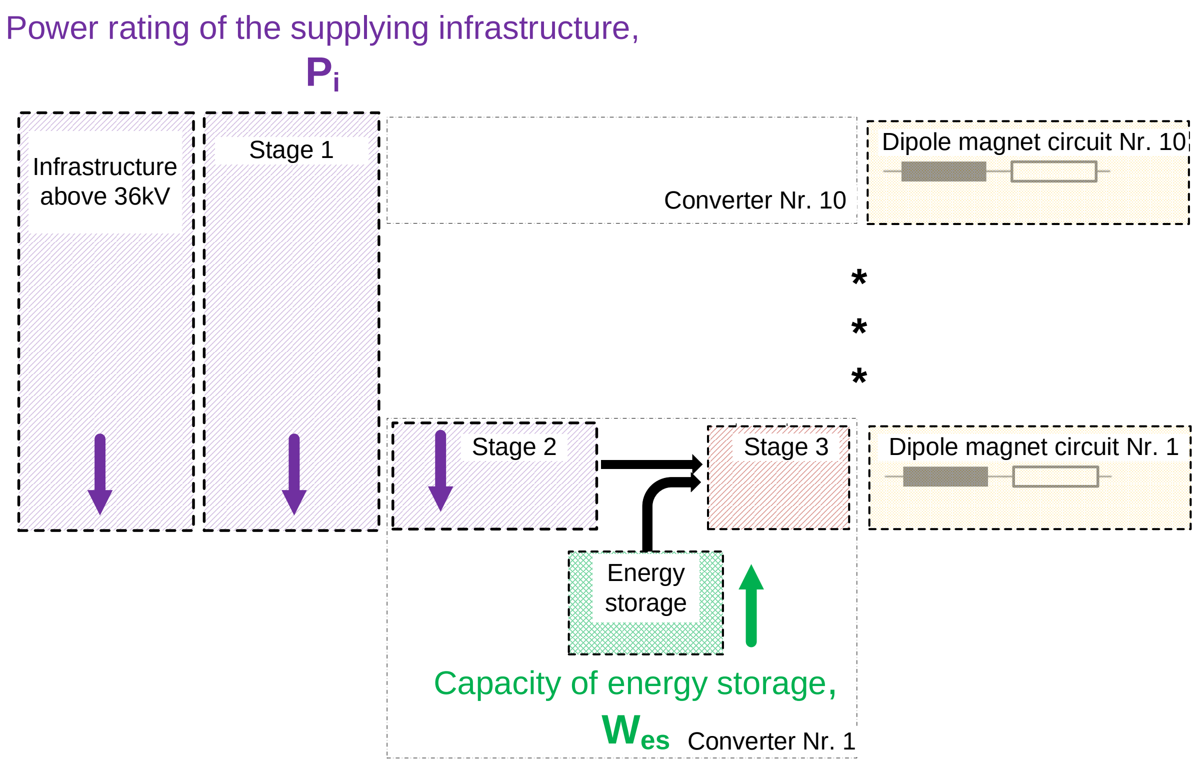

Figure 45: The optimisation principle, power rating P_i of the supplying infrastructure against the capacity of energy storage W_{es}.

The optimisation aims to find the optimum power rating and the optimum capacity of energy storage, for each of the MPS variants (see chapter 6). For better viewing the results are displayed on the level of one converter, giving the optimised P_i and the optimised W_{es}. Once the optimised converter parameters are determined, the costs can be obtained as well. Again for better viewing, the converter (stages 2 and 3) acts as a cost unit, also counting the costs for MPS stage 1 and the infrastructure for a single powering point above 36 kV. Total costs for stage 1 and the infrastructure above 36 kV are distributed equally to the 10 converters. Thus 1/10 of the costs of stage 1 and above is added to the costs of an individual. In return, the costs for the complete MPS installation at a single FCC powering point are obtained by multiplying the results by a factor of ten.

6.9.1 Cost function and optimisation variable

The optimisation variable x is the power rating P_i of the supplying infrastructure. The optimisation is done on the level of a single converter, powering a single dipole magnet circuit. From the power rating $P_{i,}$ the necessary storage capacity W_{es} can be derived directly. The optimum is found by a straight forward parameter variation, since only one optimisation variable has to be considered.

The lower limits of P_i are given by the requirement of covering the losses of stage 3 and the magnet circuit, and the minimum charging time of the battery energy storage for a good operational performance. The highest of these lower limits must be respected.

The upper limit of P_i comes from the peak power limitation of the transmission grid. This limit must not be exceeded during FCC operation. The cost function comprises costs of the complete supplying electrical infrastructure and the energy storage, both depending on the variable $x=P_i$. The algorithm searches for the minimum of a one-dimensional cost function.

$$min\{f_c(x)\} = C_i(x) + C_{es}(x) \tag{30}$$

For the supplying infrastructure and the energy storage cost models are used. These cost models are presented in the following two chapters.

6.9.2 Energy storage costs, C_{es}

The energy storage costs C_{es} depend on the capacity W_{es} (in kWh) and the specific per unit costs c_{es} (€/kWh).

$$C_{es}(x) = W_{es}(x) \cdot c_{es} \tag{31}$$

Costs as a parameter vary in the region as given in chapter 6.6.2. A fictional low value of 100 €/kWh was set to demonstrate at which price an energy storage system rated for the full capacity is the optimum solution. The total cost-span in the optimisation ranges between [100 – 1350 €/kWh].

6.9.3 Infrastructure costs, Ci

The infrastructure costs C_i include the costs for all MPS stages and equipment above the 36 kV level. The costs for the equipment above 36kV are modelled only with variable costs, depending linearly on P_i. The costs of stage 1 and stage 2 are modelled with a constant part, and a variable part depending linearly on the power rating P_i. All components of stages 1 and 2 have their specific cost model as shown in the figure below. The costs for stage 3 are constant and do not depend on the optimisation variable $x=P_i$.

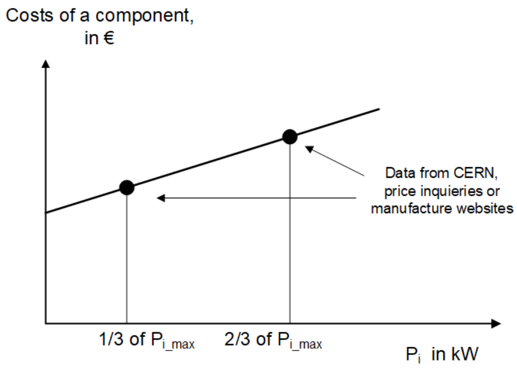

Figure 46: Model for costs of components used in the MPS topologies.

Each component has its specific cost data points. The source of these data points is either CERN, websites or price inquires at manufactures. Depending on the MPS variant (A, B, C or C*), different costs arise as their topologies consist of different components. A summary of the components used in each MPS variant is shown in the table below.

Table 26: Components used in the MPS variants. Stage 3 is not shown as it is not part of the optimisation.

Variant	Stage 1	Stage 2: converter module level[32]
A 50Hz component-based	Converter transformer[32]	AC-DC three-phase
B AC grid and solid-state transformer	Distribution transformer[33]	DC-DC single-phase; DC-DC single-phase two conversion stages with isolation transformer
C Bidirectional DC grid and solid-state transformer	Distribution transformer[33], central rectifier (AFE)[34]	DC-DC single-phase, two conversion stages with isolation transformer
C* Unidirectional DC grid and solid-state transformer	Distribution transformer[33], central rectifier (diode)[34]	DC-DC single-phase, two conversion stages with isolation transformer

For detailed cost data see the Appendix.

32 All components' costs on module level are based on CERN data.

33 Cost data is based on websites of manufacturer [98].

34 Cost data is based on price inquiries at ABB and Secheron

6.9.4 Parameters used in the optimisation

All relevant electrical parameters of the magnet circuit and the converter are shown in the table below.

Table 27: Main electrical parameters for the optimisation

Item	Unit	Value
Magnet circuit		
$I_{m\ nom}$	A	11441
R_m	Ω	0.001
L_m	H	25.08
T_r	s	1200
W_m	kWh	456
Converter		
sf[35]	-	1/0.6
$W_{es\ batt\ max}$	kWh	759.6
$u_{m\ max}$	V	300
$P_{i\ min}$[36]	kW	456
$P_{i\ max,\ cv}$[37]	MW	3.02
$P_{i\ max,\ cp}$[38]	MW	1.80

The optimised power rating P_i of the converter (and respectively the rating of the complete supplying infrastructure) varies between:

- 0-3.02 MW for constant voltage ramping
- 0-1.8 MW for constant power ramping.

The optimised battery energy storage capacity W_{es} varies between 0-759.6 kWh. The parameterized costs for specific energy storage capacity c_{es} ranges between [100 – 1350 €/kWh].

35 The considered type of energy storage is LTO batteries. As their preferred operating range is between 20-80% of their state of charge, W_m corresponds to 60% of the capacity. If all energy in the magnet is to be stored in the energy storage, the corresponding capacity is 1/0.6*W_m. Here also included is an efficiency factor of the battery.

36 See formula (63) the appendix chapter 10.8.3

37 See formula (46) in the appendix chapter 10.8.1

38 See formula (56) in the appendix chapter 10.8.2

6.9.5 The optimisation

The following subchapters show three different aspects of optimisation results.

- Firstly, the main parameters P_i and W_{es} are shown. Additionally, a graphical representation shows the optimisation method.
- Secondly, with the optimised P_i and W_{es}, the optimised converter costs are calculated. The converter acts as a cost unit, covering all MPS stages and the infrastructure above the 36kV level.
- Thirdly, the optimisation is shown with boundary conditions for P_i and W_{es}. For both of the two main parameters are minimum value is indicated.

All results are shown for the two ramping methods, constant voltage and constant power ramping. The results in the following chapters are based on calculations for which the detailed maths can be found in the appendix.

6.9.5.1 Optimised P_i and W_{es}

Below shown is the graphical representation of the optimisation in constant voltage ramping mode. For every value of c_{es}, the optimised P_i is obtained.

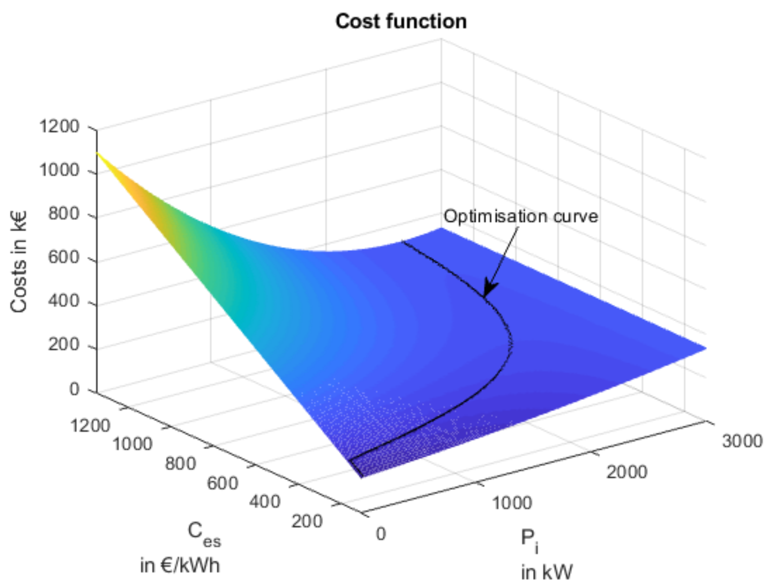

Figure 47: Graphical representation of the optimisation principle. For each value of c_{es} the optimised P_i is determined. Each of these optimised P_i points are connected via the black line. Results are for constant voltage ramping and powering variant A.

The optimised black curve is for the total range of the parametrized c_{es}. The lower the specific costs for energy storage capacity c_{es}, the more W_{es} is installed. Respectively lower is the power rating P_i. If the figure above is projected onto the x-y plane with an additional second y-axis for the corresponding optimised W_{es}, the figure below (again for variant A and constant voltage ramping) is obtained.

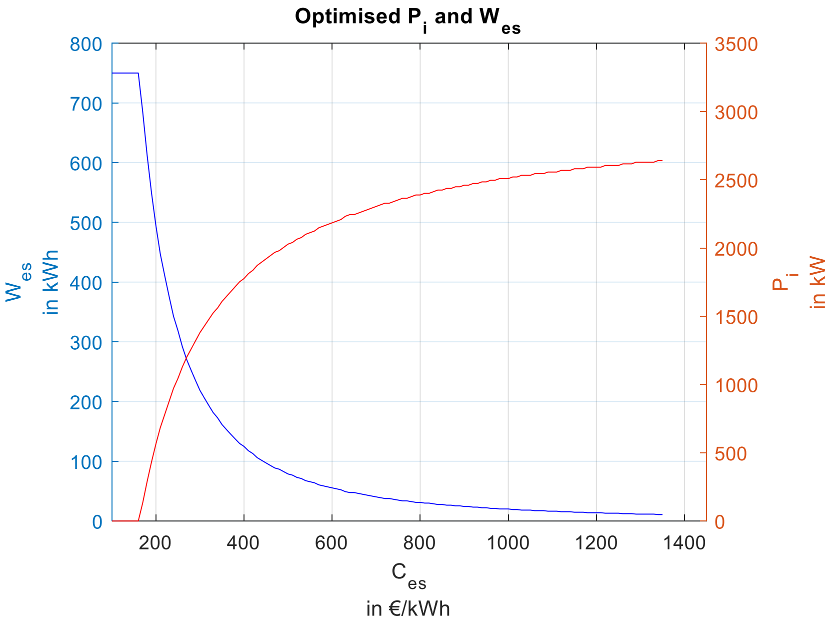

Figure 48: Optimisation result for MPS design variant A and constant voltage ramping, with c_{es} as a parameter. Results are for constant voltage ramping and powering variant A.

Important here is to identify the sensitive region with respect to c_{es}, which is here in the range of 200-600 €/kWh. If in the future, the detailed calculated c_{es} lies within this sensible range, the here presented optimisation method becomes highly interesting. This sensitivity area differs now among the MPS variants and depends heavily on the ramping method. Below is a comparison, where optimised W_{es} for each variant and each ramping method is shown, beginning with constant voltage ramping.

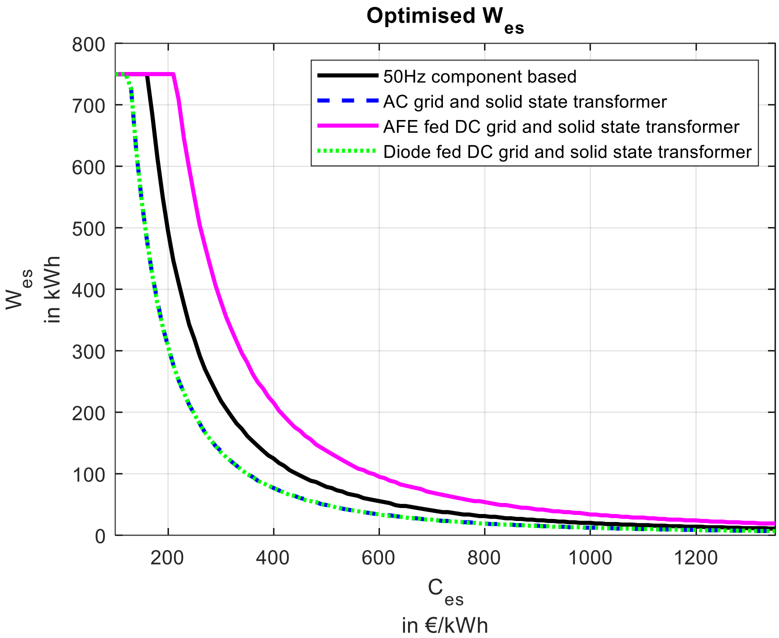

Figure 49: Optimisation results for all MPS variants in constant voltage ramping mode, with c_{es} as a parameter. Results are for constant voltage ramping.

Variant C* (diode fed DC grid with SST topology) has coincidently the same optimised W_{es} values as variant B (AC grid with SST topology). The two variants have the same slope of their infrastructure costs in €/kW (see here also chapter 6.5). Even their absolute costs are different, they have the same optimised values of P_i and correspondingly in W_{es} – their minima are located at the same place.

Below shown is the graphical representation of the optimisation in constant power ramping mode. For every value of c_{es}, the optimised P_i is obtained.

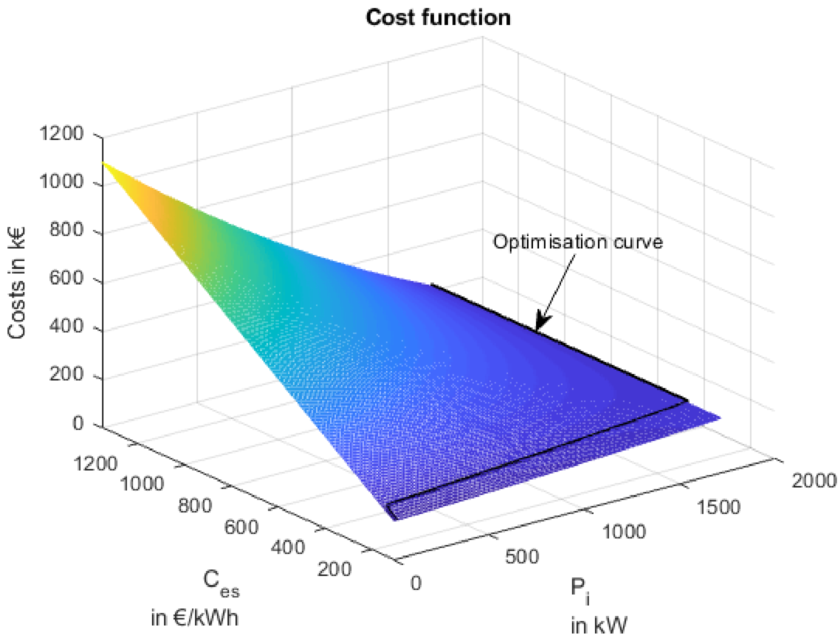

Figure 50: Graphical representation of the optimisation principle. For each value of c_{es} the optimised P_i is determined. Each of these optimised P_i points are connected via the black line. Results are for constant power ramping and powering variant A.

The optimised black curve is for the total range of the parametrized c_{es}. The lower the specific costs for energy storage capacity c_{es}, the more W_{es} is installed. Respectively lower is the power rating P_i. Below a certain c_{es}, the optimised P_i is zero.

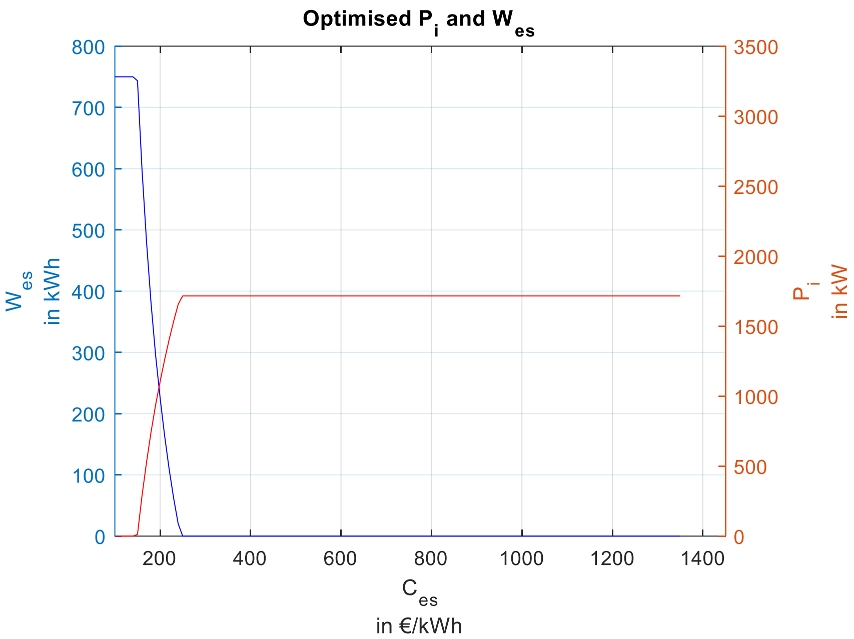

Figure 51: Optimisation result for MPS design variant A and constant power ramping, with c_{es} as a parameter.

Compared to constant voltage ramping, in constant power ramping mode the optimised value for P_i is less sensitive to energy storage costs. Only if the costs for energy storage drops below 300 €/kWh, the optimisation tells us to install energy storage capacity (if variant A is chosen).

The optimised W_{es} for all variants for constant power ramping are shown in the figure below.

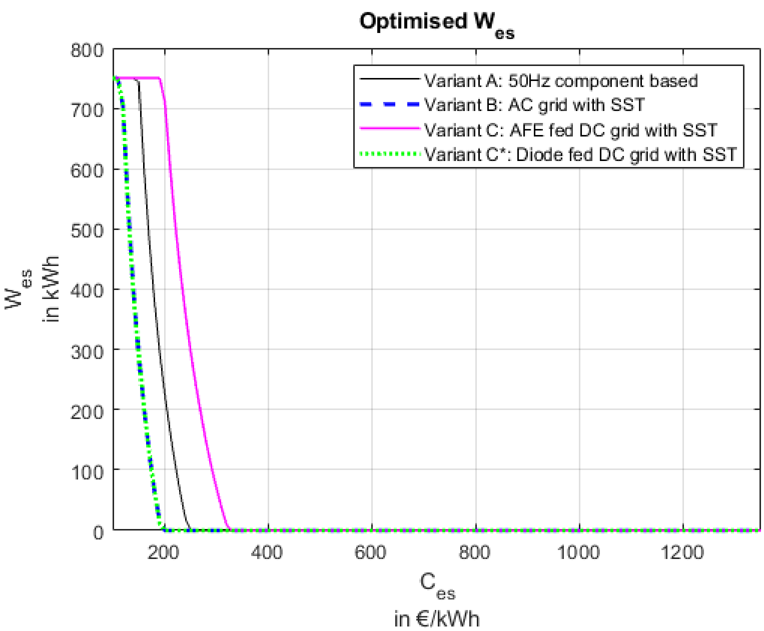

Figure 52: Optimisation results for all MPS variants in constant power ramping mode, with c_{es} as a parameter.

In constant power ramping, the optimisation has a much smaller influence region with respect to the energy storage costs c_{es}. Only if the c_{es} is cheaper than 300 €/kWh, the optimisation starts assigning a non-zero value for the optimised W_{es}. Below 100 €/kWh the optimised value for W_{es} is the full capacity i.e. 760 kWh.

If constant power ramping is finally chosen to ramp the main bending dipole magnet circuits, the optimisation of P_i and W_{es} for a given MPS variant makes only sense if the energy storage costs are in the sensitive region. Outside of this region, the result just tells categorically to install W_{es}=0 or W_{es}=full capacity.

6.9.5.2 Converter costs with optimised values P_i and W_{es}

All costs of the supplying infrastructure are assigned to the converters, see below the comparison for each variant and for each ramping strategy.

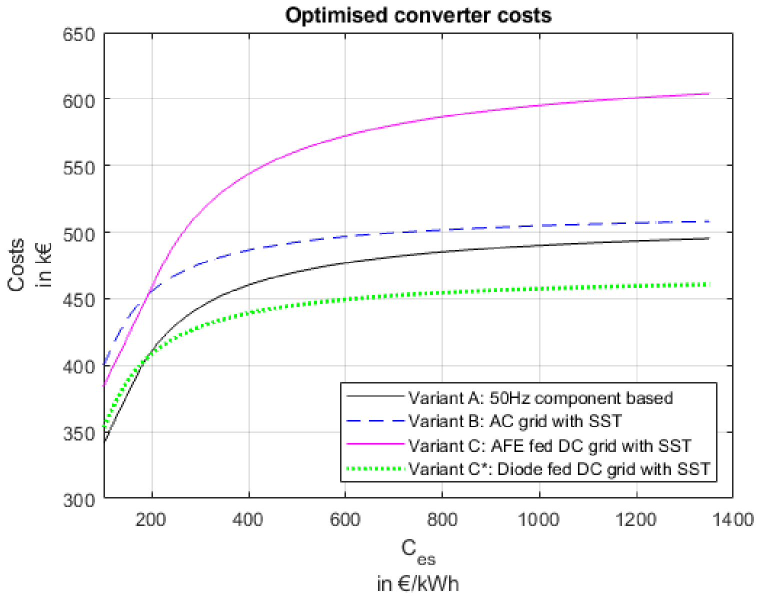

Figure 53: Optimised converter costs with constant voltage ramping, with c_{es} as a parameter.

The flat region in the higher value range of c_{es} means that the converter costs are rather independent of the energy storage costs because the optimisation assigns relatively less W_{es} and relatively high P_i.

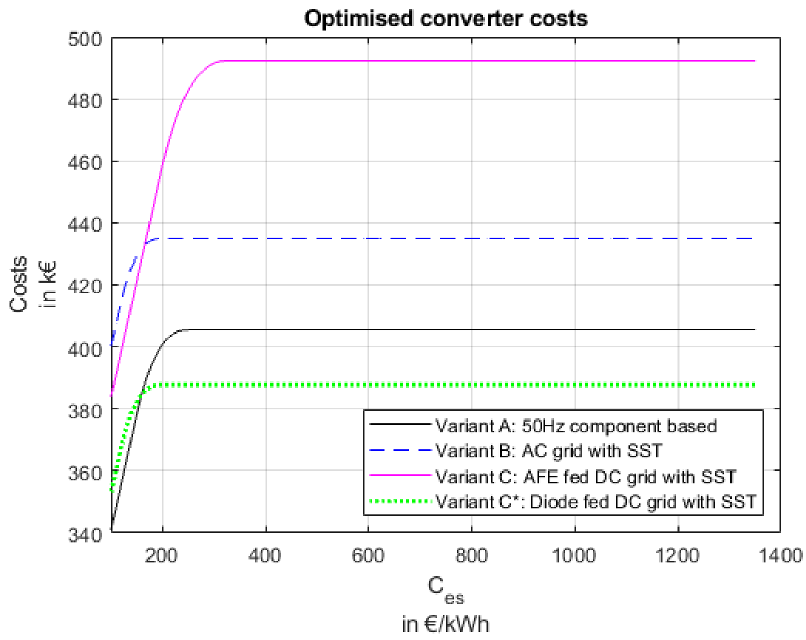

Figure 54: Optimised converter costs with constant power ramping, with c_{es} as a parameter.

For a wide range of c_{es}, the converter costs are not influenced at all. Only when c_{es} becomes very cheap, the optimisation places energy storage into the converter.

6.9.5.3 Optimisation with boundary conditions $P_{i\,min}$ and $W_{es\,min}$

The design process of the MPS considers now two boundary conditions. The first is the minimum required charging power $P_{i\,min}$ (which corresponds to a $W_{es\,max}$) to charge the energy storage during special operational conditions.[39]

The second is a concrete given peak power limitation of the transmission grid, as will appear then in the times when FCC is to be constructed. This peak power limitation leads the constraint of installing a minimum energy storage capacity $W_{es\,min}$ in the converter modules.

Assuming for example that by 2030 it turns out that 180 MW of the peak power during the ramp up can be delivered by the AC grid. On a single converter level this means P_i = 1.8 MW.

For constant voltage ramping $P_{stage\ 3\ max}$ = 3.02 MW which means a power difference of 1.22 MW, which has to be supplied by the energy storage. By using equations as shown in chapter 6.6.2, the minimum required energy storage capacity to fully ramp up the magnets is

[39] This requirement simply comes from the special when due to an emergency extraction of the energy in the magnets was activated, leaving the energy storage empty. Then within a certain time, they must be ready for the next magnet ramp up. This constraint comes from FCC operational performance requirements.

$W_{es\ min}$ = 106.8 kWh. With the boundary conditions for W_{es}, the following optimisation range is obtained.

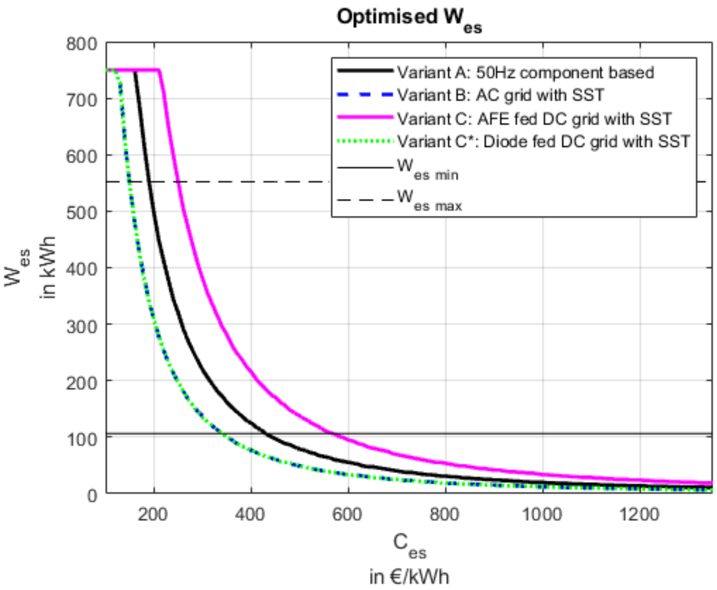

Figure 55: Optimised energy storage capacity for all variants in constant voltage ramping mode. Boundary conditions are shown for the upper and lower limit of W_{es}.

For any variant, the c_{es} values within the boundaries lead to an optimised W_{es} (respectively p_{infra}), e.g. for variant C, all points on the curve for a c_{es} between 220-560 €/kWh lead to an optimised solution.

For constant power ramping the $P_{i\ max}$=1.8 MW means a power difference of 0 kW. Thus, no minimum energy storage capacity is required, the peak power demand is covered by the AC grid. However, depending on the costs for energy storage, it might not be the optimised solution, see therefore the figure below.

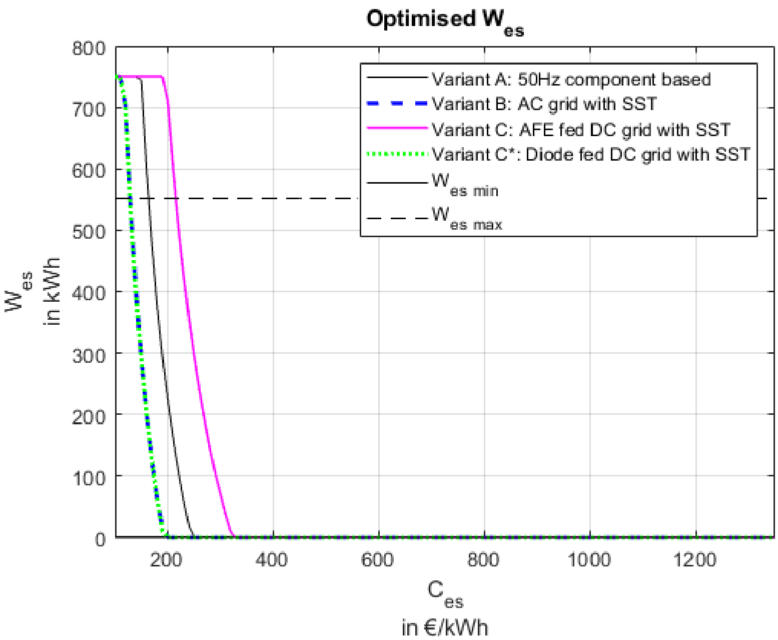

Figure 56: Optimised energy storage capacity for all variants in constant power ramping mode. Boundary conditions are shown for the upper and lower limit of W_{es}.

If it appears in the future that energy storage is very cheap, then a certain capacity should be installed in the modules, regardless if they are not needed to support peak power demands. They still have the effect of reducing the total investment costs.

6.9.6 Conclusion of the optimisation

In between the upper and lower limits of P_i and W_{es}, an optimisation algorithm gives the optimised values of P_i and W_{es}, with respect to the total investment costs.

The minimum required capacity of energy storage $W_{es\,min}$ is dictated by a potential peak power limitation of the 400 kV transmission grid. The minimum power rating of the supplying infrastructure $P_{i\,min}$ comes from the FCC operational requirement, to charge the energy storage within a certain time.

The effectiveness of this algorithm depends on the sensitive area of the energy storage costs relative to the infrastructure costs.

The sensitive area depends heavily on the ramping strategy. Constant voltage ramping has a much wider sensitive region as constant power ramping.

6.10 Conclusions

The table below summarizes the characteristics of the proposed power supply variants in a qualitative way. In all cases the converters are rated to the peak power.

Variant	Reliability	Investment costs	Losses	Converter module compactness (space demand and weight)
A 50Hz component based				
B AC grid with SST				
C AFE fed DC grid with SST				
C* Diode fed DC grid with SST				

The diode fed DC grid supplied solid state transformer in ISOP configuration is best. Thus variant C (and C*) are going to be analysed more in detail with dedicated simulation models. Variant C* is then also the basis when forming a universal DC grid, powering a large part of FCC load, and being also immune against transient voltage dips.

As variant C* is also the cheapest, the optimisation makes only sense if the costs for energy storage is very low i.e. below 400 €/kWh for constant voltage ramping and below 200 €/kWh for constant power ramping.

7 Universal and dip immune DC grid, based on the MPS variant C

To form a universal and dip immune DC grid, the powering topology for the main bending magnets - MPS variant C - can easily be extended to power many loads:

- the main bending dipoles
- Other super conducting magnets
- Warm magnets
- Cryogenic compressors

Further, the integrated energy storage (primarily used to overcome the peak power limitation from the transmission grid) can be used also to provide dip immunity to all loads powered by the DC grid. See below the representation of such a universal DC grid.

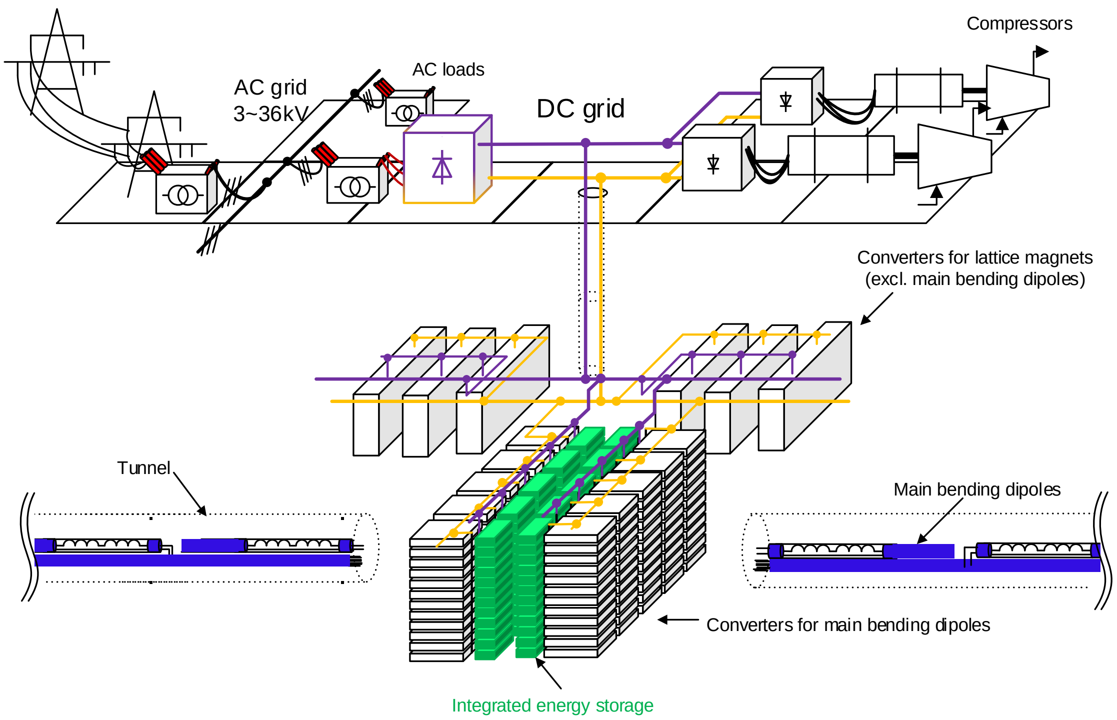

Figure 57: Representation of a universal and dip immune DC grid, powering the main bending dipoles and other loads found at particle accelerators. The integrated energy storage in the dipole converters is used for peak power demand reduction and to provide voltage dip immunity for all the load connected.

The following part of this chapter is organised in the following way. To present the situation with voltage dips at CERN, chapter 7.1 shows general statements about dips and particularly about the dips entering a potential FCC power system. A simulation model is used to predict the impacts of dips for FCC. In chapter 7.2 the transient behaviour during voltage dips of the cryogenic compressors is shown by using a dedicated simulation model. These compressors are rated up to 250MW and constitute the largest (almost) constant load of FCC. In chapter 7.3 a case study for universal and voltage dip immune DC grid (based on dipole powering topology C). A sophisticated control strategy allows to use the installed energy storage for the dipoles, also for anti-dip protection of all loads connected to such a grid.

7.1 General points concerning dips and sensitivity to dips

The protection of the particle accelerator by its own generated high energy particle beams is of high importance as the accelerator and the complete research infrastructure can be severely damaged. Variations in the voltage supply can consequently lead to variations in the magnetic field for guiding the particle beams. Before losing control of them, the beams are extracted (by strong and fast kicker magnets) and dumped (into a large graphite block) by the protection system. In the case of a complete power cut, the protection still has to work and eject the beams out of the accelerator and safely dump them.

For refilling the accelerator storage ring and regaining the desired stable beams conditions time is needed. This time is lost time for statistical data generation and it is the main cause for a dip immunity strategy for FCC.

A voltage dip is now somewhere in between of full power cut and normal conditions. Knowledge of the dip parameters on one side, dip sensitivity of the individual load and its powering equipment on the other side, is important to derive the best dip immunity strategy.

In many cases, just the supplying equipment itself is tripping during a voltage dip. In such a case, the best solution is to rise its fault ride through capability. On the contrary, an additional installed active dip mitigation device makes the situation worse, see the figure below.

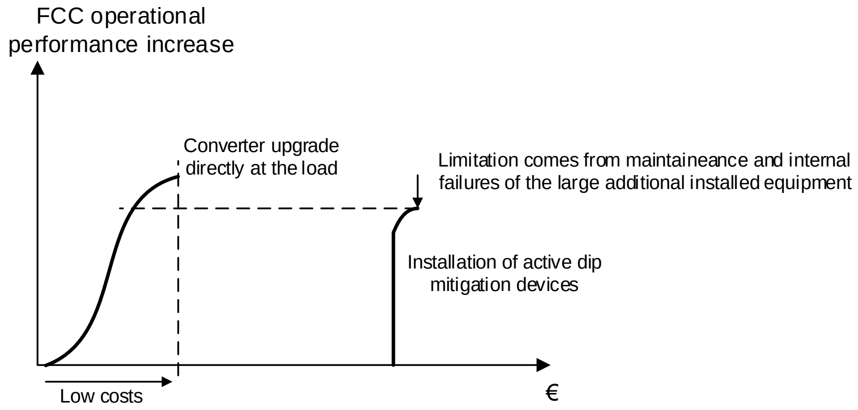

Figure 58: Principles for the dip immunity strategy of FCC.

The idea is use all knowledge, about the dips itself, how often they occur, the actual dip sensitive load or equipment, and the consequences when installing additional anti dip equipment. The problem with this kind of equipment is that it requires a lot of space, maintenance, and stops also due to internal failures.

The key is either to directly invest at the converter for the respective load – as it needs the converter anyway. Also the focus is on synergies, arising from the integrated energy storage for the dipole powering. Such synergies are realised by adequate power system design, see here chapter 7.

7.1.1 Dips at CERN

As for this report, the origin of transient voltage dips (hence on called dips) is the 400 kV transmission grid. During a fault (short circuit) the voltage at the fault location drops down to zero in the case of an ideal short circuit with the fault impedance neglected. At an arbitrary observation location, the remaining voltage will drop according to the coupling impedance between fault location and observation point. See for this reference [99].

The magnitude of the measured drop of voltage, depends then on the relative impedances between the measuring location and the short circuit location.

The duration of the dip depends then only on the protection mechanism of the transmission grid. Firstly, the fault needs to be detected by the distance relays and secondly isolated by line breakers. Distance relays are used to protect the high voltage transmission lines. Each line has one on each end. If the fault lies within a 15% region close to one end, the relay close to the fault will open within the 1st time-stage, but the one on the other end of the line waits for the 2nd time stage. The clearing time in this case can then be up to 500 ms.

The contour plot in figure below shows the clearing performance of the CERN suppling 400 kV grid, with respect to the CERN 400 kV substation.

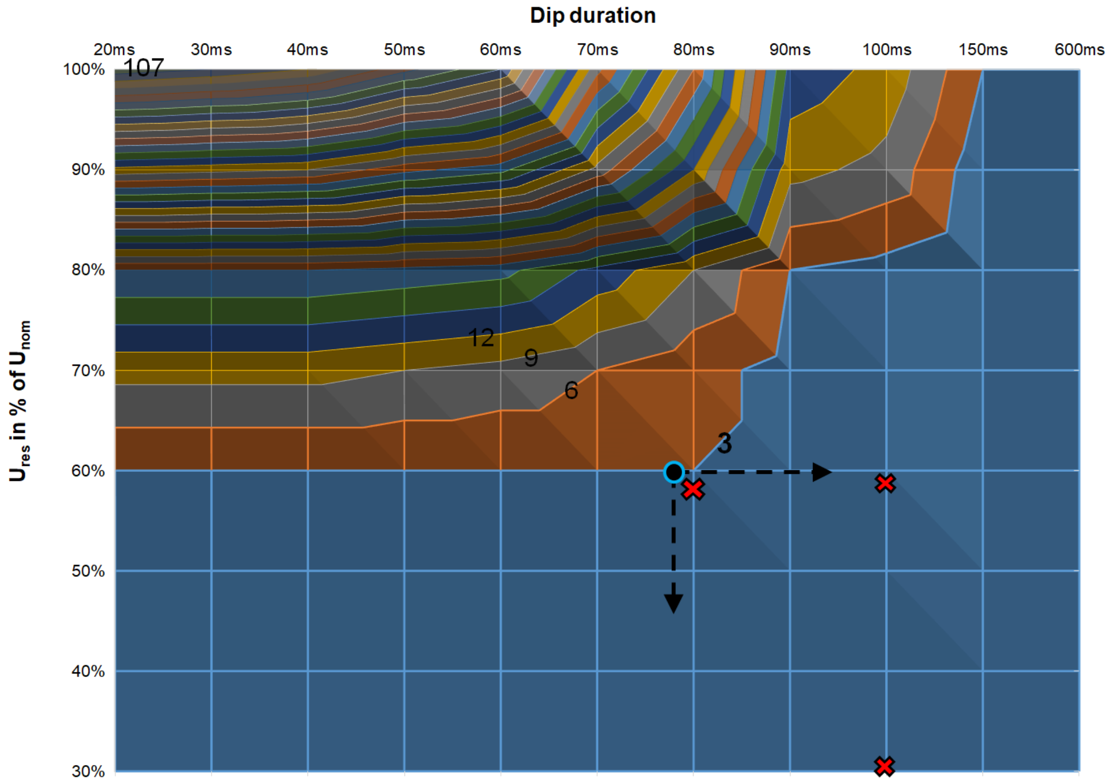

Figure 59: Contour plot for measured dips at CERN, during five years of operation. The number at the lines indicate the amount of dips which have been below the respective curve i.e. the dips with a more severe voltage-duration, e.g. at the point shown on the line ***"3"*** *it means that three dips have been somewhere in rectangular indicated by the arrows. The total number of dips were 107. The operation concerned the years 2011-2012 and 2015-2017.*

Noticeable are that only three dips lasted longer than 150ms, which indicates the clearing performance of transmission grid in that area. Further, a total number of 107 dips during 5 years of operation are counted. To predict the amount of dips and to evaluate the situation for FCC, the following chapter gives the answer.

7.1.2 Dips at CERN considering the powering of the FCC

The power supply of FCC has three direct connections to 400 kV substations. The substations are Bois-Tollot, Genissiat and Cornier (see Figure 2).

A simulation model, developed at Graz University of Technology by Professor Herwig Renner, is used to predict the dip situation for FCC. As calibration reference, actual dip measurements of the LHC are used. See here also the appendix.

Basis of the simulation model is the whole ENTSO-E transmission grid with all 400 kV and 220 kV transmission lines and substations. At chosen 400/220 kV substation a short circuit is initiated and the residual voltage at the CERN 400 kV substation is simulated. The residual voltage at CERN is indicated by a colour code at the fault location and refers to a percentage of $U_{nominal}$

- Black: above 90%
- Green: between 90-80%
- Yellow: between 80-70%
- Blue: between 70-50%
- Red: between 50-20%
- Magenta: below 20%

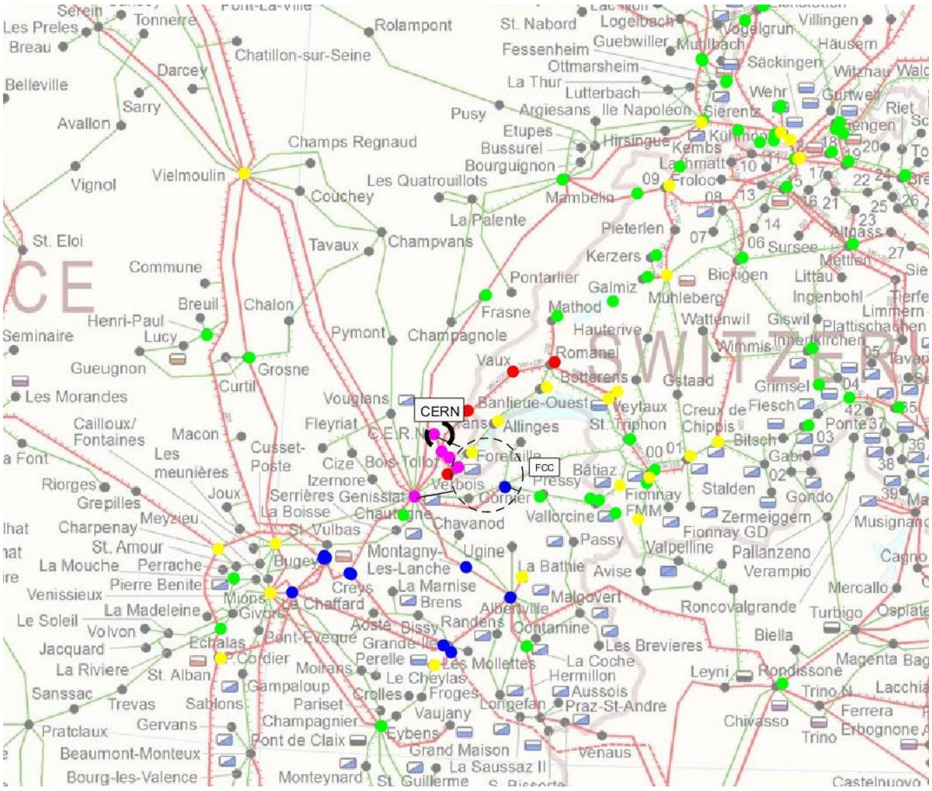

Figure 60: Transmission grid effected by transient voltage dips. The colour in the substations indicated the voltage drop seen at the substation CERN, if a short circuit is initiated at the very coloured substation.

If the surrounding area of 200-500 km of the substation CERN transfers a fault to CERN-substation, then the additional two substations (Genissiat and Cornier) for FCC do not collect extra dips which were not accounted before already. FCC is electrically small in comparison with the transmission grid's dip sensitive area.

For FCC the same amount of dip events as for LHC are to be expected.

7.2 Case study for dip sensitivity analysis of the cryogenic system

The experience at the LHC reflects the fact, that ASDs used at the cryogenic system are sensitive to voltage dips (for a detailed event see the appendix). Also in literature ASDs are found to be among transient voltage dip sensitive load [100–103].

The goal of this case study is to analyse the behaviour of the ASD with the most demanding specifications, as needed for the Turbo-Brayton refrigeration process foreseen for FCC (see the figure below).

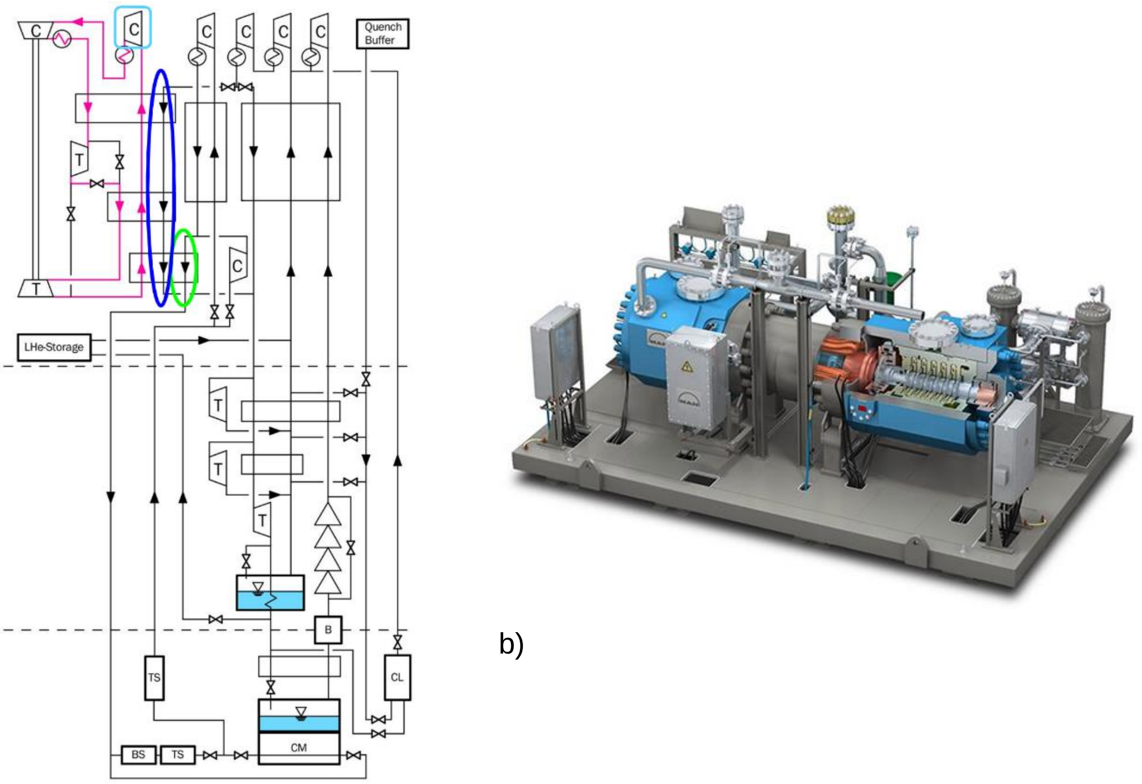

b)

a)

Figure 61: At the left side shown is principle layout of the cryogenic distribution for one plant. The Turbo-Brayton cycle is highlighted in magenta. It contributes to cold mass cooling (blue circle) and beam screen cooling (green circle). The in cyan encircled part is the compressor-motor. courtesy to. This compressor-motor unit is shown on the right side, with courtesy of MAN [104] as a potential supplier.

Two aspects are important here:

- the behaviour of power electronic converter part of the ASD during a voltage dip →dip sensitivity of equipment,
- the rotational speed of the compressor-motor system to evaluate a potential drop in pressure and volume flow reduction→dip sensitivity of the cryogenic process.

7.2.1 The simulation model

The full simulation model consists now of the compressor-motor unit and the power electronic converter. All relevant parts used in the simulation study are shown in the figure below.

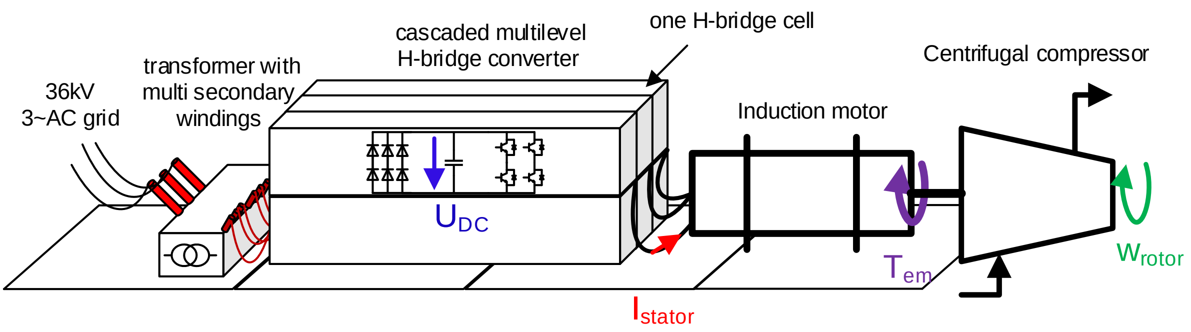

Figure 62: Simulation model consisting of ASD (converter and induction motor) and the centrifugal compressor as load. The analysed quantities have a colour indication.

The converter transformer is on the primary side connected to the 36kV 3~AC grid, and has on the secondary side multiple isolated windings. Each of these secondary windings are connected then to one of the converter cells. Each cell is supplied equally.

For this application, modular converter topologies could be used. Among them are modular multilevel converter (MMC)[105], solid state transformer [106], or cascaded H-bride based topologies (CHB) [107–111]. The advantages of a CHB are that no balancing or starting up issues occur and that higher power levels are easily reached by series connection of the cells (see the reference [112] for a comparison of multilevel topologies). This has led also to an industrial acceptance, and several suppliers are available e.g. ABB [113], Siemens [114] and WEG [115]. Finally, for the simulation model, a five-level cascaded H-bridge converter is chosen, see the figure below.

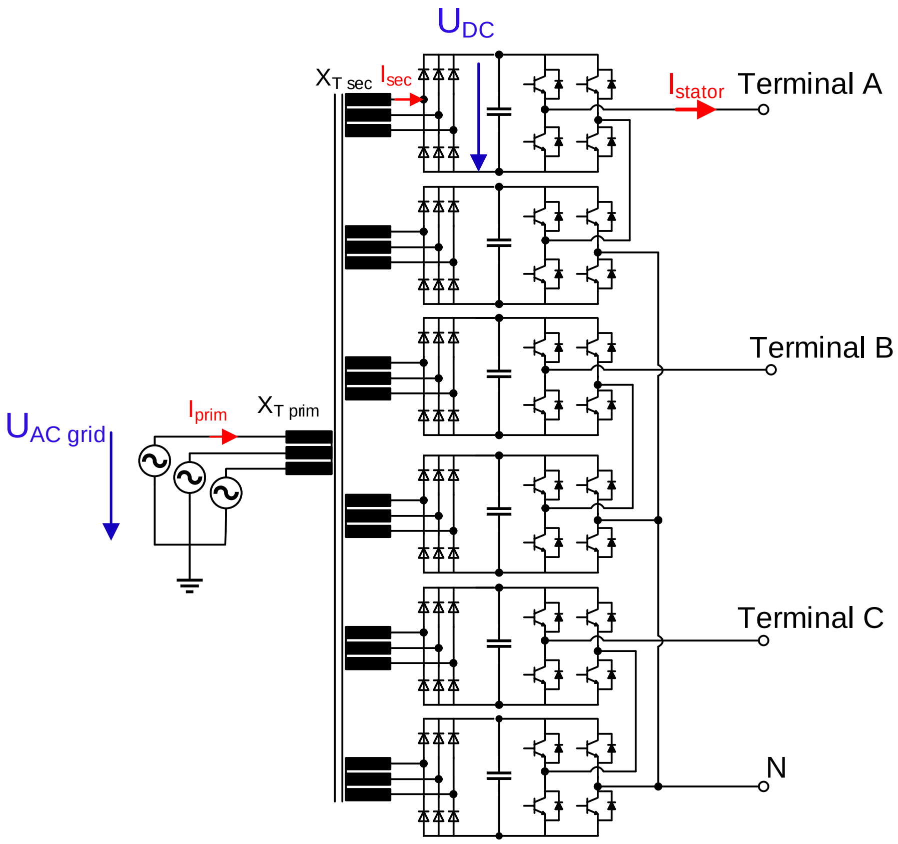

Figure 63: Topology of the five-level CHB converter used in the simulation model.

The implemented converter control is based on Direct Torque Control (DTC) and Space Vector Modulation (SVM). In particular, it is a 2D SVM algorithm using a look-up table. The actual torque and flux are estimated by measurements of stator currents and voltages. The torque and flux reference comes from a speed controller. To calculate the respective errors, hysteresis comparators are used. The SVM gives then the pulses for the IGBTs in the H-bridge cells.

In this power range, two-pole cage induction motors are the preferred design due to economic reasons[116]. The chosen induction motor in the simulation model is a single cage, two-pole asynchronous motor, with wye connected stator windings. For the operation in the field-weakening area, the motor-torque reduction must be considered. The torque of the induction motor for frequencies above the nominal frequency is proportional to 1/f and the break down torque proportional to 1/f². See here also [117].

The compressor load is modelled as a quadratic function, depending on the rotation speed of the rotor. At zero rotation speed, the load is also zero and at nominal rotation speed (200 Hz=12000 U/min) the mechanical load is 10 MW.

The analysed quantities are:

- voltage in one of the converters cells U_{DC}
- current flowing in the stator winding of the induction machine
- torque produced by the induction machine
- the rotation speed of the compressor→this allows to see if the refrigeration process itself is disturbed

For the detailed specifications and simulation parameters see the table below.

Table 28: Parameter for the simulation study

Parameter	Value	Remark
Short circuit capacity at the connection point to the 36kV 3~AC grid	1000 MVA	
Power rating of the converter transformer	12 MVA	For the converter six cells are needed, thus the transformer has six secondary isolated windings
Secondary voltage of the converter transformer, phase-phase RMS	1750 V	Is used as a parameter. A higher secondary voltage means additional margin during a dip.
Power rating of the converter	12 MVA	Inclusive a margin, and respecting a power factor of the induction motor of 0.93 and an efficiency of 97% at rated output power P_{mech} = 10 MW
U_{DC}, nominal cell voltage	2200 V	At rated output power of the ASD
Capacitance of the filter capacitor of one H-bridge cell	30 mF	Is used as a parameter. A higher capacity means additional margin during a dip.
U_{stator}, phase-phase RMS	6.22 kV	
P_{mech} of the induction motor	10 MW	
Total inertia of the compressor-motor unit	150 kgm²	The rotor inertia is estimated with 130kgm² (technical catalogue from ABB [118] and in addition comes 20kgm² from the centrifugal compressor (for the calculation see the appendix)

7.2.2 Simulation results

Simulation results for three-phase dip -50%/100 ms.

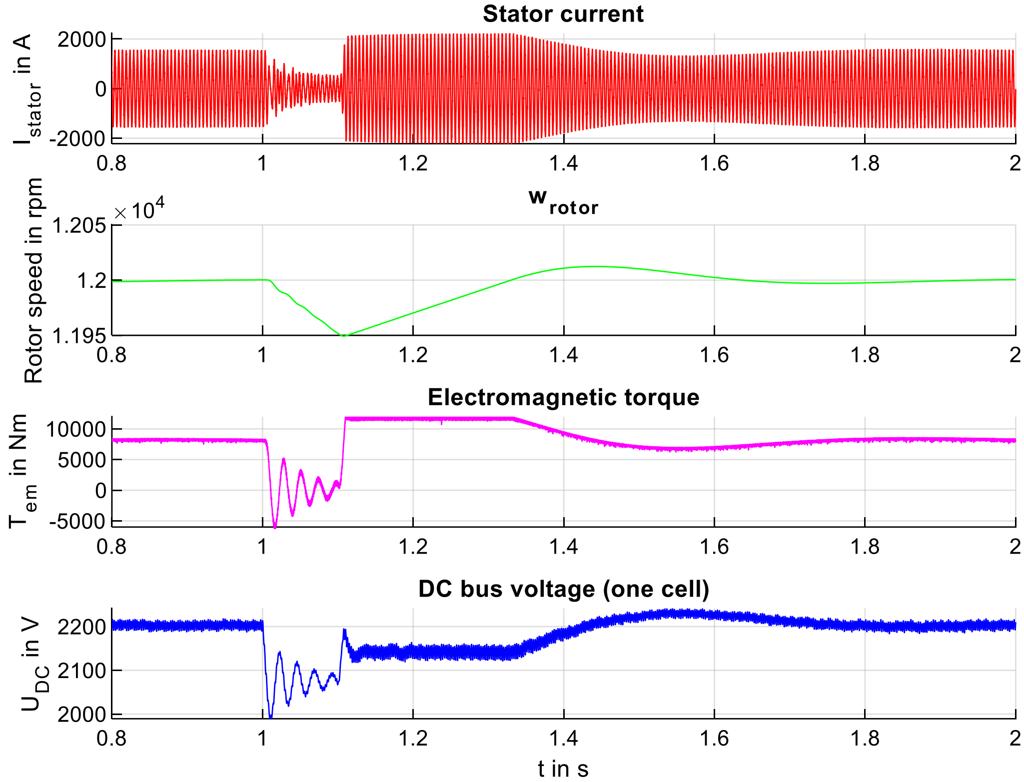

Figure 64: Simulation result, showing the mechanical dynamics and the converter behaviour for a three-phase dip with -50%/100 ms.

At the beginning of the voltage dip at t=1s, the DC voltage in the cells drops. Below a certain limit, no torque is produced anymore and the rotor speed declines. At the end of the voltage dip, the DC cell voltage is recharged and the converters continuous the operation and re-accelerates the rotor. The main goals are already proved in the above figure – the converter runs through the fault and mechanical process is immune as the speed drops only marginally. However, in the next simulation a much realistic dip is used and also additional ASD design parameters are evaluated.

Simulation results for one-phase dip -50%/100 ms.

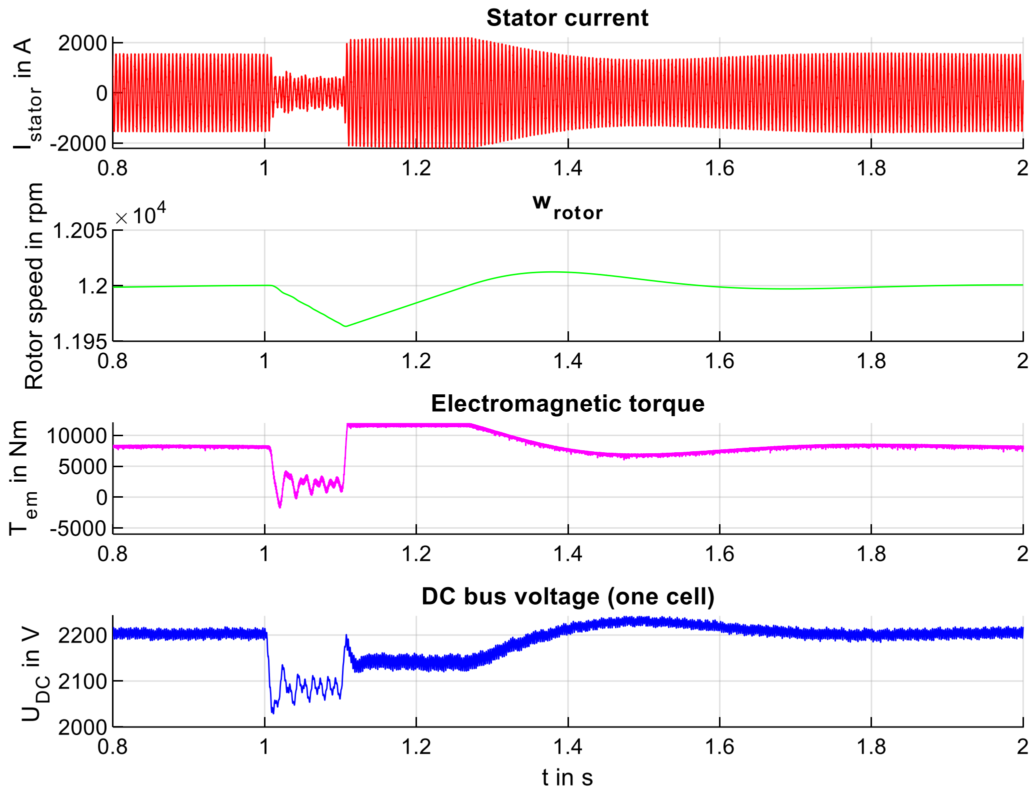

Figure 65: Simulation result, showing the mechanical dynamics and the converter behaviour for a one-phase dip with -50%/100 ms.

As the dip is less severe, the DC cell voltage does not drop as much and also during the dip, a certain electromagnetic momentum could be produced also during the dip. After the dip, the normal operation continuous.

Noticeable in all the simulations before is that there is a certain lower limit of DC cell voltage until a continuous operation (full torque is produced) is possible. From simulation it is obtained that the limit is about 2100V DC minimum cell voltage. Once this limit is undertaken, no torque is produced.

Two modifications lead to a higher operational margin, increased capacity or increased secondary transformer voltage, see the following two figures.

Simulation results for one-phase dip -50%/100 ms with increased capacity of the H-bridge cells, from 30 mF to 150 mF.

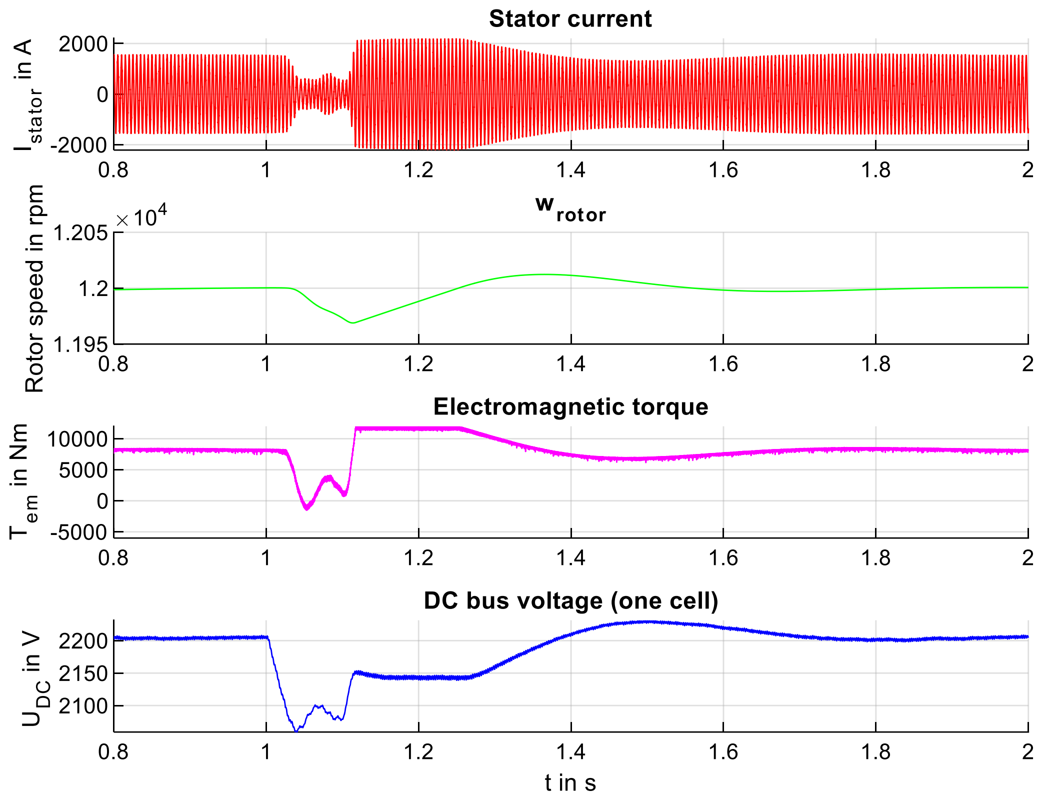

Figure 66: Simulation result, showing the mechanical dynamics and the converter behaviour for a one-phase dip with -50%/100 ms, now with five-times increased capacity of the H-bridge cells.

Even with five-times increased capacity, the normal operation during a voltage dip is prolonged, during the rest of the dip, the torque on the compressor is still reduced. Due to the output power, the increased capacity has only little effect.

With the knowledge of the lower DC cell voltage limit, a new design for the secondary voltage of the converter transformer is the key. Of course, this new voltage level must be respected in the overall design e.g. at the isolation of the stator coils. See the figure below with the new designed DC cell voltage.

Simulation results for one-phase dip -50%/100 ms with increased secondary voltage of the converter transformer, from 1750 to 2050 V.

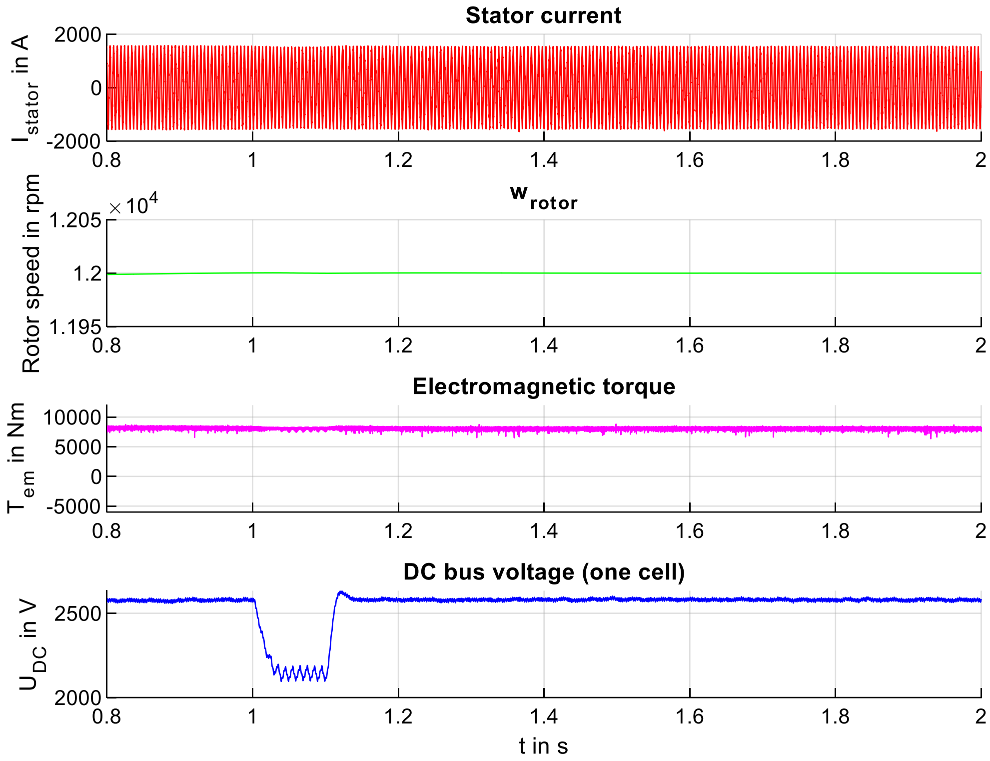

Figure 67: Simulation result, showing the mechanical dynamics and the converter behaviour for a one-phase dip with -50%/100 ms, now with increased DC cell voltage.

Due to the new designed DC cell voltage, the ASD provides a constant torque to the compressor load, without any disturbance at all.

7.2.3 Conclusions

Process dip immunity is guaranteed due to the high inertia of the compressor motor system. The drop of pressure and volume flow during a severe voltage dip remains within the normal operational margin. After the voltage dip, the control restarts producing electromagnetic torque. This ASD fault ride through capability is already in the guaranteed specifications of medium voltage motor drive suppliers. The minimum U_{DC}, obtained from the simulation model, is additional knowledge supporting the ASD design. By increasing the H-bridge cell voltage accordingly, the full torque is provided to the compressor load during the complete voltage dip duration. Additionally, if the cryogenic compressors were to supplied by an MMC topology[40], the powering with a universal dip immune DC grid can be considered, see chapter 7 and chapter 7.3.

[40] The MMC topology offers advantages as low harmonics, high efficiency and high availability [28].

7.3 Case study of dip immune universal DC grid

To show the proof of concept for a universal dip immune power system, a dedicated simulation model is used. The main goal is to show the capability of releasing power from the integrated energy storage to compensate the voltage dip and thus allowing a continuous supply of all the load connected to the power system. The case study uses as load the main bending dipole converter and an additional constant power load (CPL). The other CPL load can be for example the cryogenic compressors.

The simulation model is downscaled in terms of power rating. As only one dipole converter (instead of 10 converters for the full system) is used. Further only four converter modules are connected in ISOP configuration (the full converter has at least 12 modules).

Also, the constant power load (CPL) is downscaled accordingly. The following power rating relations are obtained:

- $P_{mag} / P_{stage\ 2} = 4/1$
- $P_{stage\ 2} / P_{CPL} = 1.3/1$
- $P_{stage\ 1} / (P_{stage\ 2} + P_{CPL}) = 1.5/1$

The full simulation model with the time dependent power flows is shown in the figure below.

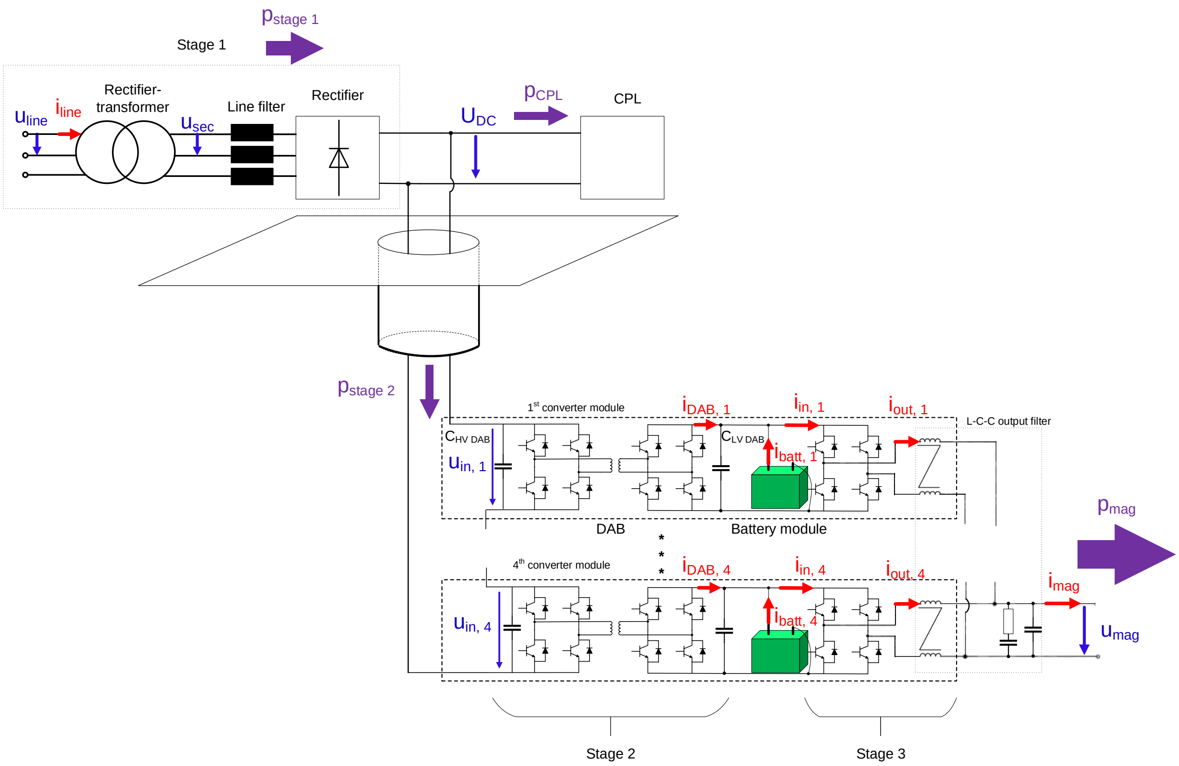

Figure 68: Simulation model of the universal and dip immune DC grid.

The effect of the integrated energy storage on the power flow is seen directly. The main part for the magnet power comes from the batteries.

7.3.1 Topology and simulation model description

Below follows the stage wise description of the considered powering topology. The core part is the powering topology for the main bending dipole magnet, as analysed in chapter 6.

7.3.1.1 Stage 1

This is the DC grid forming stage. It is rated to the power demand of the converter for the main bending dipoles, and the sum of the other load connected to it.

The optimised energy storage capacity is not taking the full recovered energy from the magnet circuits. With this universal DC grid, the energy can be partly consumed and partly restored in the energy storage. This also gives flexibility for the rectifier stage 1 design, as it doesn’t have to be bidirectional anymore if less than the full capacity of energy storage is installed.

The rectifier has an inductive line filter. No specific DC bus filter needs to be used as the converter modules have a capacitor as input filter. Connected in the ISOP configuration, these capacitors work automatically as filter for the DC grid as well.

7.3.1.2 Stage 2 (dipole converter on module level)

The main purpose of this stage is to perform galvanic isolation of the magnet circuit from the AC grid (and stage 1 as other magnet circuits would influence each other via the common DC bus) and to control the charging and discharging of the integrated energy storage.

Important here is the bi-directionality of stage 2. The energy storage can be charged but also discharged by stage 2. Thus, it is possible to use the energy storage to stabilise the whole DC grid during a voltage dip, coming the AC grid above 36kV.

The chosen topology is the dual active bridge (DAB) as it fulfils all requirements and has potential for optimisation in terms of weight, volume and has a high efficiency (due to zero voltage switching and application of wide band gab switches), compared to other topologies.

For the power transfer with the DAB, dual phase shift is chosen as it eliminates reactive power flow in the DAB and reduces the output voltage ripple [119, 120]. Thus also the output capacitor can be minimised. See the formula below for the power transfer characteristics.

$$P_{DAB} = \frac{n_{DAB} \cdot u_{in} \cdot u_{out}}{2 \cdot f_{sw\,DAB} \cdot L_{DAB}} \cdot (D2 \cdot (1 - D1 - D2) + D1 - D2^2 \qquad (32)$$

Many operational regions are possible by using certain ranges of the inner phase shift D1, and the outer phase shift D2.[41] In the figure below, the chosen operational range of the DAB in the converter modules is shown.

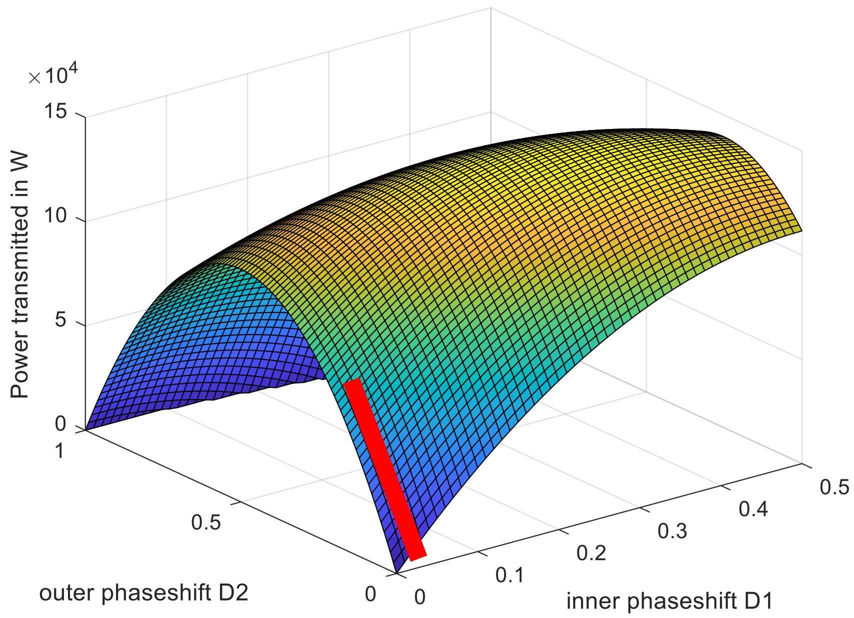

Figure 69: Power transfer characteristic of the DAB with dual phase shift control, the red strip indicates the defined operational range used in the simulation model.

The voltage and current levels are chosen such that standard components from the industrial market can be used. The input voltage on the high voltage side of the DAB (u_{in}) is about 850V. Thus for IGBTs a voltage rating of 1700V can be chosen, to achieve a derating of 50%. For current rating an overload capability of 100%, and a ripple factor of 20% is considered. With an input voltage of 850V and a peak power rating of the DAB of 70kW, the current rating becomes I_{IGBT}=70kW/850V*2*1.2 = 197A.

The output voltage of the DAB (u_{out}) on the low voltage side is 325V. Thus 1200V IGBTs can be chosen. The current rating with an overload capability of 100%, and a ripple factor of 20% the current rating becomes I_{IGBT}=70kW/325V*2*1.2 = 517A.

The filter $C_{LV\ DAB}$ on the low voltage side of the DAB is designed with respect to:

[41] The outer phase shift is between the H-bridge on the high voltage side and the H-bridge on the low voltage side. The inner phase shift is within the H-bridge, whereby the duty cycle between two legs of the H-bridge is adjusted.

- current demand of the stage 3 DC-DC converter: the maximum input current of stage 3 is to be delivered by the capacitor.
- voltage ripple considerations: any voltage ripple on the low voltage DC bus leads to a ripple of the current flowing in the battery. As the battery is directly connected, the current ripple depends also on the internal battery resistance R_{batt}.

The current rating for the capacitor is derived by calculating the RMS current flowing into the capacitor, and it depends on the input current required from the stage 3 (DC-DC magnet supply stage).

The current rating for the capacitor is derived by calculating the RMS current flowing into the capacitor, and it depends on the input current required from the stage 3 (DC-DC magnet supply stage).

$$\begin{gathered} i_{RMS} = \frac{i_{m\,nom}}{n} \cdot Form \\ Form = \sqrt{D \cdot (1-D)}, with\ D = \frac{u_m}{u_{out}} = \frac{260V}{325\ V} \rightarrow Form = 0.4 \\ i_{RMS} = \frac{11.4kA}{12} \cdot 0.4 = 381A \end{gathered} \tag{33}$$

To add some margin, twice the value could be taken as RMS current rating of the capacitor.

From simulation it is obtained that a value of $C_{LV\ DAB}$=150mF, lead to a voltage ripple of +/-50mV. With an internal battery resistance of R_{batt}=33mΩ the peak current ripple flowing into the battery is +/-1.5A. The relatively high capacity is needed as it allows a direct connection of the battery to the low voltage DC bus of the converter modules. Further optimisation of the controller or an additional converter between the battery and low voltage DC bus can reduce the capacity. However, the main objective is to show the working principle of the control to use the batteries for ramping the magnets and to provide dip immunity for the DC grid.

7.3.1.3 Stage 3 (dipole converter on module level)

The main purpose is to deliver a share of the magnet current i_m. The topology is a 4-quadrant DC-DC converter, with a L-C-C output filter. Each module has a coupled output filter inductor. After the paralleling of all modules, two capacitor filter branches are connected in parallel.

The main H-bridge is rated to the peak power needed to ramp of the magnet circuit i.e. 251kW for constant voltage and 283kW for constant power ramping. To improve the performance of the DC-DC output stage, the 3-level PWM with frequency doubling (3L2FSW or unipolar PWM) is chosen for the PWM strategy. Compared to the 2-level PWM (also called bipolar PWM), the output voltage ripple is reduced by up to a factor of 16, whereby the switching losses remain the same. Due to the 3L2FSW strategy and the interleaving of the output modules, a very high apparent switching frequency on the output modules is achieved. With the four modules (in this case study) connected in ISOP, an apparent switching frequency of 8-times the DC-DC switching frequency is achieved. For the 325V voltage level, the 1200V IGBT class can be chosen. The current rating with 50% overload and 20% ripple for a 283kW rated DC-DC is then I_{IGBT} = 283kW/325V*1.5*1.2 = 1.57kA.

7.3.2 The control strategy

The complete control concept can be separated into the DC grid forming control (stage 1) and the converter control (stage 2 and stage 3), whereby the control of stage 2 constitutes the core of the concept. It is explained by looking at the level of a single converter module.

The stage 2 system starts at the high voltage side of the dual active bridge (primary side of the DAB) and ends after the low voltage DC bus filter capacitor (secondary side of the DAB).

The stage 3 system starts at the low voltage DC bus of the converter module i.e. after the DC bus filter of stage 2, and ends after the two capacitor output filter branches, where the required magnet voltage u_m is applied on the magnet circuit.

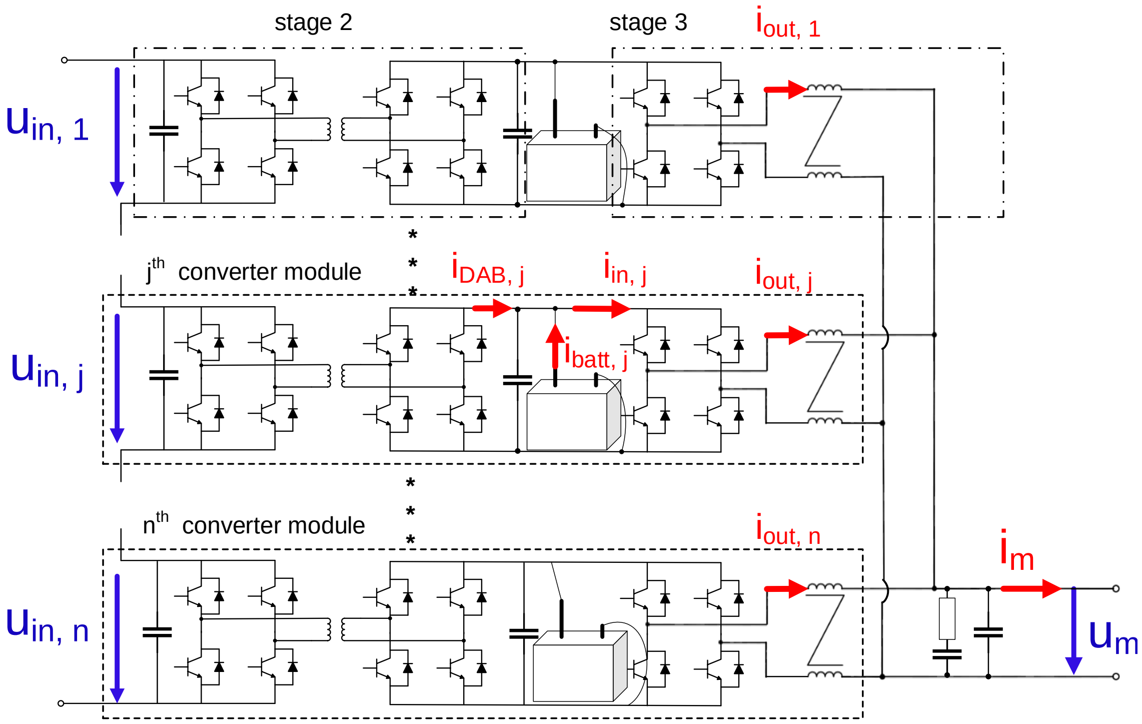

Figure 70: Converter module representation for identifying the control variables.

The control system need to solve the following points:

- Input voltage sharing (IVS) and output current sharing (OCS): For modular converters in ISOP configuration, the IVS and OCS need to be coupled, otherwise the converter becomes instable [121, 122]. The IVS loop will balance $U_{in,1\text{-}n}$ by acting on stage 3 of the respective module. OCS is then achieved automatically. Stage 2 and stage 3 are acting interactively.
- The stage 2 peak shaving control supplies the magnet power demand until its own power limit is reached (i.e. until $i_{DAB\ limit}$). From this point on, the battery delivers the power requested from the magnets (i.e. i_{batt} starts flowing out of the battery). Stage 2 control achieves also anti-dip protection.
- Stage 3 control achieves the correct ramping of the magnet.

7.3.2.1 Stage 2 control

The main task is to control i_{batt}, flowing in and out of the energy storage, see the figure below.

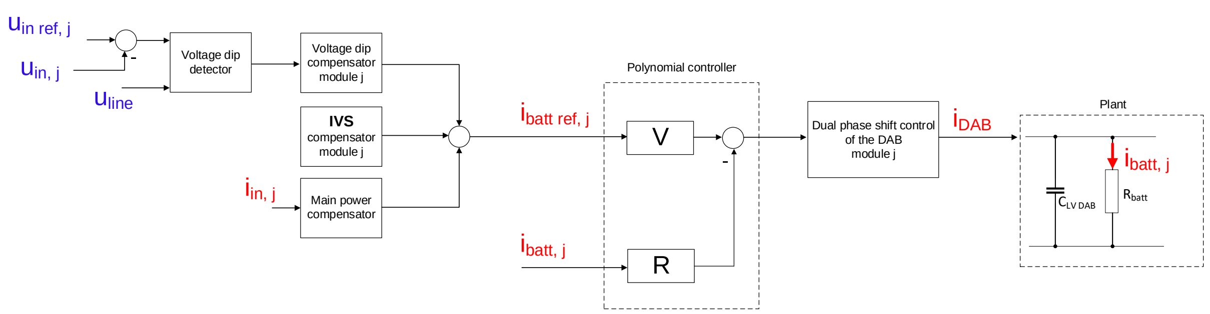

Figure 71: Control structure of stage 2.

The reference the battery current, $i_{batt\ ref}$ consists of several parts. The upper part achieves the voltage dip compensation. If a voltage dip is dropping the input voltage u_{in}, the compensator gives a demand for a positive battery current i.e. a current flowing out of the battery. By adjusting the phase shift of the DAB, the power flow is redirected from the output side to the input side. Thus the input voltage is kept stable.

The middle part comes from the IVS compensator. Any mismatch of input voltages must be “transferred through” the complete module until the load is reached (thus the IVS compensator signal acts also on stage 3). Only by this “transferring” IVS (and OCS) can be achieved.

The lower part is to control the power flow of the DAB during the normal magnet operation. During the ramping, the DAB delivers respectively receives current within its rated power.

A digital polynomial controller is used to control i_{batt}. The polynomials V and R are designed to follow a ramp shape reference and to reject periodic disturbances which are coming from the switching of the stage 3 converter.

The output signal of the controller acts on the dual phase shift control of the DAB. The DAB delivers the current i_{DAB} to plant, which is modelled as a parallel connection of the low voltage side filter $C_{LV\ DAB}$ and the internal battery resistance R_{in}.

7.3.2.2 Stage 3 control

The control of stage 3 is completely independent of stage 2, but for the IVS compensating part. Its main purpose is to follow a given reference for the magnet current i_m.

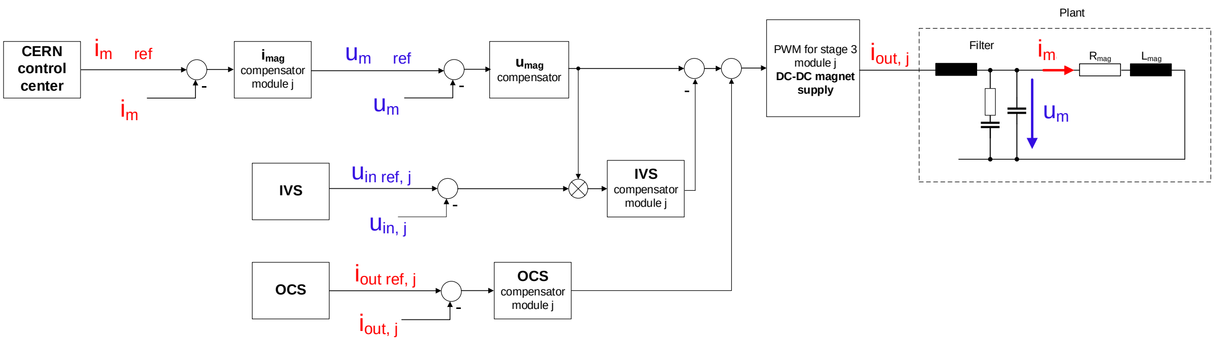

Figure 72: Control structure of stage 3.

The control structure consists of a cascade of two loops, the outer current loop for i_m and the inner loop for u_m. On the PWM signal of the DC-DC converter acting in total 3 components. The main part coming from the i_m-u_m-compensator cascade, which need to fulfil the tracking and ripple performance to stay within 1ppm in magnet current precision.

Further the IVS compensator is acting on the output DC-DC of stage 3, as it is the only way to balance the ISOP configured converter. The references for the module input voltages are calculated dynamically [122]. See below the figure for the IVS.

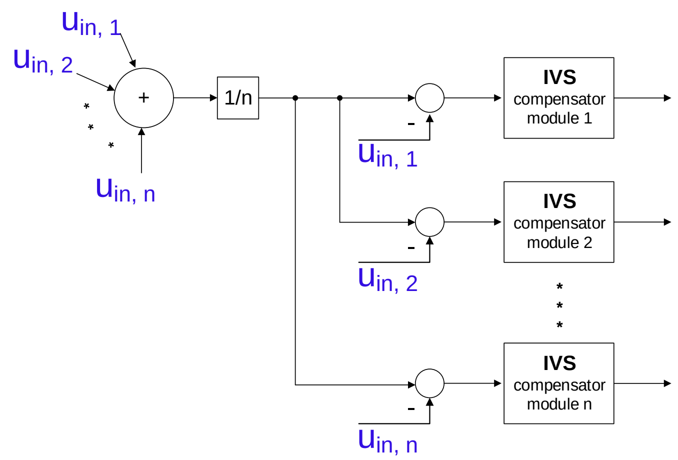

Figure 73: Control structure of the IVS.

If IVS is achieved, then automatically OCS is achieved as well. However, the third part acting directly on the output DC-DC is the OCS loop. The reference of the respective output current i_{out} of the module is just the magnet current i_m divided by the number of modules.

7.3.3 Simulation model parameter summary

All power electronic based systems are using switching models for IGBTs. The energy storage is a generic model for lithium-ion based batteries. It provides all relevant charge and discharge characteristics. For the simulation the linear region at 50% of state of charge is used. No temperature or aging effects are considered, as the simulation only focus on some seconds of operation. Thus a constant internal resistance R_{batt} is assumed. This value is also used for controller design (see chapter 0) and losses calculations (see chapter 6.8.4). The other load connected to the DC grid is modelled by a controlled current source.

Table 29: Simulation model parameters

Item	Unit	Value
SCC at 36kV level	MVA	1000
Rating of the rectifier transformer	MVA	0.4
Rating of the other load on the DC bus	kW	100
Peak power rating DAB (on module level)	kW	70kW
U_{sec} of rectifier transformer	kV	2.66
u_k of rectifier transformer	In %	5
Line filter inductance	p.u.	0.01
$u_{in, nom}$	V	850
$u_{out, nom}$	V	325
$f_{sw\ DAB}$	kHz	5
$C_{in\ DAB}$	mF	15
$C_{LV\ DAB}$=150mF	mF	150
L_{DAB}	mH	0.25
Dead time between IGBT switching in one H-bridge leg	µs	10
Simulation model time step	µs	5
Controller sampling time step	µs	25
$f_{sw\ stage\ 3}$	Hz	100
L_m	H	25.08
R_m	mΩ	1
R_{batt}	mΩ	0.033
Dips' magnitude	In % of U_{nom}	-50
Dips' duration	ms	100

7.3.4 Simulation results

The scenario comprises two voltage dips coming from the transmission grid, penetrating the 36kV distribution grid at the FCC surface powering point where the dipoles and other sensitive loads are connected.

The first dip is happening at t=1 s, which is 4 s before the peak magnet current is reached (at t=5 s). The second dip happens shortly before the transition from the ramp up to the flat top phase (at t=4.95 s). This second dip is very challenging to mitigate, as the transition from ramp up (full power demand) to flat top (suddenly very low power demand) is already difficult to master for the control, without considering dips.

For a precise analysis of the control system, the real magnet inductance (L=25.08 H) is used. As the magnet cycle would last 4h, only parts are highlighted. An initial magnet current of 1950 A (t=0 s) is set, then the ramp up continues until 2000 A (t=5 s). At this point the flat top phase starts and magnet voltage is reduced fast to a very low voltage level to drive i_m through the super conducing magnet circuit. See the figure below.

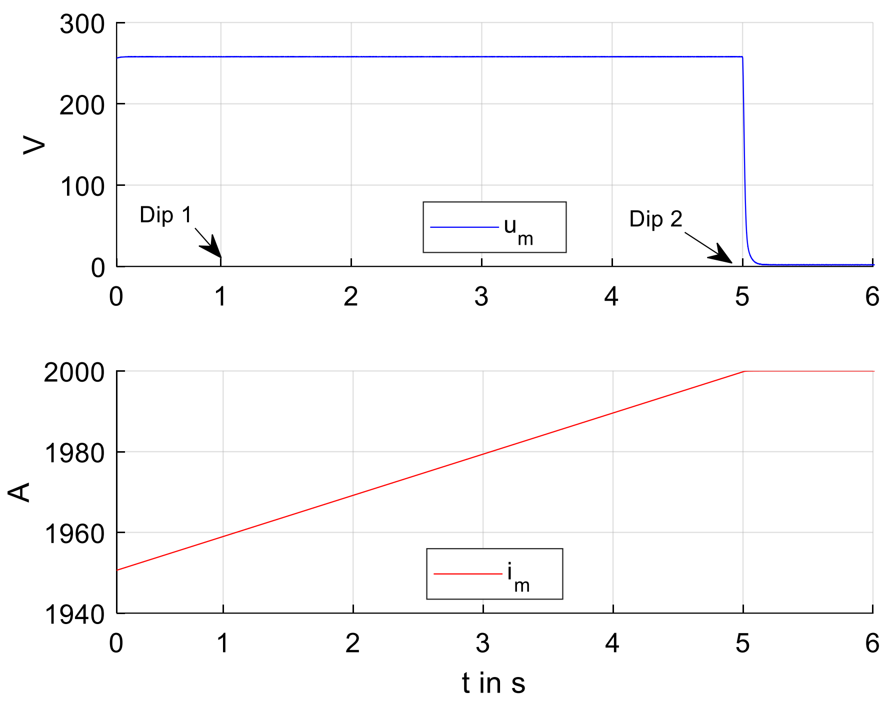

Figure 74: Voltage dip scenario, two dips happing during the magnet operation at critical points. Dip 1 at a high power demand and dip 2 during the transition between ramp up and flat top.

Having defined now the scenario, the simulation results are presented in two phases. In the first phase the effect of a voltage dip on the complete power system is shown without activation of the dip protection. In the second phase, the dip protection is activated.

7.3.4.1 No dip protection

During the voltage dip, the rectifier voltage drops to a very low level, and the converter input voltages u_{in1-4} decrease.

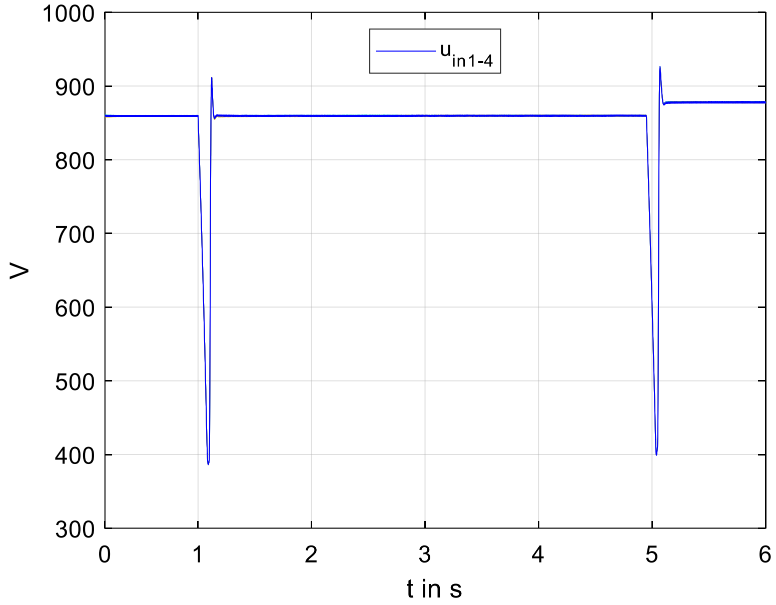

Figure 75: Converter input voltages, and no dip mitigation is activated.

The voltage drops more than -50% of the nominal.

In general, voltage dip sensitivity of equipment is often related to its protection against high currents. High currents appear right after a voltage dip as the result of recharging and re-energizing. The voltage and current at the 36 kV 3~AC distribution grid are shown below.

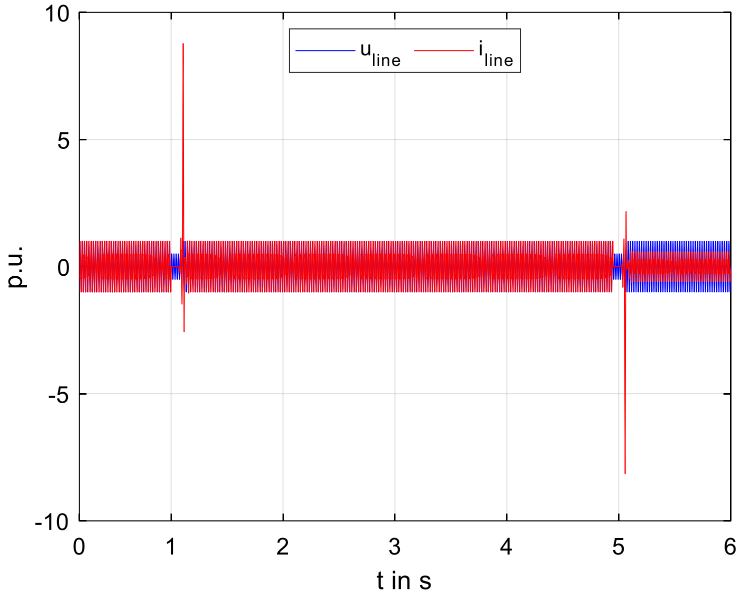

Figure 76: Line current and line voltage at the 36 kV level, and no dip mitigation is activated.

The uncontrolled recharging currents reach almost 10-times the nominal current. This leads to a triggering of over current protection devices.

A voltage dip can also overstress an equipment internal compensation mechanism, which is not designed for such a heavy disturbance. At the LHC the saturation of the active output filter leads to a converter tripping in the event of a voltage dip. However, for the MPS design with integrated energy storage, not disturbance is seen on the stage 3 DC-DC output.

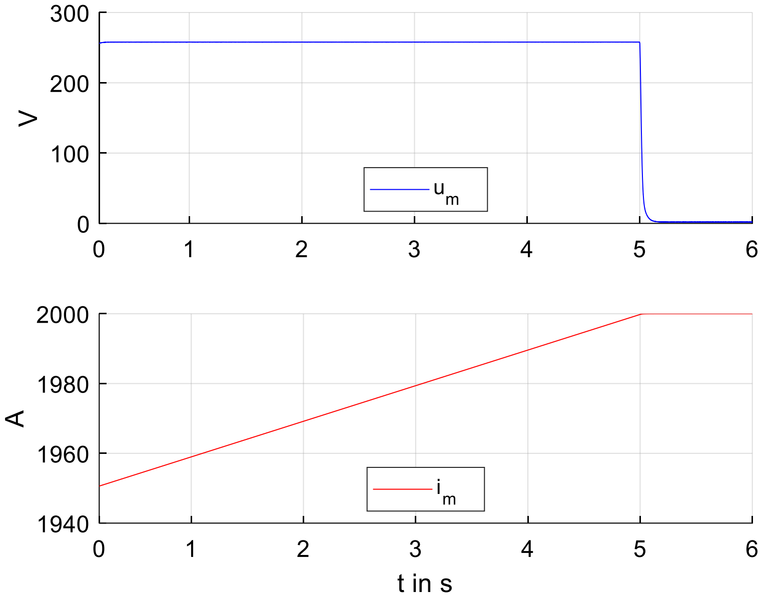

Figure 77: Magnet voltage and magnet current. Due to the connected battery, no disturbance is observed during the voltage dips.

7.3.4.2 Active dip mitigation

The stabilizing effect of the battery is no used “back-wards”, by reversing the power flow of the DAB, and drawing additional current out of the battery. The reduction of power from the DAB will increase for a short time the battery current i_{batt} flowing out the battery, see the figure below.

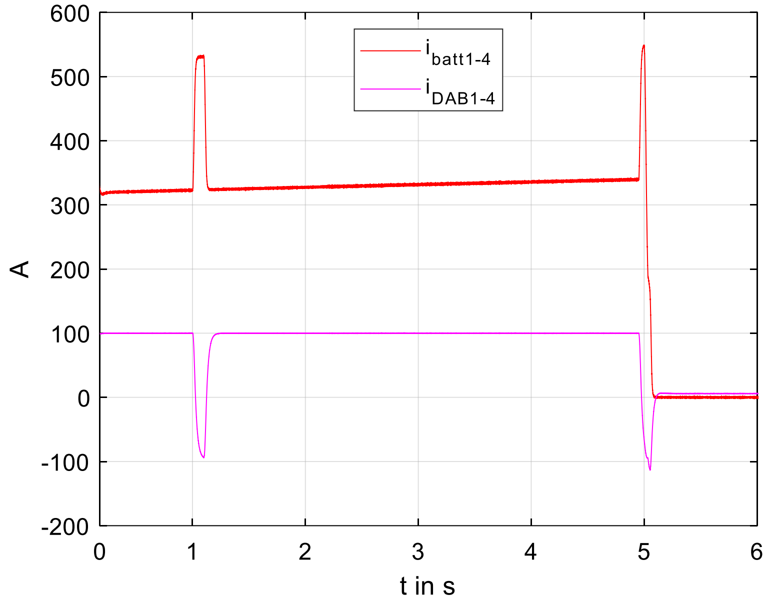

Figure 78: Currents from the DAB and the battery of the respective converter modules with active dip mitigation.

The power flow reversal of the DAB will increase for a short time the battery current i_{batt} flowing out the battery. This keeps the input voltages of the converters u_{in}1-4 stable within a deviation band of +/-10%.

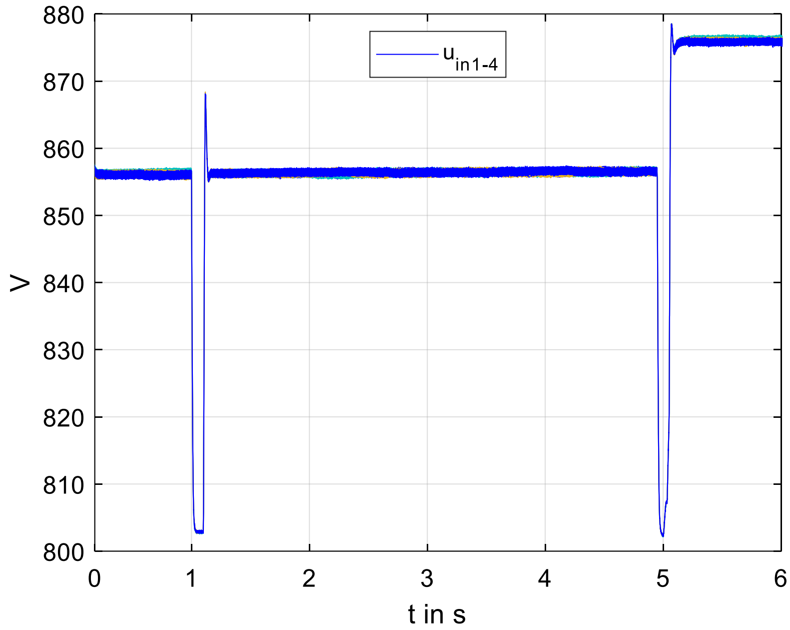

Figure 79: Converter input voltages with active dip mitigation.

The voltages do not drop more than -7%. All load connected to the DC bus of the grid are supplied continuously.

Thus the universal DC grid runs successfully through the voltage dip. See below the comparison between no counter measure and with active dip mitigation.

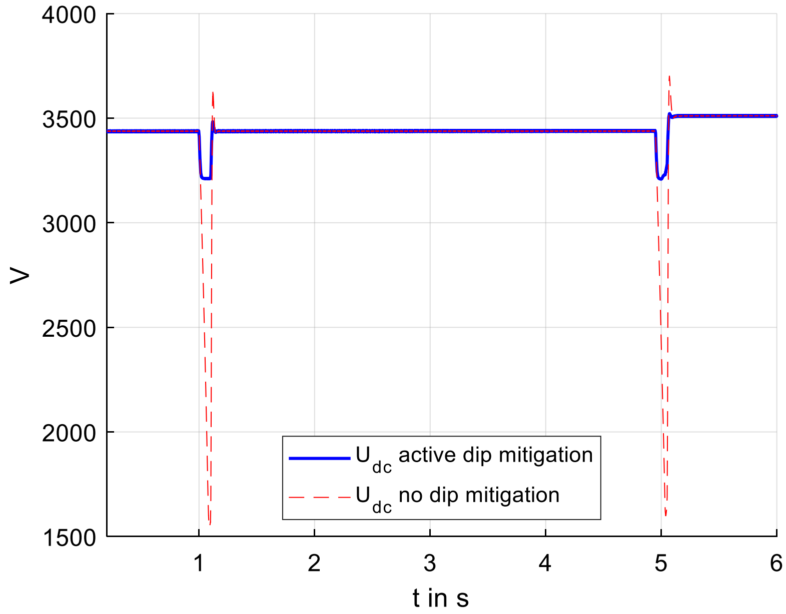

Figure 80: Comparison of the DC grid voltage, with and without active dip mitigation.

As the converter input capacitors are kept almost charged, high recharge currents after the voltage dip are avoided. No overcurrent protection will be triggered.

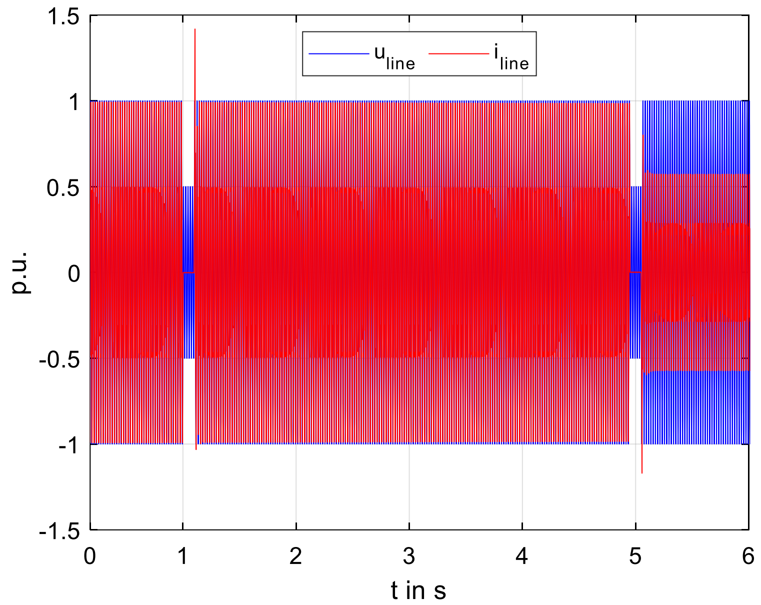

Figure 81: Line current and line voltage at the 36 kV level with active dip mitigation.

The re-charging currents are kept below 1.5 p.u. of the line current.

7.3.5 Conclusions

Very severe voltage dips are mitigated with the proposed dipole converter control system and the universal DC grid runs successfully through the fault. Even dips happening at the challenging transition phase from the ramp up to the flat top are handled by the control system.

Almost no discharge of the input capacitors (and thus of the whole DC bus) is observed and high re-charging currents are avoided. Thus no tripping of overcurrent protection relays is occurring. The overall DC power system is optimised as the integrated battery energy storage is used in a double sense.

The proposed method requires adequate rating of stage 2, in order to power the other load connected to the DC bus. Further the battery must have sufficient power density.

In terms of energy storage capacity, chapter 6.9 gives the minimum required capacity needed to cover the power peaks during the magnet ramp up. This capacity is easily sufficient to cover also the energy needed to mitigate the transient voltage dip.

8 Conclusion and discussion

The conclusions are drawn under the primary research question “What is the optimised power system design for FCC?”.

To answer this, FCC is actually analysed from a load side perspective, by looking below the 36kV level and focusing on the most challenging loads, which are the main bending dipoles and the cryogenic compressors. The final converter design for the main bending dipoles – the MPS variant C – has integrated energy storage for power peak shaving and the DC supplied ISOP converter leads to a reduction of space and weight of the equipment installed. The topology can also be used for other magnets (lattice and insertion type), and the complete powering topology for the main bending dipoles can also be extended to power even the cryogenic compressors and provide dip immunity to any dip sensitive load.

AC vs. DC power system design

Any power system design for a future research infrastructure needs to evaluate upcoming technologies which promise advantages. DC-based power systems have advantages against AC depending on the load (or application) and its constraints. The space restrictions in the underground and the hard accessibility, makes a DC based surface-underground power transfer favourable. Savings in space demand and equipment weight are realised. A ISOP converter module with middle frequency components and DC supply saves more than 50% of space and weight, compared to the AC variant with 50 Hz components. A supply with a DC grid has the great advantage of avoiding power imbalances when connection the ISOP configured converter for the main bending dipoles, as these converters have a single-phase input stage. More importantly, synergies can be realised with a common DC grid. A central DC grid can power many loads and can also provide dip immunity if the DC grid is formed by a dedicated rectifier [56]. The rectifier is then designed as a robust unidirectional converter with boost stage. The compensation effect is realised by drawing high currents during the dip. Thus, attention must be paid to have enough short circuit power at the connection point.

Converter for the main bending magnets

The power system design for the main bending dipoles starts from the 36kV voltage level down to the low voltage output stage supplying the main bending magnet circuits. In total there are 100 main bending dipole circuits, each with its converter, located around the 98 km FCC tunnel. All converters need to operate simultaneously without tripping. This brings up the very first design requirement – reliability.

The reliability requirement is only achieved with modular converter topologies, using additional modules as hot spares. In particular, when a double redundant converter topology for the main bending dipoles is chosen, FCC achieves at least a 3-times higher reliability as LHC. The modular converter design can be considered also for other loads, depending on their required level of reliability.

To transfer high power into the underground on one side, and the specifically high current demand of the magnets, make input-series output parallel topologies very applicable. Due to the input-series connection a high voltage for high power transfer can be connected on the input side, and due to the output-parallel connection, a high current can be delivered. The optimised DC voltage level for the best powering variant – MPS variant C – lies in the range of 13-15kV. In this range the operational and fault current levels can be handled by available equipment, and keeping on the other hand the insulation stress of ISOP converter input stages as low as possible.

To cover the power peaks, which arise from the dipole ramping, energy storage needs to be considered. With the integrated energy storage, instabilities as analysed in the chapter peak power discussion are also mitigated without the need to consider the available short circuit power at the point of common connection. Another advantage of the modular topology (besides the high reliability) is concerning the integration of battery energy storage systems as they can best be connected to low DC voltage bus. The proposed powering topology offers a direct connection of the battery energy storage, without using a converter interface. The battery current is controlled by the main converter control.

The best powering topology for the main bending dipoles is the DC grid supplied solid state transformer in ISOP configuration – MPS variant C – as it has the lightest and smallest equipment. If the DC grid is formed by a unidirectional converter – MPS variant C* – it becomes also the cheapest powering variant.

Optimised integration of energy storage

When using the MPS variant C (or C*) a synergy lies in the usage of the integrated energy storage to provide dip immunity for other important loads of FCC. The first stage of the MPS is the actual DC grid. Other magnets and the cryogenic compressors can easily be added to the DC bus, if the rating of the rectifier is increased accordingly. When using the already installed energy storage for dip mitigation, the MPS reverses the power flow for a short time and takes energy out of the batteries to stabilise the DC bus. The only requirement is that the power rating of the second stage of the MPS needs to be adapted accordingly.

The capacity of the energy storage depends firstly on the actual peak power limitation of the transmission grid, and secondly on the ramping strategy. An algorithm is used to calculate the required minimum capacity. Further, the algorithm gives the investment cost optimised capacity and the corresponding optimised rating of the supplying infrastructure. As the costs for supplying infrastructure have been merely drawn at a certain moment from comparable power converters at CERN, their real costs might be different. However, the method of how the optimised power rating and energy storage capacity are derived remains valid in any case.

The energy storage costs have been used as a parameter to obtain the sensitive region of the optimisation. For the assumed supplying infrastructure and power converter costs in this work the following specific results are obtained. For constant voltage ramping the sensitive region is 100-600 €/kWh and for constant power ramping it is 100-300 €/kWh. If in the future when FCC is to be constructed, the energy storage costs are for example about 500 €/kWh, close attention to the optimisation should be paid if constant voltage ramping is chosen. In the case of constant power ramping, the optimisation is not sensitive and the energy storage capacity is then only governed by the power limitation of transmission grid.

Strategy for dip immunity

Power grid disturbances as transient voltage dips, which have their origin in the 400 kV grid, are to enter the FCC power supply. A dip leads to a variation of the voltage supply this leads consequently to a deviation of the particle beam orbit, until the protection system dumps the beam. The restart consumes time, which is lost time for physics data gathering. This type of disturbance is troubling CERN already now, and will also troubling the powering the FCC.

If one has a power converter supplied load, and the power converter of the load is dip sensitive i.e. it trips during a dip, then the most efficient measure is to act directly on the design of this very power converter. It is either the physical installation of energy storage or a software upgrade aiming for fault-ride-through capabilities. Thus, the final dip immunity strategy follows the concept of using the power converters which have to used anyway and give additional design recommendations (i.e. fault ride through capability), which the manufactures of the converters have to guarantee. The strategy is based in principle on three parts:

1. Analysis of dips in terms of duration, magnitude and frequency: this is important for dip immunity upgrades of the power converters.
2. Analysis of the actual dip sensible load of FCC: this shows all relevant loads which are affected by dips. From LHC experience and literature research it can be concluded that in most cases it is just the power converter itself which trips in the event of a dip, and only the warm magnets and cold compressors (both have a small power rating) are in connection with an actual sensitive process.
3. Possible countermeasures: for each load respectively each supplying power converter a solution is shown.

To 1.: The important conclusion is that the dips will happen with the same frequency, duration and magnitude as they are happening now. The reason is that FCC is small with respect to the 400 kV transmission grid, and the connection to two additional 400 kV substations does not “collect” additional voltage dips. This has been proofed by a dedicated dip simulation model, developed at Graz University of Technology, which was calibrated with data of dips measured at CERN.

To 2 and 3.: It must be evaluated if either the process itself is dip sensitive, or if just the supplying power converter is tripping. In both cases, the supplying power converter should be directly upgraded.

Super conducting main bending magnets: their time constant is long enough to withstand a voltage dip. The supplying converter needs to be upgraded in terms of fault ride through capabilities. Additionally, the integrated battery energy storage automatically makes any grid disturbance transparent to the load. An upgrade of the main bending power system – the MPS variant C – leads to a dip immune power supply for various and large loads of FCC.

All other super conducting magnets: The process itself is not sensitive to short voltage variations as the time constant is still long enough. However, the converter control needs to be sophisticated enough to run the converter through the fault. The main risk is that the converter itself trips to any failure (internal or external) and initiates a beam abort.

The radio frequency (RF) system has as power source klystrons, and klystrons in turn need a high DC voltage as input source. In the LHC the converter for the high DC voltage itself trips due to equipment overcurrent protection, and not due process sensitivity. For any future RF system MMC converters are the preferred choice as the voltage and power rating fits perfectly. MMCs can easily be designed to mitigate voltage dips, as they have integrated capacitor energy storage.

Warm magnets: Their short time constant (due to their low inductance) and also their special optical function constitutes them to the most dip sensitive load of FCC. Here no variation of the voltage on the magnet is allowed, thus an active dip mitigation is necessary. A possible solution is to design the supplying power converter with integrated capacitor energy storage. This was also the solution for the respective warm magnet supply of the LHC.

Cryogenic cold compressors

The cold compressors are in relation with a real dip sensitive process and their supplying adjustable speed drive (ASD) needs upgrades in form of (additional) energy storage to keep the output voltage perfectly stable. Their rating for the total FCC cryogenic system is in the order of some hundreds of kW.

Cryogenic warm compressors

The large warm compressor systems are all powered by ASDs and their total rating is about one third of FCC i.e. in the range of 200MW. The cooling process itself will not notice the dip. Due to the compressors heavy mass they have stored enough kinetic energy to run through the voltage dip. On the other side, the ASDs also need to run through the fault i.e. the under voltage protection (of the DC link) must not trip and also the overcurrent protection when recharging the DC link must not trip. Further the control needs to “pick up” the load at the end of the disturbance and continue with supplying the nominal mechanical torque. All design requirements for dip immunity of the ASD have been analysed and confirmed in the cryogenic compressor case study. The implemented ASD controller in the simulation model uses space vector modulation and direct torque control. During the voltage dip the ASD remains online without producing torque for the compressor, thus keeping also the DC link voltage on high level. Right after the voltage dip, the DC link capacitors safely recharge and the ASD continues with normal operation. The rotor speed only marginally slows down during the dip and within a second after dip is already back to nominal rotational speed.

Universal and dip immune DC grid

The points above show how to gain dip immunity for each load separately. Another option to guarantee full dip immunity for FCC is to form a universal and dip immune DC grid by upgrading the power supply for the main bending dipoles – the MPS variant C (or C*). The energy storage for peak power covering is also providing immunity against transient voltage dips, optimally for a large part of the FCC load. The case study for the dip immune universal DC grid proofs the concept and highlights also the good performance of the control strategy. When the DC voltage is undermining a certain threshold due to a voltage dip, stage 2 of the MPS starts drawing current out of the battery, thus sustaining the main DC bus. After the dip the DC capacitors of the ISOP converter input stages are safely recharging. This concept works also during the critical point when the transition from ramping mode to flat top is occurring. The DC grid has thus a great potential of playing a mayor role when designing a universal and dip immune power supply of FCC.

9 References

[1] CERN Courier, *A giant leap for physics – CERN Courier.* [Online]. Available: https://cerncourier.com/a/a-giant-leap-for-physics/ (accessed: Feb. 11 2021).

[2] CERN Courier, *CERN thinks bigger – CERN Courier.* [Online]. Available: https://cerncourier.com/a/cern-thinks-bigger/ (accessed: Feb. 11 2021).

[3] D. Bozzini, *Supply and distribution of electrical energy: FCC week 2017, Berlin.* [Online]. Available: https://indico.cern.ch/event/556692/contributions/2496901/attachments/1468815/2272040/Supply_and_Distribution_of_Electrical_Energy.pdf (accessed: Feb. 2 2021).

[4] D. Bozzini, *Conceptual powering layouts FCC-hh, FCC-ee and HE-LHC: FCC week 2018, Amsterdam.* [Online]. Available: https://indico.cern.ch/event/656491/contributions/2921119/ (accessed: Feb. 2 2021).

[5] A. Abada *et al.,* "FCC-hh : The Hadron Collider," *The European Physical Journal*, vol. 228, no. 4, pp. 755–1107, 2019.

[6] *About ARIES | ARIES.* [Online]. Available: https://aries.web.cern.ch/index.php/about-aries (accessed: Feb. 17 2021).

[7] *4th Workshop Energy for Sustainable Science at Research Infrastructures.* [Online]. Available: http://www.eli-np.ro/4ess/ (accessed: Feb. 17 2021).

[8] T. Höhn, *Application of Energy Storage in Power Converters for Particle Accelerators: 4th Workshop Energy for Sustainable Science at Research Infrastructures, 23-24 November 2017, Magurele, Romania.* [Online]. Available: https://indico.eli-np.ro/event/1/contributions/56/attachments/79/117/1_Presentation_ESS_in_PC_Thomas_Hoehn.pdf (accessed: Feb. 17 2021).

[9] M. Kempkes, I. Roth, M. P. Gaudreau, J. L. Lancelot, and P. Dupire, "Pulsed power systems for ESS klystrons," *Conference Proceedings - IEEE Applied Power Electronics Conference and Exposition - APEC*, 2015-Octob, pp. 1–4, 2015, doi: 10.1109/PPC.2015.7297036.

[10] M. Jankovic, A. Watson, J. Clare, P. Wheeler, and D. Aguglia, "Grid interface challenges and candidate solutions for the Compact Linear Collider's (CLIC) klystron modulators," *2013 IEEE 14th Workshop on Control and Modeling for Power Electronics, COMPEL 2013*, Clic, pp. 1–6, 2013, doi: 10.1109/PPC.2013.6627691.

[11] J. Tao *et al.,* "ITER coil power supply and distribution system," *IEEE Energy Conversion Congress and Exposition: Energy Conversion Innovation for a Clean Energy Future, ECCE 2011, Proceedings*, pp. 1–8, 2011, doi: 10.1109/SOFE.2011.6052201.

[12] E. Coulinge, J. P. Burnet, and D. Dujic, "High-current low-voltage power supplies for superconducting magnets," *Proceedings - 2018 IEEE 18th International Conference on*

Power Electronics and Motion Control, PEMC 2018, 2017-Decem, pp. 1–6, 2017, doi: 10.1109/PEE.2017.8171666.

[13] D. Salomonsson and A. Sannino, “Low-voltage DC distribution system for commercial power systems with sensitive electronic loads,” *IEEE Transactions on Power Delivery*, vol. 22, no. 3, pp. 1620–1627, 2007, doi: 10.1109/TPWRD.2006.883024.

[14] H. Kakigano, Y. Miura, and T. Ise, “Low-voltage bipolar-type dc microgrid for super high quality distribution,” *IEEE Transactions on Power Electronics*, vol. 25, no. 12, pp. 3066–3075, 2010, doi: 10.1109/TPEL.2010.2077682.

[15] A. Sannino, G. Postiglione, and M. H. Bollen, “Feasibility of a DC network for commercial facilities,” *IEEE Transactions on Industry Applications*, vol. 39, no. 5, pp. 1499–1507, 2003, doi: 10.1109/TIA.2003.816517.

[16] R. Billinton, *Reliability Evaluation of Power Systems*. Boston, MA: Springer, 1996.

[17] K. C. Kapur and M. Pecht, *Reliability engineering*. Hoboken, NJ: Wiley, 2014.

[18] S. Peyghami, F. Blaabjerg, and P. Palensky, “Incorporating Power Electronic Converters Reliability Into Modern Power System Reliability Analysis,” *IEEE Journal of Emerging and Selected Topics in Power Electronics*, vol. 9, no. 2, pp. 1668–1681, 2021, doi: 10.1109/JESTPE.2020.2967216.

[19] H. S. Chung, H. Wang, F. Blaabjerg, and M. Pecht, Eds., *Reliability of power electronic converter systems*. London: The Institution of Engineering and Technology, 2016.

[20] S. Yang, A. Bryant, P. Mawby, D. Xiang, L. Ran, and P. Tavner, “An Industry-Based Survey of Reliability in Power Electronic Converters,” *IEEE Transactions on Industry Applications*, vol. 47, no. 3, pp. 1441–1451, 2011, doi: 10.1109/TIA.2011.2124436.

[21] N. Barberis Negra, O. Holmstrm, B. Bak-Jensen, and P. Sorensen, “Aspects of Relevance in Offshore Wind Farm Reliability Assessment,” *IEEE Trans. On Energy Conversion*, vol. 22, no. 1, pp. 159–166, 2007, doi: 10.1109/TEC.2006.889610.

[22] M. Jankovic, “High power modular converters for grid interface applications,”

[23] M. Stieneker and R. W. de Doncker, “Medium-voltage DC distribution grids in urban areas,” *2013 IEEE 14th Workshop on Control and Modeling for Power Electronics, COMPEL 2013*, pp. 0–6, 2016, doi: 10.1109/PEDG.2016.7527045.

[24] M. Starke, L. M. Tolbert, and B. Ozpineci, Eds., *AC vs. DC distribution: A loss comparison*, 2008.

[25] D. Nilsson and A. Sannino, “Efficiency analysis of low-and medium-voltage DC distribution systems,” *Power Engineering Society General â€¦*, pp. 1–7, 2004, doi: 10.1109/PES.2004.1373299.

[26] F. Wang, Y. Pei, D. Boroyevich, R. Burgos, and K. Ngo, “Ac vs. dc distribution for off-shore power delivery,” *Power*, pp. 2113–2118, 2008, doi: 10.1109/IECON.2008.4758283.

[27] A. Verdicchio, P. Ladoux, H. Caron, and C. Courtois, “New Medium-Voltage DC Railway Electrification System,” *IEEE Transactions on Transportation Electrification*, vol. 4, no. 2, pp. 591–604, 2018, doi: 10.1109/TTE.2018.2826780.

[28] A. Gomez-Exposito, J. M. Mauricio, and J. M. Maza-Ortega, “VSC-Based MVDC railway electrification system,” *IEEE Transactions on Power Delivery*, vol. 29, no. 1, pp. 422–431, 2014, doi: 10.1109/TPWRD.2013.2268692.

[29] L. Abrahamsson, T. Kjellqvist, and S. Ã–stlund, “High-voltage DC-feeder solution for electric railways,” *IET Power Electronics*, vol. 5, no. 9, pp. 1776–1784, 2012, doi: 10.1049/iet-pel.2011.0219.

[30] J. Fabre, P. Ladoux, E. Solano, G. Gateau, and J. M. Blaquiere, “MVDC Three-Wire Supply Systems for Electric Railways: Design and Test of a Full SiC Multilevel Chopper,” *IEEE Transactions on Industry Applications*, vol. 53, no. 6, pp. 5820–5830, 2017, doi: 10.1109/TIA.2017.2747498.

[31] A. Verdicchio, P. Ladoux, H. Caron, and S. Sanchez, “Future DC Railway Electrification System - Go for 9 kV,” *Proceedings - 2018 IEEE 18th International Conference on Power Electronics and Motion Control, PEMC 2018*, pp. 1–5, 2019, doi: 10.1109/ESARS-ITEC.2018.8607304.

[32] R. M. Cuzner and G. Venkataramanan, “The status of DC micro-grid protection,” *Power*, pp. 1–8, 2008, doi: 10.1109/08IAS.2008.382.

[33] R. M. Cuzner and D. A. Esmaili, “Fault Tolerant Shipboard MVDC Architectures,” *2015 International Conference on Electrical Systems for Aircraft, Railway, Ship Propulsion and Road Vehicles (ESARS)*, pp. 1–6, 2015, doi: 10.1109/ESARS.2015.7101536.

[34] B. Z. Jin, G. Sulligoi, R. Cuzner, L. Meng, J. C. Vasquez, and J. M. Guerrero, “Next-Generation Shipboard DC Power System,” pp. 45–57, 2016, doi: 10.1109/MELE.2016.2544203.

[35] A. Q. Huang, “Medium-Voltage Solid-State Transformer: Technology for a Smarter and Resilient Grid,” *IEEE Industrial Electronics Magazine*, vol. 10, no. 3, pp. 29–42, 2016, doi: 10.1109/MIE.2016.2589061.

[36] A. Q. Huang and R. Burgos, “Review of Solid-State Transformer Technologies and Their Application in Power Distribution Systems,” *IEEE Journal of Emerging and Selected Topics in Power Electronics*, vol. 1, no. 3, pp. 186–198, 2013, doi: 10.1109/JESTPE.2013.2277917.

[37] J. E. Huber and J. W. Kolar, “Volume/weight/cost comparison of a 1MVA 10 kV/400 V solid-state against a conventional low-frequency distribution transformer,” *Conference Proceedings - IEEE Applied Power Electronics Conference and Exposition - APEC*, pp. 4545–4552, 2014, doi: 10.1109/ECCE.2014.6954023.

[38] J. E. Huber and J. W. Kolar, “Solid-State Transformers: On the Origins and Evolution of Key Concepts,” *IEEE Industrial Electronics Magazine*, vol. 10, no. 3, pp. 19–28, 2016, doi: 10.1109/MIE.2016.2588878.

[39] M. Steiner and H. Reinold, “Medium frequency topology in railway applications,” *2007 European Conference on Power Electronics and Applications, EPE*, 2007, doi: 10.1109/EPE.2007.4417570.

[40] S. M. Mousavi Gazafrudi, A. Tabakhpour Langerudy, E. F. Fuchs, and K. Al-Haddad, “Power Quality Issues in Railway Electrification: A Comprehensive Perspective,” *IEEE Transactions on Industrial Electronics*, vol. 62, no. 5, pp. 3081–3090, 2015, doi: 10.1109/TIE.2014.2386794.

[41] C. Zhao *et al.,* “Power electronic traction transformer-medium voltage prototype,” *IEEE Transactions on Industrial Electronics*, vol. 61, no. 7, pp. 3257–3268, 2014, doi: 10.1109/TIE.2013.2278960.

[42] X. He, J. U. N. Peng, and S. Member, “A Novel Advanced Traction Power Supply System Based on Modular Multilevel Converter,” *IEEE Access*, vol. 7, pp. 165018–165028, 2019, doi: 10.1109/ACCESS.2019.2949099.

[43] M. Stieneker, *Analysis of Medium-Voltage Direct-Current Collector Grids in Offshore Wind Parks*: E.ON Energy Research Center, RWTH Aachen University, 2017. Accessed: Feb. 9 2021. [Online]. Available: http://publications.rwth-aachen.de/record/689894/files/689894.pdf

[44] A. Kara, D. Amhof, P. Dahler, Ag, A B B, and H. Gruning, “Power supply quality improvement with a dynamic voltage restorer (DVR),” *APEC '98 Thirteenth Annual Applied Power Electronics Conference and Exposition*, pp. 986–993, 1998.

[45] Dirk Vandeplassche, Jean-Luc Biarrotte, Holger Podlech, and Horst Klein, *The myrrha linear accelerator*, 2011. [Online]. Available: https://www.researchgate.net/publication/266461795_The_myrrha_linear_accelerator

[46] I. Josifovic *et al.,* “A 600 kW Power Supply for Particle Accelerators Insensitive to Electrical Network Perturbations Acknowledgments Keywords,” *2016 18th European Conference on Power Electronics and Applications, EPE 2016 ECCE Europe*, pp. 1–10.

[47] “Design and Experimentation of a Dynamic Voltage Restorer Capable of Significantly Reducing an Energy-Storage Element,” vol. 44, 2008.

[48] J. G. Nielsen, F. Blaabjerg, and N. Mohan, “Control strategies for dynamic voltage restorer compensating voltage sags with phase jump,” *APEC 2001. Sixteenth Annual IEEE Applied Power Electronics Conference and Exposition (Cat. No.01CH37181)*, vol. 2, pp. 1267–1273, 2001, doi: 10.1109/APEC.2001.912528.

[49] J. G. Nielsen and F. Blaabjerg, “A detailed comparison of system topologies for dynamic voltage restorers,” *IEEE Transactions on Industry Applications*, vol. 41, no. 5, pp. 1272–1280, 2005, doi: 10.1109/TIA.2005.855045.

[50] “Multiterminal HVDC systems in urban areas of large cities,” vol. 13, 1998.

[51] W. Lu and B. Ooi, “Premium Quality Power Park Based on Multi-Terminal HVDC,” vol. 20, no. 2, pp. 978–983, 2005.

[52] C. Du, S. Member, M. H. J. Bollen, and E. Agneholm, “A New Control Strategy of a VSC â€“ HVDC System for High-Quality Supply of Industrial Plants,” *IEEE Transactions on Power Delivery*, vol. 22, no. 4, pp. 2386–2394, 2007.

[53] T. Hoehn, T. Slettbakk, F. Blanquez, K. Kahle, and J. Burnet, “Back-to-Back HVDC Modular Multilevel Converter for Transient Voltage Dip Mitigation in Passive Networks,” in *2019 21st European Conference on Power Electronics and Applications (EPE '19 ECCE Europe)*, 2019, P.1-P.10.

[54] M. Saeedifard and R. Iravani, “Dynamic performance of a modular multilevel back-to-back HVDC system,” *IEEE Transactions on Power Delivery*, 2010, doi: 10.1109/TPWRD.2010.2050787.

[55] D. Roiu, R. Bojoi, L. R. Limongi, and A. Tenconi, “Dynamic Performance of Grid Connected AC / DC Voltage Source Converter under Voltage Dips Transient Conditions,” *Power*, pp. 2794–2800, 2009.

[56] T. Hoehn, F. Blanquez, K. Kahle, J. -P. Burnet, and H. Renner, “Voltage Dip Mitigation Techniques for Medium-Voltage DC Networks,” in *2019 IEEE Third International Conference on DC Microgrids (ICDCM)*, 2019, pp. 1–7.

[57] M. Prioli, *Dipole circuit layout and protection for FCC-hh: FCC week 2018, Amsterdam.* [Online]. Available: https://indico.cern.ch/event/656491/contributions/2947278/attachments/1630615/2599139/Circuit_layout_and_protection_Prioli.pptx (accessed: Feb. 9 2021).

[58] O. Bruening, “Mechanisms for Beam Losses and their Time Constants,” *Chamonix XI*, pp. 264–269.

[59] C. Wan, M. Huang, C. K. Tse, S. C. Wong, and X. Ruan, “Nonlinear behavior and instability in a three-phase boost rectifier connected to a nonideal power grid with an interacting load,” *2012 IEEE Energy Conversion Congress and Exposition (ECCE)*, vol. 28, no. 7, pp. 3255–3265, 2013, doi: 10.1109/TPEL.2012.2227505.

[60] F. R. Blanquez, T. Höhn, K. Kahle, and J. Burnet, “FCC magnet powering concepts and requirements,” *EDMS: 2113162*, 2018. [Online]. Available: https://indico.cern.ch/event/656491/contributions/2947279/attachments/1631201/2601864/Magnet_Powering_Concepts_TEEPC__FCCWeek2018.pdf
#search=blanquez%20AND%20EventID%3A656491

[61] C. Kotnig, “Analysis and Design of the Cryogenic System of the Future Circular Collider CERN-THESIS-2018-085,” June, 2018.

[62] M. Chorowski *et al.,* “Towards the conceptual design of the cryogenic system of the Future Circular Collider (FCC),” *IOP Conference Series: Materials Science and Engineering*, vol. 278, no. 1, 2017, doi: 10.1088/1757-899X/278/1/012097.

[63] *Pulling together: Superconducting electromagnets | CERN.* [Online]. Available: https://home.cern/science/engineering/pulling-together-superconducting-electromagnets (accessed: Mar. 8 2021).

[64] F. Bordry and H. Thiesen, “LHC inner triplet powering strategy,” in *PACS2001. Proceedings of the 2001 Particle Accelerator Conference (Cat. No.01CH37268)*, 2001, 633-635 vol.1.

[65] K. Sharifabadi, L. Harnefors, H. P. Nee, S. Norrga, and R. Teodorescu, “Design, control and application of modular multilevel converters for HVDC transmission systems,” *Design, Control and Application of Modular Multilevel Converters for HVDC Transmission Systems*, pp. 1–386, 2016, doi: 10.1002/9781118851555.

[66] “Nexans: Power Cables 1 – 30 kV,” vol. 2012. [Online]. Available: https://www.nexans.de/eservice/Germany-de_DE/fileLibrary/Download_540171919/Germany/files/Starkstrom_DuGB_12okt12_klein.pdf

[67] L. Felsberger, B. Todd, and D. KranzlmÃ¼ller, “Cost and Availability Improvements for Fault-Tolerant Systems Through Optimal Load-Sharing Policies,” *Procedia Computer Science*, 2019, doi: 10.1016/j.procs.2019.04.080.

[68] R. Alemany Fernandez *et al.,* “FCC-hh turn-around cycle,” December, 2016. [Online]. Available: https://cds.cern.ch/record/2239138?ln=en

[69] P. W. Hammond, “A new approach to enhance power quality for medium voltage AC drives,” *IEEE Trans. on Ind. Applicat.*, vol. 33, no. 1, pp. 202–208, 1997, doi: 10.1109/28.567113.

[70] N. Hildebrandt and D. Dujić, “Supply Grid Synchronization and Operation of a Filterless Cascaded H-Bridge based Grid Emulator,” in *IECON 2019 - 45th Annual Conference of the IEEE Industrial Electronics Society*, 2019, pp. 5769–5774.

[71] D. DujiÄ‡, F. Kieferndorf, and F. Canales, “Power electronic transformer technology for traction applications-An overview,” *Electronics*, vol. 16, no. 1, pp. 50–56, 2012, doi: 10.7251/ELS1216050D.

[72] R. Burkart and J. W. Kolar, “Component cost models for multi-objective optimizations of switched-mode power converters,” *Conference Proceedings - IEEE Applied Power Electronics Conference and Exposition - APEC*, pp. 2139–2146, 2013, doi: 10.1109/ECCE.2013.6646971.

[73] J. E. Huber, D. Rothmund, and J. W. Kolar, “Comparative evaluation of isolated front end and isolated back end multi-cell SSTs,” *ECCE 2016 - IEEE Energy Conversion Congress and Exposition, Proceedings*, pp. 3536–3545, 2016, doi: 10.1109/IPEMC.2016.7512863.

[74] E+I Engineering | Electrical Engineering Solutions, *High Powerbar (Europe) | E+I Engineering | Electrical Engineering Solutions.* [Online]. Available: https://www.e-i-eng.com/hpb-eu/ (accessed: Mar. 11 2021).

[75] Eaton, *W-VACi Medium Voltage Circuit Breakers.* [Online]. Available: https://www.eaton.com/SEAsia/ProductsSolutions/Electrical/ProductsServices/PowerDistributionComponents/MediumVoltageCircuitBreakers/W-VACiMediumVoltageCircuitBreakers/index.htm#tabs-3 (accessed: Mar. 11 2021).

[76] J. E. Quiroz, S. N. Laboratories, and M. J. Reno, “DC Microgrid Protection : Review and Challenges DC Microgrid Protection : Review and Challenges,” August, 2018.

[77] Sécheron, *DC circuit breakers for other industries - Sécheron.* [Online]. Available: https://www.secheron.com/products-solutions/ess/dc-circuit-breakers/for-other-industries/ (accessed: Mar. 11 2021).

[78] M. Heidemann, G. Nikolic, A. Schnettler, A. Qawasmi, N. Soltau, and R. W. de Donker, “Circuit-breakers for medium-voltage DC grids,” *2016 IEEE PES Transmission & Distribution Conference and Exposition-Latin America (PES T&D-LA)*, Mmc, pp. 1–6, 2016, doi: 10.1109/TDC-LA.2016.7914153.

[79] M. Brenna, F. Foiadelli, and D. Zaninelli, *Electrical railway transportation systems*. Hoboken, New Jersey: Wiley IEEE Press, 2018. [Online]. Available: https://onlinelibrary.wiley.com/doi/book/10.1002/9781119386827

[80] R. D. White, “AC/DC Railway Electrification and Protection,” in *IET 13th Professional Development Course on Electric Traction Systems*, 2014, pp. 1–42.

[81] ALSTOM, *Hesop: Saving energy and costs in a single solution.* [Online]. Available: https://www.alstom.com/our-solutions/infrastructure/hesop-saving-energy-and-costs-single-solution (accessed: Mar. 18 2021).

[82] A. Verdicchio, P. Ladoux, H. Caron, and C. Courtois, “New Medium-Voltage DC Railway Electrification System,” *IEEE Transactions on Transportation Electrification*, vol. 4, no. 2, pp. 591–604, 2018, doi: 10.1109/TTE.2018.2826780.

[83] D. Lawes, L. Ran, and Z. Xu, “Design of a Solid-State D . C . Circuit Breaker for Light Rail Transit Power Supply Network,” *2015 International Conference on Electrical Systems for Aircraft, Railway, Ship Propulsion and Road Vehicles (ESARS)*, pp. 350–357, 2014, doi: 10.1109/ECCE.2014.6953414.

[84] J. Yang, J. E. Fletcher, and J. O'Reilly, “Multiterminal DC Wind Farm Collection Grid Internal Fault Analysis and Protection Design,” *IEEE Transactions on Power Delivery*, vol. 25, no. 4, pp. 2308–2318, 2010, doi: 10.1109/TPWRD.2010.2044813.

[85] L. Tang and B. T. Ooi, “Locating and isolating DC faults in multi-terminal DC systems,” *IEEE Transactions on Power Delivery*, vol. 22, no. 3, pp. 1877–1884, 2007, doi: 10.1109/TPWRD.2007.899276.

[86] M. E. Baran and N. R. Mahajan, “Overcurrent Protection on Voltage-Source-Converter-Based Multiterminal DC Distribution Systems,” *IEEE Trans. Power Delivery*, vol. 22, no. 1, pp. 406–412, 2007, doi: 10.1109/TPWRD.2006.877086.

[87] M. Thong, A. Cheong, and H. Wijaya, “Overview of DC traction protection scheme for Singapore rapid transit system,” *2005 International Power Engineering Conference*, pp. 1–587, 2005, doi: 10.1109/IPEC.2005.206975.

[88] E. Cinieri, A. Fumi, V. Salvatori, and C. Spalvieri, “A new high-speed digital relay protection of the 3-kVdc electric railway lines,” *IEEE Transactions on Power Delivery*, vol. 22, no. 4, pp. 2262–2270, 2007, doi: 10.1109/TPWRD.2007.898585.

[89] J. D. Park, “Ground fault detection and location for ungrounded DC traction power systems,” *IEEE Transactions on Vehicular Technology*, vol. 64, no. 12, pp. 5667–5676, 2015, doi: 10.1109/TVT.2015.2388785.

[90] X. Zhang, H. Peng, H. Wang, and M. Ouyang, “Hybrid Lithium Iron Phosphate Battery and Lithium Titanate Battery Systems for Electric Buses,” *IEEE Transactions on Vehicular Technology*, vol. 67, no. 2, pp. 956–965, 2018, doi: 10.1109/TVT.2017.2749882.

[91] J. McLaren, P. Gagnon, K. Anderson, E. Elgqvist, R. Fu, and T. Remo, “Battery Energy Storage Market: Commercial Scale, Lithium-ion Projects in the U.S,” *Large Energy Storage Systems Handbook*, pp. 153–181, 2016.

[92] R. Fu, T. Remo, and R. Margolis, “2018 U . S . Utility-Scale Photovoltaics- Plus-Energy Storage System Costs Benchmark,” *National Renewable Energy Laboratory*, November, p. 32, 2018. [Online]. Available: https://www.nrel.gov/docs/fy19osti/ 71714.pdf.%0Ahttps://www.nrel.gov/docs/fy19osti/71714.pdf

[93] W. Cole and A. W. Frazier, “Cost Projections for Utility- S cale Battery Storage Cost Projections for Utility- S cale Battery Storage,” *Nrel*, June, 2019.

[94] W. Cole and A. W. Frazier, “Cost Projections for Utility-Scale Battery Storage : 2020 Update Cost Projections for Utility-Scale Battery Storage : 2020 Update,” June, 2020.

[95] *2016 California Fire Code Amendments for Battery Storage (002).pdf*.

[96] A. F. Blum and T. Long, JR., “Hazard Assessment of Lithium Ion Battery Energy Storage Systems,” *Fire Hazard Assessment of Lithium Ion Battery*, February, pp. 5–28, 2016, doi: 10.1007/978-1-4939-6556-4.

[97] "International standard, IEC 62619: Secondary cells and batteries containing alkaline or other non-acid electrolytes – Safety requirements for secondary lithium cells and batteries, for use in industrial applications," *VDE*, 2017.

[98] *Technical Data Distribution Transformers TUNORMA and TUMETIC: Siemens Power Engineering Guide.* [Online]. Available: http://www.tekhar.com/Programma/Siemens/SIVACON_SICUBE/pict/Tunorma.pdf (accessed: Feb. 12 2021).

[99] H. Renner and M. Sakulin, "Calculation of voltage dips in meshed grids," in *2004 11th International Conference on Harmonics and Quality of Power: Lake Placid, NY, 12 - 15 September, 2004*, Lake Placid, NY, USA, 2004, pp. 666–671.

[100] P. Enjeti and S. M. Ieee, "A Low Cost Approach to Improve the Performance of an Adjustable Speed Drive (ASD) under Voltage Sags and Short-Term Power Interruptions," *APEC '98 Thirteenth Annual Applied Power Electronics Conference and Exposition*, pp. 587–591, 1998.

[101] A. von Jouanne, P. N. Enjeti, S. Member, and B. Banerjee, "Assessment of Ride-Through Alternatives for Adjustable-Speed Drives," September 2016, 1999, doi: 10.1109/28.777200.

[102] M. Bongiorno, "Control of Voltage Source Converters for Voltage Dip Mitigation in Shunt and Series Configurations Department of Electric Power Engineering," 2004.

[103] M. H. J. Bollen, *Understanding power quality problems: Voltage sags and interruptions*. New York, Hoboken, New Jersey, Piscataway, New Jersey: IEEE Wiley-Interscience; IEEE Xplore, 1999.

[104] MAN Energy Solutions, *MAN Energy Solutions sealed HOFIM and MOPICO compressors.* [Online]. Available: https://www.man-es.com/oil-gas/products/compressors/sealed-compressor (accessed: Mar. 2 2021).

[105] M. Hiller, D. Krug, R. Sommer, and S. Rohner, "A new highly modular medium voltage converter topology for industrial drive applications," *Power*, Cc, pp. 1–10, 2009.

[106] S. Inoue and H. Akagi, "A bidirectional isolated dc-dc converter as a core circuit of the next-generation medium-voltage power conversion system," *IEEE Transactions on Industrial Electronics*, vol. 22, no. 2, pp. 535–542, 2007, doi: 10.1109/TPEL.2006.889939.

[107] F. Khoucha, S. M. Lagoun, K. Marouani, A. Kheloui, and M. E. H. Benbouzid, "Hybrid cascaded H-bridge multilevel-inverter induction-motor-drive direct torque control for automotive applications," *IEEE Transactions on Industrial Electronics*, vol. 57, no. 3, pp. 892–899, 2010, doi: 10.1109/TIE.2009.2037105.

[108] N. M. Nordin, N. R. Idris, and N. A. Azli, "Direct torque control with 5-level cascaded H-bridge multilevel inverter for induction machines," *Proceedings of the 2011 14th*

European Conference on Power Electronics and Applications, EPE 2011, pp. 4691–4697, 2011, doi: 10.1109/IECON.2011.6120084.

[109] W. Song and A. Q. Huang, “Fault-tolerant design and control strategy for cascaded H-bridge multilevel converter-based STATCOM,” *IEEE Transactions on Industrial Electronics*, vol. 57, no. 8, pp. 2700–2708, 2010, doi: 10.1109/TIE.2009.2036019.

[110] S. Khomfoi, L. M. Tolbert, and B. Ozpineci, “Cascaded H-bridge multilevel inverter drives operating under faulty condition with AI-based fault diagnosis and reconfiguration,” *Proceedings of IEEE International Electric Machines and Drives Conference, IEMDC 2007*, vol. 2, pp. 1649–1656, 2007, doi: 10.1109/IEMDC.2007.383677.

[111] J. E. Huber and J. W. Kolar, “Optimum Number of Cascaded Cells for High-Power Medium-Voltage AC-DC Converters,” *2015 International Conference on Electrical Systems for Aircraft, Railway, Ship Propulsion and Road Vehicles (ESARS)*, vol. 5, no. 1, pp. 213–232, 2017, doi: 10.1109/JESTPE.2016.2605702.

[112] L. G. Franquelo, J. Rodriguez, J. I. Leon, S. Kouro, R. Portillo, and M. A. Prats, “The age of multilevel converters arrives,” *IEEE Industrial Electronics Magazine*, vol. 2, no. 2, pp. 28–39, 2008, doi: 10.1109/MIE.2008.923519.

[113] “ABB drives ACS5000 2 to 36 MW,” [Online]. Available: https://library.e.abb.com/public/3775bd6155454c3ea2f6479933965d5f/ACS5000_medium_voltage_drive_catalog_3BHT490501R0001_RevK_EN.pdf

[114] “SINAMICS PERFECT HARMONY GH180,” 2018.

[115] WEG, “MVW3000 - MEDIUM VOLTAGE,”

[116] R. Gottkehaskamp, “Electrical design of high-speed induction motors of up to 15 MW and 20000,” July 2002, 2018, doi: 10.1049/cp.

[117] B. Bose and B. K. Bose, *Modern Power Electronics and AC Drives // Modern power electronics and AC drives*. Upper Saddle River, NJ: Prentice Hall.

[118] ABB, “High voltage general purpose motors: Technical catalog,” [Online]. Available: https://library.e.abb.com/public/02d0c32655ce4afb8813182c6fc4623f/HV_CTO_catalog_9AKK107307_RevC_EN_09-2020_lower.pdf

[119] H. Bai and C. Mi, “Eliminate reactive power and increase system efficiency of isolated bidirectional dual-active-bridge dc-dc converters using novel dual-phase-shift control,” *IEEE Transactions on Power Electronics*, vol. 23, no. 6, pp. 2905–2914, 2008, doi: 10.1109/TPEL.2008.2005103.

[120] B. Zhao, Q. Song, and W. Liu, “Power Characterization of Isolated Bidirectional Dual-Active-Bridge DC–DC Converter With Dual-Phase-Shift Control,” *IEEE Transactions on Power Electronics*, vol. 27, no. 9, pp. 4172–4176, 2012, doi: 10.1109/TPEL.2012.2189586.

[121] W. Chen, K. Zhuang, and X. Ruan, “A Input-Series- and Output-Parallel-Connected Inverter System for High-Input-Voltage Applications,” *IEEE Transactions on Power Electronics*, vol. 24, no. 9, pp. 2127–2137, 2009, doi: 10.1109/TPEL.2009.2019578.

[122] R. Ayyanar, R. Giri, and N. Mohan, “Active input-voltage and load-current sharing in input-series and output-parallel connected modular dc-dc converters using dynamic input-voltage reference scheme,” *IEEE Transactions on Power Electronics*, vol. 19, no. 6, pp. 1462–1473, 2004, doi: 10.1109/TPEL.2004.836671.

[123] A. Verweij, *Status of FCC-hhmain magnet circuit layout, powering and protection.* [Online]. Available: https://indico.cern.ch/event/727555/contributions/3452831/attachments/1870059/3077208/Circuit_layout_and_protection_Verweij.pdf

[124] H. Akagi, T. Yamagishi, N. M. L. Tan, Y. Miyazaki, S. I. Kinouchi, and M. Koyama, “Power-loss breakdown of a 750-V 100-kW 20-kHz bidirectional isolated DC-DC converter using SiC-MOSFET/SBD dual modules,” *IEEE Transactions on Industry Applications*, vol. 51, no. 1, pp. 420–428, 2015, doi: 10.1109/TIA.2014.2331426.

[125] U. Nicolai, “Determining Switching Losses of SEMIKRON IGBT Modules,” *Application note AN1403*, pp. 1–15, 2014. [Online]. Available: https://www.semikron.com/de/service-support/downloads/detail/semikron-application-note-determining-switching-losses-of-semikron-igbt-modules-en-2014-08-19-rev-00.html

[126] S. Mao, T. Wu, X. Lu, J. Popovic, and J. A. Ferreira, “Three-phase active front-end rectifier efficiency improvement with silicon carbide power semiconductor devices,” *ECCE 2016 - IEEE Energy Conversion Congress and Exposition, Proceedings*, 2016, doi: 10.1109/ECCE.2016.7855515.

[127] T. Tevetoglu, “Production Quality and Reliability Demnstration,” *EDMS 1837569*, 2017, doi: 10.1017/CBO9781107415324.004.

[128] J. Schwenk, “Evaluation and improvement of the design for reliability process of the FGClite,” *EDMS 2025801*, 2018.

[129] *Specifications / Oil immersed Transformer / Fuji Electric Global.* [Online]. Available: https://www.fujielectric.com/products/oil-immersed_transformer/specifications.html (accessed: Feb. 12 2021).

[130] “Cast Resin Transformers,” [Online]. Available: www.sgb-smit.com

[131] J. Taufiq, “Power electronics technologies for railway vehicles,” *Fourth Power Conversion Conference-NAGOYA, PCC-NAGOYA 2007 - Conference Proceedings*, pp. 1388–1393, 2007, doi: 10.1109/PCCON.2007.373146.

[132] J. W. Kolar, “Converter for Telecom Applications,” *Power*, pp. 824–831, 2007.

[133] J. Biela, D. Aggeler, S. Inoue, H. Akagi, and J. W. Kolar, “Bi-directional isolated DC-DC converter for next-generation power distribution - Comparison of converters using Si

and SiC devices," *IEEJ Transactions on Industry Applications*, vol. 128, no. 7, pp. 1–10, 2008, doi: 10.1541/ieejias.128.901.

[134] G. Ortiz, D. Bortis, S. Member, J. Biela, J. W. Kolar, and S. Member, "Optimal Design of a 3 . 5-kV / 11-kW DC â€“ DC Converter for Charging Capacitor Banks of Power Modulators,"

[135] M. Claesens, D. Dujic, F. Canales, J. K. Steinke, P. Stefanutti, and C. Veterli, "Traction transformation: A power-electronic traction transformer (PETT)," *ABB Review*, no. 1, pp. 11–17, 2012.

[136] M. Jaritz and J. Biela, "Optimal design of a modular series parallel resonant converter for a solid state 2.88 MW/115-kV long pulse modulator," *IEEE Transactions on Plasma Science*, vol. 42, no. 10, pp. 3014–3022, 2014, doi: 10.1109/TPS.2014.2332880.

10 Appendix

10.1 Stability analysis at a powering point of FCC

To show the instability occurrence, the equivalent circuit shown below was used. As an aggregated model, it represents all ten converters to power the total magnet circuit load.

In the simulation model, all voltages will be referred to the low voltage side of the converter transformer, which is U_{source}=150 V (line to neutral).

The following per unit system and parameters have been used to trigger the instability:

Table 30: Per unit system used for the simulation model

Base for p.u. system DC side (aggregated converter model)		
Base power	P_{DC}=30 MW (or 30 MVA)	Power at the DC load
Base voltage	U_{DC}=500 V	Bus voltage
Base current (the aggregated value is taken here)	$I_{DC}=P_{DC}/U_{DC}$=60 kA	Load current
Base for p.u. system AC side		
Base power per phase	$P_{AC} = P_{DC}/3$ = 10 MVA	
Base voltage, the low voltage side of the converter transformer is the reference	U_{source}=150 V	line-to-neutral voltage
Base current	$I_{AFE\_1} = P_{AC}/U_{source}$=66,67 kA	current flowing into the AFE at terminal 1 (aggregated value)
Base impedance	$Z_{base}=U_{source}/I_{AFE\_1}$=2.25 mΩ	
Base inductance	$L_{base}=Z_{base}/(2*pi*50)$=7.17 µH	

Table 31: Simulation model parameters

Reference voltage is the low voltage side of the converter transformer U_{source}=150 V (line to neutral); Note: the ohmic resistance of the transformer windings has been neglected in the conversion from u_k to X_T			
		remarks	Values for inductances of L_{source} and L_{filter}
SCC at 135 kV level	600 MVA (200 MVA per phase)	=20 p.u. (of P_{AC})	X_{SCC} in p.u.=1/20=0.05 p.u. of Z_{base} X_{SCC}= 0.1125 mΩ
Main transformer	90 MVA, u_k=15% (30 MVA per phase)	Base power is 3-times higher, → Z_{base} has to be divided by 3	X_T in p.u.= 1/3*15% =0.05 p.u. of Z_{base} X_T = 0.1125 mΩ
L_{source} is the sum of the grid equivalent inductance (SCC) and the transformer inductance			ΣX =225 µΩ → L_{source}=0.72 µH
Converter transformer	30 MVA, u_k=7% (10 MVA per phase)	Same base power	X_T in p.u.= 7%= 0.07 p.u. of Z_{base} X_T = 0.158 mΩ
Filter for AFE	Filter inductance = 0.1 p.u.	POPS[42] AFE has a filter of 0.14 p.u. with U_{20}=1950 V and $P_{3\text{-}phase}$=2.5 MVA	$X_{AFE\ filter}$ in p.u.= 0.1 p.u. of Z_{base} X_{AFE}=0.225 mΩ
L_{filter} is the sum of the converter transformer inductance and the AFE dedicated filter inductance			ΣX =383 µΩ → L_{filter}=1.22 µH
Additional load	P = 60 MW + Q= 15 MVAr	P=2 p.u. of P_{DC} Q=0.5 p.u. of P_{DC}	

The cause for the breakdown is a mismatch of active power needed on the DC side and active power which could be transferred over the grid connection. As the DC voltage will start to drop, the reference for Id will increase more and more until the line current Id goes into limitation. Thus the DC voltage continues to drop and the converter goes into the non-linear operation of over modulation, which means in this case that the PWM signal will drop pulses. The converter actually is then consuming mainly reactive power from the grid, and the converter cannot come back to normal operation by just reducing the load parameters.

[42] POPS stands for Power system for PS (Proton synchrotron at CERN) main magnets. The topology of this converter has an AFE as input stage.

10.2 Calibration for the voltage dip simulation model, predicting the number of dips at the FCC powering

For the calibration actual measured dip data from CERN is used. This data comprises the location of the dip (in accordance with the transmission grid operation RTE), the duration and the magnitude.

The CERN data is extracted from the accelerator fault tracker (AFT) and the TI logbook.

Both, the simulation and measurement are with respect to voltage at the CERN distribution grid.

Table 32: Comparison of measured dip data and the simulation model results

Date and location of the dip	Measurement	Simulation
22. May 2011, 400 kV line Albertville – Rondissone; monophase	-7% of $U_{nominal}$ for 70 ms measured at LHC	Between 90-80% of $U_{nominal}$
28. May 2011, 225 kV line Cize – Fleyriat; monophase; four successive	-9%/60 ms -6%/70 ms -6%/65 ms -6%/70 ms, measured at LHC	Above 90% of $U_{nominal}$
1. May 2012, 400 kV line Chamoson – Bois-Tollot; two successive two-phase dips	-38%/70 ms then after 1400 ms -44%/100 ms, measured at LHC	Between 50-20% of $U_{nominal}$
7. Mai 2012 400 kV Charpenay – St Vulbas n2	-9%/60 ms measured at LHC	Above 90% of $U_{nominal}$
8. July 2012 400 kV Bayet – Grepilles – Charpenay	-8%/60 ms measured at LHC	Above 90% of $U_{nominal}$
24. June 2016, 400 kV Bois-Tollot –Verbois, trees on the line	-44%/80 ms RTE measurement at Bois Tollot	Below 20% of $U_{nominal}$
30. June 2016, 400 kV CHAMOSON - BOIS-TOLLOT, monophase	-40%/80 ms, measured at LHC	Between 50-20% of $U_{nominal}$
17. September 2016, Creys-Genissiat	-50%/70ms RTE measurement at Bois Tollot	Between 70-50% of $U_{nominal}$
14. June 2017, 225 kV line Genissiat – Vouglans, three-phase	-11%/80 ms measured at LHC	Above 90% of $U_{nominal}$
29. June 2017, 225 kV Cornier – Genissiat – Cruseilles, three phase dip measured at LHC	-20%/80 ms measured at LHC	Between 90-80% of $U_{nominal}$

10.3 Additional information for the cryogenic system case study

LHC experience, cryogenic system and voltage dips

The following example event shows the voltage dip sensitive of ASDs.

On 1. May 2012 two consecutive two-phase dips on the 400 kV line Chamoson-Bois Tollot occurred
(-38%/70 ms and after 1.4s -44%/100 ms).

Due to this event the ASD driven cold compressors at P2 stopped.

The remarks obtained from the logbook are: cryogenic recovery took hours but recovered before injector chain, and the cryogenic support team considers readjusting of ASD tolerance.

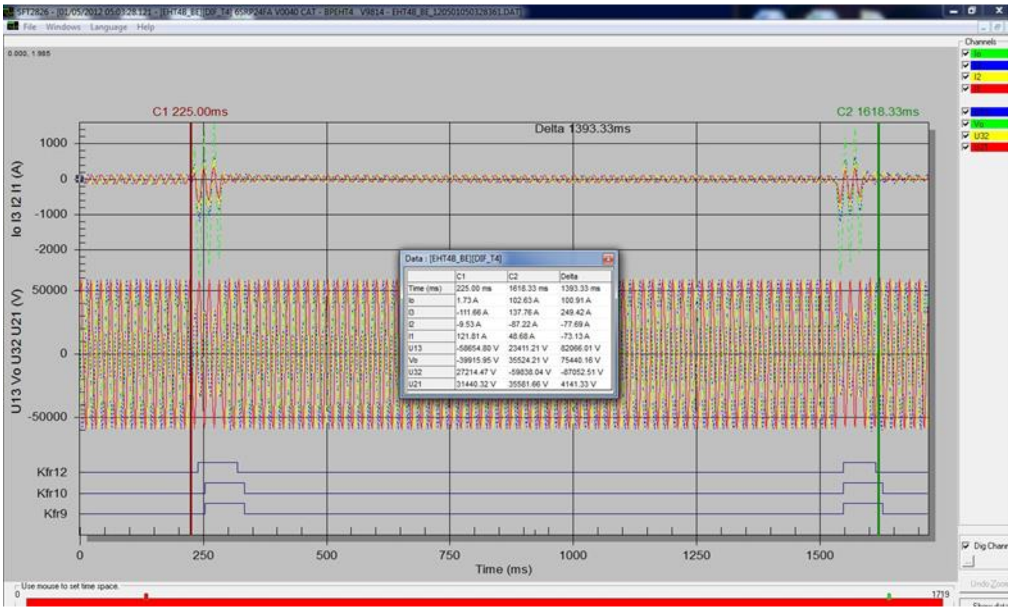

Figure 82: Measurement at the 66 kV level at CERN, two consecutive dips are measured.

Inertia of the centrifugal compressor

The centrifugal compressor consists of pure axe parts and impeller parts. One pure axe part and one impeller part form one compressor step.

For the pure axe part, the inertia is calculated with by using a homogeneous cylinder.

For the impeller part (consist of an axe and wings on it), a mass distribution factor is used to estimate their inertia.

This factor is given by:

$$factor_{mass\ distr.} = 2 \cdot x \cdot y\text{^}2 + 1 \tag{34}$$

Here is x the relation of the mass of the impeller wings to the impeller axe-part.

Y is the relation of the equivalent radius for the mass-concentration point of the wings, to the mass of the impeller axe-part (due to its non-linearity this parameter is hard to estimate).

For the bearings 5% of the sum is added.

This gives total the total inertia for seven compressor steps, of 20 kgm².

	Axe		Impeller		Impeller wings				
density	7500	kg/m^3	7500	kg/m^3	x				
radius	0,1	m	0,1	m	Mass relation: wings to axe				
length	0,1	m	0,03	m	1,8				
mass distr. factor	1		8,569						
					y				
	Mass		Mass		Radius relation: equ. radius mass point of wings to axe				
	23,562	kg	7,0686	kg	1,45				
	Inertia		Inertia						
	0,11781	kgm^2	2,59515736	kgm^2					
Inertia 1-step	2,71296736	kgm^2							
Inertia 7-steps	18,9907715	kgm^2							
bearings add 5%	0,94953857	kgm^2							
Total inertia	19,9403101	kgm^2							

10.4 FODO cell

To guide the particle beam around the arcs, several types of magnets need to aligned correctly. The elementary beam guiding structure is the focusing-defocusing (FODO) cell. Each FODO cell has a length of 213m and consists of 12 dipoles, 2 quadrupoles (and other magnets as sextupoles, octupoles, etc.), required for beam guiding. The arcs are filled with the FODO cells, whereby the magnets within are connected electrically together into circuits. This gives then a certain number of dipole circuits and quadrupole circuits. For the dipoles, safety and optimisation considerations lead to a number of up to 44 series connected magnets [123] [57]. For the quadrupoles, a circuit should be as long as to cover half of the long arc. This gives the number of circuits, presented in the table below:

Table 33: Number of circuits for the lattice main dipoles and lattice main quadrupoles.

	Number dipole circuits with 44 in series	Main quadrupole circuits with 37 in series
A short arc has 15 FODO cells (=180 dipoles, 30 quadrupoles	4 (+1 circuit with less than 44 series connected)	1
FCC has 4 short arcs in total	16	4
A long arc has 36,5 FODO cells (=438 dipoles, 73 quadrupoles) →1 quadruple circuits has up to 37 magnets	10	2
FCC has 8 long arcs in total	80	16
Total number of magnet circuits is:	**96** (+4 short circuits)	**20**

10.5 Loss-model for the analysis of the MPS losses

For the loss model the following nomenclature is used

The losses are divided into the **no-load losses P_0** (e.g. iron losses in a transformer), and the load-dependent losses.

P_{fe} for iron losses in transformer core (50 Hz and middle frequency transformers).

P_{aux} for auxiliaries' losses in power electronic based converters.

For the dual active bridge, a special case for losses during incomplete zero voltage switching (ZVS) are considered. They are maximal at $P_{load}=0$. When the load level reaches 20% of P_{rated}, these losses are zero.

$P_{snubber}$ for snubber losses during incomplete ZVS.

The **load-dependent losses** at **P_{load}** of the respective equipment are split into:

P_{cu} for copper losses in transformer windings (50 Hz and middle frequency transformers).

P_{sw} for switching losses in power electronics (IGBTs, diodes).

P_{cond} for conduction losses in power electronics (IGBTs, diodes) and resistive losses in the AC grid.

$P_{passives}$ for losses in filters in power electronic based converters.

All equipment loss values used here refer to its rated power.

To represent the losses for the full load-range an interpolation between $P_{load}=0$ and $P_{load}=P_{rated}$ is used. See the following three sub-chapters.

10.5.1 50Hz-Transformers

For the distribution grid transformer, a P_{fe} of 0.25% (iron losses), and a P_{cu} of 2% of P_{rated} are assumed.

For the converter transformer a P_{fe} of 0.5%, and a P_{cu} of 3.5% at P_{rated} are assumed.

The power losses in between $P_{load}=0$ and $P_{load}=P_{rated}$ follows the curve represented by the formula below.

$$P_{total\ loss} = P_0 + \left(\frac{p_{load\ transformer}}{P_{rated}}\right)^2 \cdot (P_{cu}) \tag{35}$$

10.5.2 IGBT based power electronic converter stages

For the loss analysis of the dual active bridge (DAB), a loss breakdown for a 100 kW DAB prototype as shown in [124] is used. The overall losses are split into iron losses (middle frequency transformer), switching losses (P_{sw}) and conduction losses (P_{cond}).

P_{cond} losses are proportional to a square of the current I and contain P_{cu} of the transformer, and conduction losses of the switches.

For the P_{sw} losses, Semikron estimated a linear (~I) relation [125]. Akagi assumed in [124] three components, a linear, a quadratic and an independent term. He concluded the ~I² term to be the most dominant.

At P_{load}=0, the losses contain iron losses and snubber losses due to incomplete ZVS. Full ZVS requires a minimum current in the power transfer inductor to charge and discharge a pair of snubber capacitors. At P_{load}~20% of P_{rated} full ZVS is assumed, and no snubber losses are occurring.

Thus, the total loss behaviour during the magnet cycle shown in Figure 43, with the load ranging in between P_{load}=0 and P_{load}=P_{rated}, is described by the formula shown below:

For the **single-phase AC-DC, DC-DC H-bridges** the dual active bridge loss analysis is the basis (as the DAB is the combination of two H-bridges with a middle frequency transformer). The ZVS-behaviour and the magnetic losses are not existent in these topologies, thus also no P_{fe} and $P_{snubber}$ are occurring.

$$P_{total\ loss} = P_0 + \left(\frac{p_{load\ H-bridge}}{P_{rated}}\right)^2 \cdot (P_{sw} + P_{cond}) \tag{36}$$

The DC-DC H-bridge for the magnet supply has in the flat top phase a particular low efficiency. This is due to the low magnet voltage (~12 V) and high magnet current (~11.4 kA). In the loss analysis, a higher loss value is considered for the flattop phase.

For the **three-phase active front end (AFE)**, losses at passive components are accounted in addition to switching and conduction losses [126]. Their total loss behaviour between P_{load}=0 and P_{load}=P_{rated}, is described by the formula shown below:

$$P_{total\ loss} = P_0 + \left(\frac{p_{load\ AFE}}{P_{rated}}\right)^2 \cdot \left(P_{sw} + P_{cond} + P_{passives}\right) \tag{37}$$

10.5.3 Summary of all loss model parameters

The table below shows for each of the conversion stages, the assumed loss numbers.

Table 34: Parameters for the loss model

Equipment	Components of losses and relation to the load	Losses at P_{load}=0	Losses at P_{load}=P_{rated}
AC grid, upstream of 36kV	SCC=1000MVA; X/R=1.34 P_{cond} ~I^2	0	1,8%
Distribution grid transformer	P_{fe}=constant, P_{cu} ~I^2	0,25% (only P_{fe})	2,25% (P_{fe}+P_{cu})
Converter transformer	P_{fe}=constant, P_{cu} ~I^2	0,5% (only P_{fe})	4% (P_{fe}+P_{cu})
AC-DC active front end, 3-phase	P_{sw}, P_{cond} and $P_{passives}$ ~I^2	0,5% (P_{aux})	6% (P_{aux} +P_{cond}+ P_{sw}+$P_{passives}$)
Dual active bridge	P_{sw} and P_{cond} ~I^2; $P_{snubber}$~I; P_{aux}=constant	2% ($P_{snubber}$ + P_{fe} + P_{aux})	7% (P_{aux} + P_{cond}+ P_{sw} + P_{fe})
AC-DC H-bridge	P_{sw} and P_{cond} ~I^2; P_{aux}~constant	0,25% (P_{aux})	5% (P_{cond} + P_{sw})
DC-DC H-bridge	P_{sw} and P_{cond} ~I^2; P_{aux}=constant	0,25% (P_{aux}) during ramp up and down; 2% (P_{cond} special case for flat top at P_{load}=1.3 MW)	5% (P_{cond} + P_{sw})

The figure below shows the losses of stages in the MPS in dependence of their rating, on the level of a single power converter powering of one main bending dipole magnet circuit.

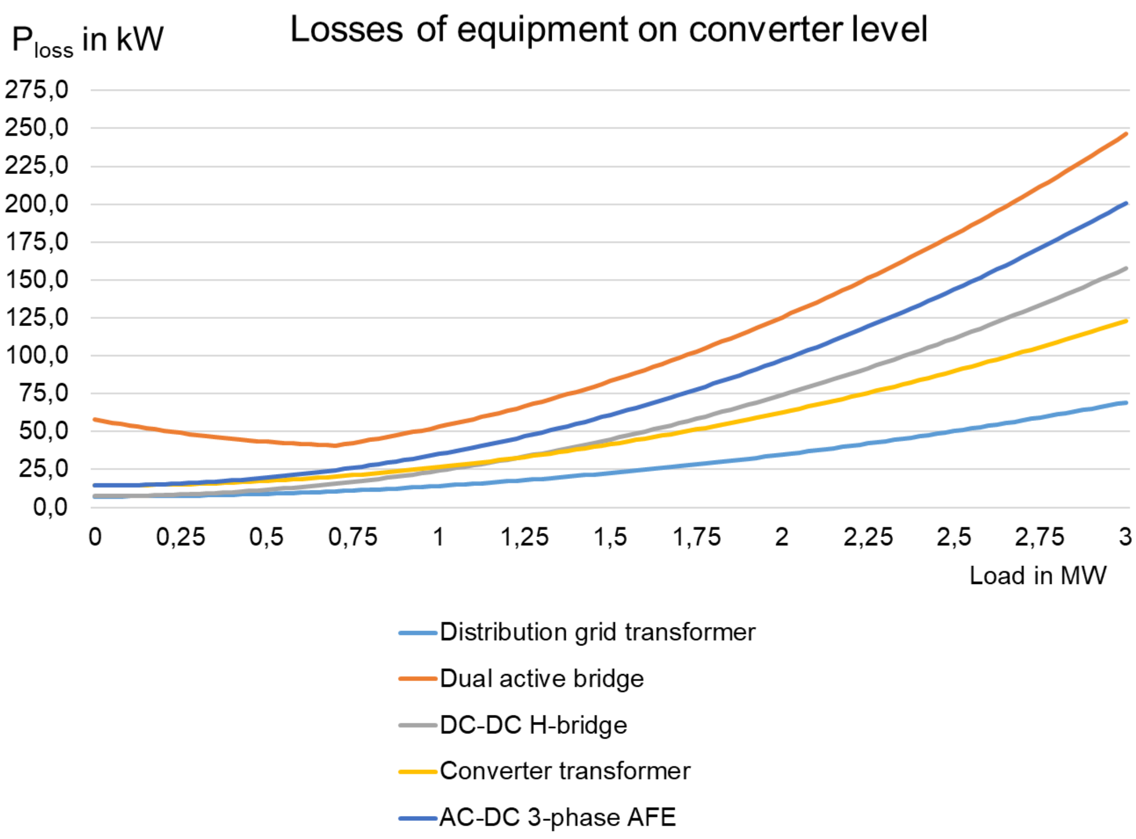

Figure 83: Losses of the equipment used in the MPS, depending on the loading. Results are shown on the level of one converter powering one main bending magnet circuit.

10.6 Reliability data from LHC

The data was extracted from the logbook of the converters. To have a better estimation, the following years of operation where taken: 2015, 2016, 2017 and 2018.

Decisions were taken, which of the recorded logbook failure entries are accounted now to the sphere of the converter and which ones are rather accounted to the outside domain. See also the fault tolerant design for CERNs FGClite in [127, 128].

Table 35: Mean time to failure for the RPTE converter

Year	2015	2016	2017	2018
Number of faults	0	3	7	4
Days of operation	260	267	232	260
Number of converters	8	8	8	8

MTBF in hours		17 088	6 363	12 480

The non-modular thyristor based RPTE is the converter for the main bending dipoles of LHC.

For FCC, a modular converter based on switch mode modules is foreseen. As an orientation, the table below shows the LHC data for a low current switch mode converter.

Table 36: Mean time to failure for the RPLA converter

year	2015	2016	2017	2018
Number of faults	5	4	10	2
Days of operation	260	260	232	260
Number of converters	768	768	768	768
MTBF in hours	958 464	1 198 080	479 232	2 396 160

10.7 Dipole converter simulations for other conditions than in the main chapter

Following chapter 7.3.4, here are simulation results with different parameters than in the table shown in 7.3.2.1. See the table below.

Table 37: Changed parameter with respect to chapter 7.3.2.1

Item	Unit	Value
R_{batt}	mΩ	9.67

The simulation results are shown below.

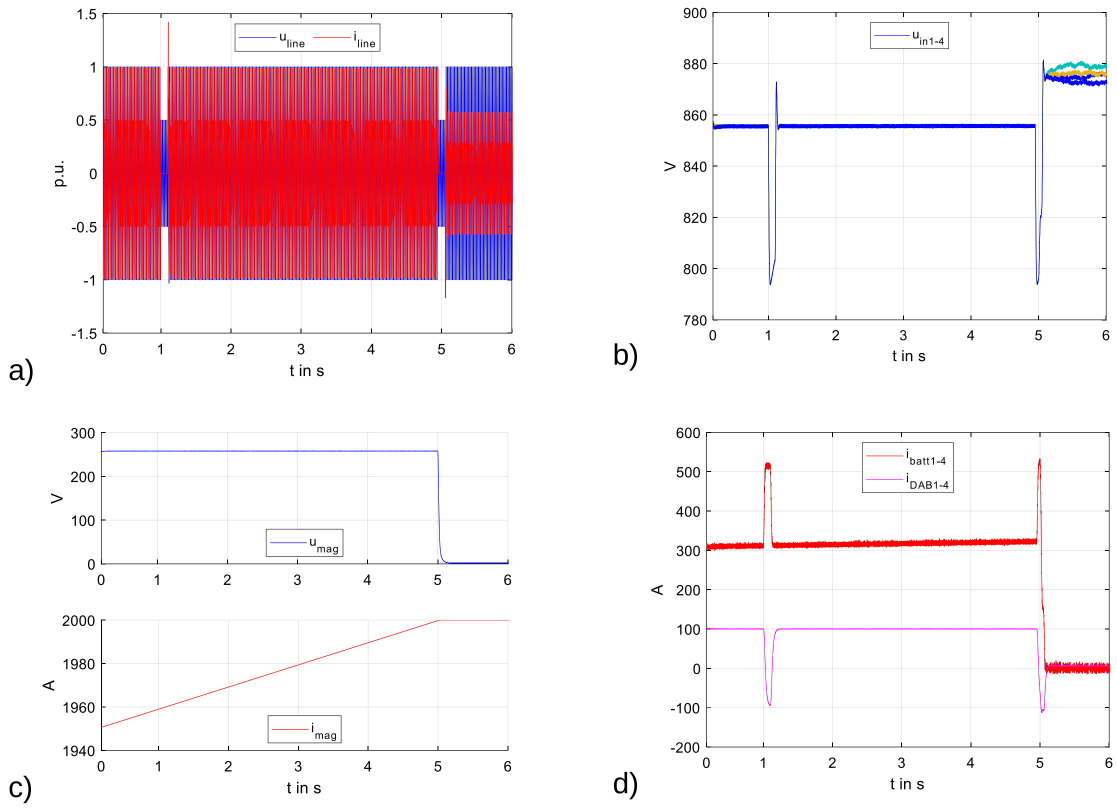

Figure 84: Simulation results following chapter 7.3.4 with different parameters. Shown are: a) AC grid line-line voltage and line current; b) input voltages of the converter modules; c) magnet current and voltage; d) current from the DAB and the battery.

The system is at its borders. Especially during the flat-top phase (starting at t=5 s), the battery ripple is relatively high and the IVS is struggling to keep the input voltages balanced.

However, i_m and u_m do not suffer at all from the voltage dip and the DC voltage of stage 2 (sum of all input voltages u_{in}) is kept within the +/- 10% band.

10.8 Calculations for chapter 6.9

The aim is to show mathematically the relation between supplying infrastructure rating P_i and the required energy storage capacity W_{es} for both ramping methods.

10.8.1 Constant voltage ramping

In constant voltage ramping, a **constant voltage** on the inductance of the magnet circuit is applied:

$$\frac{di_m(t)}{dt} = \frac{i_m(t = T_r)}{T_r} = \frac{11441A}{1200s} = 9.53\frac{A}{s}$$
$$\rightarrow u_{L_m} = const. = L_m \cdot \frac{di_m}{dt} = 25.08H \cdot 9.53\frac{A}{s} = 239V \tag{38}$$

The power rating P_i of the supplying infrastructure has to be high enough to cover the power demand $p_{stage\ 3}$, thus covering losses in MPS stage 3 and the magnet circuit. This way the energy storage can be dimensioned without considering losses outside of the energy storage (see chapter 6.6.2). For one converter $p_{stage\ 3}(t)$ is:

$$p_{stage\ 3}(t) = p_m(t) + p_{loss\ stage\ 3}(t) \tag{39}$$

Whereby the power on the magnet circuit p_m is respecting the ohmic losses in the magnet circuit with:

$$p_m(t) = u_m(t) \cdot i_m(t) = \{u_{L_m}(t) + i_m(t) \cdot\ R_m\} \cdot i_m(t) \tag{40}$$

The losses of the magnet circuit can be calculated with:

$$p_{loss\ m}\ (t) = R_m \cdot i_m(t)^2 \tag{41}$$

The peak losses of the magnet circuit can be calculated with:

$$P_{loss\ m\ max} = R_m \cdot i_m(T_r)^2 = 0.001Ohm \cdot 11441A^2 = 130.8kW \tag{42}$$

The peak power required to ramp up the magnet with constant voltage (including $P_{loss\ m\ max}$) is:

$$P_{m\ max} = \{u_{L_m}(T_r\ ) + i_m(T_r\ ) \cdot\ R_m\} \cdot i_m(T_r\ ) = \{239V + 11441A \cdot 1m\Omega\} \cdot 11441A = 2.87MW \tag{43}$$

With the losses for the converter output stage (stage 3 of the MPS):

$$p_{loss\ stage\ 3}(t) = \begin{cases} P_0 + \left(\frac{p_m(t)}{P_{m\ max}}\right)^2 (P_{sw} + P_{cond.}) \\ with\ P_0 = 0.25\%, (P_{sw} +\ P_{cond.}) = 5\%\ of\ P_{m\ max} \end{cases} \tag{44}$$

$$P_{loss\ stage\ 3\ max}(t) = 0.0525 \cdot 2.87MW = 150.6kW \tag{45}$$

This gives the total power demand of the output stage (stage 3) of one converter.

$$P_{stage\ 3\ max}\ = P_{m\ max} + P_{loss\ stage\ 3\ max} = 3.02MW \tag{46}$$

For 10 converters in total, this gives a peak power of 30.2MW, which need to be supplied by the full MPS and the overlaying AC grid above 36kV, thus P_i needs to be rated to $P_{stage\ 3\ max}$.

If the rating **P_i** is to be reduced due to energy storage, the time **$t_i(x)$** until the power demand $p_{stage\ 3}$ reaches the limit **$x=P_i$** is calculated by using the relations:

$$\begin{gathered} with\ u_{L_m} = const. \\ \rightarrow i_m(t) = \frac{u_{L_m}}{L_m} \cdot t \end{gathered} \tag{47}$$

Which leads then to an explicit function of t for the $p_{stage\ 3}$:

$$\begin{gathered} p_{stage\ 3}(t) = \left\{ P_0 + \left(\frac{(U_{L_m} + \frac{u_{L_m}}{L_m} \cdot t \cdot R_m) \cdot \frac{u_{L_m}}{L_m} \cdot t}{P_{m\,max}} \right)^2 (P_{sw} + P_{cond.}) \right\} + \\ + \left\{ u_{L_m} + \frac{u_{L_m}}{L_m} \cdot t \cdot\ R_m \right\} \cdot \frac{u_{L_m}}{L_m} \cdot t = x \rightarrow t_i(x) \end{gathered} \tag{48}$$

For the exact solution, a polynomic function of order n=4 needs to be solved. In order to show a simplified solution, all losses are neglected now.

This gives for ti(x) the simple relation:

$$t_i(x) = \frac{x \cdot L_m}{{u_{L_m}}^2} \tag{49}$$

Using now also a simplified $p_{stage\ 3}$ power demand the following is obtained:

$$p_{stage\ 3}(t) = \{u_{L_m}\} \cdot \frac{u_{L_m}}{L_m} \cdot t \tag{50}$$

The energy transferred by the supplying infrastructure with the power rating **x** during a full ramp up is shown below. Until the time $t_i(x)$, the supplying infrastructure can supply the total power demand $p_{stage\ 3}$:

$$W_i(x) = \int_{t=0}^{t_i(x)} p_{stage\ 3}(t) \cdot dt + \int_{t_i(x)}^{T_r} x \cdot dt \tag{51}$$

The total losses during the ramp-up are calculated with

$$W_{loss} = \int_{t=0}^{T_r} \{p_{loss\ stage\ 3}(t) + p_{loss\ m}\,(t)\} \cdot dt \tag{52}$$

This gives finally the required energy storage capacity with:

$$W_{es} = W_m + \ W_{loss} - W_i \tag{53}$$

10.8.2 Constant power ramping

The calculation for this ramping method differs from constant voltage ramping, as it foresees a constant $p_{stage\ 3}$ during a large part of the ramp-up. In the beginning, the current rises faster by applying the maximal output voltage of stage 3. The condition is that after the ramp-up, the energy for the magnet circuit, and the losses are covered. Considered are losses in MPS stage 3 and the magnet circuit. This way the energy storage can be dimensioned without considering losses outside of the energy storage (see chapter 6.6.2).

To determine the time $\mathbf{t_{i\ max,\ cp}}$ the and the upper power limit $P_{stage\ 3\ max}$ the equation below needs to be solved:

$$\int_0^{t_{i\ max}} p_{stage\ 3}(t) \cdot dt + \int_{t_{i\ max}}^{T_r} P_{stage\ 3\ max} \cdot dt = W_{mag} + W_{loss} \tag{54}$$

The first integral is the part where the voltage on the magnet circuit u_m is the maximal output voltage $u_{m\ max}$ of stage 3. For one converter, the power demand at the output modules p(t) is:

$$p_{stage\ 3}\,(t) = \left\{ P_0 + \left(\frac{\frac{u_{m\ max}^2}{R_m}(1 - e^{-\frac{R_m}{L_m} \cdot t})}{p_{m\ max,\ cp}} \right)^2 (P_{sw} + P_{cond.}) \right\} + \frac{u_{m\ max}^2}{R_m}(1 - e^{-\frac{R_m}{L_m} \cdot t}) \tag{55}$$
$$t = t_{i\ max} \rightarrow p_{stage\ 3}\,(t) = P_{stage\ 3\ max}$$

With the explicit function in t above, the integral border t_{imax} can be found by setting $p_{stage3}(t) = P_{stage\ 3\ max}$, and then solving the equation for t_{imax}.

The second integral is over the constant power $P_{i\ max,\ cp}$. After the ramp-up time T_r, the sum of the energy stored in the magnet circuit (W_m) and all losses ($W_{loss\ m}$ and $W_{loss\ stage\ 3}$) is transferred.

Solving the formula (54) with the integral borders found in (55) leads to:

$$P_{stage\ 3\ max,\ cp} = P_{i\ max,\ cp} = 1.8 MW \tag{56}$$

With integrated energy storage, $\mathbf{P_{i\ max,\ cp}}$ could be reduced to $\mathbf{x=P_i}$.

The time $\mathbf{t_i(x)}$ until the now **reduced** power limit $\mathbf{x=P_i}$ is reached is even faster, and is calculated with:

$$u_m(t \le t_i) = u_{m\,max}$$
$$i_m(t) = \frac{u_{m\,max}}{R_m}(1 - e^{-\frac{R_m}{L_m} \cdot t})$$
$$p_{stage\,3}(t) = \left\{ P_0 + \left(\frac{\frac{u_{m\,max}^2}{R_m}(1 - e^{-\frac{R_m}{L_m} \cdot t})}{p_{m\,max,\ cp}} \right)^2 (P_{sw} + P_{cond.}) \right\} + \frac{u_{m\,max}^2}{R_m}(1 - e^{-\frac{R_m}{L_m} \cdot t}) = \boldsymbol{x} \rightarrow t_i(x) \quad (57)$$

For the exact solution, the quadratic function needs to be solved. In order to show a simplified solution, all losses are neglected and the current is assumed to rise linearly.

This gives for ti(x) the simple relation:

$$t_i(x) = \frac{x \cdot L_m}{{u_{m\,max}}^2} \quad (58)$$

Using now also a simplified $p_{stage\ 3}$ power demand the following is obtained:

$$p_{stage\,3}(t) = \{u_{m\,max}\} \cdot \frac{u_{m\,max}}{L_m} \cdot t \quad (59)$$

The energy transferred by the supplying infrastructure with the power rating **x** during a full ramp up is shown below. Until the time $t_i(x)$, the supplying infrastructure is able to supply the total power demand $p_{stage\ 3}$:

$$W_i(x) = \int_{t=0}^{t_i(x)} p_{stage\,3}(t) \cdot dt + \int_{t_i(x)}^{T_r} x \cdot dt \quad (60)$$

The total losses during the ramp-up are calculated with

$$W_{loss} = \int_{t=0}^{T_r} \{p_{loss\,stage\,3}(t) + p_{loss\,m}\,(t)\} \cdot dt \quad (61)$$

This gives finally the required energy storage capacity with:

$$W_{es} = W_m + W_{loss} - W_i \quad (62)$$

10.8.3 Minimum power rating of the supplying infrastructure, $P_{i\ min}$

The minimum power rating $P_{i\ min}$ is the same for both, constant voltage and constant power ramping and is calculated by considering:

- the minimum charging time in case the energy storage is empty (see chapter 6.2),
- the losses of the magnet circuit (on converter level),

- the losses of stage 3 of the MPS (on converter level)

$$P_{i\,min} = max\{p_{\min charging\ if\ ES\ is\ empty}, p_{\min to\ cover\ losses}\} = \\ = max\{456kW, 130.8kW + 151.2kW\} = 456kW \tag{63}$$

10.9 Cost model data for chapter 6.9

The basis of the cost model for all equipment is that the total costs consist of constant part and a part depending linearly on the power rating.

Stating the model with costs = k0+k(x) with x being the power rating in kW, appropriate data to derive k0 and k(x) are taken.

For the distribution grid transformer in the power range of 4.5-30.2MW, k0 and k(x) are based on manufactures websites [98, 129] .

- 135kV/36kV transformer: k(x)=23.1€/kW (only variable costs are considered as the transformer is needed also for other loads at the FCC powering point).
- 36kV/xxx kV transformer: k0=69 000€, k(x)=23.1€/kW

For the central rectifier stations in the power range of 4.5-30.2MW, the k0 and k(x) are based on price inquires at ABB and Secheron.

- Diode: k0=93 000€, k(x)=7€/kW
- Bidirectional AFE: k0=400 000€, k(x)=50€/kW

The converter topology components on module level (power range is 38-251kW) i.e. converter transformer, AC-DC and DC-DC single stages are based on the CERN designed converters SIRIUS and PANDORA, in the following schema:

- Converter module single conversion stage (AC-DC and DC-DC single phase). The cost is based on the SIRIUS and PANDORA H-bridge.
- Converter module single conversion stage (AC-DC three-phase). The cost is based on the SIRIUS and PANDORA H-bridge with +25% as overhead.
- Converter module double conversion stage (DC-DC with isolation transformer, two full bridges). The cost is based on the SIRIUS and PANDORA H-bridge with +50% as overhead.

10.10 Power density values

For the comparison of powering topologies, the following power density values are used.

The weight and volume taken for 50Hz components are taken from manufacturer specifications, and the transformer-rectifier combination is from literature.

Table 38: Assumed power density values for

line frequency transformers, and transformer-rectifier combinations

	Power density	Specific power density
	kg/kW	dm3/kW
Line frequency transformer and rectifier combination[37]	3.9	4.5
1MVA 50Hz cast resin transformer from company SGB[130]	2.65 (average value from the 1MVA class)	3.2
250kW DC-DC Full bridge, non-isolated, with 600V DC bus filter capacitor 100mF, from Electronicon	0.5 (estimated)	0.5 (estimated)

Calculation example: Variant A stage 2, a 38kW rectifier-transformer module has a weight of 3.9kg/kW*38kW=148kg and a volume of 4.5dm³/kW*37.5kW=171dm³.

Calculation example: Variant A stage 1, a 4.5MW transformer has a weight of 2.65kg/kW*4.56MW=12.1tons and a volume of 3.2dm³/kW*4.56MW=14.6m³.

For solid state transformer, the reported values from scientific research prototypes are taken.

Table 39: Solid State Transformer and their reported power densities from literature

	Power density	Specific power density		Power density	Specific power density
	kg/kW	dm3/kW		kg/kW	dm3/kW
SST, AC-DC-DC			SST, DC-DC		
ALSTOM 1.5 MW prototype [131]	2.06	2.15	5 kW series parallel resonant [132]		0.1
Bombardier 3MW prototype [39]		0.58, no line filter, no cooling	Estimated from a 3D CAD model [133]	0.72	0.53
1 MVA SST prototype, comparison with 50 Hz transformer [37]	1.3	1.6	15 kW full bridge unidirectional converter [134]		0.65
ABB 1.2 MW prototype [135]	3.75	2, estimated from picture	180 kW SPRC module for long puls modulator [136]		0.22

Table 40: Assumed power density values for the Solid State Transformer based topologies

Power density	Specific power density	Power density	Specific power density
kg/kW	dm3/kW	kg/kW	dm3/kW
2	2	1.5	1.5
DC-DC-AC: unidirectional or bidirectional, with mf isolation transformer; DC-DC-DC: unidirectional or bidirectional, with mf isolation transformer		DC-DC: unidirectional or bidirectional, with mf isolation transformer	
Note: a value close to the ALSTOM prototype is chosen, other sources show values above but also below.		Note: the assumed values are rather conservative assumptions as higher densities are reported in literature. In case of a DC grid supply, the AC-DC stage including the filter stage is shifted to the central rectifier and does not contribute to the weight and size of the SST.	

Calculation example: Variant B stage 2, a 38kW AC-DC-DC module has a weight of 2kg/kW*38kW=76kg and a volume of 2dm^3/kW*38kW=76dm^3.

Calculation examples for case study 1:

The AC based powering of the general 50Hz load is done by a transformer (18kV/0,4kV). The load of 4.4MW leads then to a volume of 3.2dm^3/kW*4400kW=14.1m^3 and also to a weight of 2.65kg/kW*4400kW=11.7tons.

The DC-based powering of the general 50Hz load is done by a DC-DC-AC solid-state transformer. The load of 4.4MW leads then to a volume of 2dm^3/kW*4400kW=8.8m^3 and also to a weight of 2kg/kW*4400kW=8.8tons.

The AC based powering of the low inductance superconducting magnets is done by a distribution transformer, a transformer-rectifier combination and a unidirectional DC-DC converter. To a rating of 1MW, this gives a volume of (3.2+4.5+1.5) dm^3/kW*1000kW=9.2m^2 and a weight of (2.65+3.9+1.5) kg/kW*1000MW=8.05tons.

The DC-based powering of the low inductance superconducting magnets is done by a unidirectional DC-DC solid-state transformer. To a rating of 1MW, this gives a volume of 1.5dm^3/kW*1000kW=1.5m^3 and a weight of 1.5kg/kW*1000MW=1.5tons.

10.11 Case study 1: existing particle accelerator, detailed load items found at LHC point 2

The table below summarizes all load found at the LHC point 2. For the case study the load is summarized according to their category.

Table 41: Detailed load representation at LHC point 2

Load and related optical or general function	Electrical parameter and powering equipment	Location of the power converter, voltage dip sensitivity, and other additional remarks
MAGNETS		
Muon arm spectrometer, normal conducting	I=33kA, U=170V, P=5.6MW; Thyristor converter	On the surface; Current protection of powering equipment triggers converter shut down; new proposal is switch mode converter; no polarity switch necessary anymore
Dimuon arm spectrometer, normal conducting	I=6.5kA, U=950V, P=6.2MW; Thyristor converter	On the surface; Current protection of powering equipment triggers converter shut down during a dip
Compensator, In total three normal conducting magnet circuits	I=650A, U=160V P=0.1 MW per circuit; Thyristor converter	On the surface; Highly dip sensitive load, two circuits are monitored by the FMCM
Insertion quadrupoles, 6 superconducting magnet circuits	I=4kA, U=8V P=32 kW per circuit; Switch mode converter, Input stage: 3~AC 400V/90A diode bridge	Underground gallery next to the shaft
Insertion quadrupoles, 16 superconducting magnet circuits	I=6kA, U=8V, P=48 kW per circuit Switch mode converter, Input stage: 3~AC 400V/90A diode bridge	Underground gallery next to the shaft
Insertion dipoles and inner triplet superconducting circuits, 4+2	I=8kA, U=8V, P=64 kW per circuit; Switch mode converter, Input stage: 3~AC 400V/90A diode bridge	Underground gallery next to the shaft
Orbit correctors 60A 8V Orbit correctors 752 converters in total	I=60A, U=8V P=0.5 kW per circuit; Switch mode converter, Input stage: 3~AC 230V/2A diode bridge	Arc
Trim Quadrupoles, SSS correctors, Spool pieces, 12 circuits	I=600A U=10V P=6 kW per circuit; Switch mode converter	Underground gallery next to the shaft

Octupoles, orbit correctors 50+8 circuits	I=120A, U=10V P=1.2 kW per circuit; Switch mode converter, 4Q	Underground gallery next to the shaft; tunnel-cavern junction
Main focusing/defocusing quadrupoles, 4 superconducting magnet circuits	I=13kA, U=18V P=234 kW per circuit Switch mode converter, 1Q	Underground gallery next to the shaft; Apparent inductance per circuit is 0.286H
Main bending dipole, 2 superconducting magnet circuits	I=13kA, U=190V P=2.5 MW per circuit Thyristor converter, 2Q	Underground gallery next to the shaft; Apparent inductance is 15H, magnet energy recovery
INJECTION LINE FROM SUPER PROTON SYNCHROTRON		
Normal conducting magnets for the Ti2 transfer line	I=5400A, U=1800V; Thyristor converter	On the surface; Highly pulsating active and reactive load
STATIC VAR COMPENSATOR		
	Q=25Mvar	Surface; compensation of the pulsing Q load of the injection line
CRYOGENIC SYSTEM INSTALLED AT LHC-POINT 2		
Cold compressor	P=5-10kW; Connected via an adjustable speed drive	Highly dip sensitive; centrifugal compressors
Warm compressor	The total installed power of all 13 machines is 7.55MW; directly connected to the 3.3kV 3~AC grid	Screw type compressors
GENERAL LOAD		
Cooling and ventilation, auxiliaries	The total installed rating is 7.5MVA; Connected via 3~AC transformer 18\0.4kV	surface